UNIVERSITÉ DE SHERBROOKE
Faculté de génie
Département de génie chimique et de génie biotechnologique

Barrière thermique de $Ba(Mg_{1/3}Ta_{2/3})O_3$ dépose par projection plasma de précurseurs liquides : contrôle des phases et de la microstructure

$Ba(Mg_{1/3}Ta_{2/3})O_3$ Thermal Barrier Coating Deposited by Liquid Precursor Plasma Spray: Phases and Microstructure Control

Thèse de doctorat ès sciences appliquées

Spécialité : génie chimique

HUIDONG HOU

Jury : Jocelyn Veilleux, ing., PhD (Directeur)
François Gitzhofer, ing., PhD (Co-directeur)
Christian Moreau, PhD
Gessie Brisard, PhD
Nadi Braidy, ing., PhD

Sherbrooke (Québec), Canada

Juin 2020

À mes parents et ma mère patrie

la République populaire de Chine

RÉSUMÉ

Cette étude explore une nouvelle voie pour déposer des revêtements d'oxydes complexes pour les barrières thermiques (TBC) $Ba(Mg_{1/3}Ta_{2/3})O_3$ (BMT) à partir de précurseurs liquides. Les dépôts sont faits en utilisant la projection par plasma radiofréquence (RF) à couplage inductif, qui diffère de la technique la plus fréquemment utilisée dans le domaine, à savoir la projection plasma à air (APS) en courant continu (DC).

Parmi les matériaux oxydes connus, le BMT a le point de fusion le plus élevé (2900-3100 °C). En conséquence, il est considéré comme l'un des matériaux candidats TBC les plus prometteurs pour le domaine aéronautique. En raison des limites imposées par la décomposition des matières premières du BMT, principalement causée par l'évaporation du Mg pendant le processus APS, et à la faible durée de vie des revêtements lamellaires denses, des précurseurs liquides ont été choisis comme matière première dans ce travail. En effet, ils peuvent atténuer la décomposition des matières premières en ajoutant un excès de Mg dans le mélange initial de précurseurs. En outre, les précurseurs liquides, normalement préparés par des solutions et/ou des suspensions de particules solides à l'échelle nanométrique, facilitent la formation d'une structure colonnaire. Par conséquent, le procédé adopté dans ce travail est nommé projection plasma hybride de suspension (SPS) / précurseur liquide (SPPS). La spectroscopie photoélectronique X (XPS) a été utilisée pour évaluer quantitativement l'évaporation des éléments pendant la projection par plasma. L'analyse thermique thermogravimétrique / différentielle (TG / DTA) a été réalisée pour étudier la formation de BMT. La phase et la microstructure ont été analysées par diffraction des rayons X (XRD) et par microscopie électronique à balayage (SEM), respectivement. Le diagnostic du plasma a été effectué par spectroscopie d'émission optique (OES).

Ce projet a d'abord prouvé que la synthèse d'oxydes complexes et le dépôt de revêtement peuvent se produire simultanément dans les processus hybrides SPS/SPPS ou SPPS. Le mécanisme de formation et la corrélation entre la phase principale du BMT et quatre autres phases secondaires ($BaTa_2O_6$, $Ba_3Ta_5O_{15}$, $Ba_4Ta_2O_9$, $Mg_4Ta_2O_9$) ont été clairement discutés. Les paramètres clés (puissance du plasma, distance de projection, préchauffage du substrat, chimie des précurseurs et taille des particules en suspension) ont été étudiés afin d'optimiser la structure des phases et le taux de dépôt des revêtements projetés.

En outre, cette recherche a démontré la faisabilité de l'application de RF SPPS pour déposer un revêtement de BMT ayant une microstructure contrôlable. Les structures lamellaires, colonnaires et à fissures verticales denses du BMT peuvent toutes les trois être obtenues en ajustant les paramètres de projection. Ce résultat représente une opportunité d'appliquer la projection plasma RF dans le domaine des TBC, en plus de celle de la projection plasma DC et

du dépôt physique en phase vapeur par faisceau d'électrons (EB-PVD). Une courte distance de projection et une distribution bimodale de la taille des gouttelettes atomisées ont été identifiées comme des conditions préalables clés à la formation de colonnes. Des paramètres tels que la rugosité du substrat, la concentration en précurseur et le taux d'alimentation ont été étudiés pour connaître leur influence sur la morphologie en colonne.

Une microstructure TBC distinctive, à savoir avec des grains verticaux, a été trouvée dans les revêtements BMT projetés. Le nouveau matériau et la microstructure se distinguent de tous les autres TBC courants. La structure de phase des grains verticaux a été analysée à l'aide d'une cartographie élémentaire et de diagrammes de phases ternaires BaO-MgO-Ta_2O_5. Le mécanisme de formation des grains verticaux a été discuté en termes de gradient de température. Enfin, sur la base de la microstructure optimisée dans ce travail et d'autres propriétés physiques du coefficient de dilatation thermique, le BMT présente le potentiel d'agir comme un revêtement de protection thermique sur un alliage de niobium dans un avenir prévisible.

Mots-clés : Revêtement, barrière thermique, projection plasma de précurseurs liquides, $Ba(Mg_{1/3}Ta_{2/3})O_3$, synthèse des matériaux, évolution de la microstructure, grains verticaux.

ABSTRACT

This study explores a new route to deposit complex oxide thermal barrier coatings (TBCs) $Ba(Mg_{1/3}Ta_{2/3})O_3$ (BMT) from liquid precursors, using a radio frequency (RF) induction plasma spray (IPS), which differs from the most frequently used technique, direct current (DC) air plasma spray (APS).

Among the known oxide materials, BMT has the highest melting point (2900-3100 °C). Accordingly, it is envisioned as one of the most promising TBC candidate materials for the aeronautic field. Due to the limits imposed by BMT feedstock decomposition mainly caused by Mg evaporation during the APS process, and to the low service lifespan of dense lamellar coatings, liquid precursors were chosen as feedstock in this work. Indeed, they can attenuate feedstock decomposition by adding an excess of Mg into the initial precursor mixture. Furthermore, liquid precursors, normally prepared by solution and/or nanoscale solid particles suspensions, facilitate the formation of columnar structures. Therefore, the process adopted in this work is named hybrid suspension plasma spray (SPS)/ solution precursor plasma spray (SPPS). X-ray photoelectron spectroscopy (XPS) was used to evaluate quantitatively the element evaporation during plasma spraying. Thermogravimetric / differential thermal analysis (TG/DTA) was applied to investigate the BMT formation. The phase and microstructure were analyzed by X-ray diffraction (XRD) and scanning electron microscopy (SEM), respectively. Plasma diagnostic was performed by optical emission spectroscopy (OES).

This project first proved that complex oxide synthesis and coating deposition can occur simultaneously in the Hybrid SPS/SPPS or SPPS processes. The formation mechanism and the correlation between the main BMT phase and four other secondary phases ($BaTa_2O_6$, $Ba_3Ta_5O_{15}$, $Ba_4Ta_2O_9$, $Mg_4Ta_2O_{9)}$ were discussed clearly. The key parameters (plasma power, spraying distance, substrate pre-heating, precursor chemistry and particle size of suspended particles), were explored in order to optimize phase structure and deposition rate of as-sprayed coatings.

In addition, this research demonstrated the feasibility of applying RF SPPS to deposit BMT coating with an adjustable microstructure. Lamellar, columnar and dense vertically-cracked structures of BMT can be tuned by adjusting the spraying parameters. This result represents an opportunity to apply RF plasma spray in the TBCs field, in addition to that of DC plasma spray and EB-PVD. Short spray distance and bimodal atomized droplet size distribution were identified as key prerequisites for column formation. Parameters such as substrate roughness, precursor concentration and feed rate were studied with regards to the columnar morphology.

A distinctive TBC microstructure, namely vertical grains, was presented in the as-sprayed BMT coatings. The novel material and microstructure differentiate themselves from any commonly-seen TBCs. The phase structure of vertical grains was analyzed with the assistance of elemental mapping and BaO-MgO-Ta_2O_5 ternary phase diagrams. The formation mechanism of vertical grains was discussed in terms of temperature gradient. Finally, based on the microstructure optimized in this work and other physical property of thermal expansion coefficient, BMT presents the potential for acting as a thermal protection coating on niobium alloy in the foreseeable future.

Key words: Thermal barrier coatings, liquid precursor plasma spray, $Ba(Mg_{1/3}Ta_{2/3})O_3$, material synthesis, microstructure evolution, vertical grains.

REMERCIEMENTS

Tout d'abord, merci à mes directeurs Jocelyn Veilleux et François Gitzhofer de m'avoir accueilli pour étudier et vivre au Canada. Avant de vous rencontrer, je n'aurais jamais pensé avoir l'opportunité d'étudier à l'étranger. Au cours de la période doctorale de cinq ans, ces deux professeurs m'ont donné des orientations académiques et ont cultivé ma pensée logique. Jocelyn a toléré tous mes défauts et a enduré ma faible maîtrise de l'anglais. Je me souviens encore quand je suis venu au Canada pour la première fois et avoir vu Jocelyn, j'étais tellement nerveux que je ne pouvais pas parler. Tous les articles ont été révisés à plusieurs reprises par Jocelyn, et cela m'a également permis de participer à de nombreuses conférences internationales. Peu importe les problèmes que j'ai rencontré lors des expérience, François savait quelle méthode devait être utilisée pour résoudre le problème réel. Dans mon esprit, François ressemble plus à un magicien. Il y a un vieux proverbe en Chine, « un jour en tant qu'enseignant et toute une vie en tant que père ». En ce moment, je voudrais remercier les deux directeurs pour leurs conseils. Je me souviendrai de votre gentillesse pour la vie.

De plus, j'ai envie de remercier chaleureusement Prof. Nadi Braidy. Merci pour vos précieux commentaires sur ma thèse. Vos commentaires ont grandement amélioré le niveau de ma thèse. Vous êtes le professeur le plus rigoureux et le plus strict que j'aie jamais vu. Je suis content de ne pas être ton étudiant, mais le plus souvent, j'envie tes étudiants.

Je tiens à remercier les membres de mon comité Prof. Christian Moreau, Prof. Gessie Brisard et Prof. Nadi Braidy pour le temps qu'ils ont passé en revue et à approuver ma thèse.

Je suis particulièrement reconnaissant envers Kossi Béré. Quand j'ai commencé les expérimentations, j'étais particulièrement insouciant et ne prêtais pas attention à la sécurité. C'est vous qui me rappeliez sans cesse à l'ordre, suite à quoi j'ai développé de bonnes habitudes de travail. Je crois que cette habitude me sera bénéfique pour la vie. Merci à Stéphane Gutierrez, Charles Bertrand, Sonia Blais et Carl Saint-Louis du Centre de Caractérisation des Matériaux pour leur accueil et leur pédagogie. Merci à Marc G. Couture et André Bilodeau pour votre support technique.

Merci à Sylvie Lebrun, France Auclair, Louise Carbonneau, Louise Chapdelaine et Maude Pilon-Beauregard pour leur soutien administratif d'une efficacité hors norme. Merci de votre patience avec moi pour résoudre mes différents problèmes, malgré la barrière de la langue.

Merci à mon collègue Jérôme Menneveux. Nous avons passé le plus de temps ensemble, à faire des expériences et à aller aux États-Unis pour des conférences. Merci à mes collègues Faranak Barandehfard, Edwin Rodriguez, Romain Fernique, Taki Eddine Aissou, Louis-Simon Perreault et Nicolas Dumaresq pour votre aide altruiste. J'ai toujours su que, lorsque je rencontrais un problème expérimental, je pouvais demander de l'aide à Edwin; et quand j'ai rencontré un problème dans la rédaction, j'ai demandé de l'aide à Taki. Quant aux autres choses particulièrement difficiles, il est certainement juste de trouver Romain. En plus, merci à Fanny Casteignau, c'est toi qui m'as corrigé ma prononciation française, malgré que mon français soit encore très mauvais jusqu'à aujourd'hui.

Le Canada est vraiment un pays magnifique et charmant. J'ai été très triste récemment quand j'ai pensé que j'allais partir d'ici. Je voudrais vraiment vivre ici pour toujours. Je considérerai le Canada comme ma deuxième mère patrie. J'espère que je pourrai revenir ici à l'avenir avec ma famille.

TABLE OF CONTENTS

LIST OF FIGURES

LIST OF TABLES

LIST OF ACRONYMS

Abbreviations	Definition
APS	Atmosphere / Air Plasma Spray
BLT	$BaLa_2Ti_3O_{10}$
BMT	$Ba(Mg_{1/3}Ta_{2/3})O_3$
CMAS	Calcium-Magnesium-Alumina-Silicate
CMCs	Ceramic Matrix Composites
DC	Direct Current
DVC	Dense Vertically Cracked
EBC	Environmental Barrier Coating
EB-PVD	Electron Beam Physical Vapor Deposition
EDS	Energy-Dispersive X-ray Spectroscopy
EMI	Electromagnetic Interference
FOD	Foreign Object Damage
FSZ	Fully Stabilized Zirconia
FWHM	Full Width at Half Maximum
GNC	Glycine Nitrate Combustion
GOF	Goodness of Fit
HVOF	High Velocity Oxygen Fuel
ICDD	International Centre for Diffraction Data
ICP	Inductively Coupled Plasma
ICPS	Inductively Coupled Plasma Spraying
LA-BSE	Low Angle Backscattered Electron
LAMT	$La(Al_{1/4}Mg_{1/2}Ta_{1/4})O_3$
LG	Laser-Glazing
LPPS	Low Pressure Plasma Spray
Nb521	Nb-5W-2Mo-1Zr, wt. %
OES	Optical Emission Spectroscopy
PS-PVD	Plasma Spray-Physical Vapor Deposition
RF	Radio Frequency
SEM	Scanning Electron Microscopy
SLPM	Standard Litre Per Minute
SPPS	Solution Precursor Plasma Spray
SPS	Suspension pPlasma Spray
St	Stokes number
TBCs	Thermal Barrier Coatings

TEC	Thermal Expansion Coefficients
TEOS	Tetraethyl Orthosilicate
TG-DTA	Thermogravimetric- Differential Thermal Analysis
TGO	Thermally Grown Oxide
TIT	Turbine Inlet Temperature
TTB	Tetragonal Tungsten Bronze
T/W	Thrust-to-Weight ratio
VIPS	Vacuum Induction Plasma Spraying
VPS	Vacuum Plasma Spray
WPF	Whole Pattern Fitting
XPS	X-ray Photoelectron Spectroscopy
XRD	X-ray Diffraction
YAG	Yttrium Aluminum Garnet
YSZ	Yttria Stabilized Zirconia

CHAPTER 1

Introduction

An increasing number of high-temperature components are used in modern industrial applications such as turbines, industrial furnaces and engines [1, 2]. In order to increase the thermal efficiency and decrease the energy consumption, the operating temperatures were continuously increased up to a point where it exceeded or approached the melting points of traditional metal, inter-metallic and high-temperature alloys [3]. Rather than investing in the development/usage of new high-temperature alloys, surface modification is identified as the most effective and economical way to withstand the increasing temperatures. As such, thermal barrier coatings (TBCs), as thermal insulation component, are deposited on hot-path components [1]. The state-of-the-art thermal insulation material is yttria stabilized zirconia (YSZ). Still, long period exposure beyond 1200 °C results in sintering of YSZ, which increases the thermal conductivity and Young's modulus, finally decreasing the functionality of TBCs and inducing a tendency for fracture/failure [4]. This initiated a wide-spread exploration of new TBCs materials. Among the candidates is the complex perovskite $Ba(Mg_{1/3}Ta_{2/3})O_3$ (BMT), which is considered the most refractory oxide (melting point around (2900-3100 °C) ever known to science [5]. Compared to YSZ (melting point of 2700 °C), BMT is proposed for service at higher temperatures since its melting point and sintering temperatures are higher. Another interesting features of BMT are good phase stability and large volumetric expansion at high temperature. The later can effectively reduce the thermal expansion mismatch between the metallic substrate and ceramic coating.

The traditional coating preparation method is the air plasma spraying (APS) process which includes many steps for feedstock preparation such as powder synthesis, agglomeration and

sintering. Besides, preparation of BMT coating by APS is usually accompanied by a secondary crystallographic phase, which consists of the decomposed product and can induce the fracture of the coating [4-6]. Furthermore, due to the lamellar coating structure without vertical cracks (release thermal stress), the service life is also severely limited [6].

When replacing the powder feedstock by liquid precursors, either a suspension of nano or submicron particles or a solution of precursors, the resulting plasma spray techniques are called suspension plasma spray (SPS) [7] and solution precursor plasma spray (SPPS) [8]. The increased strength of as-sprayed coating is based upon a micro-structural difference from that of APS. SPS/SPPS coatings normally possess the following characteristics: tiny splats and corresponding short splat boundaries, vertical segmented cracks, non-pyrolyzed precursors. The service life of SPS/SPPS coatings have been improved compared to their APS counterparts [9]. In addition, since commercial BMT powders are not available, adopting the liquid precursor could simplify the feedstock preparation procedure.

The following contents will first describe the history of TBCs materials development and their preparation methods in chapter 2. Chapter 3 will show the project objectives. The experimental results will be discussed and presented in the form of 3 articles published in peer-reviewed journals. These three articles will focus on the phase structure, microstructure and special application of BMT, respectively, and will be presented in chapters 4, 5 and 6. Finally, the conclusions and the recommendations will be discussed in chapter 7.

CHAPTER 2

State of the art

2.1. Thermal Barrier Coatings (TBCs)

2.1.1 Introduction of TBCs

The advanced aero-engines have higher requirements including high performance (thrust-to-weight ratio (T/W)), light weight, low cost, low emission and low noise. It is known that high turbine inlet temperature (TIT) definitely increases the aero-engine efficiency [10]. The austenitic stainless steel was used as the substrate material of blade in the first Whittle engine in year 1941. At that time, the TIT was around 700 °C and the thrust was 450 kg. The TIT of a modern gas turbine is higher than 1500 °C and the thrust exceeds 22 500 kg. The improved engine performance has been accomplished by replacing austenitic steels with high capability material, for example, nickel-base super alloys in blades [11]. Currently, the gas-turbine engines installed for aircraft, marine propulsion and land-based power generation normally use super alloys with melting points ranging from 1230 °C to 1315 °C [12]. The continuous high TIT increases the risk of structural failure caused by material oxidation, melting, creep and thermal fatigue etc. [12]. The protection from high temperature structural failure has been facilitated by three principal materials developments:

> *« dramatic advances in alloy design to produce alloy compositions that are both more creep resistant and oxidation resistant; advances in casting technology that have facilitated not only the casting of large single-crystal super alloy blades and vanes but also the intricate internal channels in the blades to facilitate cooling; and the development of a viable coating technology to deposit a conformal, thermally insulating coating on turbine components» D.R. Clarke et al.* [13].

The developments of the first two fields have been reviewed and discussed extensively elsewhere [14]. Developing new alloys in the first field needs large capital investment. The intricate internal channels design in the second field has special heat transfer geometries and drilling holes, which are used to perform film cooling. In film cooling, a compressor discharges air to cool the hot-path components surface by passing through the drilling holes [15]. The film cooling can decrease the working temperature almost by 200 °C. However, this process adds to the engine burden, which causes a large amount of energy loss. It is better to use this air to perform work in the turbine rather than for cooling purposes.

The third field, thermal insulating coating, has been demonstrated to be a feasible technology for protecting components. This thermal insulating coating made of a thin layer of low-thermal conductivity ceramics is referred to as thermal barrier coating (TBC). Nowadays, TBCs are being applied to offer thermal insulation to metallic substrates from the high temperature gas in the hottest part of gas-turbine engines, as shown in Figure 2.1 [16]. The temperature of hot gas stream falls 100~300 °C after it passes through TBCs (thickness 100~500 μm) and reaches the top surface of metallic substrate surface. This function has ensured modern gas-turbine engines to work in an environment where the gas temperatures are higher than the melting temperature of the super alloy (~1300 °C), hence increasing the TIT and engine efficiency [1]. Combining film cooling with high-grade TBCs, the hot gas temperature may fall 300~500 °C in total. It offers the possibility of developing a new generation of aero engine with the TIT estimated above 1700 °C in the future, as seen in Figure 2.2 [17].

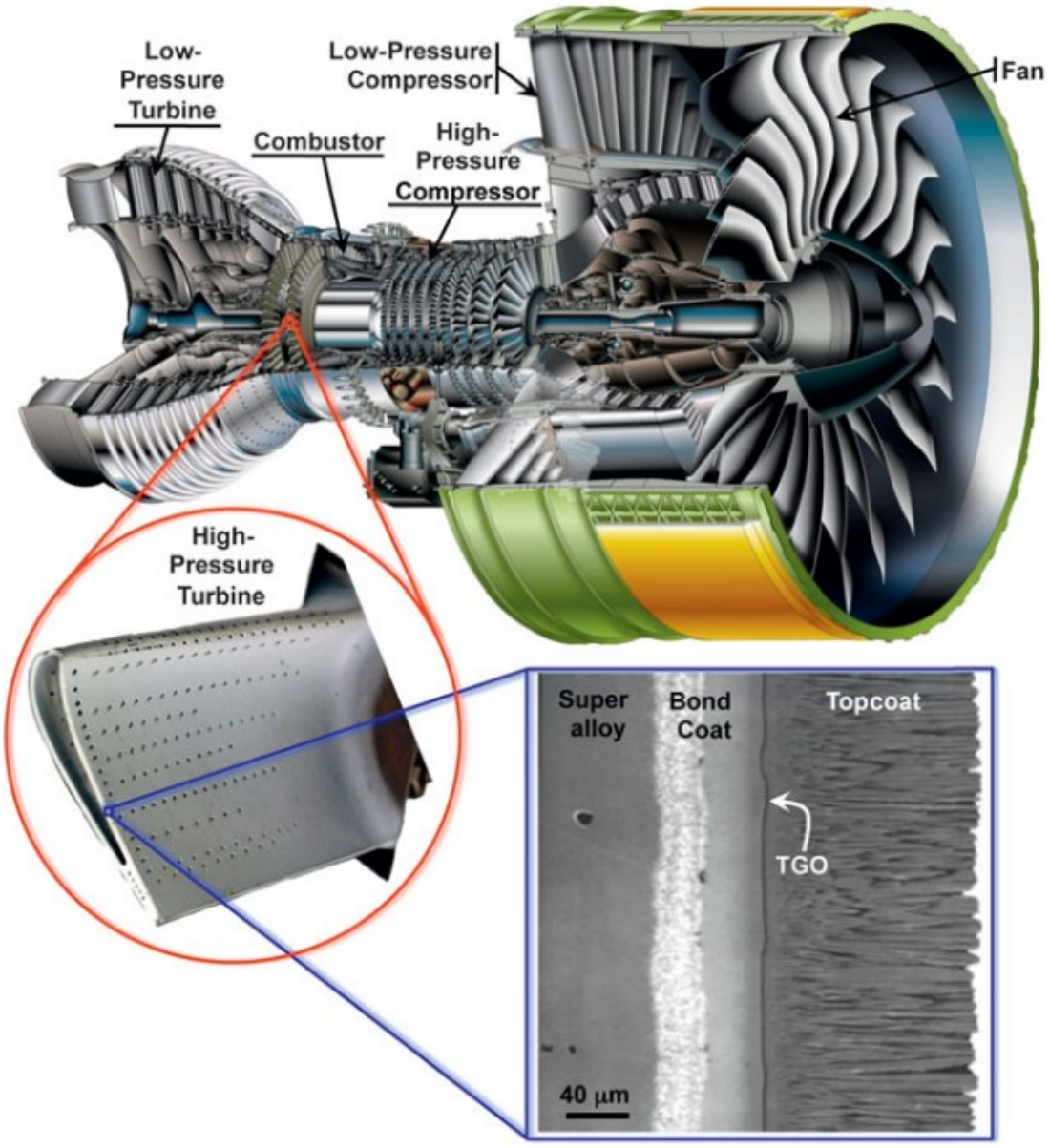

Figure 2.1 Cutaway view of Engine Alliance GP7200 aircraft engine, photograph of a turbine blade (~10 cm long) with TBC from the high-pressure hot section of an engine [16]

The TBCs service environment is normally accompanied by severe conditions such as high temperature, erosion, thermal cycling and extreme stress. Based on the different components to be protected, the evaluation indicators to qualify TBCs vary. For example, when applying TBCs in commercial jet engines for aircrafts, it is expected to withstand thousands of take-offs and landings. When using TBCs in industrial gas-turbine engines, exceeding 30,000 hours of

operation is required [1]. After several decades of development, the stability of TBCs has been improved significantly. However, the premature failure of TBCs by spallation, which exposes the metallic substrate to high temperature gases, is still a catastrophic phenomenon. The major failure mechanisms of TBCs can be summarized as follow: (a) the large lateral cracks caused by thermal-expansion mismatch and thermal stresses accumulated during thermal cycling process [18]; (b) the interface oxidation which induces residual stresses in the thermally grown oxides (TGO) [19]; (c) the changes of compositions (secondary phases generation), microstructures (porosity reduction) and interfacial morphologies (large cracks) [1]; (d) the so-called foreign object damage (FOD) [17].

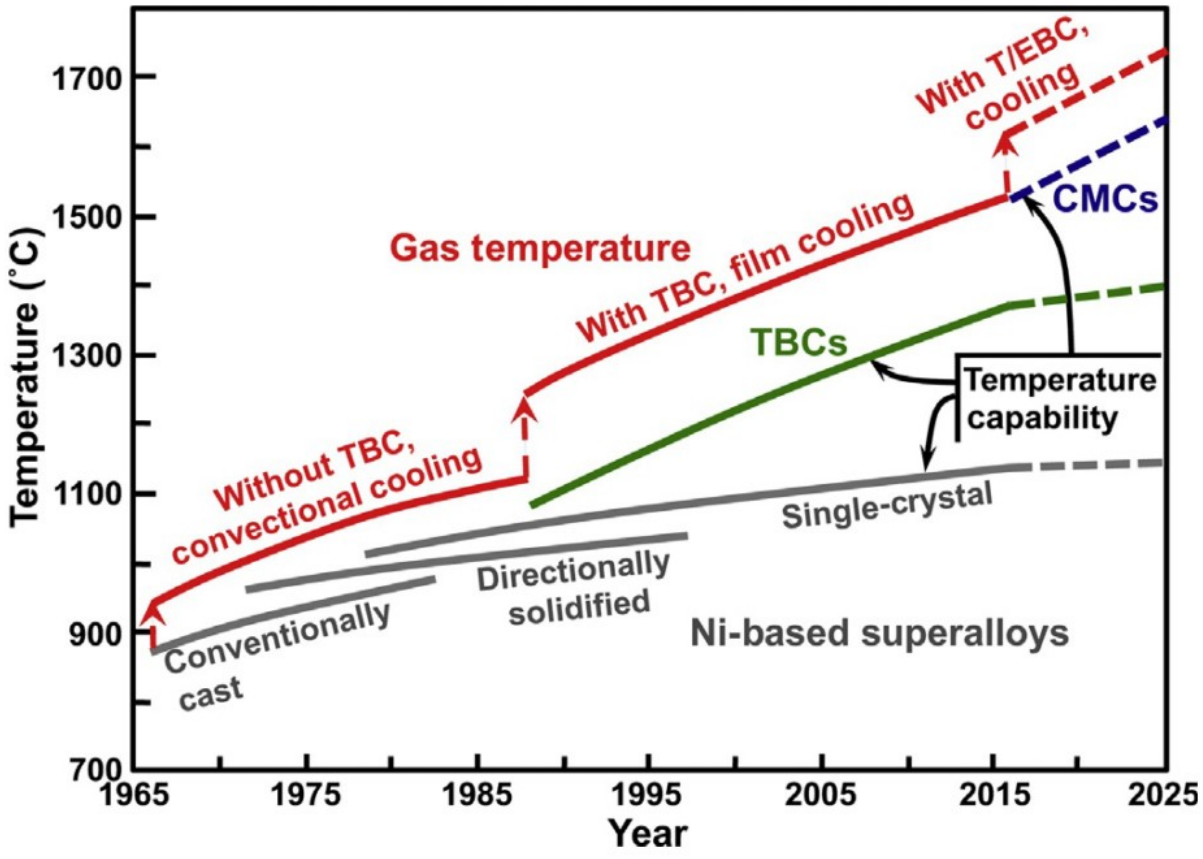

Figure 2.2 Progression and projection of temperature capabilities of Ni-based superalloys (grey), TBCs (green, rough estimates), ceramic matrix composites (CMCs) (blue, rough estimates) and thermal/environmental barrier coatings (T/EBCs) gas-turbine engine materials, and maximum allowable gas temperatures with cooling (red, rough estimates) [17]

2.1.2 Structure of TBCs

The structure of TBCs comprises three different configurations, double-layer, multiple-layer and gradient layer. Each configuration is suitable for different applications [20]. Right now, the double-layer structure made of bond coat and ceramic top coat is the most frequently used configuration and has been applied in industry (Figure 2.3) [1].

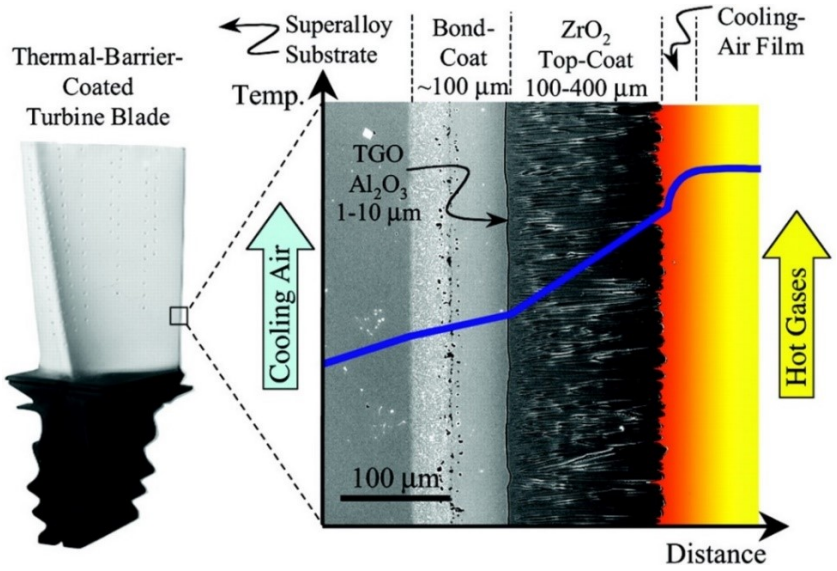

Figure 2.3 A schematic diagram of cross-sectional image of TBC, showing the temperature reduction caused by the air-cooling and TBC [1]

In Figure 2.3, the metallic substrate is usually made of nickel- or cobalt-based super alloy. The compressed cooling air passes through the internal hollow channel and comes out from the well-separated drilling holes. Therefore, the first temperature gradient is built from the core of hot gases to the coating top surface. The temperature deceases again after the function of TBCs. Ultimately, the temperature gradient is shown by the blue curve line in Figure 2.3. The common super alloys characterized by a polycrystalline form, are normally prepared by the method of investment casting. Some advanced super alloys, produced by Rolls-Royce, are in single-crystal form. In order to obtain some specific performance requirements, such as anti-oxidation, anti-hot corrosion, high-temperature strength and ductility, 5 to 12 additional elements are added into the cast super alloys [1, 21]. For the purpose of relieving the thermal mismatch between the

ceramic top coat and the metallic substrate, as well as increasing the anti-oxidation property of the substrate, an oxidation-resistant metallic bond coat with a thickness of 75-150 μm is deposited between the substrate and the top coat. Ceramic top coat provides the thermal insulation and is typically made of Y_2O_3-stabilized ZrO_2 (YSZ).

Gradient-layer (functionally-graded) structure solves the interface incompatibility between the ceramic top coat and the metallic bond coat [22]. Compared to an abrupt shift of properties in double-layer TBCs, a gradient TBCs with a superior composition grading contributes to a slower transition in performances from metallic bond coat to ceramic top coat [23]. Due to the complex preparation process of gradient TBCs, its structure is hard to control [20].

2.1.3 TBCs Material

2.1.3.1 Bond coat material

MCrAlY-type bond coats (M = Co and/or Ni) are commonly used to protect metallic substrates from oxidation and to improve adhesion of ceramic TBCs. Co and/or Ni are the constituents of this alloy [20]. Ni reacts with Al to form a high melting temperature intermetallic compound NiAl or Ni_3Al. Still, they tend to react with sulfur and form a low melting point eutectic system. Co can form a more stable intermetallic compound with Al, CoAl. The combination of Ni and Co is beneficial for the properties of anti-oxidation/corrosion [11]. Cr is used for ensuring the anti-thermal corrosion and for inducing the formation of alumina, which can be used up to 1200 °C [20]. Y (< 1 wt. %) is added to improve the adhesion of the alumina film [11]. Until now, MCrAlY coatings typically contain 17-30 wt. % Cr and 6-12 wt. % Al. The ternary Ni-Cr-Al system microstructure is well established and reliable ternary phase diagrams are also available [24].

Because of the different thermal expansion coefficients (TEC) between Al_2O_3 film and the bond coat, the rapid oxidation of MCrAlY bond coat often leads to the spallation of the Al_2O_3 film,

which is one of its main failure mechanisms. Designing bond coats with extremely low oxidation rates is a key step to developing reliable TBC systems. Adding some minor elements such as Y, Ti and Si to MCrAlY compositions could improve the properties of bond coat [25].

NiAl is a promising bond coat material because of its high melting point (1638 °C), low density (5.9 g/cm^3) and high elastic modulus (240 GPa) which can form protective oxide film above 1200 °C [23]. Its TEC is very close to that of Ni-based super alloys [26]. Doping with some trace elements or oxide, such as Y_2O_3, Au/Pt and Dy may decrease the oxide growth rate and increase the adhesion of oxide film as well as the resistance to oxidation during cycling [27-29].

2.1.3.2 Top layer material

The criteria used to evaluate TBC materials should consider the followings: (1) high melting temperature, (2) high thermal expansion suited with the metallic substrate, (3) low sintering rate, (4) chemical inertness, (5) low thermal conductivity, (6) good bonding and interface compatibility with the metallic substrate and (7) no phase transition between the ambient environment and the service conditions [3]. Right now, only a few materials partially meet these requirements. Furthermore, the materials that can be used in real industrial applications are rare.

Commonly used ZrO_2

ZrO_2 (zirconia) is considered as the most popular TBCs material for its excellent properties such as high melting point (2973 K), low thermal conductivity (λ=2.17 Wm^{-1}K^{-1}, 1273 K), high TEC (α=15.3×10^{-6} K^{-1}, 1273K, TEC decreases abruptly after doped by Y_2O_3) etc. [3]. ZrO_2 possesses three different allotropes, monoclinic (m), tetragonal (t) and cubic (c), according to Figure 2.4 [30]. Raising the temperature up to 1170 °C, the phase structure of pure zirconia transforms from monoclinic to tetragonal. Meanwhile, a volume change of 3~9 % and crack formation also occur during this process [31].

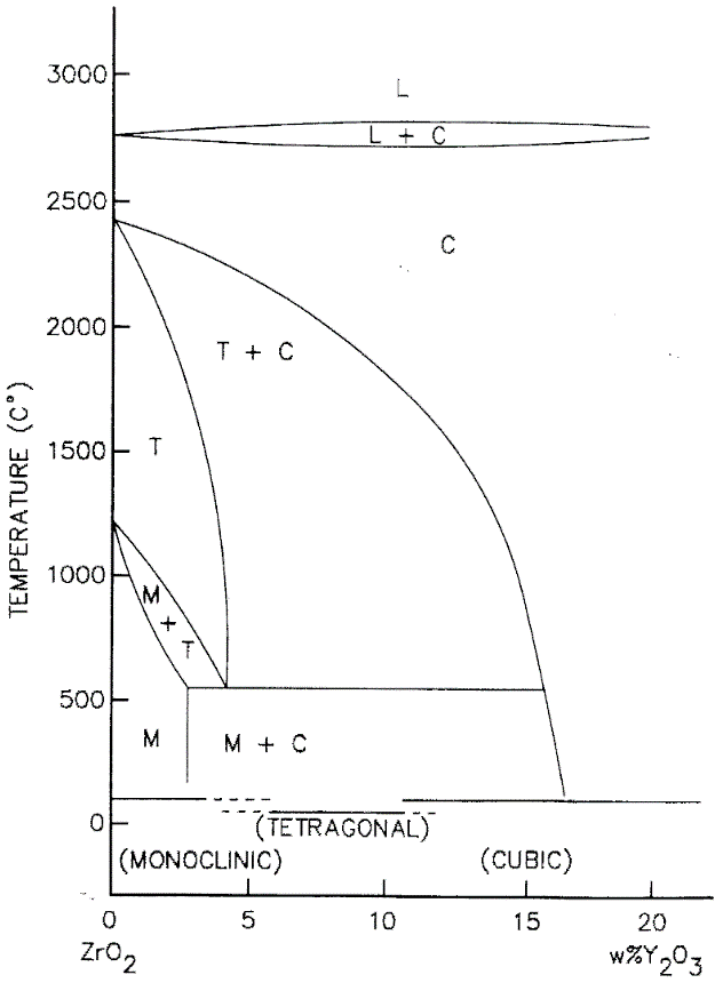

Figure 2.4 Phase diagram of ZrO_2-Y_2O_3 system [30]

Stabilizers, such as CaO, MgO and Y_2O_3 can suppress this phase transition [1]. In the history of manned flight vehicle, the first applied TBCs material was CaO stabilized zirconia (CSZ), which was deposited on the exhaust nozzle of the X-15 manned rocket plane [32]. Early TBCs mainly used 22 wt.% MgO stabilized ZrO_2 [33]. The gas sulfuration may separate CaO and MgO from ZrO_2, which decreases their stabilizing function [34]. Y_2O_3 was eventually considered as the most suitable stabilizer for ZrO_2. Compared to CaO and MgO stabilized ZrO_2, yttria-stabilized zirconia (YSZ) coatings show excellent anti-corrosion property against V_2O_5 and Na_2SO_4 (combustion products of fuel) [3]. Since then, YSZ has been set as a standard for more than 30 years [35]. The amount of Y_2O_3 also affects the thermal shock property of YSZ. When the

composition exceeds 17 wt. %, the cubic phases can be retained down to room temperature which is referred to as a fully stabilized zirconia (FSZ). It was estimated that all phase transformations could be avoided and that the coating would achieve an excellent lifetime. However, the thermal cycling tests presented a different result. According to the thermal cycling life of YSZ coatings with various Y_2O_3 amount (Figure 2.5) [36], the coating shows its maximum lifetime when the concentration of Y_2O_3 in ZrO_2 is around 6 wt. %. This result was attributed to their good fracture toughness [31, 37]. Therefore, the ideal ZrO_2-Y_2O_3 TBCs should adopt an optimum Y_2O_3 concentration at which the longest life is reached. Until now, in commercial technical systems, 6 to 8 wt. % (7~9 mol. %) Y_2O_3 is added to obtain a metastable, partially stabilized tetragonal zirconia (6~8 wt. % YSZ) that effectively suppresses detrimental phase transformations [20].

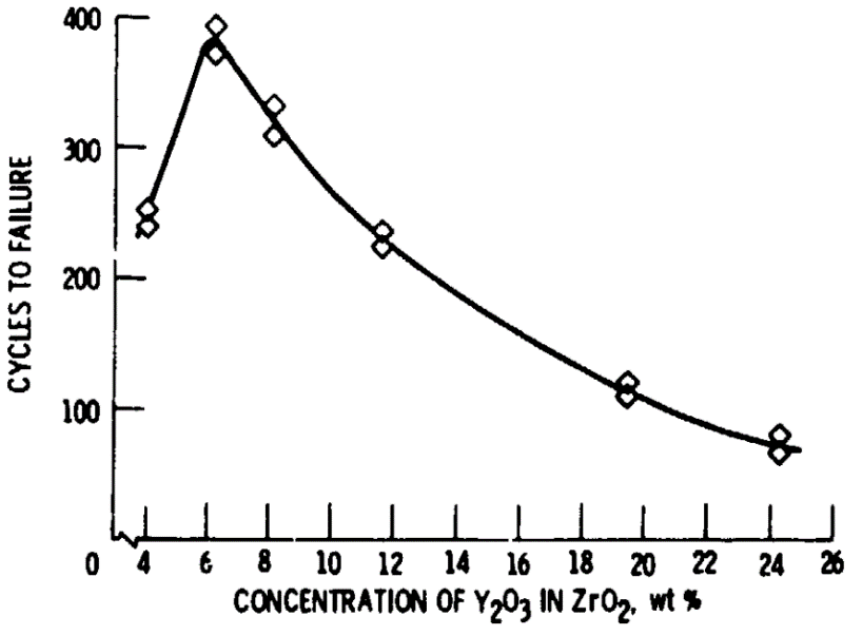

Figure 2.5 Thermal cycling life of ZrO_2 TBCs doped with different Y_2O_3 (wt. %) amount [36]

Independently of the fabrication path (i.e. air plasma spraying (APS) or electron beam physical vapor deposition (EB-PVD)), due to the short cooling time of sprayed splats (APS process) and

deposition from gas phase (EB-PVD process), only a metastable tetragonal phase YSZ, t' phase, will form instead of the equilibrium phases, which consist of monoclinic and cubic. The metastable tetragonal phase remains stable at low temperature. However, t' phase will transform to tetragonal and cubic phases above 1200 °C owing to thermal diffusion [31]. During the subsequent cooling process, the tetragonal phase will transform to monoclinic, accompanied with volume expansion and cracks formation in the coating [3].

YSZ coatings contain a large number of oxygen ion vacancies, which facilitate the oxygen transportation inside the coatings. An accelerated oxidation process occurs between the ceramic layer and the metallic one, resulting in the formation of TGO. This kind of oxide is one of the main failure mode as indicated in section 2.1.1, which occurs frequently in the component of gas turbine covered with thin YSZ coating [3].

Other ceramics

Al_2O_3 is an inert ceramic which possesses a very high hardness and oxygen barrier property. Compared with YSZ, Al_2O_3 is an oxygen resistant material, which may solve the oxidation of metallic coat at ceramic-metallic coat interface. It has only one stable phase, α-Al_2O_3, among all Al oxides. Normally, the as-sprayed Al_2O_3 coating mainly shows metastable phases such as δ and γ -Al_2O_3. During thermal cycling process, these metastable phases will transform into α-Al_2O_3 with an obvious volume change ($\gamma \rightarrow \alpha$, around 15 %) leading to the formation of micro-cracks [38]. Besides, Al_2O_3 has high thermal conductivity and very low TEC which restrict its application in TBCs field [3].

Mullite, a compound of SiO_2 and Al_2O_3 with the chemical formula $3Al_2O_3 \bullet 2SiO_2$, is also a significant TBCs material with low thermal conductivity and high thermal stability. Right now, mullite is mainly employed to protect the diesel engines, which are usually used at a lower service temperature [39].

New generation TBCs material

Pyrochlore

The pyrochlore structure with chemical formula $A_2B_2O_7$ is also a popular TBCs material for its lower thermal conductivity, lower sintering and high thermal stability. The most commonly seen materials with pyrochlore structure are rare earth zirconate oxides, $Ln_2Zr_2O_7$ (Ln: La, Sm, Eu, Nd, Yb and Gd) [40-44]. For example, $La_2Zr_2O_7$ (33.3 at. % La_2O_3) remains phase-stable up to its melting point [3], which solves the phase transition dilemma perfectly. The main disadvantage of $La_2Zr_2O_7$ is its low thermal cycling life. By comparing the TEC of $La_2Zr_2O_7$ (9×10^{-6} K^{-1}) and other commonly seen materials such as YSZ ($10\sim11\times10^{-6}$ K^{-1}) [35], CoNiCrAlY ($13\sim16\times10^{-6}$ K^{-1}) [45] and nickel-based substrate (16×10^{-6} K^{-1}) [3], the low thermal cycling life of $La_2Zr_2O_7$ can be attributed to its large TEC mismatch with that of the substrate. The measured linear TEC of a group of rare-earth zirconate pyrochlores $Ln_2Zr_2O_7$ (Ln: La, Nd, Sm, Eu, Gd) is distributed in the range of $8\sim11\times10^{-6}$ K^{-1} (298-1500 K). As the ionic radius of the Ln-site decreases (from La to Gd), the TEC of $Ln_2Zr_2O_7$ compound increases. In other words, $Gd_2Zr_2O_7$ has the largest TEC in the group of rare-earth zirconate pyrochlores [46]. In this regard, double-layer ceramics TBCs with a bottom layer of YSZ and a top layer of pyrochlore $Gd_2Zr_2O_7$ was designed [42]. The thermal cycling lifetime of the double-layer coatings was obviously improved [35, 47]. Besides, the thermal conductivity of pyrochlores ($A_2B_2O_7$) can be decreased by A-site doping, the thermal conductivities of $La_{1.7}Gd_{0.3}Zr_2O_7$, $La_{1.7}Yb_{0.3}Zr_2O_7$ and $La_{1.7}Gd_{0.15}Yb_{0.15}Zr_2O_7$ are lower than that of the undoped $La_2Zr_2O_7$ [40]. However, it is not easy to deposit pyrochlore coatings using thermal spray. The loss of constituents (La_2O_3 from $La_2Zr_2O_7$) during spraying was observed [35].

Hexaaluminates

Lanthanum hexaaluminate shows extended structural and chemical stability up to 1400 °C [48]. The nominal composition of Lanthanum hexaaluminate is (La, Nd)$MAl_{11}O_{19}$, where M

represents Mg, Mn, Zn, Cr and Sm [35, 49]. Particularly, the Young's modulus of $LaMgAl_{11}O_{19}$ is only half that of YSZ [48]. As such, $LaMgAl_{11}O_{19}$ alleviates the accumulation of thermal stresses. Due to the rapid quenching of molten feedstock during spraying process, the as-sprayed coating of $LaMgAl_{11}O_{19}$ normally contains an amorphous phase. A phenomenon of recrystallization occurs over the temperature range from 800 °C to 1200 °C. This process is accompanied by a volume shrinkage of the free standing coatings [48].

Perovskites

Perovskites are a third interesting material class for TBCs application. Compared with other types of oxides, perovskites, with the nominal chemical formula ABO_3, are characterized by low thermal conductivities, high TEC and high melting points. Particularly, perovskites can gain many new properties after extensive substitution of ions at the A and B sites [50]. Zirconates such as $SrZrO_3$ and $BaZrO_3$ are representative perovskites materials. $BaZrO_3$ showed a premature spallation during thermal cycling tests because of its comparatively poor thermal stability [51]. $SrZrO_3$ was not marked as a candidate TBCs material due to its phase transitions at high temperatures [50, 52].

Complex perovskites form

$BaLa_2Ti_3O_{10}$ (BLT), $La(Al_{1/4}Mg_{1/2}Ta_{1/4})O_3$ (LAMT) and $Ba(Mg_{1/3}Ta_{2/3})O_3$ (BMT) are three representative complex perovskite materials. BLT is a layered perovskite. The as-sprayed BLT coating presented a stoichiometric composition [53]. This result indicates that no element evaporation occurs during the APS process. However, the low melting point of BLT limits its application. It is worthwhile to carry out further evaluation whether it can be used in service above 1200 °C. LAMT possesses a lower thermal conductivity (~2 $Wm^{-1}K^{-1}$ bulk material) than that of BMT. Besides, its TEC (~$11\times10^{-6}K^{-1}$ bulk material) is comparable to YSZ [54]. Until now, the investigations to apply LAMT and BMT as TBCs were carried out together [6]. Since BMT is the main research object of this thesis, the next section will systematically introduce the structure, properties and characteristics of BMT.

2. 2. BMT material

2.2.1. BMT – a perovskite-based structure

Perovskite is a group of compounds with the chemical formula ABX_3. Generally, X is O^{-2} but other large ions, for instance F^{-1} and Cl^{-1}, are also possible. A is a cation such as alkali, alkali earth or rare earth element possessing a radius similar to the O anion [55]. After suitable structural modification and chemical manipulation, perovskite can produce a wide array of phases with various functions, as described in Figure 2.6 [56]. $Ba_3^{2+}Mg^{2+}Ta_2^{5+}O_9$ (BMT), characterized by the highest melting point, is presented in this picture.

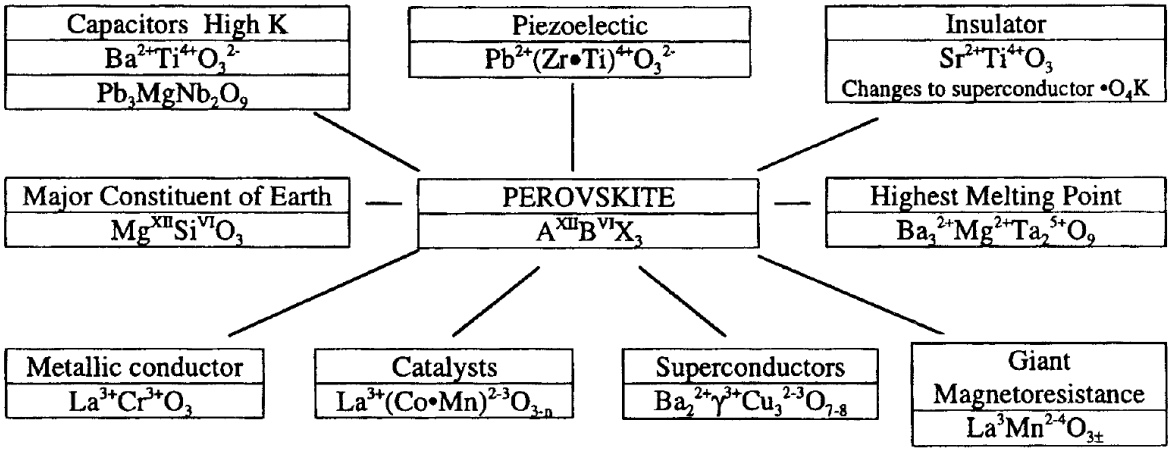

Figure 2.6 Multifunctional perovskite structure [56]

Roy et al. summarized the multiple ion substitutions at the sites of A, B or both (Figure 2.7) [57]. This map includes some prototypes of useful substitutions applied in the perovskite structure. For example, the $A_3B^{2+}B_2^{5+}O_9$ is the prototype of $Sr_3NiNb_2O_9$ and $Ba_3MgTa_2O_9$. The former material is a kind of relaxor [56] and the later one is widely used in the field of microwave dielectrics [58-60].

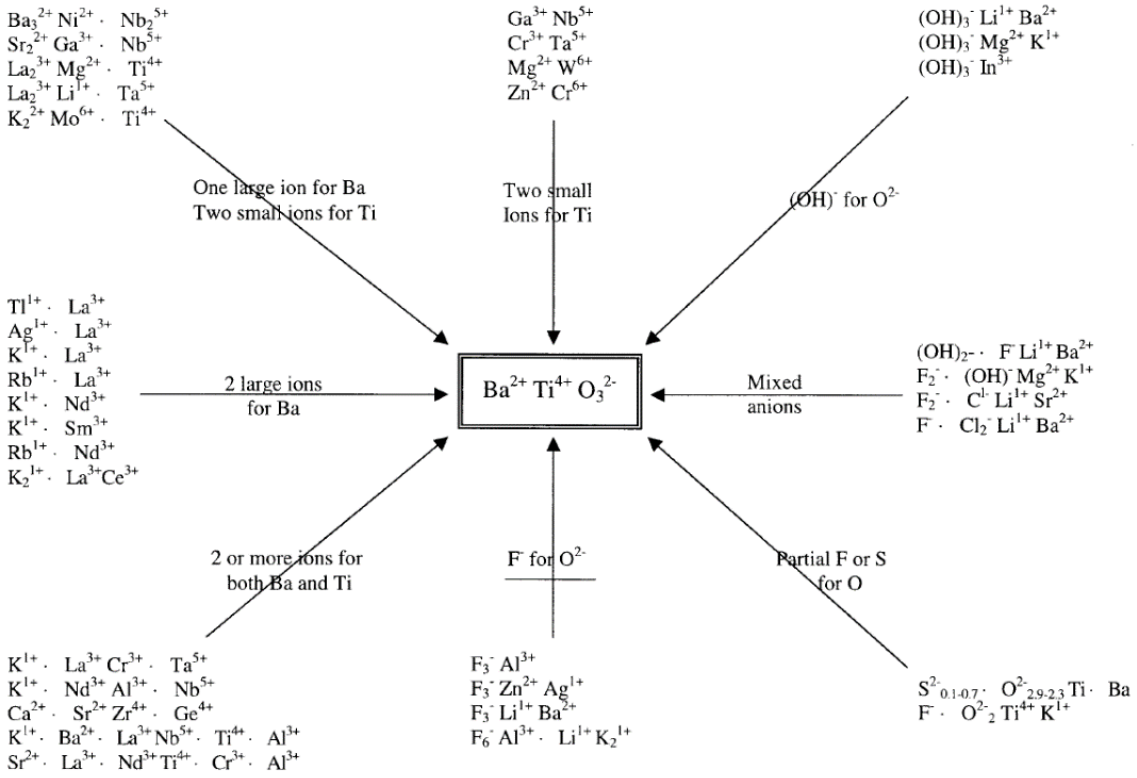

Figure 2.7 Multiple ion substitution of perovskite structure [57]

2.2.2. BMT phase structure.

Janaswamy S. et al. calculated the cubic BMT structure by the Rietveld profile refinement method [61, 62]. All the atoms occupy the special positions listed in Table 2.1. In this cubic structure, Ba and O ions form a close-packed plane whose normal direction is towards [111]. Ta and Mg atoms randomly occupy the centre site of an octahedron, which is built by six oxygen atoms. From the view of the periodic crystal space, Ta/Mg atoms are at the body center of the cube. Accordingly, the cubic BMT structure is referred to as the disordered phase. The distance between Ta/Mg and O is 2.04420(2) Å. The distance between Ba and O is 2.89050(3) Å. Ba atom and twelve O atoms form a cubo-octahedron as seen in Figure 2.8.

Table 2.1 Positional parameters of BMT (a=4.08840(4) Å) with cubic phase [62]

Atom	x	y	z	Wyckoff
Ba	0	0	0	1a
Mg	1/2	1/2	1/2	1b
Ta	1/2	1/2	1/2	1b
O	0	1/2	1/2	3c

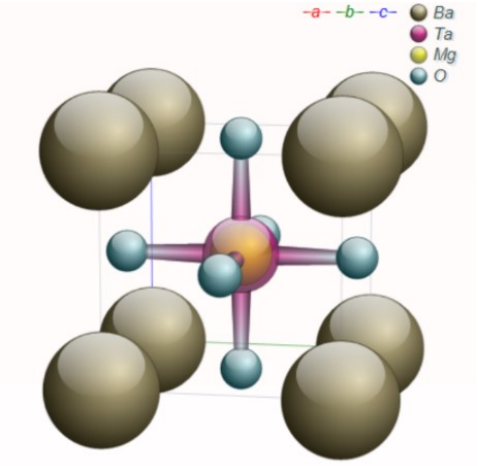

Figure 2.8 Crystal structure of BMT with simple cubic phase [62]

It is known that BMT is isomorphous with $Sr(Mg_{1/3}Ta_{2/3})O_3$ in ordered structure. There is a transition from disordered phase (cubic BMT) to ordered phase (hexagonal BMT) in the process of heat treatment [61]. The ordering changes the relative bond length between the atoms and often leads to symmetry breaking. In the case of BMT, the cubic lattice transforms to a hexagonal one upon ordering. The structural parameters of hexagonal BMT (a=5.7737 Å, c=7.092 Å) are given in Table 2.2.

After arraying B site cations along the body diagonal of the cubic lattice, BMT develops a strong ordering with hexagonal symmetry. New planes including Mg^{2+} and Ta^{5+} ions, respectively, are arranged with a three-layer repeat sequence (–Ta^{5+}-Mg^{2+}-Ta^{5+}-) [64]. The crystal structure of BMT with hexagonal phase is shown in Figure 2.9.

Table 2.2 Structural parameters of BMT with hexagonal phase [63]

Atom	x	y	z	Wyckoff	Occupancy
Ba *site1*	0.0	0.0	0.0	1a	1
Ba *site2*	0.33333	0.66666	0.6648	2d	1
Mg *site1*	0.0	0.0	0.5	1b	0.940(5)
Ta *site1*	0.0	0.0	0.5	1b	0.060(5)
Ta *site2*	0.33333	0.66666	0.1762	2d	0.970(2)
Mg *site2*	0.33333	0.66666	0.1762	2d	0.030(2)
O *site1*	0.5	0.0	0.0	3e	1
O *site2*	0.169	-0.169	0.308	6i	1

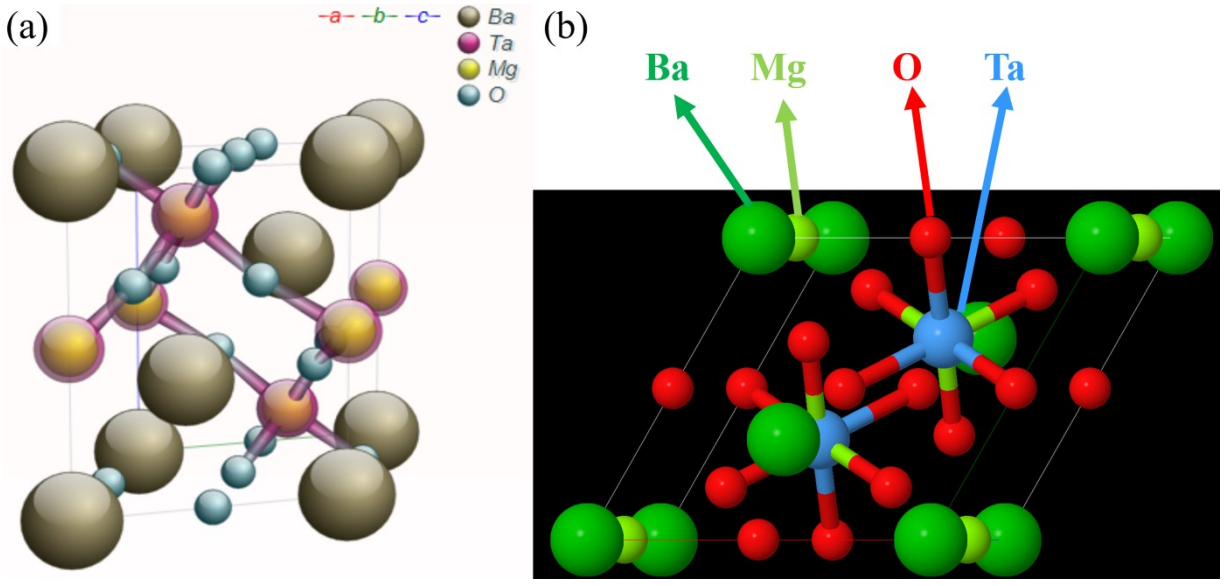

Figure 2.9 Crystal structure of BMT with hexagonal phase (a) front view and (b) top view [63]

When there are large differences in size or ionic charge between different B site ions (B' and B"), these B-site ions tend to be orderly arranged during preparation [65]. For $Ba(Sr_{0.33}Ta_{0.67})O_3$ and $Ba(Ca_{0.33}Ta_{0.67})O_3$ with large B-site radii differences of 0.44 Å and 0.31 Å, respectively, it is easy to obtain the fully ordered phase [65]. The degree of long-range ordering is low for

compounds whose difference of B-site ions radii is small. It can also explain the occurrence of disordered BMT phase in most cases because the difference of B-site ionic radii of BMT, Mg^{2+} 0.67 Å and Ta^{5+} 0.68 Å, is only 0.01 Å. Since BMT also has a large charge difference of B-site ions (Mg^{2+} and Ta^{5+}), the ordered BMT phase was finally achieved after a heat treatment at 1400 °C by increasing the calcination time from 10 h [61] to 24 h [65]. In some special situation, for example replacing Ba by Sr, small ionic radius of A-site may also promote the ordering transformation [66].

Srinivas J. found that the ordering degree of B-site is determined by the calcination temperature [62]. A completely disordered BMT was synthesized by heating a mixture of $BaCO_3$, MgO and Ta_2O_5 at 1300 °C for 10 h. Ordered phase started to form above 1400 °C and retransformed to disordered phase above 3000 °C. As such, in order to obtain a complete ordered BMT, the calcination temperature must be increased to 1600 °C.

2.2.3 The preparation of BMT powder

2.2.3.1 Traditional solid-state synthesis

Equation 2.1 is the traditional solid-state reaction equation for BMT. Yonghan Fan et al. investigated the mechanisms and kinetics of BMT formation processes. The detail processes can be decomposed into 5 steps, as shown in equation (2.1a) to (2.1e) [58]. Reactions (2.1a) and (2.1b) start at 700 °C, while reactions (2.1c) to (2.1e) start at 800 °C. Three reactions [2.1a – 2.1c] process simultaneously from 800 °C to 1000 °C. When the temperature is higher than 1000 °C, the reactions [2.1c – 2.1e] control the phase formation. BaO and Ta_2O_5 form as by-products. Consequently, it is generally considered that it is difficult to synthesize pure BMT phase by traditional solid-state method.

$$BaCO_3 + 1/3MgO + 1/3Ta_2O_5 \rightarrow Ba(Mg_{1/3}Ta_{2/3})O_3 + CO_2\uparrow \quad (2.1)$$

$$BaCO_3 + Ta_2O_5 \rightarrow BaTa_2O_6 + CO_2\uparrow \quad (2.1a)$$

$$BaTa_2O_6 + 3BaCO_3 \rightarrow Ba_4Ta_2O_9 + 3CO_2 \uparrow \quad (2.1b)$$

$$Ba_4Ta_2O_9 + MgO \rightarrow 3Ba(Mg_{1/3}Ta_{2/3})O_3 + BaO \quad (2.1c)$$

$$3BaTa_2O_6 + MgO \rightarrow 3Ba(Mg_{1/3}Ta_{2/3})O_3 + 2Ta_2O_5 \quad (2.1d)$$

$$BaO + Ta_2O_5 \rightarrow BaTa_2O_6 \quad (2.1e)$$

2.2.3.2 B-site precursor method

In the traditional method, two kinds of B-site oxides (MgO and Ta_2O_5) compete for the prior reaction with A-site $BaCO_3$. Finally, only a mixture of BaO, MgO and BMT was obtained instead of the pure BMT. Tai-Kwang Park [59] et al. proposed a modified solid state synthesis method called B-site precursor method, which has been applied in A(B', B")O_3 compositions to enhance perovskite-formation yields. As for $Ba(Mg_{1/3}Ta_{2/3})O_3$, the B-site precursor method means to synthesize B-site precursor ($MgTa_2O_6$) first, as shown in equation (2.2a). This reaction processes at 1250 °C. The prepared $MgTa_2O_6$ is then reacted with $BaCO_3$ at 900 °C to synthesize the pure BMT, as seen in equation (2.2b)

$$MgO + Ta_2O_5 \rightarrow MgTa_2O_6 \quad (2.2a)$$

$$MgTa_2O_6 + 3BaCO_3 \rightarrow 3Ba(Mg_{1/3}Ta_{2/3})O_3 + CO_2 \uparrow \quad (2.2b)$$

2.2.3.3 Liquid state synthesis

BMT powder synthesized by liquid state method is normally characterized by nanometer size particles [60]. The commonly seen liquid state synthesis method is also called co-precipitation [67]. Soluble salts $Ba(NO_3)_2$, $Mg(NO_3)_2$ and $TaCl_5$ are mixed to prepare a solution using ammonia. A precipitation containing three elements (Ba, Mg and Ta) is done using oxalic acid. This process is indicated by equation (2.3a). After filtration to remove the liquid (using a filter paper), the retentate is then calcined at 650 °C for 2 h to obtain BMT powder, as shown in equation (2.3b).

$$3Ba(NO_3)_2 + 2TaCl_5 + Mg(NO_3)_2 + H_2C_2O_4 \rightarrow 3BaMg_{1/3}Ta_{2/3}(C_2O_4)_3 \quad (2.3a)$$

$$3BaMg_{1/3}Ta_{2/3}(C_2O_4)_3 \rightarrow 3Ba(Mg_{1/3}Ta_{2/3})O_3 \quad (2.3b)$$

2.2.4 The application of BMT

Up to today, BMT is widely used in the field of microwave dielectric [67]. However, it is hard to produce a dense BMT bulk material due to its poor sintering ability. In order to accelerate sintering, NaF or Nb_2O_5 were added to bulk BMT in the process of calcination [68, 69]. The poor sintering ability of BMT leads to a new potential application, that of being a TBCs material. The complex perovskite BMT is considered the most refractory oxide (melting temperature of 3100 °C) ever known to science [5]. This value of BMT surpasses that of YSZ (2680 °C) by at least 400 °C, and as such, its sintering temperature is expected to be higher than 1200 °C. It may satisfy the industrial requirement at present. Right now, the investigations applying BMT into TBCs field are limited [4-6, 54, 70].

Due to the large TEC discrepancy between the superalloy substrate and the coating, the lower linear expansion of the ceramic coating at TBC service temperatures leads to a large amount of stress accumulation [71]. The higher the ceramic TEC is, the less the stress accumulates. Since the TECs of commonly used super-alloy substrate IN737 ($16\times10^{-6}K^{1}$, 293~1273K) [3] and bond coat MCrAlY ($13\sim16\times10^{-6}$ K^{-1}) [45] are all higher than that of YSZ ($9.1\sim10.5\times10^{-6}$ K^{-1}, 200~1100 °C, as seen in Figure 2.10), using high TEC BMT ($9.5\sim11.1\times10^{-6}$ K^{-1}, 200~1100 °C) instead of YSZ is beneficial for TBC application. It can alleviate TEC discrepancy between topcoat and bond coat/substrate during thermal cycling. In addition, the TEC of BMT is higher than that of other new generation TBC materials [70]. It should be noticed here that all the values were obtained on bulk materials.

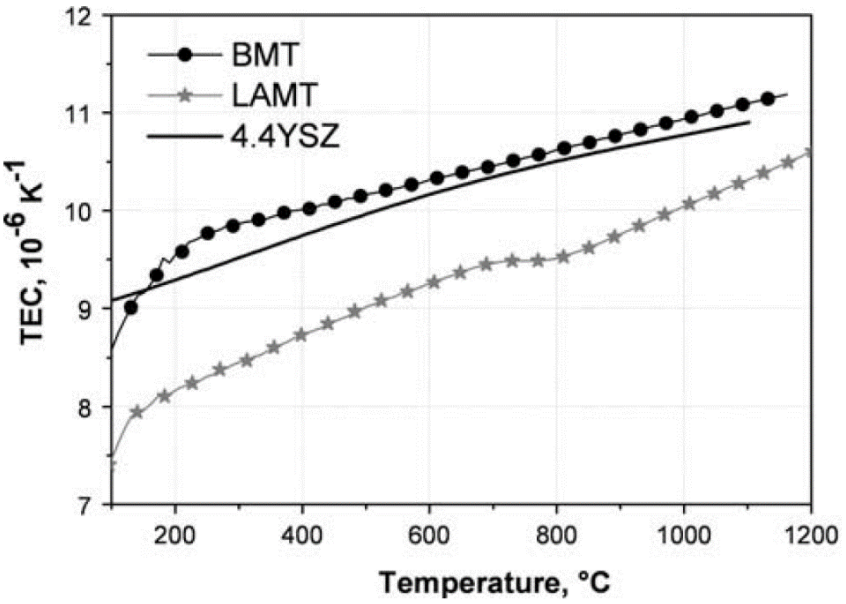

Figure 2.10 TEC vs. temperature curves of BMT, LAMT and 4.4YSZ (4.4 mol. % YSZ corresponding to ~7.8 wt. % YSZ) [5]

As indicated above, the sintering phenomenon reduces the strain tolerance and increases the Young's modulus. The higher Young's modulus induces more thermal stress accumulation in the situation of identical thermal strain. On the one hand, Young's modulus of BMT is lower than that of YSZ, which is propitious to TBC application, according to Table 2.3. On the other hand, BMT has the lowest value of fracture toughness, which might be attributed to the existence of secondary phases such as $BaTa_2O_6$ and $Ba_3Ta_5O_{15}$ [5]. Exploring methods to reduce the secondary phases will be a key point of this work.

Table 2.3 Mechanical properties of the different bulk samples [5]

Composition	Young's Modulus	Hardness	Fracture toughness
	GPa	GPa	$MPa \cdot m^{1/2}$
BMT	186±2	12±2	~0.7
LAMT	174±2	13±2	~0.6
YSZ, t' phase	210±10	13±1	~3

In order to compare YSZ, BMT and other TBC candidate materials such as $Gd_2Zr_2O_7$ [72], hexa-aluminates [35] and yttrium aluminum garnet (YAG) [73], some key properties were summarized in Table 2.4. It should also be clarified that there are some discrepancies for the measured values in different papers due to the different sample preparations and measurement conditions. For example, sintered samples with different porosities or densities may show different thermal conductivities. But they offered a reference for acquaintance of properties. As for BMT, bulk sample preparation process included sintering at 1600 °C for 10 h followed by hot pressing (~80 MPa) at 1600 °C for 3h. The phase structure of BMT can be surely considered as ordered hexagonal phase according to the work of Srinivas J. et al. [62]. Ruyan Guo et al. pointed that the BMT phase transition from ordered phase (high-level ordered B-site cations) to disordered phase (random distribution of B-site cations) only results in a general decrease of 0.42% in molecular volume [64]. Dilatometric tests of BMT (up to 1200 °C) showed that this phase transition is not disastrous for the material structure [5, 74].

Table 2.4 Property comparison of YSZ and other TBC candidate materials

Properties	YSZ	$Gd_2Zr_2O_7$	Hexa-aluminates	YAG	BMT
Melting temperature (°C)	2680	>2000	>1800	1970	3100
Maximum operating temperature (°C)	1200	<1550	>1500	>1500	>1400
Coefficient of thermal expansion (10^{-6}/K)	9.1-10.5	9-11	9.5-10	7.5	9.5-11.1
Thermal conductivity (at 1000 °C, W/mK)	2.2-2.9	1.2-1.7	1.9-3.8	3.2	2.7
Phase transformation volume change (%)	3-5	-	-	-	0.4

The preparation process of BMT feedstock includes the material synthesis, spray drying and post-calcination. After a long heat treatment, the phase structure of BMT feedstock is generally considered to be an ordered hexagonal phase. During the real thermal spray process, the hexagonal structure of BMT feedstock transforms to cubic phase in the as-sprayed coating, as seen in Figure 2.11a, 2.11b and 2.11d. The formation of the metastable cubic phase is due to the rapid cooling of molten feedstock during spray process. In the subsequent annealing, cubic phase reverts to the hexagonal one (Figure 2.11e) [6]. This process is accompanied by the precipitation of $Ba_3Ta_5O_{15}$, which has a low melting point (lower than 1860 °C) and leads to a premature sintering during service. Similar phenomenon of phase transition and precipitation of $Ba_3Ta_5O_{15}$ is also observed in the tests of thermal cycling, as shown in Figure 2.12 [5, 70].

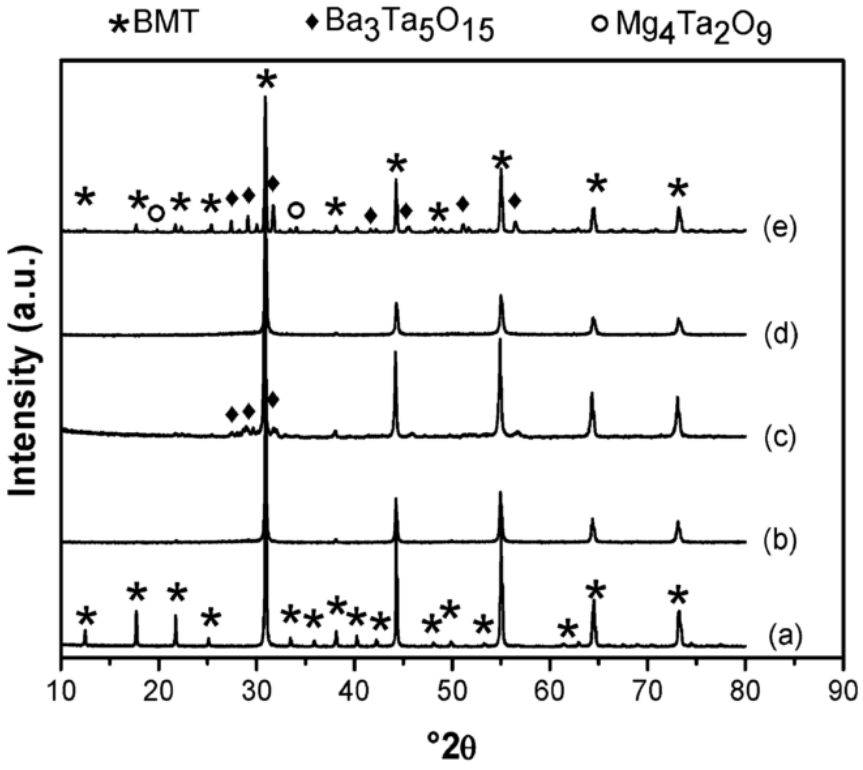

Figure 2.11 XRD profiles of BMT produced with stoichiometric starting compositions; (a) feedstock, (b) as-sprayed coating and (c) annealed coating at 1500 °C, while the non-stoichiometric composition with excess Ba and Mg are (d) as-sprayed coating and (e) annealed coating at 1500 °C [6]

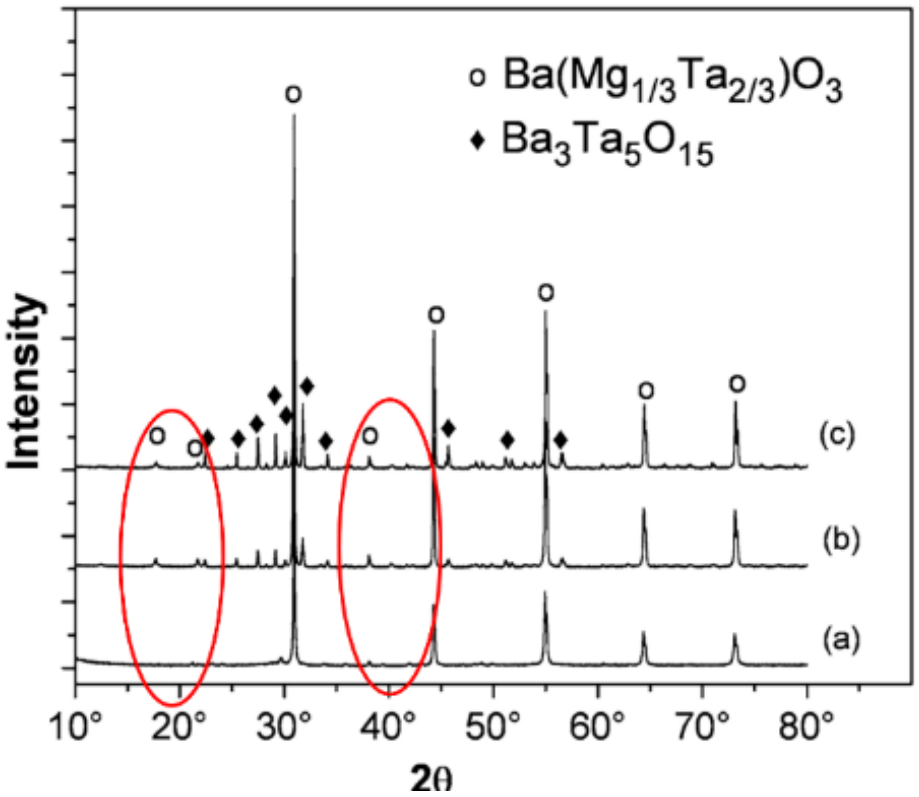

Figure 2.12 XRD profile of double-layer BMT/YSZ coatings (a) as-sprayed (b) after 560 cycles at 1242 °C /1038 °C and (c) after 167 cycles at 1339 °C /1003 °C (coating surface/ substrate backside) temperatures. The circles indicate the peaks representing the ordered phases [5]

Due to the material decomposition and secondary phases formation (Mg-deficient phase), applying plasma spray techniques to deposit complex oxide coatings such as BMT is still a challenge. The secondary phases in as-sprayed BMT and LAMT coatings could be clearly distinguished in SEM images, as indicated by white arrows in Figure 2.13 [6]. However, the XRD profile of as-sprayed BMT coating doesn't comprise the Mg-deficient phase (Figure 2.11b). The formation of secondary phases is due to the loss of oxide components of Ba and Mg during APS process. Even when adding an excess of Ba and Mg to compensate their losses in APS process, the as-sprayed and as-annealed coatings show similar results, as shown in Figure 2.11d and 2.11e.

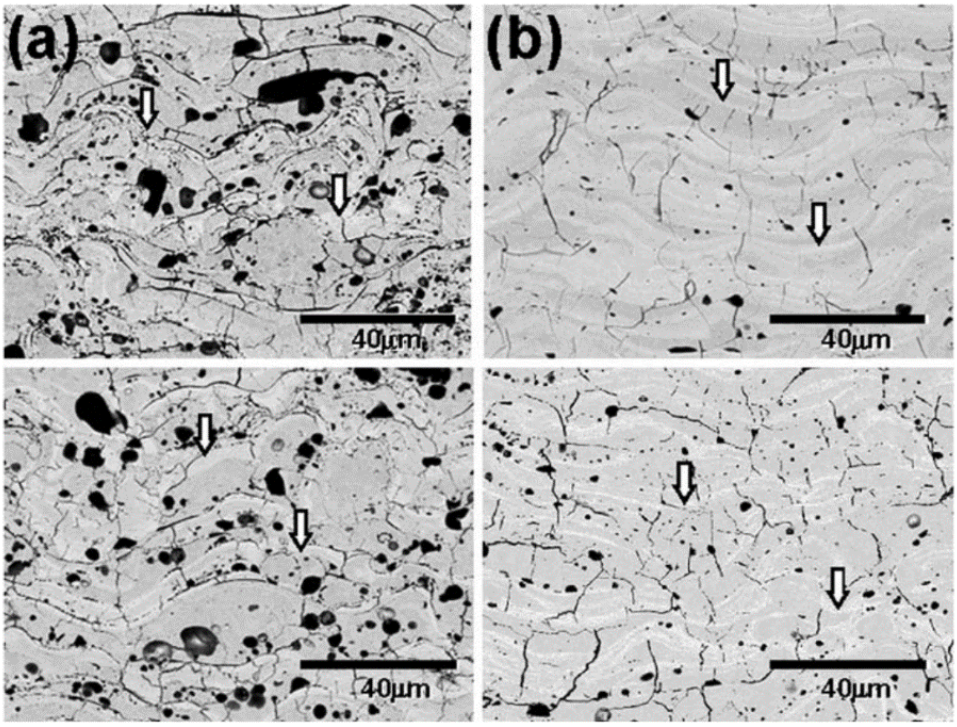

Figure 2.13 Cross-sectional images of as-sprayed coatings of (a) BMT and (b) LAMT. Below are their corresponding coatings heat treated at 1500 °C for 3h. The arrows point the secondary phases characterized by thin white shades. The large black phases are speculated to be Mg-rich phases and porosities which are not mentioned in the original reference [6]

In addition to BMT and LAMT, the decomposition phenomenon is a common problem encountered among other perovskites [35] as well as pyrochlores such as $La_2Zr_2O_7$ and $Gd_2Zr_2O_7$ [54]. For example, when preparing the $SrZrO_3$ coating by APS, SrO volatilized much more compared to ZrO_2 because of its higher vapor pressure, resulting in as-sprayed coating composition that deviated from stoichiometric $SrZrO_3$ [70]. Due to the evaporation of MnO_2, the simple structure perovskite $LaMnO_3$ tends to decompose in suspension plasma spraying. However, when doping $LaMnO_3$ with an excess of MnO_2, the decomposition could be fully eliminated [75].

Until now, the decomposition of BMT in APS has not been solved thoroughly. This problem leads to the deposition of non-stoichiometric phases, which has negative effects on the coating performance, especially its thermal cycling life. The results of BMT coatings thermal cycling

tests are summarized in Table 2.5 [4-6, 70]. Thermal cycling life of single YSZ coating is cited for comparison.

Table 2.5 Thermal cycling life of TBC (The data with symbol ≈ in front are rough estimate from diagrams)

TBC system	$T_{surf.}/T_{sub.}$, °C	Cycles to failure	Comments
BMT/YSZ [70]	1242/1038	560	Non applicable
BMT [5]	1215/1022	31	Large amount of parallel cracks in as-sprayed coating
BMT/YSZ [5]	1339/1003	167	Large amount of parallel cracks in as-sprayed coating
BMT [6]	1246/1048	≈150	Large amount of parallel cracks in as-sprayed coating
BMT/YSZ [6]	1245/1041	≈1700	Large amount of parallel cracks in as-sprayed coating
BMT/YSZ [4]	1240/990	1752	APS current 300A. As-sprayed coating with less secondary phase.
BMT/YSZ [4]	1221/1003	560	APS current 500A. As-sprayed coating with more secondary phase.
BMT/YSZ [54]	1400/1050	≈850	25 KW Plasma power with minimal secondary phases
BMT/YSZ [54]	1400/1050	≈180	49 KW Plasma power with more secondary phase.
YSZ [76]	1250/980	1556	EB-PVD prepared coating with vertical cracks.

It can be seen from Table 2.5 that single layer BMT shows poor thermal cycling life of 31 and 150 cycles. Fortunately, when combined with YSZ, BMT coating shows a decent result of 1752

cycles at 1250 °C, which is comparable to or exceeds the performance of single YSZ coating. This result indicates that double-layer coating system can indeed prolong the thermal cycling lifetime of new TBC materials. The morphology and cross-sectional image of BMT/YSZ coating after 1752 cycles at 1240 °C are shown in Figure 2.14 [4]. Spallation occurred at the YSZ layer and bond coat interface.

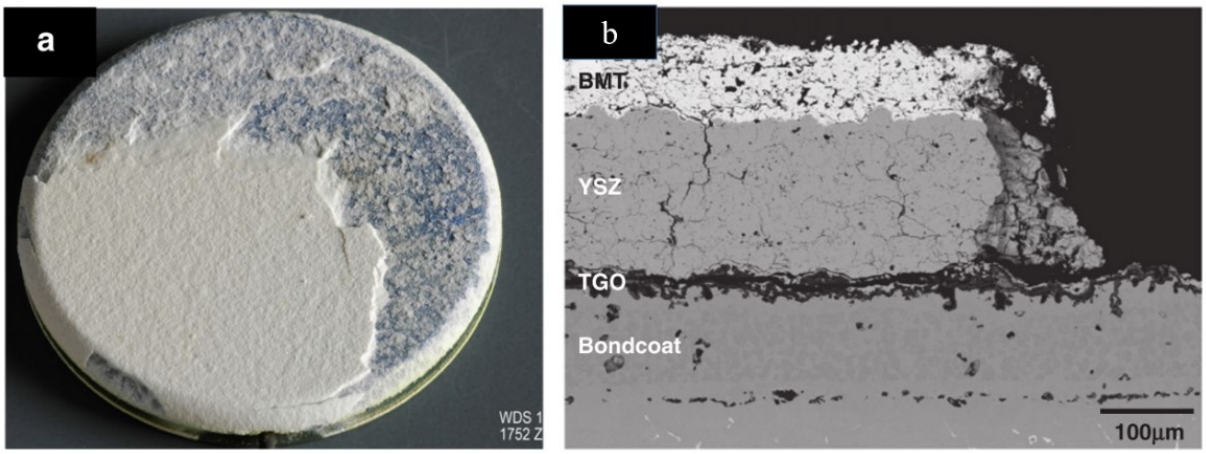

Figure 2.14 Surface morphology (a) and cross-sectional image (b) of BMT/YSZ coating after 1752 cycles at 1240 °C [4]

The accelerated growth of TGO at bond coat and YSZ interface is the first spallation reason. In addition, the lamellar microstructure and non-stoichiometric phase structure of as-sprayed coating also lead to the earlier failure during thermal cycling. Until now, the APS deposited BMT coating only shows a lamellar microstructure which is characterized by obvious parallel cracks or inter-splat delamination cracks, as seen in Figure 2.13a. These cracks may effectively decrease the thermal conductivity. However, they weaken the bonding inside the coating. Accordingly, the propagation of parallel cracks during thermal cycling results in the coating spallation. In addition, the presence of secondary phases also has a negative effect on thermal cycling life. The secondary phases possess different thermal properties compared to the main phase BMT. For example, their different expansions at high temperature may induce cracks propagation.

2.3. Fabrication method for TBCs

2.3.1. Direct current plasma spraying

2.3.1.1 Atmospheric plasma Spray

Thermal plasmas are characterized by high temperatures (around 10 000 K) that can melt or decompose any materials within a very short time [77]. For this reason, plasma spraying has been widely used to produce various metallic and ceramic coatings if the feedstock does not decompose or vaporize excessively.

> *« The D.C. plasma is initiated by a high-voltage pulse that creates a conductive path for an electric arc formed between cathode and anode. The electric arc then heats the working gas to a high temperature so that the gas is dissociated and ionized to form thermal plasma inside the plasma gun. Finally thermal plasma flows out from the nozzle exit of the gun to form plasma jet » D. Zhang et al.* [78].

Direct current atmospheric plasma spraying (DC APS as shown in Figure 2.15) is the most popular technique to deposit TBCs. Figure 2.16 presents a cross sectional image of a typical plasma-sprayed YSZ coating [79]. The lamellar structure is clearly observed. Other typical defects such as interlamellar cracks and porosities are also presented.

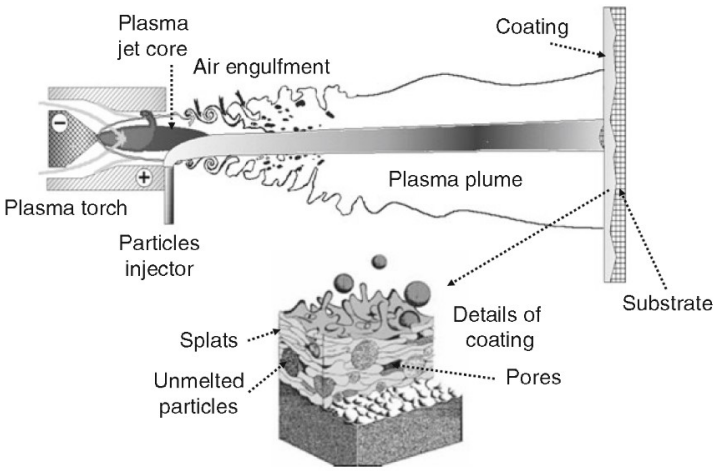

Figure 2.15 Schematic of DC APS process [79]

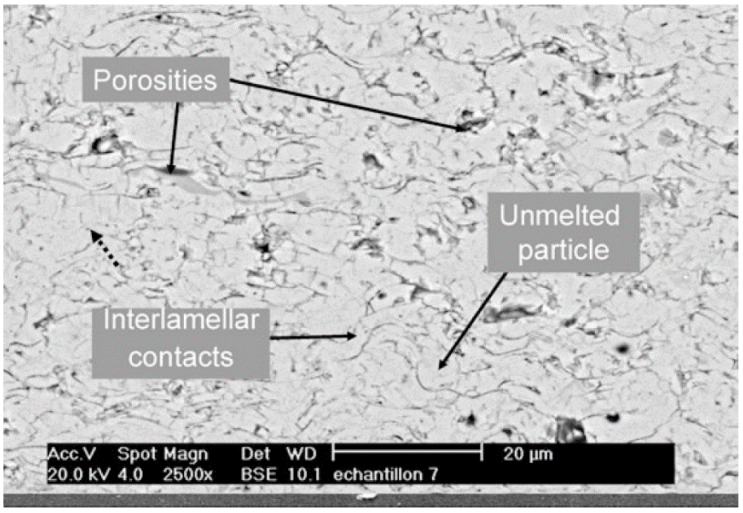

Figure 2.16 Cross-sectional image of typical air plasma-sprayed YSZ coating [79]

2.3.1.2 Low pressure/vacuum plasma spray

The development of low pressure/vacuum plasma spray (LPPS/VPS) is linked to that of bond coats for TBCs used in aero engine. It can avoid the oxidation of the metal layer that often occurs during traditional APS process. It should be mentioned that for some components, such as blade and vane, high velocity oxygen fuel (HVOF) is also used for bond coat preparation because of its extremely dense structure or lower oxidation phenomenon. LPPS usually operates in a controlled atmosphere chamber with pressures between 5 and 70 kPa (50~700 mbar), as indicated by Figure 2.17 [80]. LPPS has some obvious advantages compared to traditional APS process. It provides high particle velocity and effectively prevents the oxidation of in-flight particles. The steady jet avoids cold gas entrainment that results in uniform particle heating and acceleration. However, these advantages need a capital investment that exceeds that of an APS system by an order of magnitude. Until now, LPPS and VPS are usually used to prepare the bond coat of TBC system. As for the top coat, APS is still the most popular method.

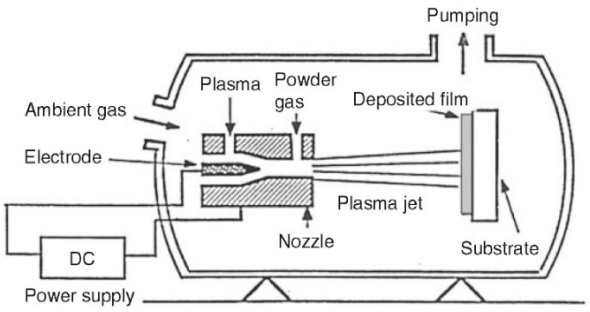

Figure 2.17 Schematic of LPPS installation [80]

2.3.1.3 D.C. Suspension/Solution Precursor Plasma Spray

The lamellar structure (Figure 2.16) is presented as an archetype describing most coatings prepared by APS or LPPS. In fact, this structure may not apply to the coatings deposited by plasma spraying of feedstocks with diameters smaller than 10 μm [81]. The decreased grain size from micrometer to nanometer level normally improves materials properties, such as physical, chemical and mechanical performance. However, introducing nanometer scale feedstock into plasma by carrier gas is impossible because of their insufficient mass and inertia. Nanometer particles tend to segregate at the boundary of the plasma plume and to disperse elsewhere instead of depositing on the substrate. Besides, due to its electrostatic interactions and low flowability, nano-powder may clog the powder feeder. Consequently, a high flow rate carrier gas is required to accelerate the dry nano-powder. However, such a high gas flow rate is known to drastically perturb the plasma jet [82]. Liquid feedstock is an alternative way to replace the dry one. When the liquid precursor is prepared by dispersing sub-micrometer or nanometer sized powders in various solvents, the resulting plasma spray technique is referred to as suspension plasma spray (SPS) [9]. Meanwhile, dissolved chemical reagents (salts or metal alkoxides) are fed in the process named solution precursor plasma spray (SPPS) [8]. Liquid carrier possesses enough momentum to make tiny particles cross the plasma stream while introducing only low feed rate of carrier gas. It has a limited effect on the plasma jet. Accordingly, the developments of the SPS and SPPS technologies are essential [81].

Ethanol and distilled water are the commonly used solvents. Liquid precursor, which are placed in a pressurized vessel or in a simple container, can be injected through a nozzle into the plasma axially or radially [83]. Generally, two different injection technologies exist. The first one is the direct injection of a liquid stream which will be broken and be further atomized in the plasma jet. The second one is to atomize the liquid before injection. Accordingly, the molten droplets formed in SPS/SPPS possess fine diameters in the range of few hundred nanometers to a few micrometers. As a result, the coatings that piled up from tiny splats normally show unique characteristics compared to that of their conventional APS counterpart [84].

The behavior of the injected suspension in a plasma can be described in several steps. When the suspension passes through the atomizer (normally using an atomization probe), the gas exerts a shear stress on the liquid. This process atomizes the suspension into many fine droplets, which are rapidly transferred into the plasma region. Then, a drag force shears a large droplet into many small ones. This process is also described as the secondary breakup or aerodynamic breakup. After aerodynamic breakup, the following stages are clearly described in Figure 2.18.

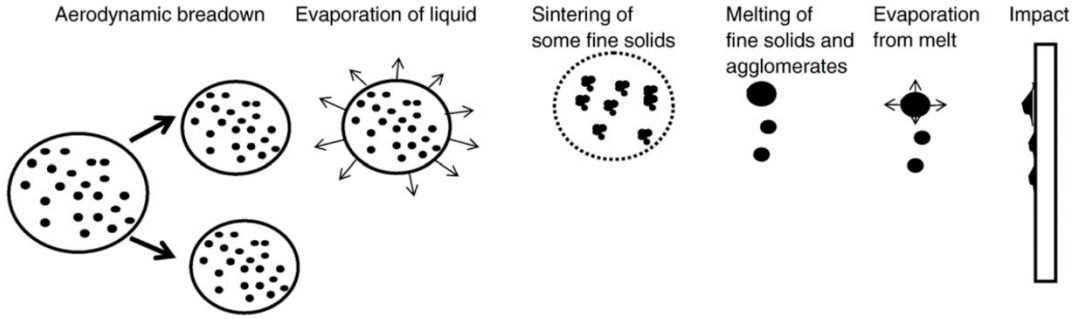

Figure 2.18 Evolutional process of a suspension droplet in the plasma [85]

Except for the aerodynamic breakup, the evolutional process of a solution in plasma is totally different from that of a suspension. In fact, the solution undergoes chemical (precipitation of solute) processes following the aerodynamic breakup. The detailed stages are summarized in Figure 2.19.

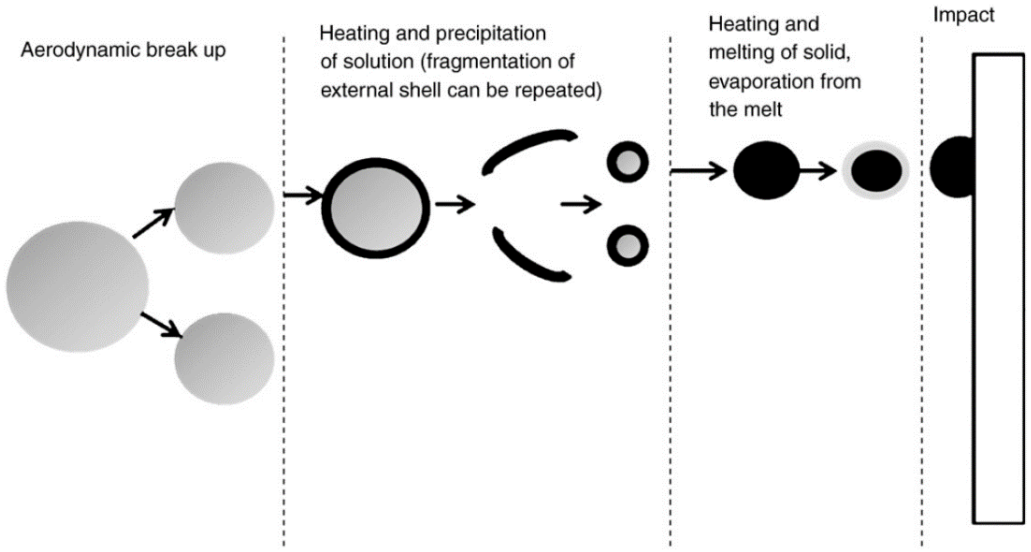

Figure 2.19 Evolutional process of a solution droplet in plasma [85]

When the feedstock size is reduced from micro to sub-micro/nanometer scale, the coating microstructure is modified significantly. In some conditions, as-sprayed SPS coating (Figure 2. 20) presents a special microstructure characterized by high density segmentation cracks with a length of at least half of the coating thickness [18]. During cooling, the thinner splats possess a lower energy release rate that give inadequate energy for propagation of parallel micro-cracks. Due to the lack of micro-cracks, tensile stress cannot be released efficiently, which induces the formation of segmented vertical cracks [84]. This microstructure provides good strain tolerance and thermal shock resistance [86].

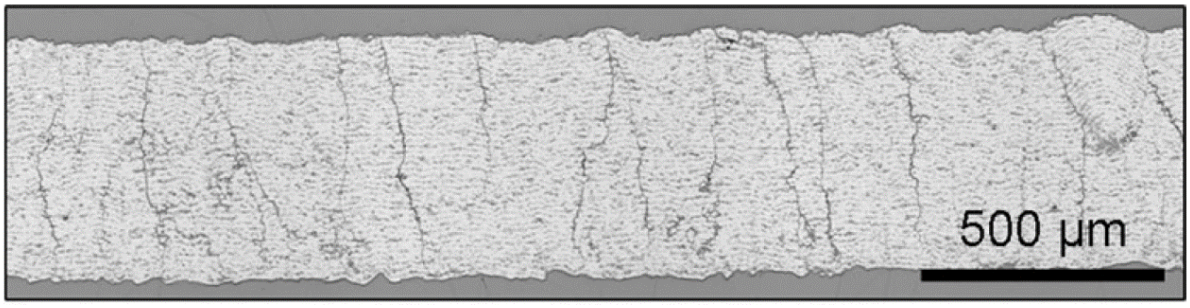

Figure 2.20 Cross-sectional image of as-sprayed SPS coating with segmented vertical cracks [86]

Columnar structure is another special microstructure deposited by SPS/SPPS, as shown in Figure 2.21 [87]. The top morphology presents a so-called cauliflower-shaped structure (Figure 2.21a). The adjacent columns coalesce to form big clusters. Intercolumnar or inter-cluster gaps exist between the columns or clusters. The large gaps, normally caused by the shadowing effect, provide new columns growth sites. The newly formed columns near the top surface are named secondary columns. The cross-sectional image (Figure 2.21b) presents cone-shaped columns, with some reversed cone shapes formed between two big columns or clusters. The columnar structure offers high thermal compliance during service. Nevertheless, the intercolumnar gaps offer direct heat/air conduction that reduce the thermal insulation effect considerably [83]. Through adjusting the spraying parameters such as feed rate, plasma gas composition, substrate surface roughness and torch linear speed, the columnar microstructures can be tuned. Columnar structures with excellent overall properties, good thermal cycling and thermal insulation effect, can also be achieved [88].

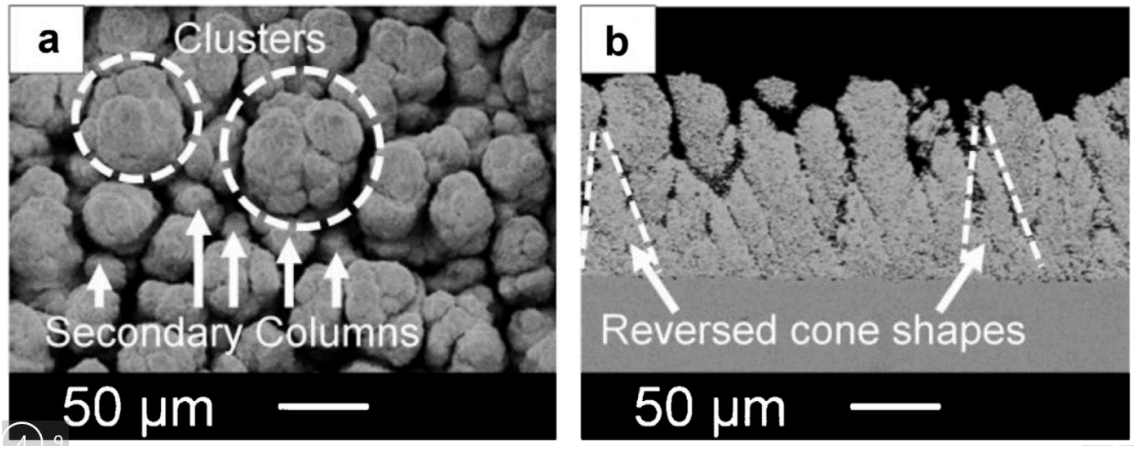

Figure 2.21 Top morphology (a) and cross-sectional image (b) of SPS deposited YSZ coating [87]

2.3.2 Radio frequency inductively coupled plasma spraying

Radio frequency (RF) inductively coupled plasma spraying (ICPS), normally called vacuum induction plasma spraying (VIPS), was developed to spray high purity and/or very dense

coatings. This method has its own special applications in the fields of fiber optics film industry, electrolyte or solid oxide fuel cells and X-ray target manufacturing [89-91]. The feedstock used in VIPS varies from micro-sized powder to suspension or solution. In order to distinguish with SPS and SPPS mentioned in section 2.3.1, the thermal spraying technology of VIPS employing suspension or solution as feedstock are called RF SPS and RF SPPS in the following content. In year 1997, the first patent of RF SPS was granted to Université de Sherbrooke [7]. Compared with conventional thermal spray technology, RF SPS can achieve much thinner coatings. Therefore, this method bridges the technological gap between thermal spray and physical/chemical vapor deposition [92].

2.3.2.1. Description of the induction plasma torch

Schematic representations of a RF ICP torch (a) and of a commercial ceramic wall ICP torch (b) are shown in Figure 2.22. The energy transfer mechanism of RF ICP is similar to that of induction heated metals. However, the plasma gases have lower electrical conductivity than most metals. The oscillator frequencies applied in RF ICP are in the MHz range (Figure 2.22a) compared to KHz range used in the field of induction heated metals. The mechanism of induction plasma can be described as follows:

> «*A high frequency voltage is applied to a water-cooled cooper coil which generates an alternating current. This current induces an axial high frequency oscillating magnetic field within the discharge cavity which creates a ring-shaped electric field normal to magnetic field lines. After the initial striking of arc or ignition of plasma gases, a similar ring-shaped alternating current (induction current) caused by the electric field sustains the plasma through Joule heating. The plasma can be sustained as a stable discharge as long as the energy coupled in to the plasma is sufficient to compensate for conductive, convective and radiative losses from the plasma to the surrounding» P.L. Fauchais et al.* [89].

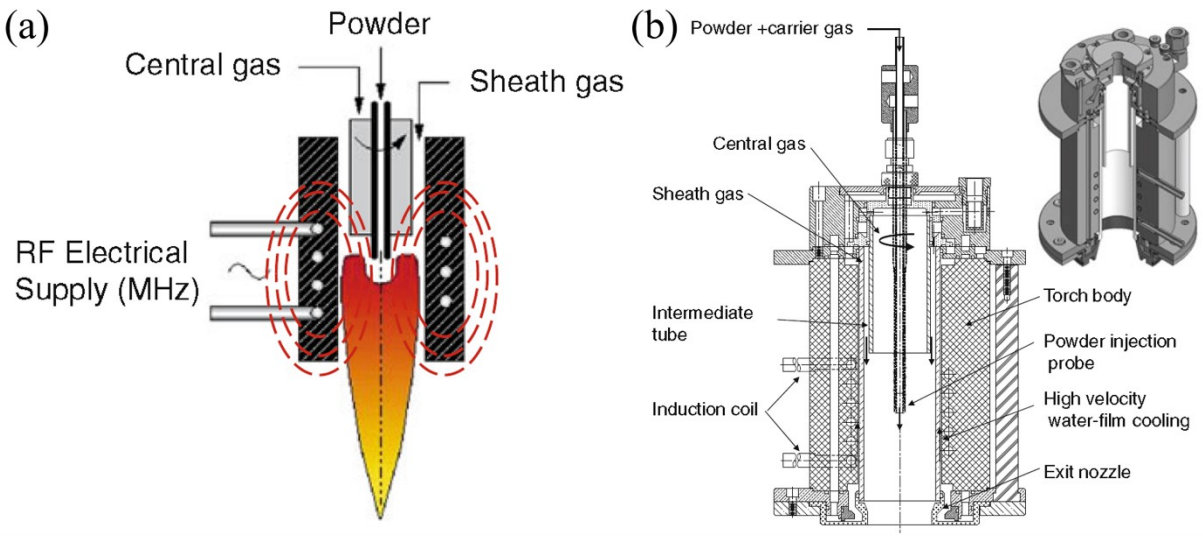

Figure 2.22 Schematic illustration of (a) a typical RF ICP torch and (b) of a commercial ceramic wall ICP torch developed by Boulos and Jurewicz [89]

Radial injection of feedstock is the predominant design used in DC plasma spraying, as indicated by the particle injector in Figure 2.15. Many fine particles, which mingle and remain in the fringes of the plasma jet during flight, cannot be well heated. Consequently, some unmelted particles are embedded in the as-sprayed coatings. As of today, only two DC torches, Axial III designed by Mettech Northwest Corp. and Twin-cathode gun designed by Aero plasma Corp., adopt axial injection [92]. However, because of the complex multiple electrodes design for these two DC torches, clogging problems happened frequently compared to previous radial injection. The axial injection is the main injection path in RF ICP torches, as seen in Figure 2.22. The internal diameters of RF ICP torches are usually 5-7 times bigger than that of the anode-nozzles of DC torches. Therefore, the gas velocities of RF ICP torch are relatively lower than that of DC plasma torch [92]. The axial injection design can send feedstock into the core zone of plasma and fully melt the feedstock, especially for the refractive materials. In addition, because of the electrodeless design, the RF ICP torch avoids the electrode contamination that happens in DC plasma spraying.

2.3.2.2 RF plasma spraying

Figure 2.23 indicates the experimental setup of typical RF plasma spray. This system consists of plasma generator, plasma gases supply, reaction chamber, sample holder, mechanical arm and vacuum pump. The feedstocks (powder, suspension and solution precursors) are fed into the RF torch by different feeders. Coating deposition is operated in a controlled atmosphere chamber. Due to the high radio frequency current, a Faraday cage is necessary to cover the torch, avoiding unacceptable electromagnetic interference (EMI) [89]. As opposed to the flexibility of a DC plasma torch, which is usually manipulated by a six-axes robot, the principal limitation of RF plasma spraying is the fixed plasma torch, which cannot move independently. Although the substrate can be moved by a three-axes robotic arm or 5-axes arm in large units, complex objects are still hard to spray.

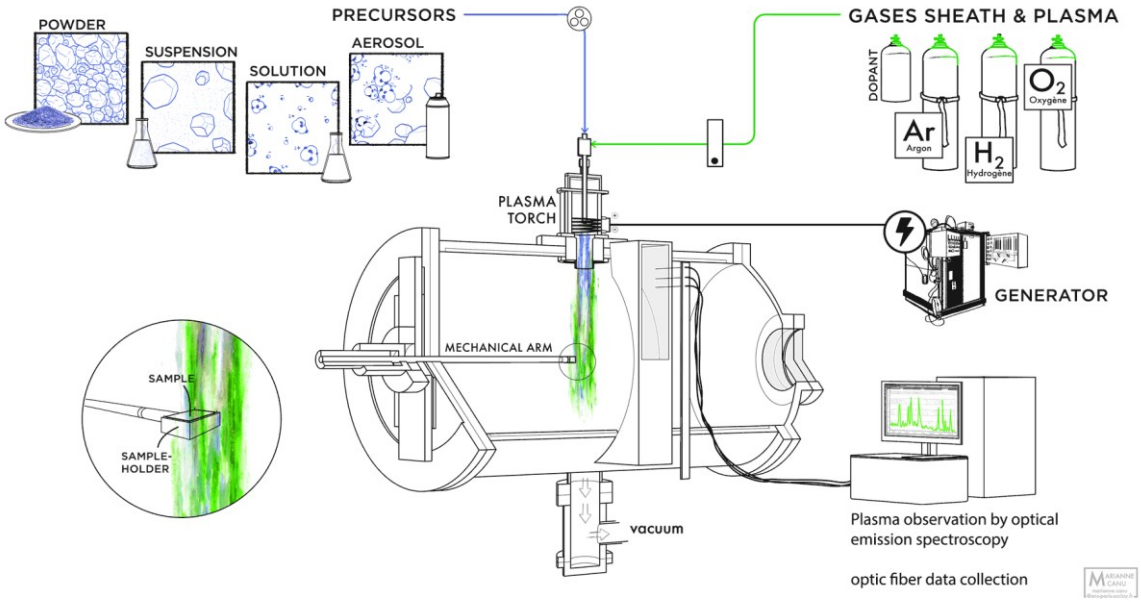

Figure 2.23 Experimental setup of RF plasma spraying

In the process of RF SPS/SPPS, the interactions between droplets and plasma as well as the coating formation processes are similar to that of DC SPS/SPPS, as indicated in section 2.3.1.3. The surface morphologies of RF SPS/SPPS deposited coatings are shown in Figure 2.24. RF

SPPS coatings are mainly nodule-like agglomerates (Figure 2.24a and 2.24b). Each agglomerate is made up of much smaller particles (20 nm in diameter). This nanoscale structure is highly porous. RF SPS coatings, by contrast, show splats-piled surfaces with diameters ranging from 0.2 to 2 μm and thickness varying from 8 to 80 nm (Figure 2.24c and 2.24d).

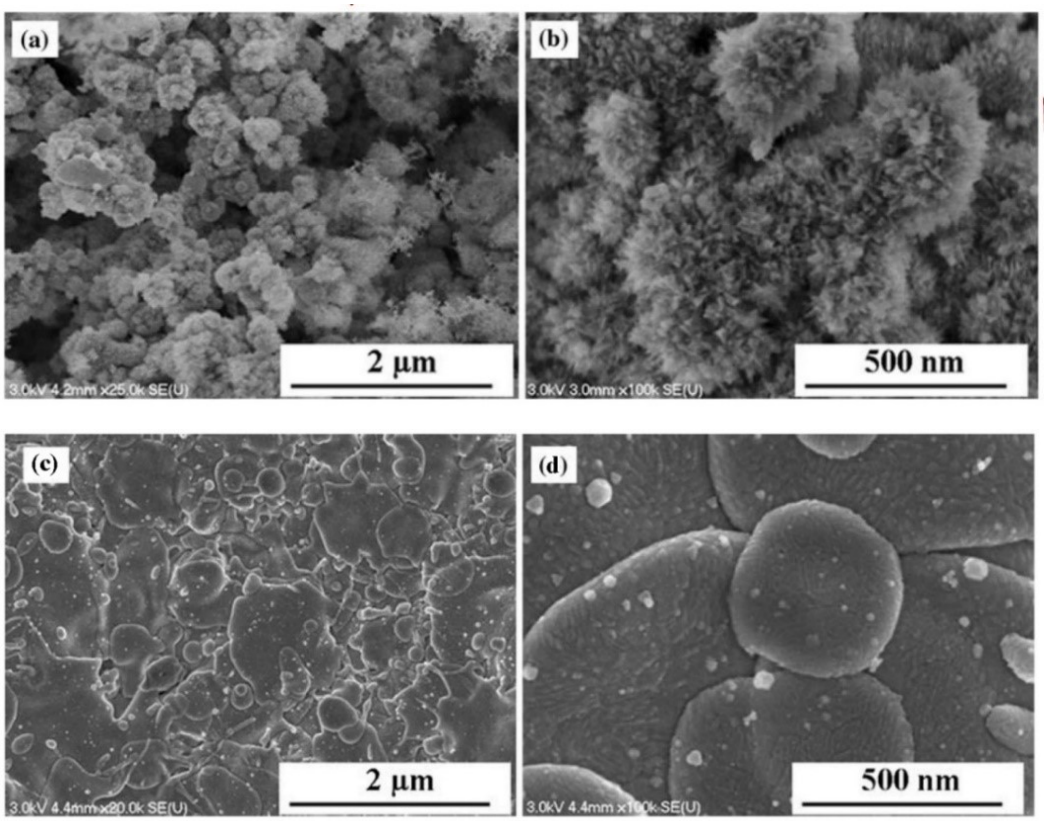

Figure 2.24 The surface morphologies of as-sprayed $Ce_{0.8}Gd_{0.2}O_{1.9}$ electrolyte by (a) (b) RF SPPS and (c) (d) RF SPS [91]

The microstructure of RF SPPS deposited coating, especially its porosity, can be adjusted by a deliberate choice of precursor/solvent couples [93]. Figure 2.25 displays the cross-sectional images of Lu_2O_3-SiO_2-ZrO_2 coatings synthesized using lutetium nitrate, tetraethyl orthosilicate (TEOS) and various zirconium precursors by SPPS, followed by 5 h annealing at 1500 °C. Because zirconium oxynitrate (83 °C) and ethanol (78 °C) have similar boiling points, the precursor decomposes almost simultaneously with the solvent evaporation process and forms coarse particles with permeable shell. Subsequently, these coarse particles form a lot of stacking

defects and a large number of pores in the coating (Figure 2.25a). By contrast, when using zirconium ethoxide instead of zirconium oxynitrate to prepare the solution precursor, the deposited coating presents an obviously different microstructure (Figure 2.25b). There is a large gap of boiling point between the precursor zirconium ethoxide (235 °C) and ethanol (78 °C). After the solvent evaporates in the plasma, the precursor precipitates and forms a dense shell at surface, which restricts the liquid phase inside the shell. This shell is an impermeable structure. The subsequent heating increases internal temperature and pressure and leads to a so-call secondary explosion. Therefore, much more tiny particles form and induce a dense structure.

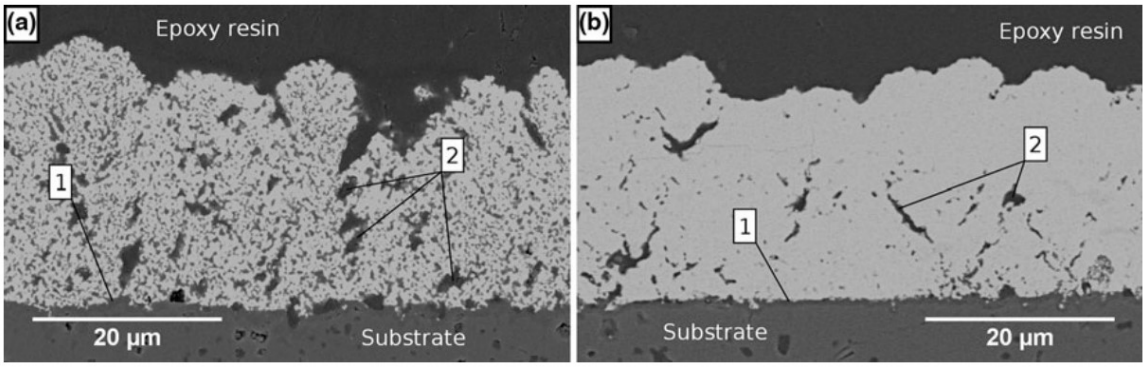

Figure 2.25 Cross sectional images of coatings synthesized from lutetium nitrate, zirconium precursor, and TEOS mixture after heat treatment at 1500 °C during 5 h with: 1—silica scale, 2—microscopic defects due to substrate roughness. (a) zirconium oxynitrate; (b) zirconium ethoxide [93]

2.3.2.3 Powder synthesis and nanometer powder preparation

Apart from coating deposition, RF ICP has two other important applications: the synthesis of complex oxides via spray pyrolysis and oxidation of a liquid precursor [94], and the preparation of nanosized powders, especially for ceramics [90, 95]. Figure 2.26 indicates the experimental setup for powder synthesis. The main difference when compared to Figure 2.23 is the shape of the reactor. The synthesized powder falls mainly on the inner wall of the vertical cylinder-shaped reactor. Because of the vacuum pump, the nano powder is sucked into the auxiliary chamber and filter. Compared to other powder synthesis methods, such as Glycine Nitrate Combustion

(GNC) or Pechini methods, the perovskite powders of $La_{0.8}Sr_{0.2}MO_{3-\delta}$ (M=Mn, Fe, or Co) synthesized by RF ICP have the smallest size and possess the largest specific surface area values [90]. This outcome also indicates that the pure perovskite powder is accessible through the RF ICP synthesis.

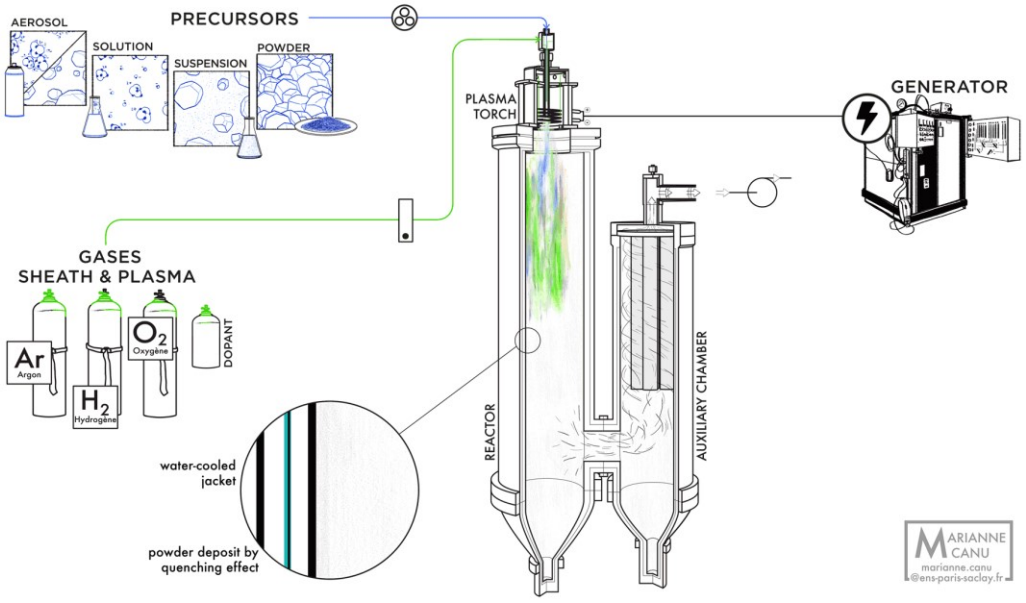

Figure 2.26 Experimental setup of RF ICP powder synthesis

The formation process of nano-powder in RF ICP includes several steps: heating, evaporation, pyrolysis (it depends on the precursors), nucleation and grain growth. Lu Jia et al. used a sampling probe to collect the nanoparticles from various radial and axial positions. Along the radial direction, samples collected from the sites far away from the central line of reaction chamber showed bigger particle sizes compared to that of collected near central line. Differences in particle sizes were also found in various sites along the axial direction. The further the sites from the nozzle, the larger the nucleation sizes were. Lower pressure and higher plasma power shorten the particle residence time in the plasma, resulting in a decreased particle size [95].

In addition to powder synthesis and coating deposition, powder spheroidisation is also a successful application of RF ICP technology. The process can improve the powder flowability

and quality, obviously. It is an important technique to prepare the feedstock for thermal spray and 3D printing [96]. It will not be further described here.

2.3.3. Electron beam-physical vapor deposition

Coatings deposited by electron beam-physical vapor deposition (EB-PVD) have special columnar microstructures which possess high anti-thermal shock properties compared to their APS counterpart. This kind of structure are mainly used for highly thermo-mechanically loaded blades of aircraft gas turbine engines [97].

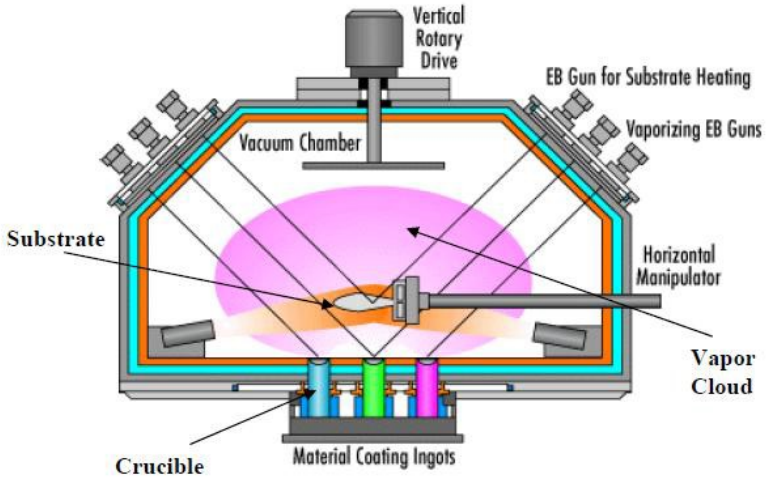

Figure 2.27 EB-PVD reaction chamber [98]

The EB-PVD chamber, as shown in Figure 2.27, mainly includes vacuum system, substrate holder controlled by horizontal manipulator, ceramic ingots to be evaporated and two kinds of EB guns for heating substrate and ingots, respectively. An EB gun produces electrons, which heat the top surface of ingots. The increased temperature causes the ingot to evaporate and subsequently to form an atmosphere filled of vapor. Then, the vapor condenses on the surface of substrate and forms a coating. During the ongoing reaction, different gases can also be fed in the vapor cloud to obtain the desired environments [98]. The conventional chamber pressure varies from 5 Pa (0.05 mbar) to 0.1 Pa (0.001 mbar), and sometimes even lower [99].

EB-PVD coatings have some special feathers such as quasi single crystalline columns, inter-columnar gaps, intra-columnar pores and voids between feather-arms, as shown in Figure 2.28. The preferred-oriented columns begin to grow on the substrate surface with an initial diameter < 2-3 μm. As the columns grow, their diameters gradually increase to 10-20 μm at the coating tip. Correspondingly, the widths of inter-columnar gaps increase from a few nanometres to 1μm [100]. The inter-columnar gaps act as preferential hot gas conduction paths and the dense columns result in rather high thermal conductivity for YSZ (1.5 $Wm^{-1}K^{-1}$) [83].

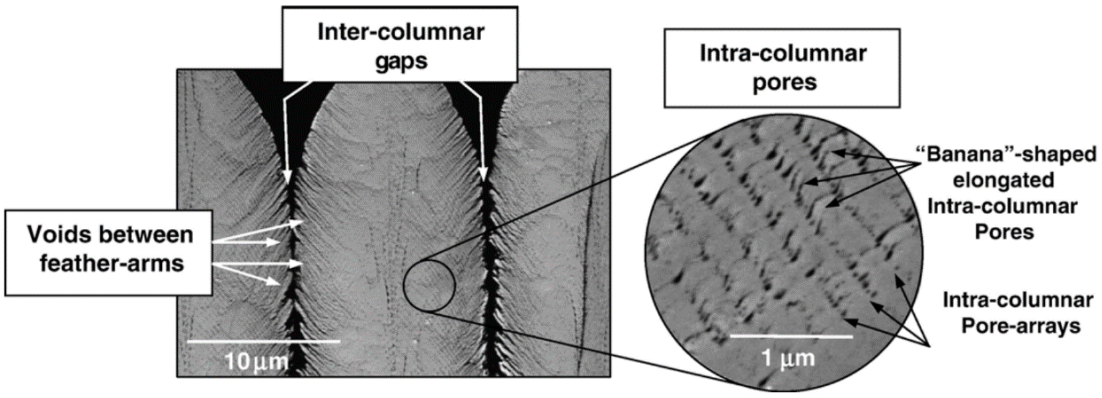

Figure 2.28 SEM images of the typical EB-PVD coating [100]

Similar to the columnar structure deposited by SPS/SPPS, the high strain tolerance of columnar structure is also a major advantage of EB-PVD coating. In addition, EB-PVD deposited columnar structure have a unique advantage, which is the excellent erosion-resistance property. Commercial aero engine is always exposed to an erosive service environment where there is a lot of dust, hail stone, sand storms and volcanic ash. These foreign objects will be mixed with hot gases and impinge on the turbine blade with various angles [101]. Especially when the surface temperature of turbine blades increased above 1240-1260 °C, atmospheric dust melts and wicks into the columns of TBCs, which is called the calcium-magnesium-alumina-silicate (CMAS) attack [102]. This erosion process normally causes a premature spallation of TBC followed by a catastrophic failure. Although the erosion degrees vary according to the type of coating material [103] and the basicity index of CMAS [104], the service life of coating against

erosive particles is finally determined by coating microstructure. A lot of investigations have proved that TBCs deposited by EB-PVD possess better anti-erosion property compared to their APS counterpart [105-107]. As seen in Figure 2.29 [106], the APS coatings are built by the continuous stacking of splats/lamellae. A large number of horizontal micro-cracks and inter-splat boundaries remain in as-sprayed coatings. The impact of foreign particles causes cracks propagation around splat boundaries and leads to flaking off in the form of blocks (Figure 2.29a). In contrast, the quasi single crystalline columns of EB-PVD coating do not contain horizontal cracks and inter-splat boundaries. The impact of erodent only causes near-surface (top 20 μm) cracks within the columns (Figure 2.29b). Because of the constraint of neighbouring columns and inter-columnar gaps, only a small piece of coating is lost from the near-surface region.

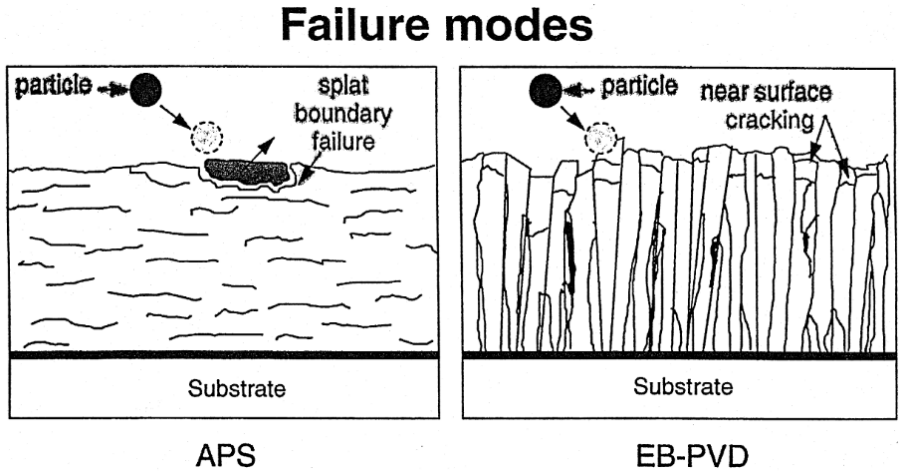

Figure 2.29 A schematic diagram of the failure modes for an APS and EB-PVD TBCs [106]

Although TBCs deposited by SPS/SPPS exhibit columnar or segmented vertical cracked structures instead of a lamellar one, as seen in Figure 2.30, the essence of coating formation mechanism, the stacking of splats, remains the same with that of APS. The impact of erosive particles causes cracks propagation approximately along both the axial and radial directions, as indicated by the lateral and conical cracks in Figure 2.31 [108]. Because the distance between cracks in segmented cracked coatings is longer than the column width in the columnar structure coating, it decreases the probability to merge these cracks with the ones originating from the

adjacent column gaps /vertical cracks. In addition, the as-sprayed segmented cracked coating is denser than the columnar coating. Consequently, the eroded crater caused in columnar coating is larger than that caused in segmented cracked one. Both of them present higher erosion levels than EB-PVD coatings. As such, even if the capital investment for EB-PVD is way higher than that of APS and SPS/SPPS, TBCs on key components in aero engine, for example turbine blades, are still deposited by EB-PVD [109].

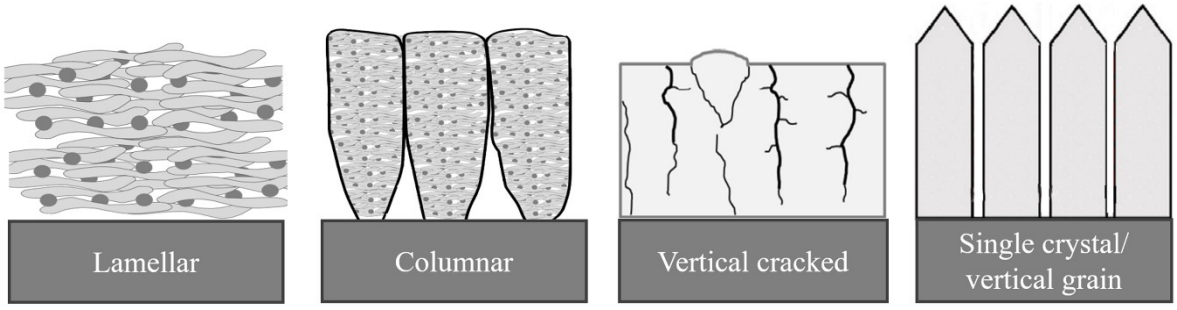

Figure 2.30 Schematic illustration of different TBCs structures: lamellar (APS) (inspired by [88]), columnar (SPS/SPPS), segmented vertical cracked (SPS/SPPS) (inspired by [110]) and single crystalline columns (EB-PVD)

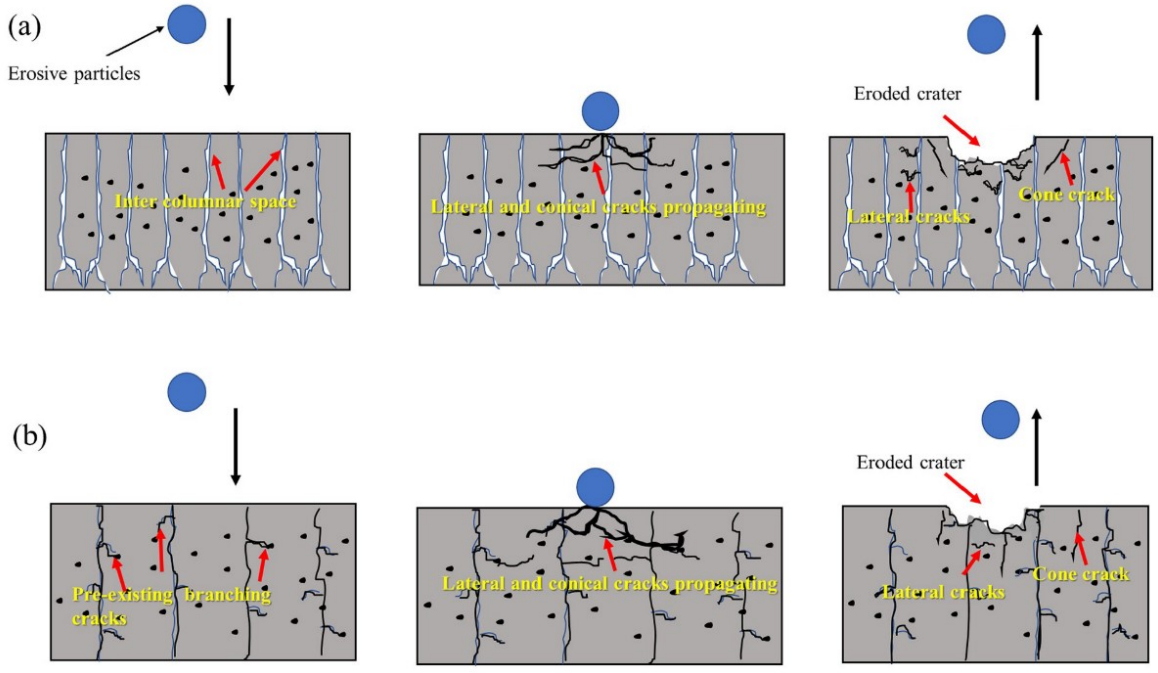

Figure 2.31 A schematic model of erosion mechanisms for (a) columnar structure coating and (b) segmented vertical cracked coating at 90° impact angle [108]

2.3.4. Plasma spray-physical vapor deposition

In EB-PVD, the vaporized coating material is transported to the substrate by a diffusion process. The coating growth rate of EB-PVD is much lower than that of plasma spraying [99]. In addition, when the substrate surfaces are not in direct line-of-sight to the coating source, such as complex geometries and shadowed areas, they are hard to coat homogeneously. Plasma spray-physical vapor deposition (PS-PVD) was developed by Sulzer Metco AG (Switzerland). The goal of this technique is to deposit various microstructure quickly via evaporation or melting of feedstock [111]. PS-PVD process was originally named thin film-low pressure plasma spraying (LPPS-TF) [112]. LPPS/VPS is the basis of PS-PVD. It is required to further reduce the reactor pressure from 5~20 KPa (LPPS/VPS) to 50~200 Pa (PS-PVD). After satisfying the dual conditions of a very low reactor pressure and a high electrical input power (around 180 kW, 3000 A) [113], PS-PVD can evaporate powder feedstocks and deposit coatings with various microstructures (lamellar, columnar and dense structures) by adjusting the parameters [114]. PS-PVD has unique characteristics. For example, by reducing the working pressure, the plasma plume is enlarged, as indicated in Table 2.6, which makes the particle velocities and temperatures homogenous. The vapor of coating materials is transported by the hot (6000~10000 K in plasma core) and supersonic (2000~4000 m/s) plasma jet at 100 Pa. By incorporating vaporized feedstock into high-velocity gas, PS-PVD can coat complex geometries and shadowed areas. The so-called non-line-of-sight deposition is becoming a meaningful capability for surface engineering techniques [99, 111].

Although the columnar structures can be obtained by EB-PVD, DC SPS and PS-PVD, the surface morphologies are different from each other due to various condensation modes. Vapor condensation is the main way of coating growth for EB-PVD. The basic morphology of the column tips is a pyramid with cut-like facets, as seen in Figures 2.32a and 2.32b [115]. In the process of PS-PVD, the evaporation phenomenon could be induced if decreasing the feed rate.

The coating growth mode is controlled by condensation and surface diffusion. Compared to EB-PVD, the pyramids of PS-PVD look coarser with many wrinkles (Figures 2.32c and 2.32d) [116]. As for DC SPS, the liquid condensation dominates the growth mode. Figure 2.32e) presents a cauliflower structure. SPS coatings are produced by molten droplets whose morphologies are totally different from that of vapor-condensed pyramids [81], as shown in Figure 2.32f.

Table 2.6 Pressures in reaction chambers of different coating preparation methods and the corresponding size of plasma [99]

Methods/Characteristics	APS	LPPS	PS-PVD	EB-PVD
Working pressure (kPa)	101	3~20	0.05~0.2	$0.1\sim 5\times10^{-3}$
Plasma length (mm)	50	500	2000	Non applicable
Plasma diameter (mm)	10	40	200~400	Non applicable

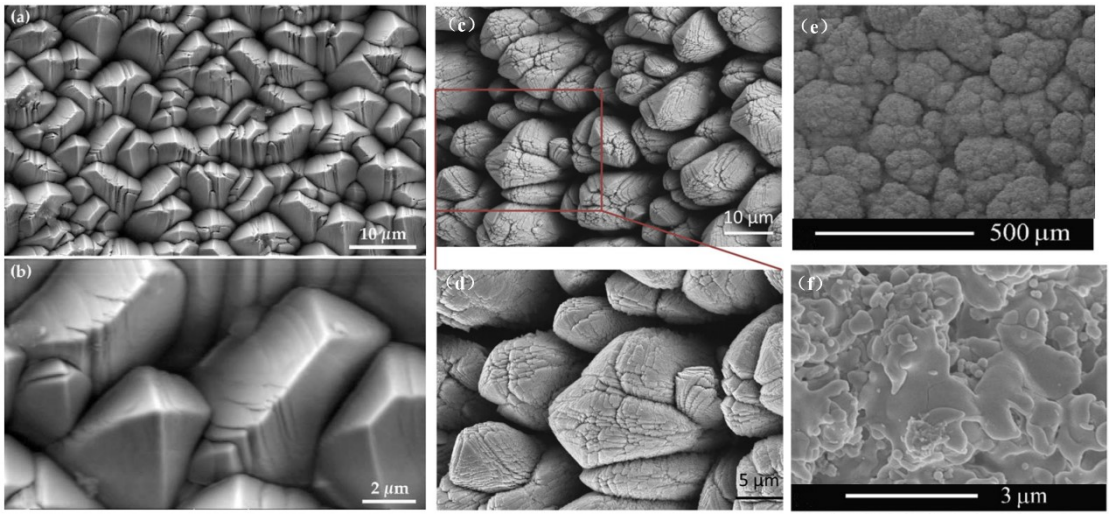

Figure 2.32 Top surface morphologies of EB-PVD (a) (b), PS-PVD (c) (d) and DC SPS (e) (f)

CHAPTER 3

Project objectives

The inlet gas temperature in the aero-engine will increase to 1540 °C and even higher after year 2020 as indicated in Fig. 2.2. The increased gas temperature facilitates improvement of engine efficiency, but it challenges the temperature limits of existing TBC materials and metallic substrates. The core of this project is to develop a ceramic material that could serve around 1400 °C. BMT is chosen as the new TBC material in this project owing to its high melting temperature and low thermal conductivity. The BMT coating deposited by the traditional spray method of APS has a dense structure and a mixture of secondary phases which leads to a low fracture roughness. Applying new technology of RF-liquid precursor plasma spray is expected to solve the major problems such as secondary phases and dense structure. In addition, the application fields and unique properties of the coatings prepared by this technology will be further discussed in this work. The main and specific objectives are summarized as follows:

3.1 Main objective

The main purpose of this project is to develop a new generation of BMT TBCs that have the potential to be used on key components of aero engine.

3.2 Specific objectives

- The first specific objective is to explore the powder synthesis using RF ICP, and to deposit BMT coatings using RF SPS/SPPS techniques from BMT precursors (suspensions or solutions). The phase transition conditions and the mechanism of BMT formation should

be identified clearly. In particular, the relation between the formation of the main phase of BMT and that of other secondary phases needs to be studied in detail for RF SPS/SPPS processes. Suitable spraying parameters for BMT coating deposition as well as plasma and precursor chemistries, should be well understood and summarised.

- The second objective is to control the growth of various BMT microstructures upon coating deposition. In order to meet the requirements of various service environments, several types of microstructures (lamellar, columnar and segmented cracked structures) need to be explored, including their mechanism of formation. This is an essential work for developing industrial applications, especially for a new TBC candidate material such as BMT.

- The last objective is to explore new TBC structure, which could be used in the harshest service environments in the field of aero engine. Columnar structure, which is characterised by inter-columnar gaps, have an excellent thermal cycling lifespan. However, when submitted to foreign objects erosion, the stacked splats will peel off quickly. It cannot offer an effective protection for turbine blade, as EB-PVD coatings do. As such, it will be attempted to deposit BMT coatings having a columnar structure with vertical grains. In addition, this work will explore a potential application for BMT, with the complete substrate – bond coat – top coat system.

This thesis presents the main results in the form of three articles, which have already been published in peer-reviewed journals. These articles correspond to the three specific objectives mentioned above.

CHAPTER 4

Material and coatings phase structure investigations

4.1 Avant-propos

Auteurs et affiliation :

- Huidong Hou : étudiant au doctorat, Université de Sherbrooke, Faculté de génie, Département de génie chimique et de génie biotechnologique.

- Jocelyn Veilleux : professeur agrégé, Université de Sherbrooke, Faculté de génie, Département de génie chimique et de génie biotechnologique.

- François Gitzhofer : professeur titulaire, Université de Sherbrooke, Faculté de génie, Département de génie chimique et de génie biotechnologique.

- Quansheng Wang : professeur, Institut de technologie de Pékin, Faculté de science des matériaux et d'ingénierie.

- Ying Liu : professeur, Institut de technologie de Pékin, Faculté de science des matériaux et d'ingénierie.

Date d' acceptation : 26 novembre 2018

État de l'acception : version finale publiée

Revue : Journal of Thermal Spray Technology

Référence : [H.Hou et al., Journal of Thermal Spray Technology, 2019, 28(1-2), 12-26]

Titre français : Projection plasma hybride d'un précurseur en suspension/solution d'un complexe de pérovskite $Ba(Mg_{1/3}Ta_{2/3})O_3$: effets des paramètres de projection et de la chimie des précurseurs sur la formation et la décomposition des phases

Contribution au document:

This scientific paper focuses on the phase structure evolution in the processes of powder synthesis and plasma spraying. As for a complex oxide, the traditional solid-state method was first applied to synthesize BMT powder and to carry out the post-calcination processes. The investigation of synthesized powder phase structure facilitated the understanding of BMT material, which was also used as the benchmark for the phase structure of as-sprayed coatings. In addition, the relation between BMT and other secondary phases as well as their formation conditions during the plasma spray processes were discussed clearly in this paper.

Current researches on BMT and its secondary phases are still limited. The available ICDD cards for $BaTa_2O_6$ (secondary phase in the process of BMT deposition) and other orthorhombic barium tantalum oxides lack data (space group symmetry, atomic coordinate, and anisotropic displacement parameters, etc.) to reliably quantify the phases. As such, the attempts to quantify the amount of each phases using Rietveld refinement were, at best, very approximate. Accordingly, the refinement results were not shown in this paper. After the paper being published, some supplementary works were carried out, which mainly focused on the calculation of BMT ordering degree by Rietveld refinement. In addition, the internal temperatures of the substrate during spraying were measured and presented. These additional results are shown in the section 4.6.

Résumé français :

Le $Ba(Mg_{1/3}Ta_{2/3})O$ (BMT) a un point de fusion élevé et est envisagé comme matériau de revêtement de barrière thermique. Dans cette étude, un procédé hybride de projection plasma d'un précurseur en suspension/solution avec une torche à plasma thermique radiofréquence est

conçu pour déposer des revêtements nanostructurés de BMT. Six combinaisons de réactifs chimiques sont étudiées comme précurseurs de revêtement : une suspension de poudre BMT et cinq suspensions de Ta_2O_5 dans des solutions à base de nitrates ou d'acétates. La spectroscopie photoélectronique à rayons X (XPS) est utilisée pour évaluer l'évaporation de l'élément Mg pendant la projection par plasma, tandis qu'une analyse thermogravimétrique / thermique différentielle (TG/DTA) est appliquée pour étudier la formation de BMT. Des paramètres tels que la chimie des précurseurs, la puissance du plasma, la distance de projection et le préchauffage du substrat sont étudiés par rapport à la structure et la phase du revêtement. Une quantité stœchiométrique de Mg deux fois plus élevée avec une puissance de 50 kW donne des meilleurs résultats lorsqu'on utilise du Ta_2O_5 nanocristallisé comme précurseur de tantale. En choisissant les nitrates comme précurseurs de Ba et Mg, on obtient du BMT cristallisé à une puissance de plasma plus faible (45 kW) par rapport aux acétates (50 kW). $BaTa_2O_6$, $Ba_3Ta_5O_{15}$, $Ba_4Ta_2O_9$, $Mg_4Ta_2O_9$ sont les principales phases secondaires observées lors du dépôt des revêtements de BMT. En raison de la complexité du processus de décomposition de l'acétate, le taux de dépôt des revêtements à partir des précurseurs de nitrates est 1,56 fois plus élevé que celui des précurseurs d'acétate.

Mots-clés : BMT, SPS/SPPS hybride, paramètres de projection, chimie des précurseurs, décomposition.

Note : À la suite des corrections demandées par les membres du jury, le contenu de cet article diffère de celui qui a été accepté.

Title: Hybrid Suspension/Solution Precursor Plasma Spraying of a Complex $Ba(Mg_{1/3}Ta_{2/3})O_3$ Perovskite: Effects of Processing Parameters and Precursor Chemistry on Phase Formation and Decomposition

Abstract:

$Ba(Mg_{1/3}Ta_{2/3})O_3$ (BMT) has a high melting point and is envisioned as a thermal barrier coating material. In this study, a hybrid suspension/solution precursor plasma spray process with a radio frequency thermal plasma torch is designed to deposit BMT nanostructured coatings. Six combinations of chemical reagents are investigated as coating precursors: one BMT powder suspension and five Ta_2O_5 suspensions in nitrate- or acetate-based solutions. X-ray photoelectron spectroscopy (XPS) is used to evaluate the element evaporation during plasma spraying, while a thermogravimetric / differential thermal analysis (TG/DTA) is applied to investigate the BMT formation. Parameters such as precursor chemistry, plasma power, spraying distance and substrate preheating are studied with regards to the coating phase structure. Twice the Mg stoichiometric amount with a power of 50 kW shows the best results when using nanocrystallized Ta_2O_5 as a tantalum precursor. When choosing nitrates as Ba and Mg precursors, crystallized BMT is obtained at lower plasma power (45 kW) when compared to acetates (50 kW). $BaTa_2O_6$, $Ba_3Ta_5O_{15}$, $Ba_4Ta_2O_9$, $Mg_4Ta_2O_9$ are the main secondary phases observed during the BMT coatings deposition. Because of the complicated acetate decomposition process, the coating deposition rate from nitrate precursors is 1.56 times higher than that from acetate precursors.

Keywords: BMT, hybrid SPS/SPPS, spraying parameters, precursor chemistry, decomposition.

4.2 Introduction

High-temperature components used in modern turbines need to endure high temperature service

environments [1]. In order to increase turbine thermal efficiency and decrease energy consumption, these temperatures were continuously increased up to a point where they led to early failure and spallation of the most widely used thermal barrier coatings (TBCs), based on yttria-stabilized zirconia (YSZ) [3]. This triggered a widespread exploration of new TBCs materials. $Ba(Mg_{1/3}Ta_{2/3})O_3$ (BMT) which was considered as the most refractory oxide ever known to science (with a melting temperature around 2900-3100 °C) [64], has been chosen as a TBCs candidate material in this study. First studied as a dielectric material, BMT showed poor sintering ability even at temperatures as high as 1600 °C [69]. This demerit as a dielectric material becomes the merit of BMT as a TBC. Compared to YSZ (melting point of 2700 °C), which sinters significantly from 1200 °C [3], BMT is proposed for service at higher temperatures since its melting point and sintering temperatures are higher. Such a high melting temperature requires a plasma process which can heat BMT into well-melted or semi-molten state and then deposit BMT coatings effectively. As such, the conventional BMT coating deposition method is Air Plasma Spraying (APS) of a BMT powder. The as-sprayed BMT coatings produced by APS typically show a mixture of secondary phase (Mg-depleted phase) and BMT, which leads to a decrease in melting temperature and low mechanical properties [4-6]. This problem is mainly caused by the Mg-evaporation during APS. An excess of Mg added to the initial precursors and suitable deposition parameters should remedy this problem. In addition, commercial BMT powders are not broadly available and feedstock powder of APS requires several preparation steps including synthesis, agglomeration and sintering steps. Therefore, it is preferable to start with precursors instead of BMT feedstock from an economical standpoint. In suspension plasma spraying (SPS) [7], submicrometer or nanometer sized powders dispersed in various solvents (usually water or ethanol) are used as feedstock, while dissolved chemical reagents (salts or metal alkoxides) are fed in solution precursor plasma spraying (SPPS) [8]. In SPPS, the complex feedstock preparation process of APS described above (synthesis, agglomeration and sintering of powders) is eliminated, as it occurs in-flight.

As-sprayed coatings prepared by SPS or SPPS show characteristic microstructures such as submicron or nanosized pores, segmented cracks and columns [86, 93, 117, 118], and most of them are proven or foreseen beneficial for the performance of TBCs in comparison to APS-deposited coatings. Still, as most direct current (D.C.) plasma torches use radial feedstock injection, the deposited coatings in SPS and SPPS often contain a large amount of unmolten nanosized particles that result from the overspray [86]. With axial injection, overspray is less likely as the feedstock is directly fed in the core of the plasma jet. This strategy is chosen in this study to feed a radio frequency inductively-coupled plasma (R.F. ICP) torch, which is also attractive to spray refractive materials such as BMT, owing to long residence times [91, 92]. The BMT precursors consist of Ta_2O_5 powders, cheaper and easier to process than Ta alkoxides, in suspension in a solution of Ba and Mg soluble salts, calling for a novel hybrid SPS/SPPS process [119]. Feedstock and deposition parameters such as precursor chemistry, Mg content, substrate pre-heating, spraying distance and plasma power are investigated with regards to the phase composition of the deposited coatings. The conditions leading to a relatively pure BMT phase are identified and discussed.

4.3 Experimental procedures

4.3.1 Feedstock preparation

Six combinations of suspensions/solutions were used in this work, as seen in Table 4.1. A mixture of water and ethanol was chosen as solvent. Water is required to dissolve Ba salts, but its evaporation consumes much more energy than ethanol once injected in the plasma. Ethanol also releases heat and increases temperature upon its combustion along the plasma jet [91]. A constant solid concentration of 10 wt. % was chosen for all the suspension/solutions. Precursor S1 was used to investigate the phase decomposition during plasma spraying. Precursors S2, S3 and S4, with different Mg stoichiometric ratios, aimed at evaluating the influence of Mg

depletion in the plasma. Regarding the solute chemistry, acetate-based precursors have a higher solubility in water compared to nitrate-based ones. As such, with acetate-based solutes, one can increase the ethanol:water ratio while keeping the same salt concentration. Thus, S4 and S5, with different salts and solvent ratios, were used to compare the effect of precursor chemistry. Precursor S5, which contains a higher percentage of ethanol, was selected to study the heating effect. Finally, precursor S6 aimed at evaluating the effect of initial Ta_2O_5 particle size. The detailed preparation of each precursor follows.

Table 4.1 List of suspension /solution precursors combinations and its corresponding plasma power used during spraying

No.	Solute	Solvent (water/ethanol)	Plasma power, kW
S1	Synthesized BMT powder	1:1	45
S2	Nanocrystallized Ta_2O_5, Ba nitrate, Mg nitrate (stoichiometric)	1:1	53
S3	Nanocrystallized Ta_2O_5, Ba nitrate, Mg nitrate (1.5 × stoichiometric qty)	1:1	53
S4	Nanocrystallized Ta_2O_5, Ba nitrate, Mg nitrate (2 × stoichiometric qty)	1:1	45/50/53kW
S5	Nanocrystallized Ta_2O_5, Ba acetate, Mg acetate (2 × stoichiometric qty)	1:3.6	45/50/53kW
S6	Spheroidized Ta_2O_5, Ba nitrate, Mg nitrate (2 × stoichiometric qty)	1:1	45/50/53kW

BMT powder for SPS

A stoichiometric BMT powder was synthesized from the mixture of Ta_2O_5, $BaCO_3$ and MgO in a muffle furnace (HEFEI KE JING Materials Technology Co., LTD., China) at 1400 °C for 2h. This synthesized BMT powder is to be used as benchmark for phase composition and to prepare

a conventional suspension for SPS (precursor S1). This synthesized BMT powder was also post-calcined for 2h at different temperatures (1100 °C - 1600 °C) to analyze the ordering degree and to evaluate BMT sintering.

Ta_2O_5 powder as tantalum precursor

The commercially available Ta_2O_5 powder purchased (Advanced Materials, USA, 73R-0802, chemical purity 99.99%), with a particle size distribution with d50=5 μm, showed serious agglomeration and poor flowability when in suspension. In fact, this Ta_2O_5 powder was dispersed in various solvents (water, ethanol, isopropanol, etc.) by ultrasonic dispersing and magnetic stirring, but upon pumping using a peristaltic pump, the powder settled in the tubing under gravitational force and induced clogging during the feeding process. To improve the stability and flowability of the Ta precursors in the synthesis of BMT, two alternatives were considered: spheroidization (to prepare precursor S6) and nanocrystallization (to prepare precursors S2-S5). In the plasma-spheroidization process, a powder feeder was employed to axially feed the commercial Ta_2O_5 powder into a R.F. ICP torch (PL-50, Tekna Plasma Systems Inc., Sherbrooke, Québec, Canada), as described in Figure 4.1 [120]. Operating parameters are shown in Table 4.2. Besides, a commercial Ta metal powder (AEE Atlantic equipment engineers, USA, chemical purity 99.8%, 1~5 μm) was axially fed in the same R.F. ICP torch to produce nanosized Ta_2O_5. The detailed parameters for the nanocrystallization process are also shown in Table 4.2.

Magnesium and barium solutions

Mg acetate $Mg(CH_3COO)_2 \cdot 4H_2O$ (Fisher BioReagents, India, BP215-500), Ba acetate $Ba(CH_3COO)_2$ (Sigma-Aldrich, Germany, 32305), Mg nitrate $Mg(NO_3)_2 \cdot 6H_2O$ (Alfa Aesar, America, 11564) and Ba nitrate $Ba(NO_3)_2$ (Sigma-Aldrich, Germany, 217571) were chosen as the acetate-based (S5) and nitrate-based (S2-S4, S6) precursors, respectively.

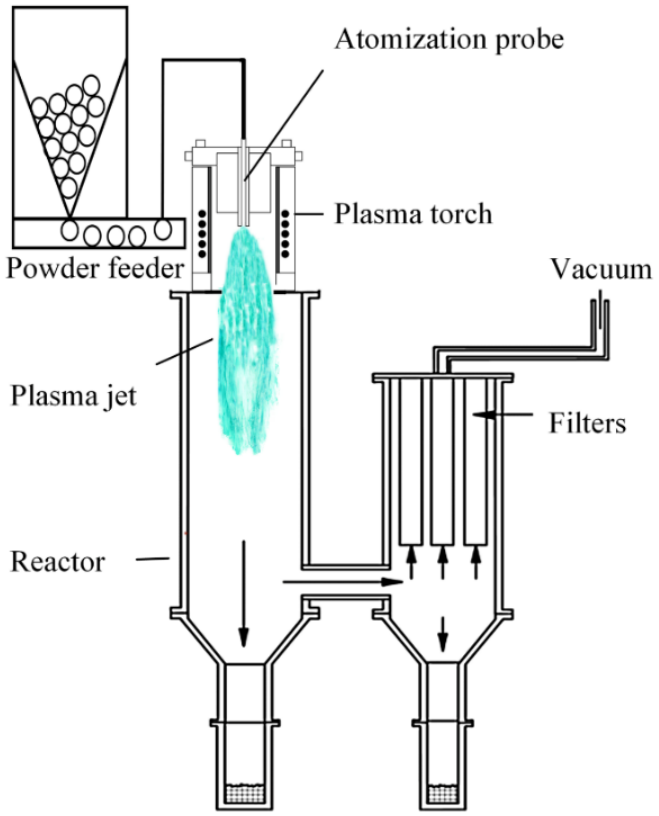

Figure 4.1 Schematic illustration of induction plasma reactor with solid-state powder feeder for the spheroidization and nanocrystallization process

Table 4.2 Plasma parameters for Ta_2O_5 spheroidization and nanocrystallization

	Spheroidization	Nanocrystallization
Sheath gas (Ar)	6 slpm	3 slpm
Sheath gas (O_2)	63 slpm	63 slpm
Sheath gas (He)	No	110 slpm
Central gas (Ar)	23 slpm	23 slpm
Feeding rate	0.2 ± 0.1 g/min	0.5 ± 0.1 g/min
Reactor pressure	33 kPa	80 kPa
Power	43 kW	58 kW

4.3.2 Preparation of BMT coating

Titanium alloy (Ti-6Al-4V) with a diameter of 12.6 mm and a thickness of 2 mm was selected as substrate. All the substrates were sand-blasted and cleaned by acetone and ethanol successively. The substrates were cooled from beneath, being in contact with the water-cooled substrate holder at the tip of the robotized arm, as shown in Figure 4.2. The liquid precursors listed in Table 4.1 were fed by a peristaltic pump to an atomizing injection probe (SDR792-02B1, Tekna Plasma Systems Inc., Sherbrooke, Quebec, Canada). To increase the plasma jet momentum towards the substrate, a 25 mm converging nozzle [118] was installed at the outlet of the torch. The plasma parameters used for coating deposition are shown in Table 4.3.

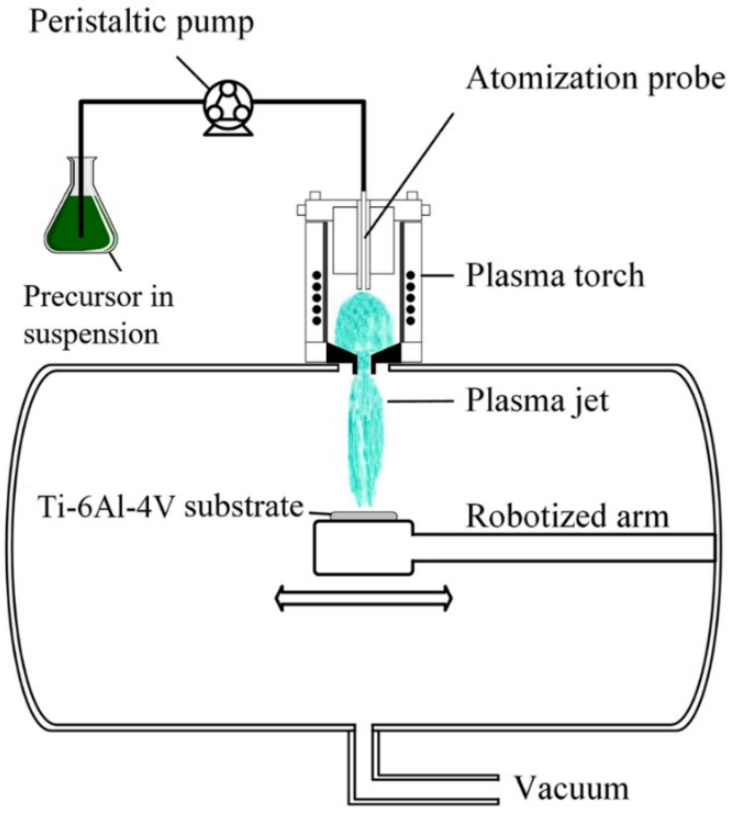

Figure 4.2 Schematic illustration of induction plasma reactor for BMT coating deposition

Table 4.3 Plasma parameters for BMT coating preparation

Sheath gas (Ar)	6 slpm
Sheath gas (O_2)	63 slpm
Central gas (Ar)	23 slpm
Feeding rate	4 ml/min
Reactor pressure	15 kPa
Power	45/50/53 kW
Stand-off distance	130/140/150 mm
Translational	50 mm/s

4.3.3 Material characterization

X-ray photoelectron spectroscopy (XPS) was used to evaluate the element loss after spraying. It was performed with a Kratos Axis Ultra spectrometer (Manchester, United-Kingdom) using a monochromatic Al Kα source (140W). The analyzer was operated in a constant energy mode, i.e. *PE* = 160 eV. The analyzed area was an oval of dimensions 300 x 700 µm. Data analysis was conducted using the Casa XPS software (version 2.3.18). Thermogravimetric / Differential Thermal Analysis (TG/DTA) (04042, Setaram, France) were applied to analyze the BMT formation process. Phase structure and microstructure were analyzed by X-ray Diffraction (XRD) (X'pert PRO, PHILIPS, Netherlands) and Scanning Electron Microscopy (SEM) (S-3000N, Hitachi, Japan), respectively.

4.4 Results and Discussion

4.4.1 Ta_2O_5 spheroidization and nanocrystallization

Figure 4.3a and 4.3b show the morphologies of the commercial Ta_2O_5 and Ta metal powders, while that of the spheroidized and nanocrystallized Ta_2O_5 powders are shown in Figure 4.3c and

4.3d, respectively. When fed into the plasma, the agglomerated commercial Ta_2O_5 powder was molten and quenched [121] to form particles having a smooth spherical appearance with a diameter around 40 µm, as seen in Figure 4.3c and Figure 4.4c. In comparison, the Ta_2O_5 nanopowder produced is much smaller, with d10=77 nm, d50=120 nm and d90=193 nm, as seen in Figure 4.3d and Figure 4.4d. A typical R.F. ICP nanopowder production process starts with a metal that is heated up and evaporated by the plasma jet. The resulting metal vapors are then quickly quenched to induce nucleation and to limit the particle growth to nanosizes [122]. To evaporate a large amount of Ta metal during the nanocrystallization process, the plasma power was increased to 58 kW compared to 43 kW for spheroidization. Oxygen was introduced in the sheath gas to oxidize the Ta vapors and to form Ta_2O_5. The addition of He to the sheath gas increased the thermal conductivity and enhanced the heat transfer process towards the Ta particles. The XRD diffractograms for the spheroidized and the nanocrystallized Ta_2O_5 powders are shown in Figure 4.5, the main phase structure being Ta_2O_5 for both. Still, a peak of Ta (38.47°) remained after the nanocrystallization process, but it could not be distinguished at a macroscale; the nanocrystallized Ta_2O_5 powder had a white colour.

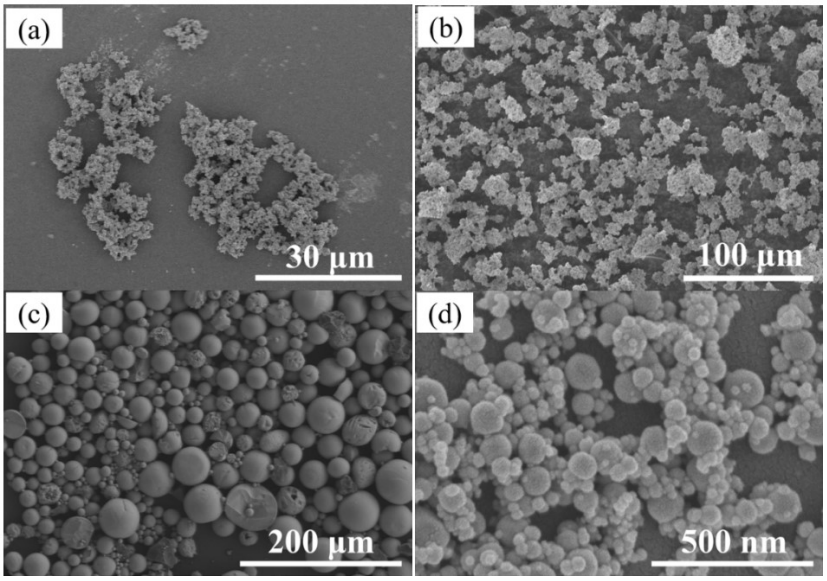

Figure 4.3 Morphologies of particles (a) commercial Ta_2O_5, (b) commercial Ta metal, (c) plasma-spheroidized Ta_2O_5 and (c) plasma-nanocrystallized Ta_2O_5

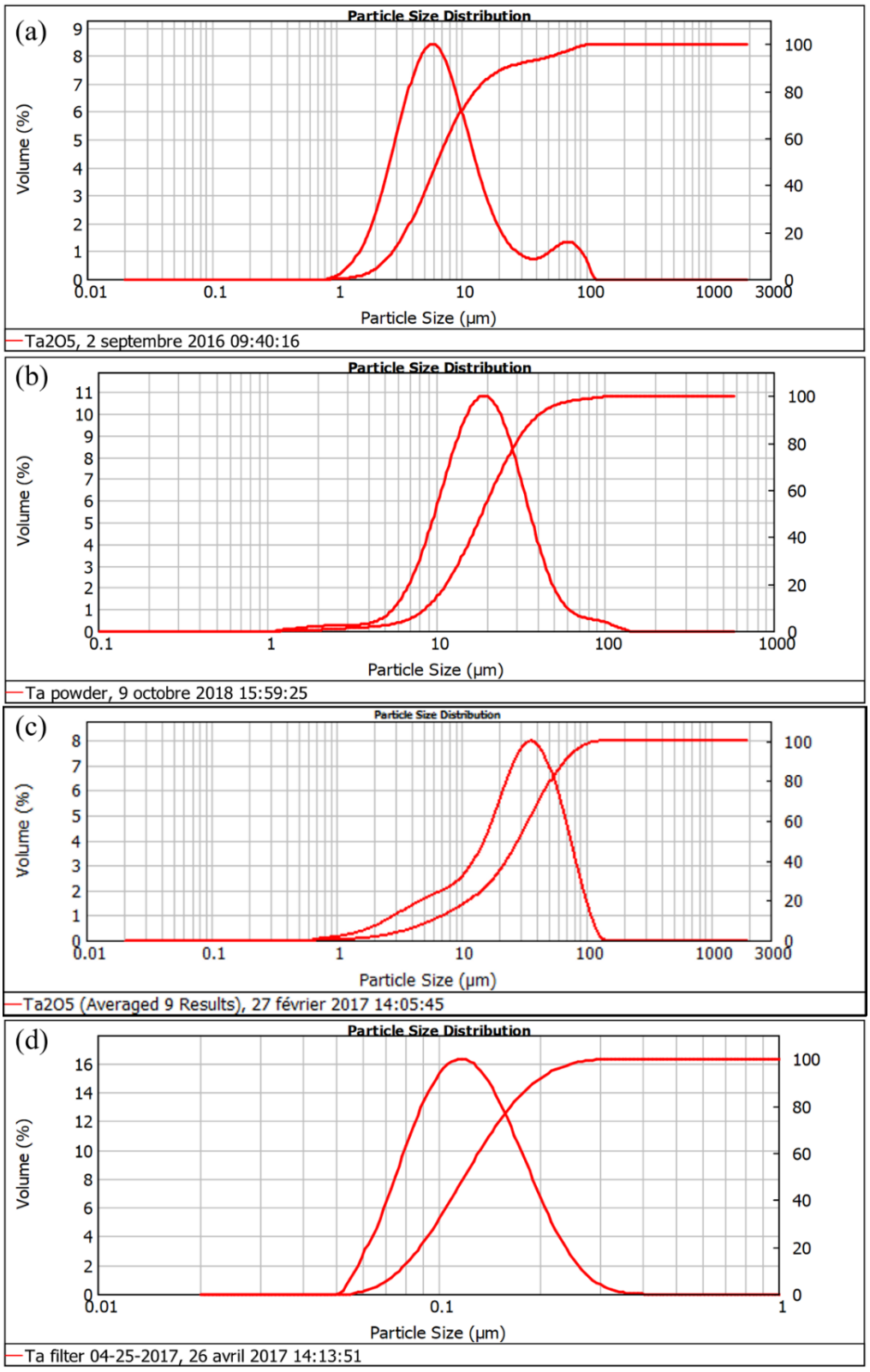

Figure 4.4 Particle size distribution of (a) commercial Ta_2O_5, (b) commercial Ta metal, (c) plasma-spheroidized Ta_2O_5 and (c) plasma-nanocrystallized Ta_2O_5

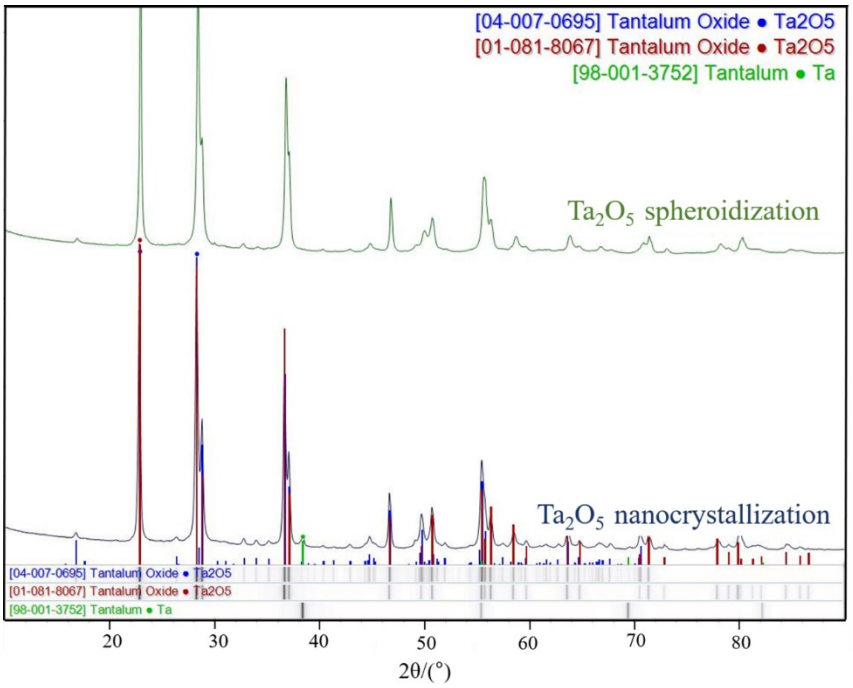

Figure 4.5 X-ray diffractograms of plasma-nanocrystallized and plasma-spheroidized Ta_2O_5

4.4.2 Characterization of synthesized and post-calcined BMT powder

The furnace-synthesized BMT powder at 1400 °C for 2h corresponds to the complex perovskite BMT phase structure (ICDD card No. 04-014-7667, PDF+4 2018), as seen in Fig. 4.6a. The peak near 17.65°, as indicated by the club symbol, corresponds to the Miller index (100) which is the strongest peak produced by the superlattice. The strongest peak in the whole pattern is shared by the disordered BMT (110) and the ordered BMT (012). The ordering degree can be calculated according to Matsumoto's formula [123],

$$S=\sqrt{\frac{(I_{100}/I_{110,012})_{obs}}{(I_{100}/I_{110,012})_{order}}} \tag{4.1}$$

where "obs" means the observed intensity of reflection peak. Mastumoto et al. indicated that the fully ordered value of $(I_{100}/I_{110,012})_{order}$ is 8.3 %. Therefore, the furnace-synthesized BMT powder has an intermediate phase, with an ordering degree of 24 %. The XRD profiles of synthesized BMT after post calcination at different temperatures are shown in Figure 4.6b. The characteristic

peak height of the ordered phase near 17.65° increases abruptly after calcination at 1400 °C. In addition, other superlattice diffraction peaks, originating from (111), (200), (112) and (103), become obvious above 1400 °C, as indicated by the red rectangles. The ordering degree fluctuates for calcination temperatures between 1100 °C and 1300 °C, and it increases sharply above 1400 °C (see Figure 4.6c). Therefore, 1400 °C appears to be a threshold temperature for the ordering transition. This observation is similar to published results where a BMT structure refinement was carried [62].

Figure 4.7 shows the morphologies of the synthesized / pre-calcined and post-calcined BMT powders at different temperatures. The synthesized BMT shows sharp edges with small particles (Figure 4.7a). After post-calcination at 1100 °C and 1200 °C, a similar microstructure with tiny particles and sharp edges is still observed (Figure 4.7b, 4.7c). The sintering neck occurred after calcination at 1300 °C, while tiny particles disappeared and plate-shaped particles started to sinter around 1400 °C. Meanwhile, the porosity decreased. After a calcination at 1500 °C, grains grew up and began to touch each other; sintering was complete. Based on these sintering observations, BMT is predicted to be used in service at temperature up to 1300-1400 °C.

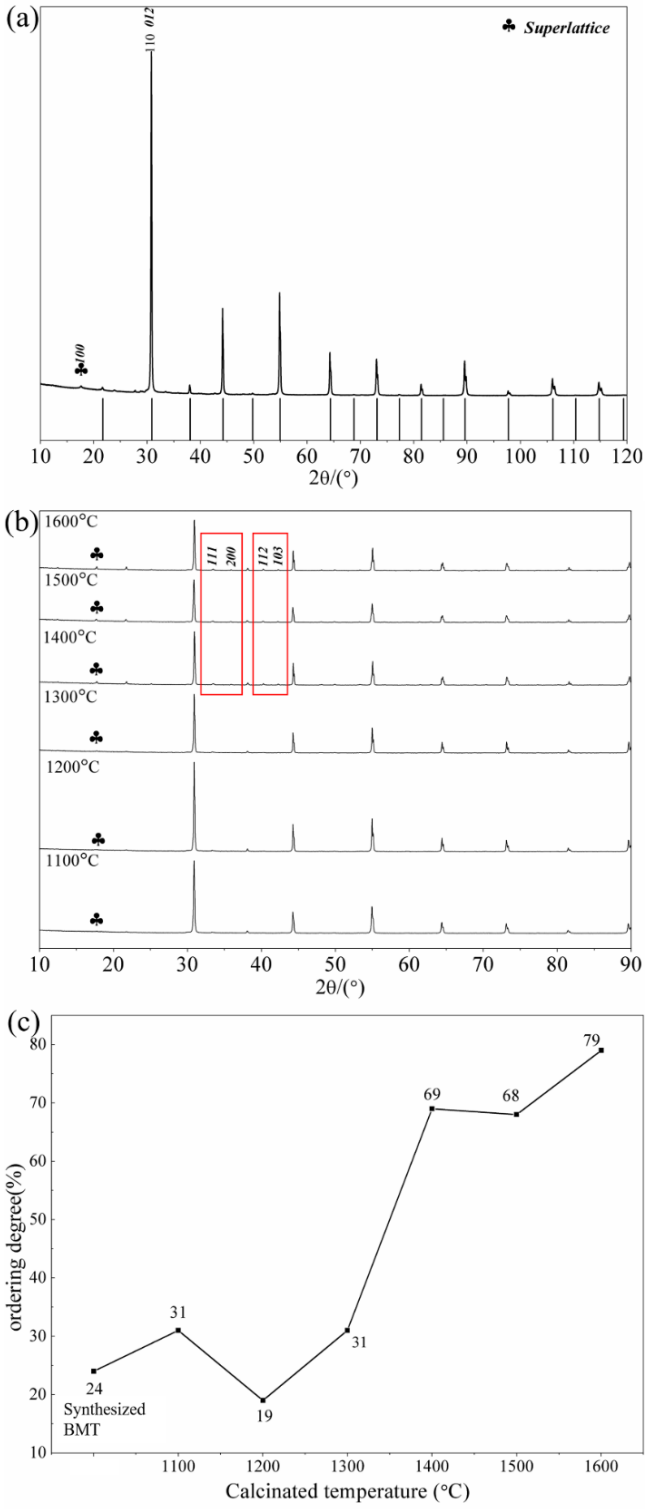

Figure 4.6 X-ray diffractograms of (a) the as-synthesized BMT powder (vertical bars represent the positions of the cubic BMT phase reflection peaks from ICDD card No. 04-014-7667) and (b) after 2h post-calcination at different temperatures. The ordering degree of each powder is illustrated in (c)

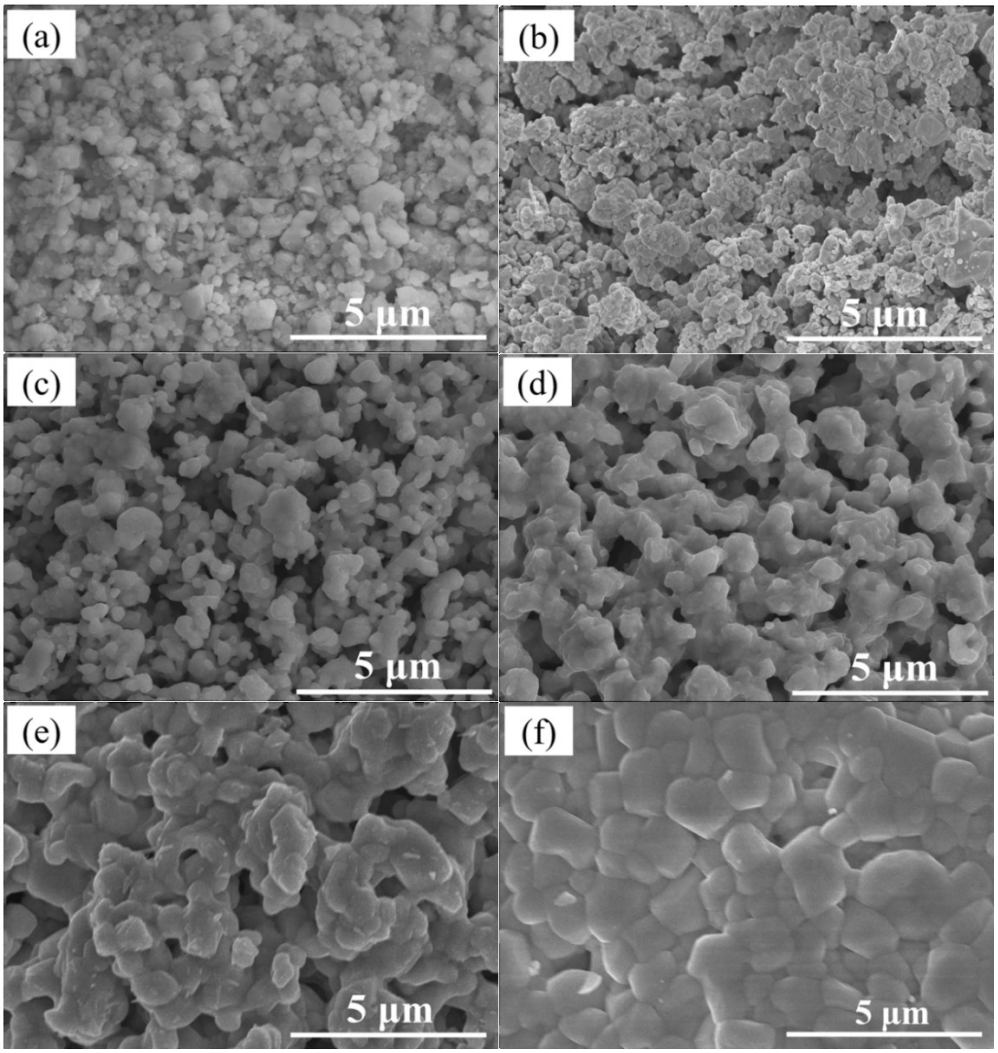

Figure 4.7 Morphologies of synthesized BMT powder (a) and after 2h post-calcination at different temperatures (b) 1100 °C, (c) 1200 °C, (d) 1300 °C, (e) 1400 °C and (f) 1500 °C

4.4.3 Phase decomposition

The coating prepared from suspension S1 and S2 (table2) were analyzed by XPS to estimate the elemental decomposition during spraying. The concentrations and Full width at half maximum (FWHM) of each element are shown in Table 4.4 and their corresponding positions are marked in Figure 4.8. The elemental composition of synthesized BMT powder is used as the reference standard. The interference of carbon is unavoidable because of the air and surface contamination. The sample was mounted on a non-conductive tape and a charge neutralizer was

used on all samples to compensate for the charging effect. Charge corrections were performed using the adventitious carbon peak set at 284.8 eV. Copper contamination is observed on the surface of the samples. It originates from the erosion of the plasma torch supersonic nozzle at high plasma power. The signal of carbon disappeared after etching with an argon ion gun. Since XPS provides semi-quantitative results, the ratios of the main elements are used to evaluate elemental losses during plasma spraying. The Mg/Ba ratio of as-synthesized BMT powder is 0.2, while it decreases to 0.1 in as-sprayed coatings from S1 and S2 precursors. The Mg/Ta ratio of 0.3 for the powder also decreases to 0.1 in both S1 and S2 conditions. Thus, in as-sprayed coatings from S1 and S2, the Mg:Ba and Mg:Ta ratios decreased to one half and one third the fed values, respectively. Losses of Ba (versus Ta) are also observed in plasma sprayed coatings. Due to its high vapor pressure, Mg tends to evaporate easily (859°C, 10 kPa; 1088°C, 100 kPa), compared to Ba (1413°C, 10 kPa; 1897°C, 100 kPa) and Ta (4666°C, 10 kPa; 5361°C, 100 kPa) [124]. In summary, it can be estimated that little or no loss of Ta occurred. In contrast, Mg was depleted by half or more, whereas Ba was mostly conserved during spraying.

The influence of the Mg amount in the precursors on the final BMT coating phase structure was further investigated. The precursors and corresponding plasma power used for that purpose were S1 (45 kW), S2 (53 kW), S3 (53 kW) and S4 (53 kW), as indicated in Table 4.1. With higher plasma powers (50 kW and 53kW), the as-sprayed coating from suspension S1 cracked frequently. Accordingly, a power of 45 kW was chosen to prepare the coating and pursue the analyses with S1. The XRD results are shown in Figure 4.9. The as-sprayed coating prepared by precursor S1 contains the Mg-depleted phases consisting of orthorhombic $BaTa_2O_6$ and $Ba_3Ta_5O_{15}$. The presence of MgO confirms the decomposition of BMT powder at high temperature. The formation of Mg-depleted phases is attributed to the decomposition of BMT and to the preferential evaporation of MgO during spraying. Similarly, APS-sprayed BMT coatings also contain $Ba_3Ta_5O_{15}$ because of Mg oxide loss, which was verified by chemical analysis [4].

Table 4.4 XPS spectral fitting parameters for different elements and their corresponding position, FWHM, concentration (At. %) and concentration ratio of main elements

	XPS spectral fitting parameters			
Type	Element	Position(eV)	FWHM(eV)	At. %
Synthesized	Ba 3d5/2	778.8	3.37	13.65
BMT powder	Mg 1s	1303.8	2.87	2.67
	Ta 4d	229.8	5.05	8.62
	O 1s	529.8	3.56	54.07
	C 1s	284.8	3.52	20.99
Coating	Ba 3d5/2	778.8	2.94	8.68
prepared by	Mg 1s	1303.8	3.24	0.77
S1	Ta 4d	229.8	4.81	7.32
	O 1s	529.8	3.27	44.16
	C 1s	284.8	2.92	36.92
	Cu 2p3/2	934.8	4.32	2.16
Coating	Ba 3d5/2	779.8	3.11	8.59
prepared by	Mg 1s	1304.8	2.98	1.07
S2	Ta 4d	229.8	4.78	8.75
	O 1s	529.8	3.28	47.44
	C 1s	284.8	3.39	32.75
	Cu 2p3/2	933.8	3.91	1.40

	Ratio of main elements		
Elements	Powder	S1	S2
Mg/Ba	0.2	0.1	0.1
Mg/Ta	0.3	0.1	0.1
Ta/Ba	0.6	0.8	1.1

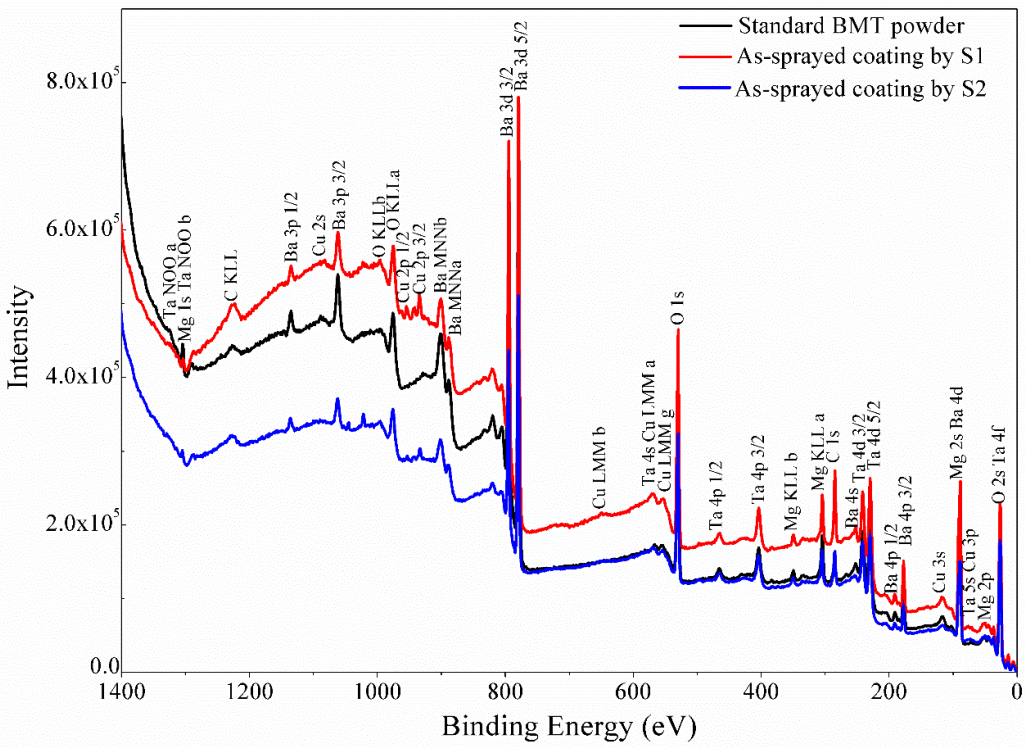

Figure 4.8 General XPS spectra for the synthesized BMT powder (black), as-sprayed coating prepared by S1 (red) and by S2 (blue)

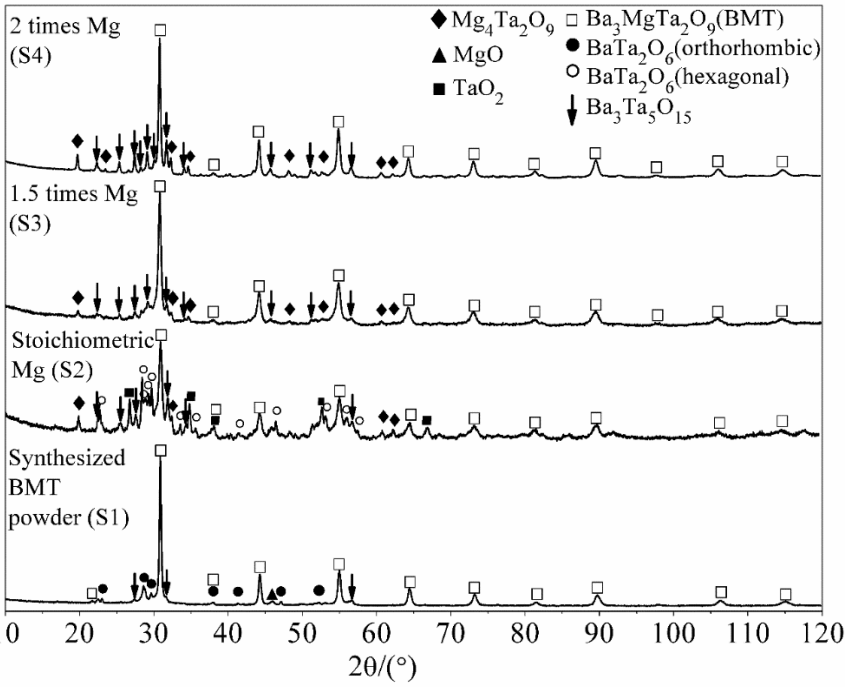

Figure 4.9 X-ray diffractograms of as-sprayed coatings prepared by S1 (45 kW), S2 (53 kW), S3 (53 kW) and S4 (53 kW) precursors, which contained different initial amounts of Mg

Due to losses of MgO and BaO, TaO_2 is left in the as-sprayed coating prepared by precursor S2. The Ta_2O_5 fed with the precursor does not appear on the diffractogram, which indicates that Ta_2O_5 probably decomposed in the plasma. Hexagonal $BaTa_2O_6$ also occurs in the coating produced from precursor S2. It is normally formed at high temperatures (between 1300-1900 °C), compared to the orthorhombic phase which forms below 1150 °C. The occurrence of orthorhombic $BaTa_2O_6$ in as-sprayed coating from precursor S1 is thus also attributed to the lower plasma power of 45 kW. Layden et al. tried to prepare the hexagonal phase by cooling from the melt, but all the different phases of $Ba_2Ta_2O_6$ were observed, including the tetragonal structure [125]. Since only two phases occurred in this work, further exploration is needed possibly discriminate all the phases. Still, it should be mentioned that tetragonal $BaTa_2O_6$ is isostructural with $Ba_3Ta_5O_{15}$, characterized by the tetragonal tungsten bronze (TTB) structure [126]. These two phases are always hard to discriminate owing to nearly identical Bragg peak positions. In addition, the only ICDD card available for tetragonal $BaTa_2O_6$ (No. 00-050-1706) shows the Bragg peak positions up to a maximum of 50°. Accordingly, the confounded phases are identified as $Ba_3Ta_5O_{15}$ in this work.

The Mg-rich phase, $Mg_4Ta_2O_9$, exists in all coatings sprayed from suspension/solution precursors (S2, S3 and S4), as shown in Figure 4.9. As such, the appearance of the Mg-rich phase cannot be solely attributed to an excess in Mg amount. Three kinds of oxides ($Mg_4Ta_2O_9$, $MgTa_2O_6$, $Mg_5Ta_4O_{15}$) exist in the binary-system of MgO-Ta_2O_5. In the bulk material, $Mg_4Ta_2O_9$ and $MgTa_2O_6$ co-exist over the range 900-1580 °C and stabilize to their respective melting temperature of 1830 °C and 1770 °C [127]. Above 1100 °C, only $Mg_4Ta_2O_9$ exists during the vapor-solid reactions for MgO-Ta_2O_5 thin films preparation [128]. This phenomenon is consistent with our working conditions, where the MgO vapor reacts with molten or semi-molten Ta_2O_5 powder.

4.4.4 Effect of heat treatment

The phase structure of BMT coatings obtained with different pre-heating, post-heating (blank plasma passes over the sample) and spraying distance was investigated using precursor S5 with a plasma power of 53 kW. In preliminary works, lower plasma power and fast cooling led to incompletely reacted products ($BaCO_3$, Ta_2O_5 and MgO etc.) and a large amount of amorphous phase in the as-sprayed coatings. A similar phenomenon also occurred in other studies. For example, when injecting a suspension containing MnO_2 and $LaCl_3$, the as-sprayed coating showed a mixture of $LaMnO_{3.15}$, La_2O_3 and Mn_3O_4, while a plasma post-heating treatment promoted the complete reaction to form $LaMnO_3$ [129]. Thus, a post-heating treatment was applied to promote the completion of the chemical reaction towards BMT and to further induce crystallization of as-sprayed coating. The XRD profiles are shown in Figure 4.10. Prolonged pre-heating and/or post heat treatment resulted in an increase of the substrate temperature, which obviously affected the phase structure. From the top pattern to the third pattern (Figure 4.10), the heating effect increases. As a result, the main peak (around 31.7°) of the secondary phase $Ba_3Ta_5O_{15}$ increases in step. The relative heights of this $Ba_3Ta_5O_{15}$ peak to the main peak of BMT around 30.8° are 57 %, 70 % and 91.3 %, respectively. It can thus be estimated that the crystallinity of $Ba_3Ta_5O_{15}$ increases. When positioning the substrate further away from the plasma torch (spray distances of 140 mm and 150 mm), the relative heights drop to 12.5 % and 8.3 %, respectively. When spraying BMT in APS conditions, other researchers showed that thermal cycling at 1339 °C increased the crystallinity of $Ba_3Ta_5O_{15}$ [6]. Kolodiazhnyi et al. considered $Ba_3Ta_5O_{15}$ as a high temperature phase that only forms above 1630 °C and as Schottky defects which spread over the interface [130]. It could explain why increasing the heat load (such as prolonging pre-heating times, adding post heat treatments and using a shorter spray distance) resulted in an increasing level of crystallinity of $Ba_3Ta_5O_{15}$. On the other hand, the crystallinity of orthorhombic $BaTa_2O_6$ (main peak around 28.8°) decreased when increasing the

heating effect. By bringing the substrate closer to the plasma torch from 150 mm to 140 mm, the relative height of $BaTa_2O_6$ drops down from 54 % to 19.4 % and the peaks broadened.

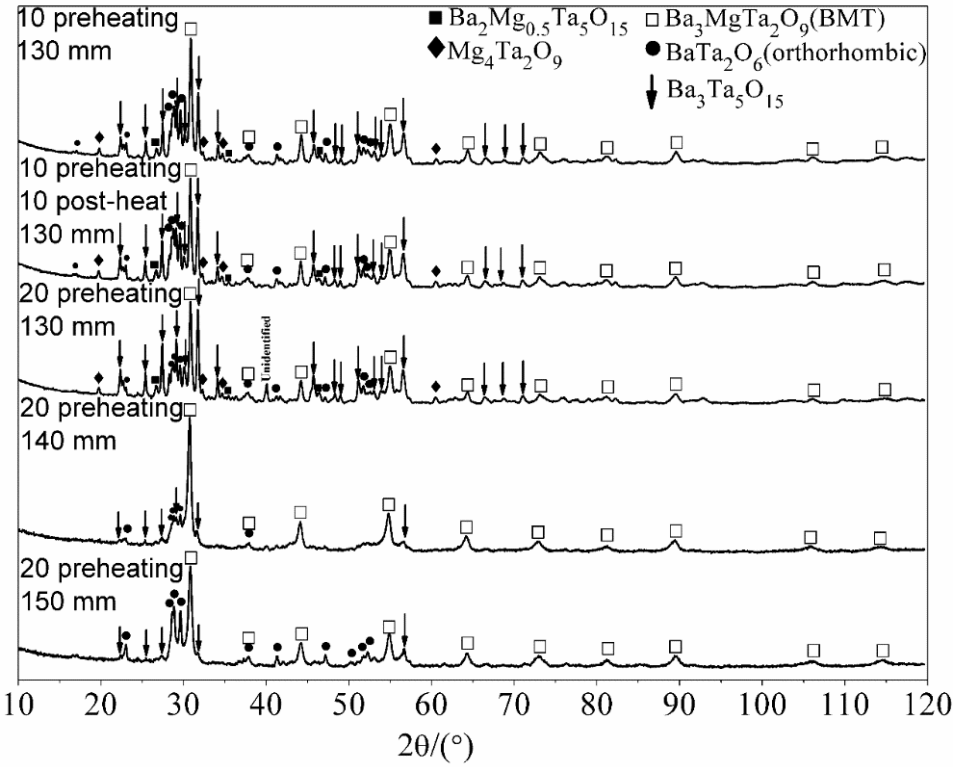

Figure 4.10 X-ray diffractograms of as-sprayed coatings prepared by precursor S5 with different pre-heating, post-heating and spraying distances using the same plasma power of 53 kW

The formation process of BMT is not a one-step reaction. $BaTa_2O_6$ acts as an intermediate product formed before BMT or as a by-product of BMT, as seen in formula (4.2–4.5) [131],

$$BaCO_3 + Ta_2O_5 \rightarrow BaTa_2O_6 + CO_2 \quad (4.2)$$

$$BaTa_2O_6 + 3BaCO_3 \rightarrow Ba_4Ta_2O_9 + 3CO_2 \quad (4.3)$$

$$Ba_4Ta_2O_9 + 1/3MgO + O_2 \rightarrow Ba(Mg_{1/3}Ta_{2/3})O_3 + 1/3BaTa_2O_6 + 3BaO \quad (4.4)$$

$$BaTa_2O_6 + 1/3MgO \rightarrow Ba(Mg_{1/3}Ta_{2/3})O_3 + 1/3Ta_2O_5 \quad (4.5)$$

It can be estimated that the relation between $BaTa_2O_6$ and BMT is that of a competitive growth. Less energy is suitable for the formation of $BaTa_2O_6$. In fact according to the reaction kinetic,

the activation energy for the formation of $BaTa_2O_6$ is 235.6 kJ/mol [58], compared to the value of 257 kJ/mol [132] for BMT. As a conclusion of this section, the best heating effect is that with a short spraying distance. Pre-heating and post heat-treatment rank second and third, respectively. In addition, to attenuate the secondary phases formation, the best parameter combination is a 140 mm spraying distance with 20 pre-heating plasma passes. These conditions are adopted for the remaining sections in this paper.

4.4.5 Precursor chemistry

The BMT coating phase structure and micro-structure are analyzed to investigate the effect of precursor chemistry (acetate-based and nitrate-based precursors). The phase structures of BMT coatings sprayed from acetate-based precursor (S5) and nitrate-based precursor (S4) are shown in Figure 4.11 and Figure 4.12, respectively.

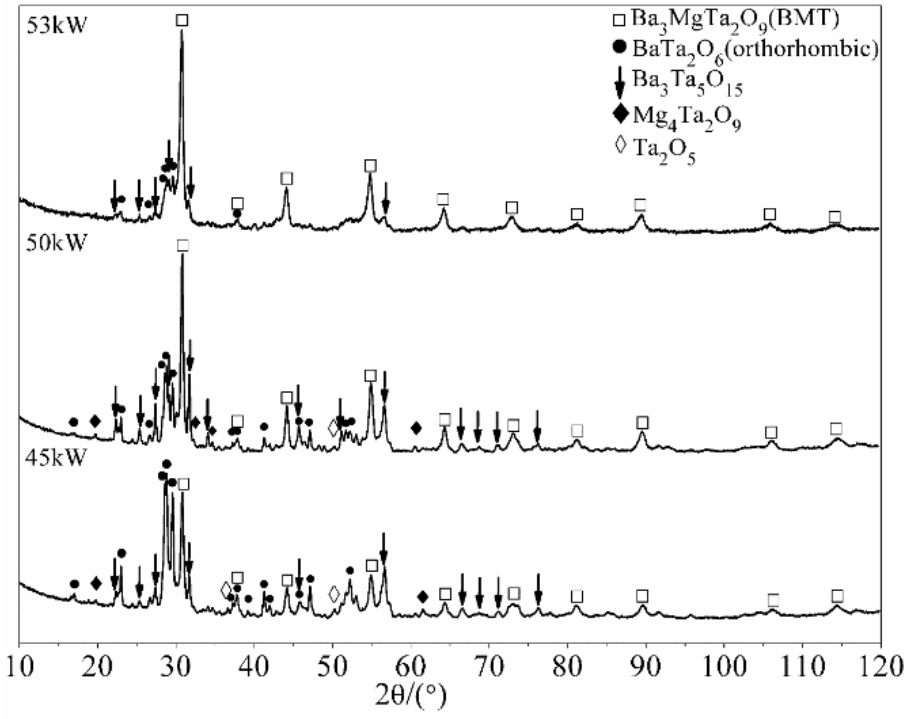

Figure 4.11 X-ray diffractograms of as-sprayed coatings prepared by acetate-based precursor (S5) with different plasma powers

When increasing the plasma power, the relative intensity between orthorhombic $Ba_2Ta_2O_6$ and BMT main peaks decreases in Figure 4.11, which supports the competitive growth mechanism. Unreacted initial Ta_2O_5 remains in as-sprayed coating at lower plasma power of 45 kW and 50 kW; relatively pure BMT is only obtained at 53 kW. In contrast, nitrate-based precursors resulted in coatings with a dominant BMT phase starting from 45 kW. A power of 50 kW is enough to deposit relative pure BMT coatings. It should be mentioned that the $BaTa_2O_6$ phases can be fully eliminated when using nitrate-based precursors, as shown in Figure 4.12.

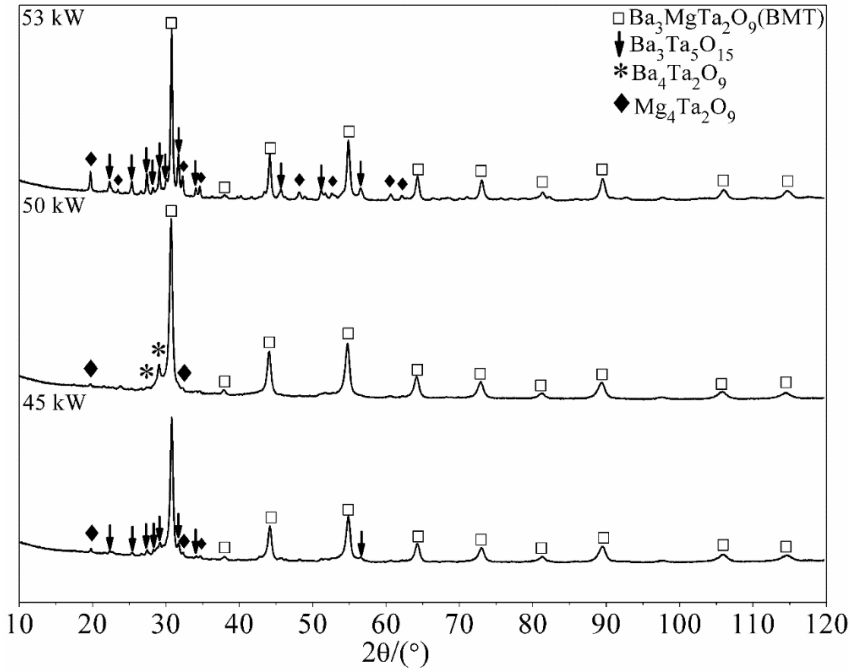

Figure 4.12 X-ray diffractograms of as-sprayed coatings prepared by nitrate-based precursor (S4) with different plasma powers

The difference in reaction processes between nitrate-based and acetate-based precursors can be explained by TG-DTA curves, as seen in Figure 4.13. The first weight loss plateau of acetate-based precursors occurs at 400 °C and stops at 500 °C, which corresponds to the decomposition of Ba acetate, as seen in formula (4.6). This decomposition is accompanied by an exothermic peak of large amplitude around 450 °C.

$$Ba(CH_3COO)_2 \rightarrow BaCO_3 + (CH_3)_2CO \quad (4.6)$$

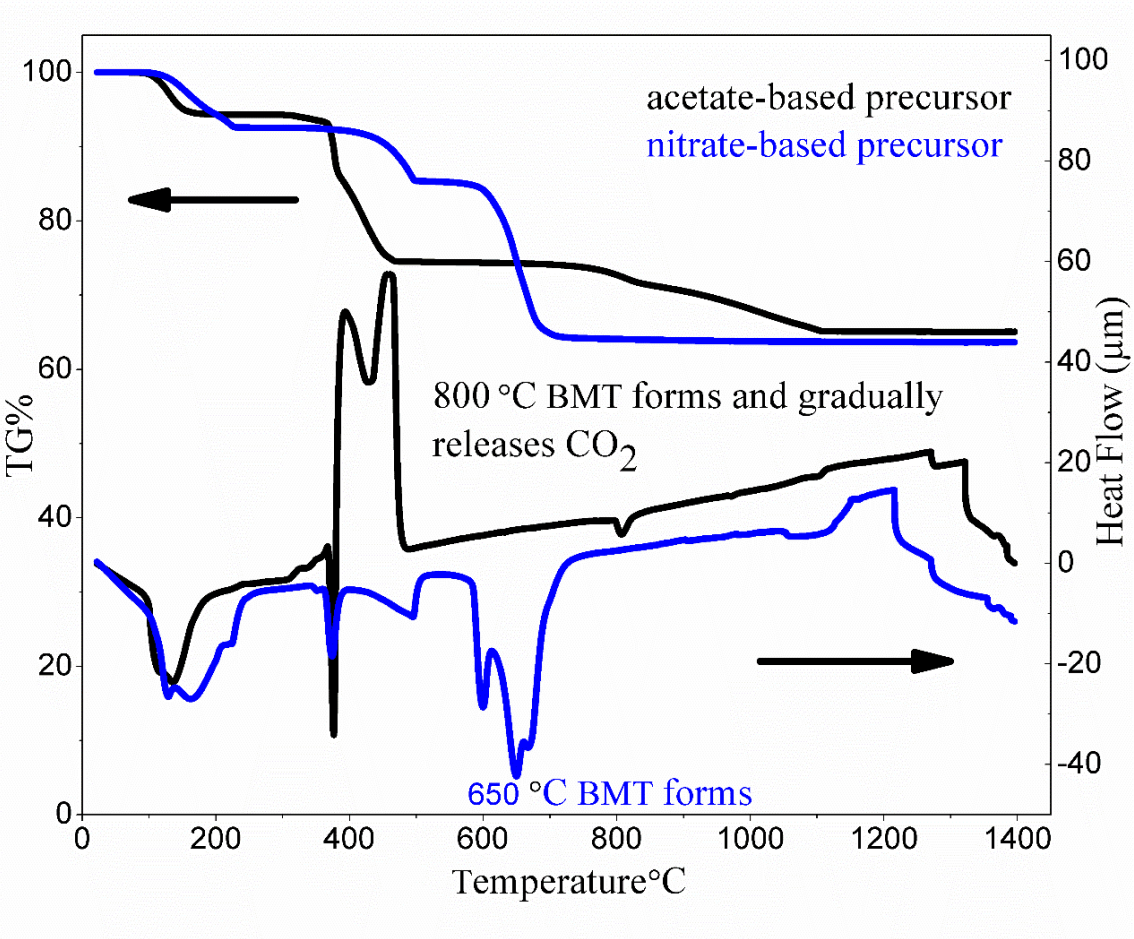

Figure 4.13 TG-DTA curves for stoichiometric acetate-based precursor (black) and nitrate-based precursor (blue)

Experiments with pure barium acetate (doesn't show in this paper) under the same TG-DTA conditions indicated that $BaCO_3$ decomposes and releases CO_2 from 800 °C up until the test limit set at 1400 °C. The decomposition speed reaches the highest speed at 1200 °C. However, for the precursor S5, this decomposition occurs from 800 °C and stops at 1100 °C, illustrating the BMT synthesis reaction and indicating that the reaction with Ta_2O_5 and MgO promoted the decomposition process of $BaCO_3$. The decomposition of $Mg(CH_3COO)_2$ occurs in one step process [133]. On the other hand, the decomposition process of $Ba(NO_3)_2$ is relatively simple from 400 °C to 700 °C and can be expressed using a simplified formula (4.7).

$$2Ba(NO_3)_2 \rightarrow 2BaO + 4NO_2 + O_2 \quad (4.7)$$

According to the DTA curve, an endothermic peak occurs at 650 °C with nitrate-based precursors; this peak is attributed to the formation of BMT. On the contrary, BMT is formed gradually at 800 °C (endothermic peak) while continuously releasing CO_2 from 800 °C to 1100 °C with acetate-based precursors. This result is similar to the conventional solid-state synthesis method which uses $BaCO_3$, Ta_2O_5 and MgO powders [67]. It can explain why nitrate-based precursors resulted in BMT dominant coatings at 45 kW and relatively pure BMT coatings at 50 kW.

The diverse reaction processes also lead to differences in splat morphologies and coating deposition rate, as seen in SEM images (secondary electron) in Figure 4.14. Coatings prepared from acetate-based precursors (Figure 4.14a) show an irregular, porous and cauliflower-like morphology with a lot of small re-solidified particles and tiny molten droplets sticking to the big splat surface. The sizes of these tiny droplets are distributed from 0.5 μm to 2 μm. Coatings prepared from nitrate-based precursors (Figure 4.14b) have a much more uniform morphology made of well molten splats and possess a good bonding. Sivakumar et al. investigated the effect of precursor chemistry (aluminum nitrate and acetic acid modified aluminum acetate) on splat formation during SPPS. Due to the substantial heat of combustion of acetic acid and to the exothermic reactions of carbonaceous species, the resulting microstructure from the acetic acid modified aluminum acetate showed a significant amount of fine spherical particles, even at lower plasma power [134]. A similar argument could explain the presence of tiny molten droplets on the big splat surface, as observed in Figure 4.14a. Organic solutes such as acetate-based precursors are interesting choices to prepare some oxide coatings such as zirconia [135] and alumina [134] because of their exothermal reactions. For some other oxides, nitrate-based precursors are preferable to form oxides, such as BaO (in this work) and Y_2O_3 [136]. Indeed, Y_2O_3 forms at a higher temperature (650 °C) when using yttrium acetate compared to yttrium nitrate (450 °C).

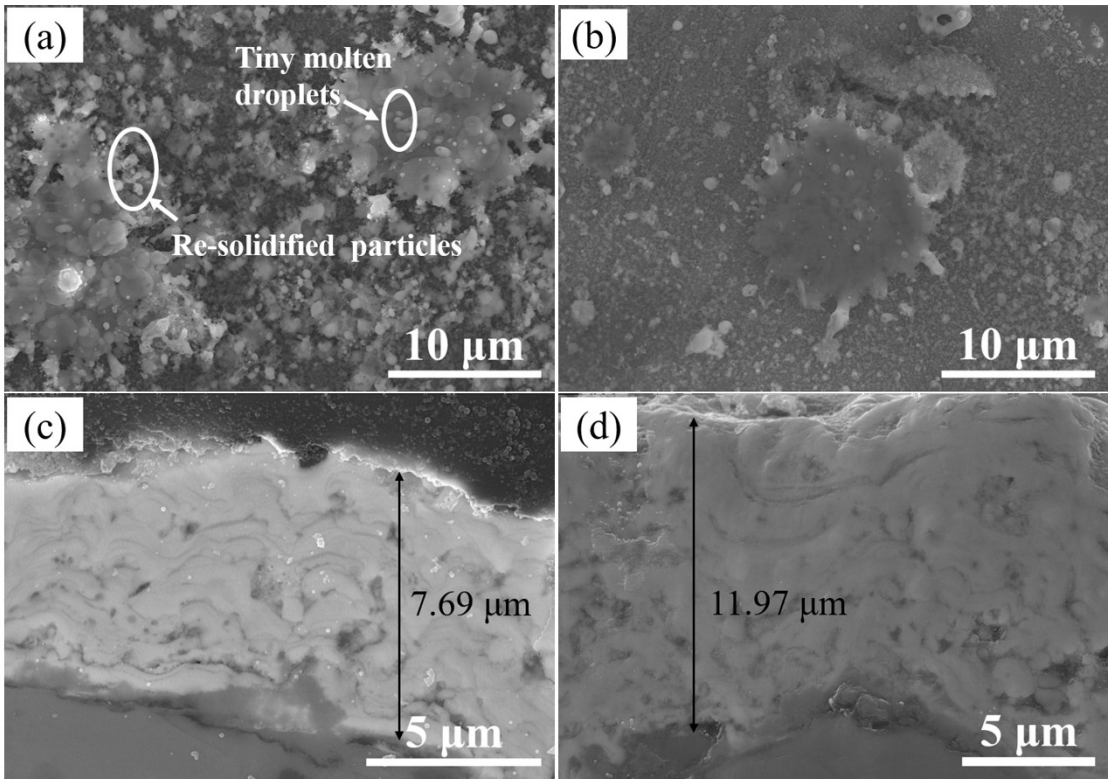

Figure 4.14 Splats morphologies and coating cross-sectional images from acetate-based precursors (a) and (c); from nitrate-based precursors (b) and (d)

Another reason that could lead to the fine droplets (Figure 4.14a) is the release of CO_2 from acetate-based precursors which breaks the big droplets into tiny ones. This phenomenon can be regarded as a secondary explosion, which is similar to the "secondary atomization" known to happen in SPPS [93]. When the plasma jet (gas flow) hits the substrate, its direction changes from perpendicular to parallel to the substrate surface. The smaller droplets mingled in the gas/plasma jet have a small Stokes number and are sensitive to changes in gas/plasma direction [137]. Oberste-Berghaus et al. proved this phenomenon using numerical modeling. Near the substrate, tiny droplets (<1 μm) will follow the gas flow, parallel to substrate surface (Ref 38)[138]. When the drag force overcomes the adhesion force, tiny droplets cannot deposit on substrate [139]. This can explain the difference in deposited coating thickness as shown in Figure 4.14c and 4.14d, after the same number of spraying loops (46 loops). The coating deposition rate from nitrate precursor is 1.56 times higher than that from acetate precursors.

Still, the maximum deposition rate was only 0.26 μm per pass, mainly because of the small feed rate and low precursor concentration required to avoid the obstruction of the injection probe. Further optimization will be needed to produce BMT TBCs at a larger scale.

4.4.6 Effect of initial Ta_2O_5 particle size

Since helium used in nanocrystallization comes with a high price tag, the spheroidization process was considered as an alternative to synthesize Ta_2O_5 powders with good stability and flowability when in suspension. Said spheroidized powders were used in the combination of precursor S6 (Table 4.1). The phase structures of BMT coatings sprayed from S6 precursors are shown in Figure 4.15. TaO_2, another Ta oxide and MgO were found in as-sprayed coating for each plasma power tested. These oxides approximately correspond to the initial reactants. The energy required to fully melt a spherical particle is shown in equation (4.8) [140]:

$$Q=1/6\ \pi d^3\rho \quad [c_p(T_m-T_0)+H_m] \tag{4.8}$$

For the same material and conditions, the density ρ, specific heat c_p, melting temperature T_m, room temperature T_0 and latent heat of fusion H_m are considered as constant. Accordingly, the particle diameter d becomes the only variable determining the required energy. The particle size of spheroidized T_2O_5 is over 100 times larger than that of nanocrystallized particles. As such, spheroidized Ta_2O_5 requires much more energy to fully melt and to react with other precursors. According to the evaporation results for Ba (see the Ta/Ba ratio in Table 4.4), Ba evaporation is more important for nitrate-based precursors (S2) compared to a pure BMT suspension (S1). Therefore, unmolten spheroidized Ta_2O_5 will reduce the reaction rate with Ba precursors, which could worsen the evaporation of Ba. The occurrence of $BaCO_3$ at 45 kW may result from the reaction between BaO and CO_2, which came from the decomposed ethanol. The transition from $Ba_3Ta_5O_{15}$ and $BaTa_2O_6$ at 50 kW to $Ba_4Ta_2O_9$ at 53 kW can be described as formula (4.9). This reaction contains the different Ta oxides as by-products.

$$Ba_3Ta_5O_{15} + BaTa_2O_6 \rightarrow Ba_4Ta_2O_9 + 2Ta_2O_5 + TaO_2 \quad (4.9)$$

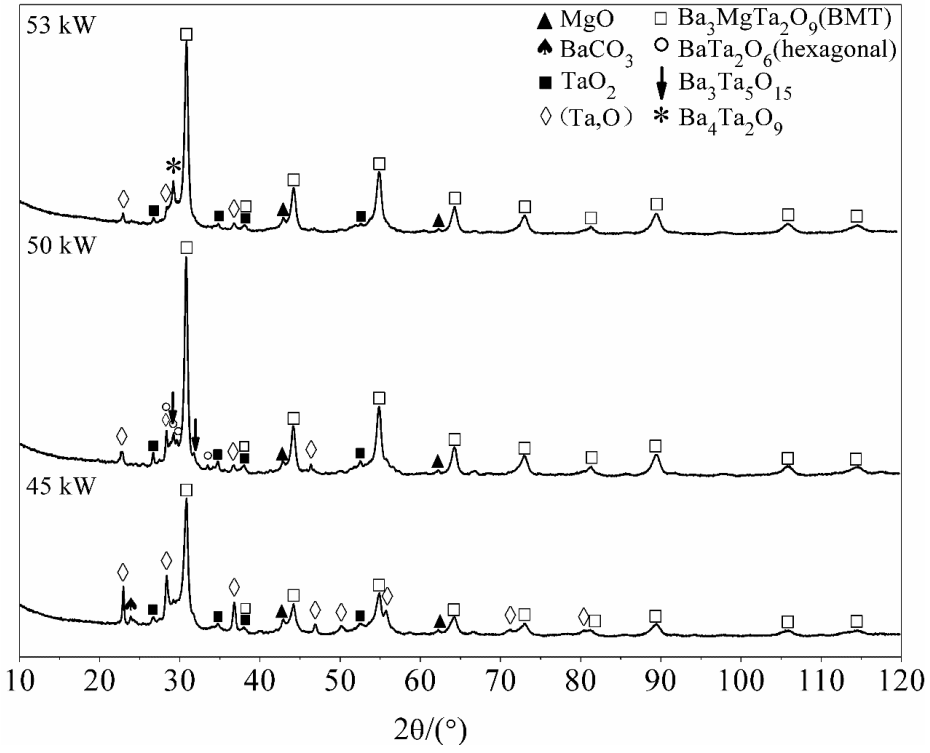

Figure 4.15 X-ray diffractograms of as-sprayed coatings prepared by precursor S6 (using spheroidized Ta_2O_5 as Ta precursor) with different plasma powers

The cross-sectional image of coating sprayed by precursor S6 with plasma power of 50kW is shown in Figure 4.16. The black dots within the rectangle correspond to MgO, while Ta oxides are formed at the interface between the substrate and the coating (black arrows). This phenomenon is identical with the XRD results in Figure 4.15.

To summarize, spheroidized Ta_2O_5 is an interesting raw material to synthesize BMT in hybrid SPS/SPPS. Still, it needs higher plasma power and slows the reaction. As a result, it intensifies the evaporation and loss of Ba.

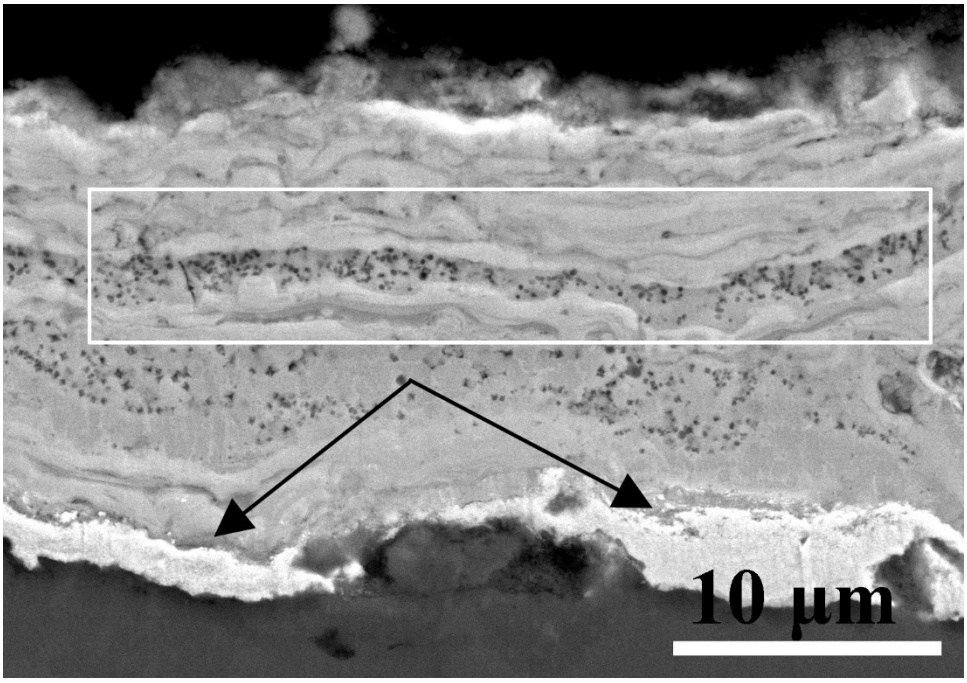

Figure 4.16 Cross-sectional images of as-sprayed coating prepared by precursor S6 (using spheroidized Ta_2O_5 as Ta precursor) with a plasma power of 50 kW

4.5 Conclusions

In the proposed hybrid SPS/SPPS process, $Ba(Mg_{1/3}Ta_{2/3})O_3$ formation and Mg evaporation happened simultaneously, together with the formation of four secondary phases: three Mg-depleted phases ($BaTa_2O_6$, $Ba_3Ta_5O_{15}$ and $Ba_4Ta_2O_9$) and one Mg-rich phase ($Mg_4Ta_2O_9$). $BaTa_2O_6$ grew competitively with BMT during the reaction. Decomposition of BMT during plasma spraying and Schottky defects resulting from higher substrate temperatures both contributed to the formation of $Ba_3Ta_5O_{15}$. $Mg_4Ta_2O_9$ was systematically observed, even in coatings sprayed from stoichiometric precursors (without Mg excess), which illustrates the complex reaction processes.

The detailed comparisons of the deposited phases from different precursors and spray conditions can be summarized as:

1. As-sprayed coatings prepared by SPS (BMT powder suspension) contained Mg-depleted phases, illustrating the preferential Mg losses during plasma spraying. In comparison, as-sprayed coating from a suspension of nanosized Ta_2O_5 powder in a solution of Ba and Mg salts showed a Mg-rich phase in addition to the Mg-depleted phases.
2. Precursor chemistry played a key role in BMT synthesis and coating preparation. Orthorhombic $BaTa_2O_6$ only occurs in coating sprayed from acetate-based precursor. Coating sprayed from nitrate-based precursor can avoid the formation of $BaTa_2O_6$ of any phase structure when using twice the stoichiometric Mg amount. Due to their complex decomposition and reaction process, acetate-based precursors resulted in coatings with lower deposition rate and complex secondary phases. In opposition, nitrate-based precursors contributed to obtaining thicker coatings with higher purity at lower plasma power (50 kW).
3. Using a large spheroidized Ta_2O_5 powder decreased the reaction rate. It resulted in incomplete reactions and intermediate products (e.g. Mg oxide, Ta oxide) were found in the as-sprayed coatings for all conditions. In contrary, nanocrystallized Ta_2O_5 powders made the complete reaction towards BMT much easier.

To obtain a relatively pure BMT coating, it was shown that twice the Mg stoichiometric amount and a power of 50 kW provided the best results when using nanocrystallized Ta_2O_5 as a tantalum precursor and nitrated-based salts as barium and magnesium precursors. Still, the low deposition rate observed needs to be improved by increasing the feed rate and the precursor concentration, among other parameters. The copper contamination in as-sprayed coatings came from the supersonic nozzle or the tip of commercial probe which is made of W-Cu alloy. When preparing the precursor, low concentration acid is suggested. In addition, applying sandpaper and ultrasonic bath to fully clean the probe tip and supersonic nozzle before use helps limit contamination.

4.6 Supplemental work

4.6.1 The protocol of ordering degree calculation by Rietveld refinement.

The ordering parameter not only represents the ordering transition degree, but also the concentration or percentage of ordered phase in a mixture of ordered and disordered BMT phases. In section 4.4.2, the ordering degree of BMT was calculated by the widely-used formula (4.1). In this formula, the peaks intensity ratio between ordered and disordered phases is used to show the relative contents. Since the peak intensity is influenced by many factors such as Lorentz polarization, multiplicity factor, preferred orientation, structure factor and temperature factor etc. [141], the formula (4.1) is not accurate enough. As such, this part describes a detailed protocol to deduce the ordering degree using Rietveld refinement.

In XRD pattern, the diffraction pattern of mixture is the weighted superposition of each phases. The weighted factor or scale factor is used to adjust the relative contribution of individual phases to the overall diffraction pattern. In a mixture, the integrated intensity of ordered phase is shown in equation (4.10) [142].

$$I_{ork} = I_0 \frac{\lambda^3 e^4 J_{ork}}{16\pi m^2 c^4 V_{or-unit}^2} V_{or} |F_{ork}|^2 L_{ork} e^{-2Mor} = S_{or} J_{ork} L_{ork} |F_{ork}|^2 \quad (4.10)$$

The subscripts *or* and *k* indicate the ordered phase and *k*th Bragg reflection, whereas S_{or}, J_{ork}, L_{ork} and F_{ork} are scale factor, multiplicity factor, Lorentz polarization factor and structure factor, respectively. The process of Rietveld refinement is to minimize the residual M (as shown in equation (4.11) by the least-squares refinement.

$$M=\sum_i W_i(Y_{io} - Y_{ic})^2 \quad (4.11)$$

Where $W_i = 1/Y_{io}$,

Y_{io} = observed intensity at the *i*th step,

Y_{ic} = calculated intensity at the *i*th step,

And the sum is the overall data points. Y_{ic} could be demonstrated by equation (4.12).

$$Y_{ic}=Y_{ib}+\sum_k I_k G_{ik} \tag{4.12}$$

Where G_{ik} is the profile function. For the two phases system, equation (4.12) could be presented as below,

$$Y_{ic}=Y_{ib}+\sum_{p=or}^{p=dis}\sum_{k=k1}^{k=k2} I_{kp}\, G_{ikp} \tag{4.13}$$

The subscripts *dis* indicates the disordered phase. *k1- k2* are the reflections contributing to data point *i* in the pattern. Substituting equation (4.10) into (4.13), a new equation (4.14) is presented as below,

$$Y_{ic}=Y_{ib}+\sum_{p=order}^{p=dis} S_p \sum_{k=k1}^{k=k2} J_{kp} L_{kp} G_{ikp} |F_{kp}|^2 \tag{4.14}$$

As such, S_{or} and S_{dis} could be calculated by substituting equation (4.14) into (4.11) in the process of least-squares refinement. Since the weight of a phase in a mixture is proportional to the product of the scale factor [143], the weight fraction of ordering phase in the mixture is given by equation (4.15),

$$W_{or}=\frac{m_{or}}{\sum_{p=or}^{p=dis} m_p}=\frac{S_{or} Z_{or} M_{or} V_{or-unit}}{\sum_{p=or}^{p=dis} S_p M_p V_{p-unit}} \tag{4.15}$$

Where M_{or}, Z_{or} and $V_{or\text{-}unit}$ are mass of formula unit, number of formula units per unit cell and unit cell volume, respectively.

4.6.2 Calculation of BMT ordering degree by Rietveld refinement.

In this section, Rietveld refinement method was carried out by MDI JADE 2010 software to calculate quantitatively the content of the ordered phase. For the powders of as-synthesized BMT at 1400 °C×2h (as mentioned in Figure 4.6a), the ICDD cards and lattice parameters used for ordered (hexagonal) and disordered (cubic) BMT are No. 04-021-4960 (a=5.7737 Å, c=7.092 Å, c/a=1.228) and No. 04-014-7667 (a=4.0893 Å), respectively. The profile function of Pseudo-Voigt（PV）was used in this process. The analysis result is shown in Figure 4.17.

WPFitted pattern means the whole pattern fitting. The estimated amount of hexagonal and cubic BMT account for 18.7 wt. % and 81.3 wt. %. The ordering degree of this powder is considered as 18.7 %.

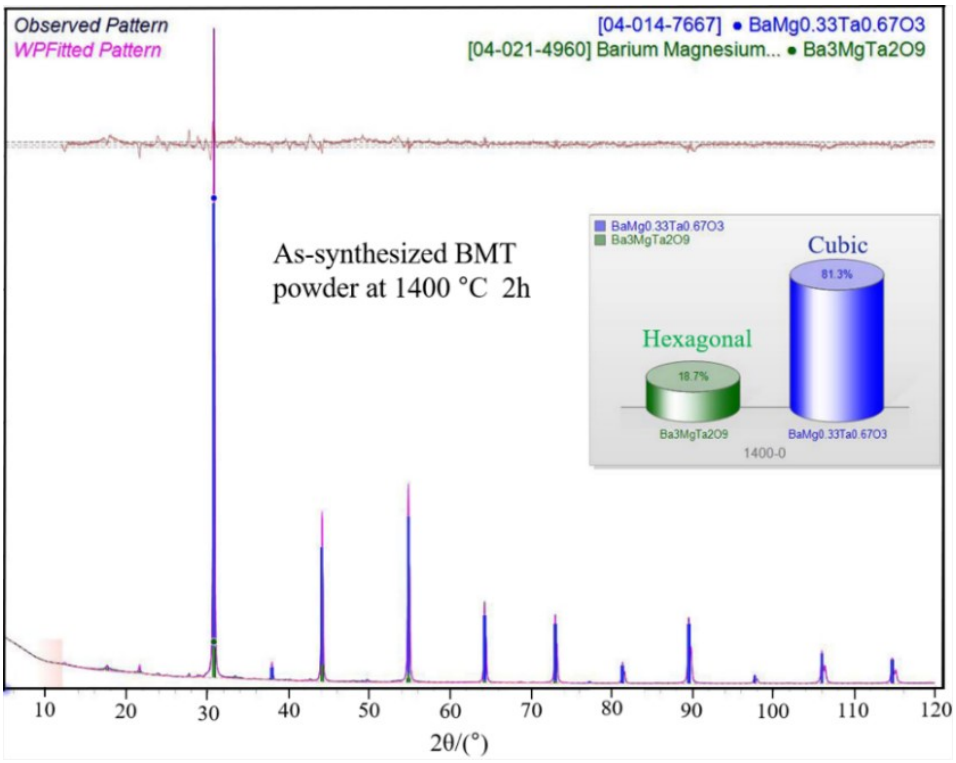

Figure 4.17 Rietveld refinment of as-synthesized BMT powder at 1400 °C×2h

For the BMT powders post-calcinated 2h at different temperatures (as mentioned in Figure 4.6b), their Rietveld refinement results are shown in Figures 4.18, 4.19, 4.20, 4.21, 4.22 and 4.23, respectively. When using the previous card of hexagonal BMT (No. 04-021-4960), the refinement quality is unsatisfactory because the atomic positions are missing from the ICDD card. In order to improve the refinment quality, the ICDD card and lattice parameters used for ordered (hexagonal) BMT are changed to No. 01-077-9509 (a=5.774 Å, c=7.094 Å, c/a=1.229). The card of disordered (cubic) phase is the same as before.

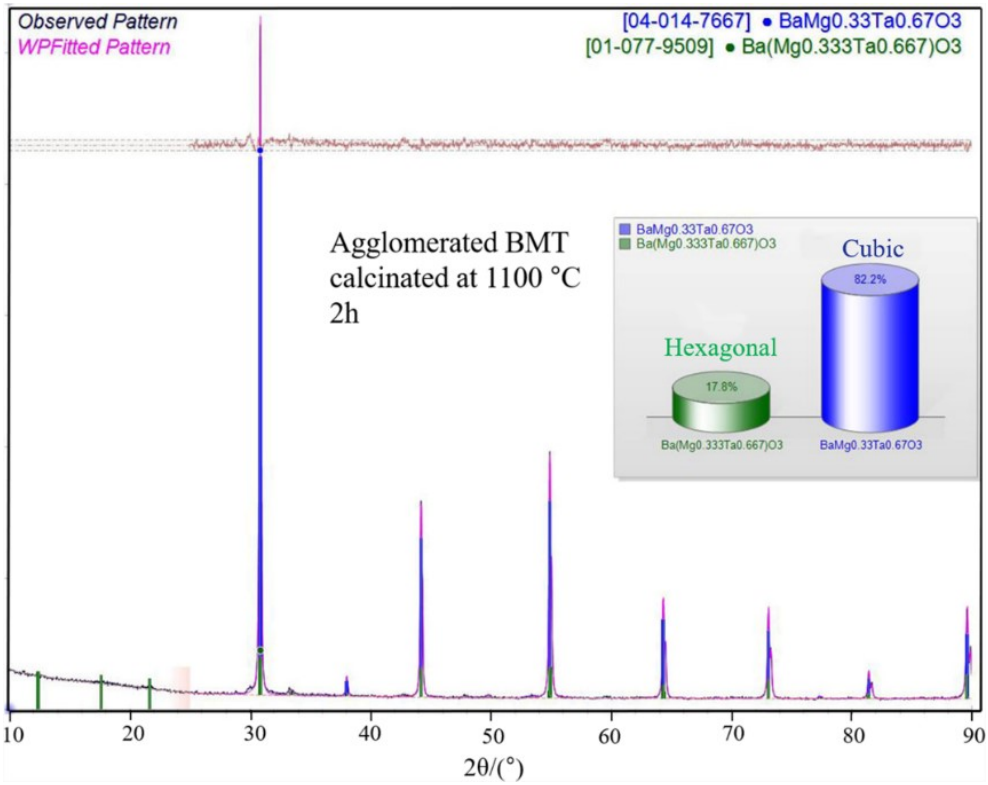

Figure 4.18 Rietveld refinment of agglomeated BMT post-calcinated at 1100 °C×2h

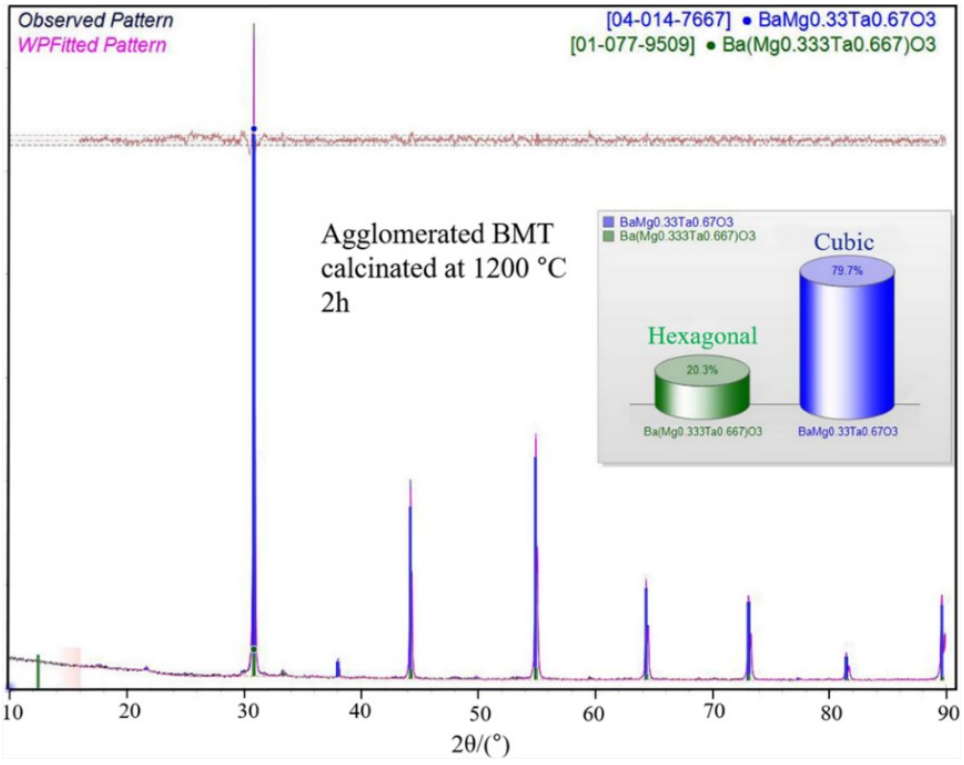

Figure 4.19 Rietveld refinment of agglomeated BMT post-calcinated at 1200 °C×2h

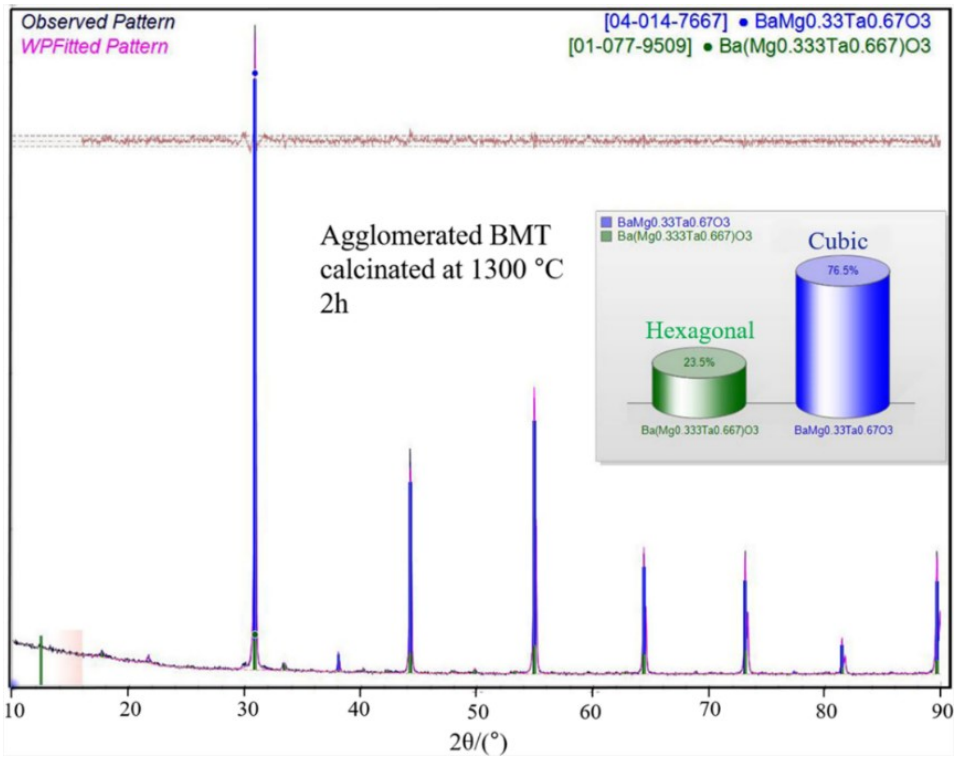

Figure 4.20 Rietveld refinment of agglomeated BMT post-calcinated at 1300 °C×2h

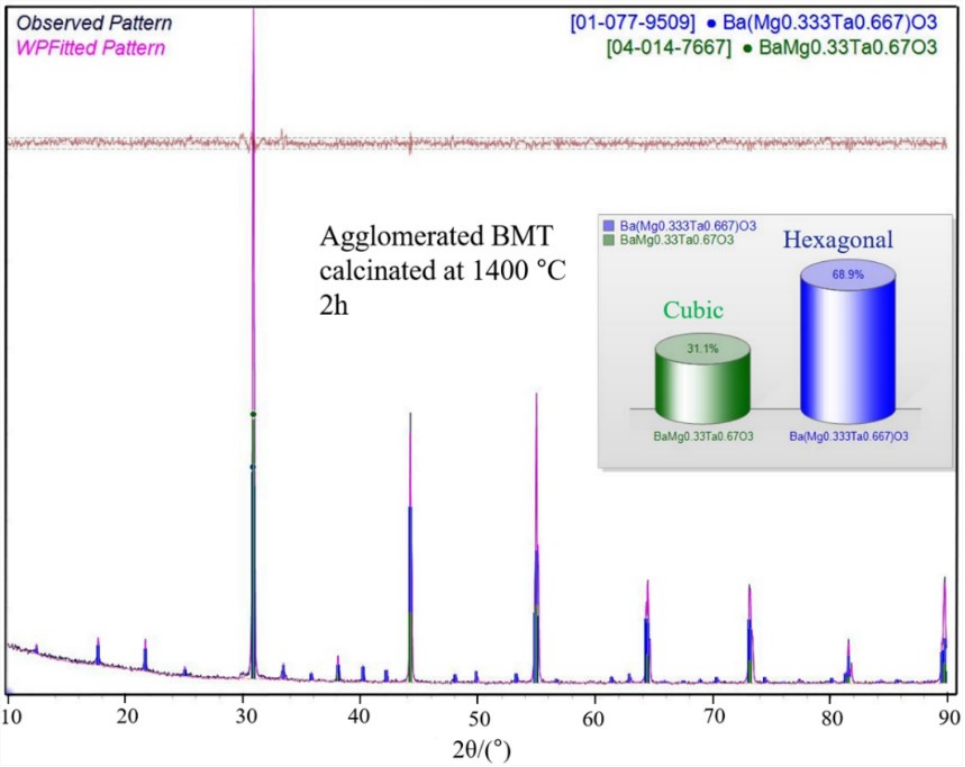

Figure 4.21 Rietveld refinment of agglomeated BMT post-calcinated at 1400 °C×2h

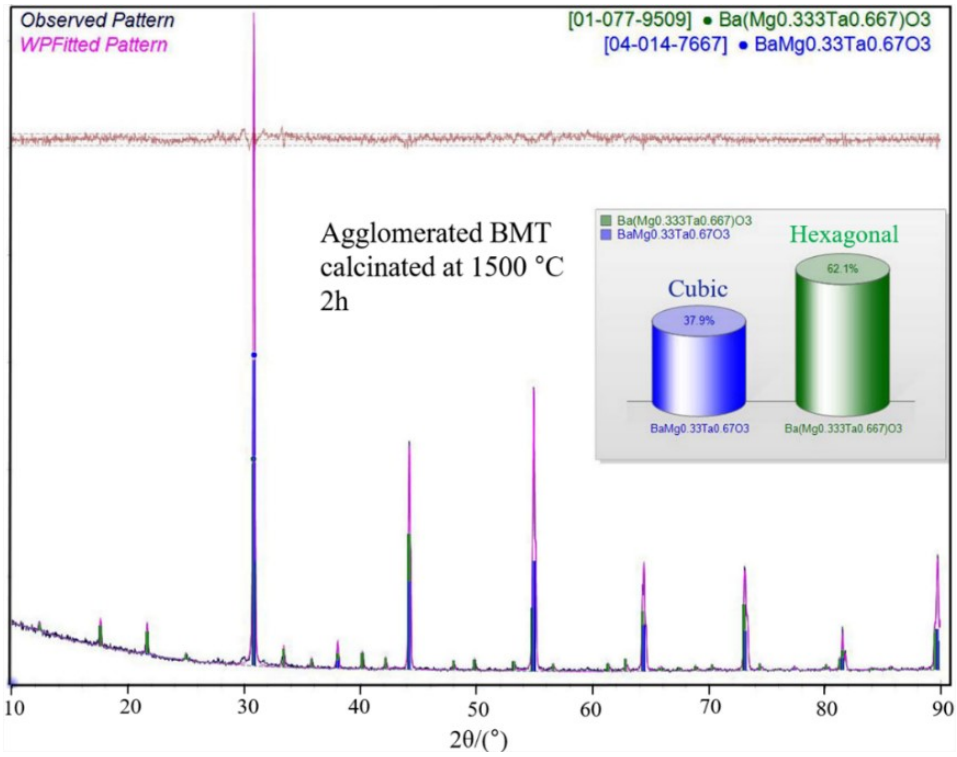

Figure 4.22 Rietveld refinment of agglomeated BMT post-calcinated at 1500 °C×2h

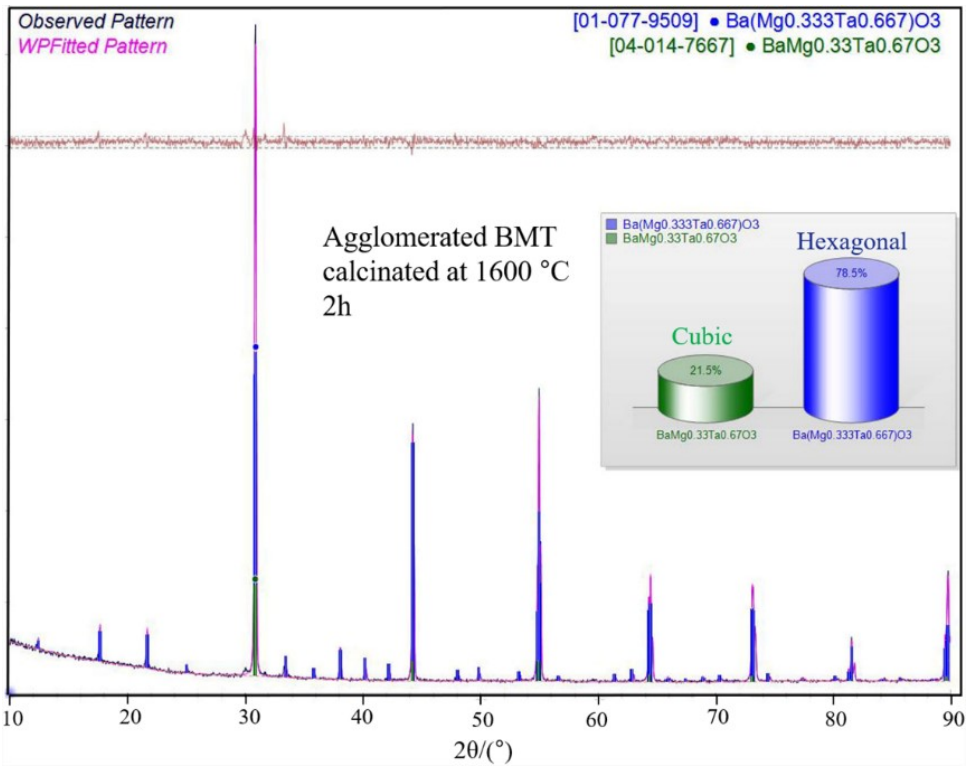

Figure 4.23 Rietveld refinment of agglomeated BMT post-calcinated at 1600 °C×2h

The estimated ordered phase amounts of powders calcinated at various temperatures account for 17.8 wt. % (1100 °C), 20.3 wt. % (1200 °C), 23.5 wt. % (1300 °C), 68.9 wt. % (1400 °C), 62.1 wt. % (1500 °C) and 78.5 wt. % (1600 °C), respectively. Comparing the calculated ordering degrees by Rietveld refinement and formula (Figure 4.6c), the results are shown in Figure 4.24. Except the data of calcinated at 1200 °C, 1400 °C and 1600 °C, there is a large ordering degree difference between the two methods at other points. Consequently, in order to obtain more accurate ordering degree, Rietveld refinement should be preferentially applied in the future work.

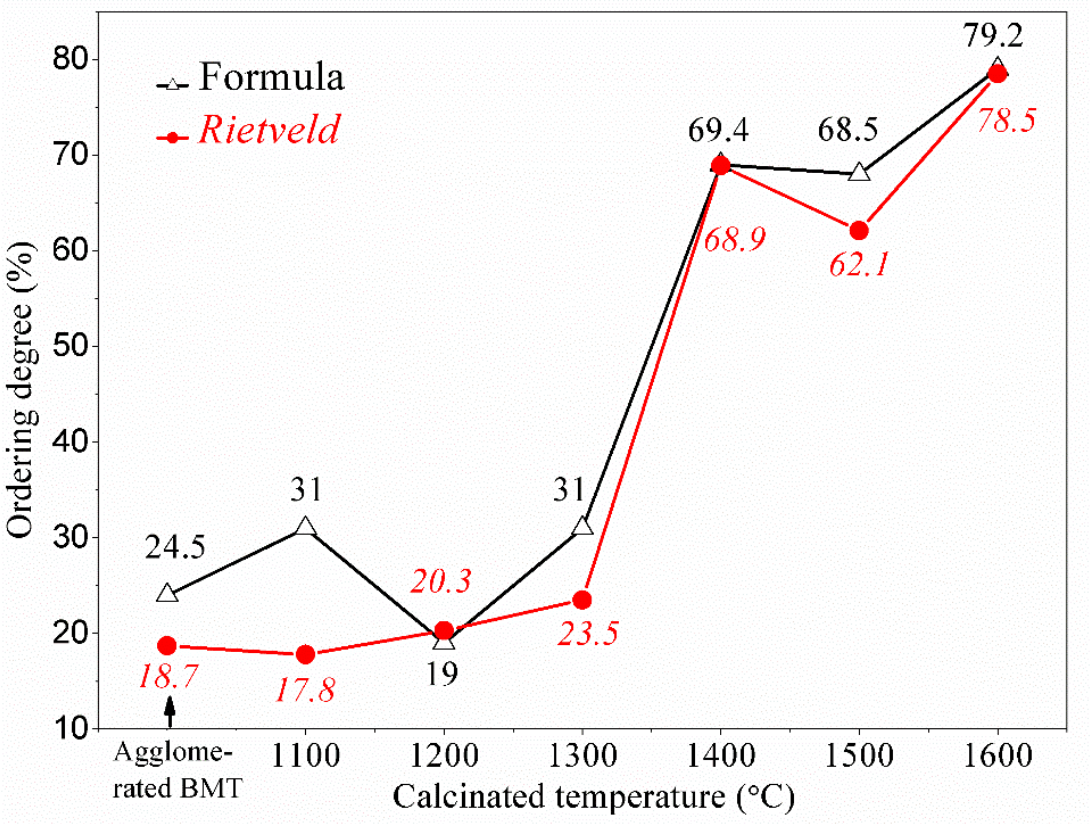

Figure 4.24 Ordering degrees of powder calcinated at various temperatures calculated by formula and Rietveld refinement

It should be clarified here that the peak height of XRD patterns do not directly correlate to quantity but, with the peak breadth, are rather related to the crystallinity of phase. The peak

heights may also be affected by the way the samples are mounted. Consequently, the formula which is widely used to calculate the BMT ordering degree is not reputed to give exact representation of ordering.

In order to obtain an accurate result by Rietveld refinement, a good XRD pattern is required first. In more detail, the step size of X-ray in the scan program should be lower to 0.0131°. Since a lot of samples were tested in the preliminary work, and in the name of efficiency, rough scan program with a step size of 0.0394° was set. It is recommended to carry out finer XRD characterization (step size around 0.0131°) of the selected samples in future work. In addition, the refined results should satisfy the basic principle of goodness of fit (GOF) less than 4 % and R_{wp} less than 20%.

4.6.3 Substrate temperature measurement

This section is the supplemental work of section 4.4.4. The substrate temperature trends during the whole spraying process can visually reflect the influence of thermal effect on the coatings. A k-type thermocouple (TJ36-NNXL-116U-36, OMEGA, USA) was used to measure the internal temperatures of the substrate. The detail configuration is shown in Figure 4.25. A hole was drilled in the center of the substrate and in the copper holder. The thermocouple was passed through the copper holder to reach the core of the substrate, where it was in direct mechanical contact with the substrate material. The measured temperature curves during spraying are shown in Figure 4.26. Once the spraying starts, the temperature increases faster because the heat builds up faster than the heat removal from the cooling system. The coating is an insulator, which acts as an intrinsic heat barrier working against the cooling process placed below the substrate.

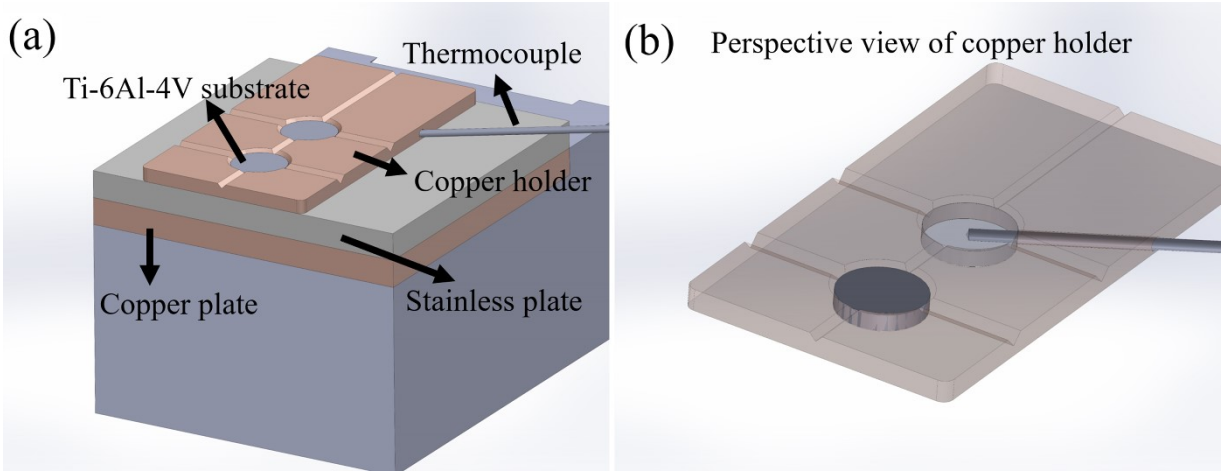

Figure 4.25 Configurations of sample holder and substrate temperature measurement

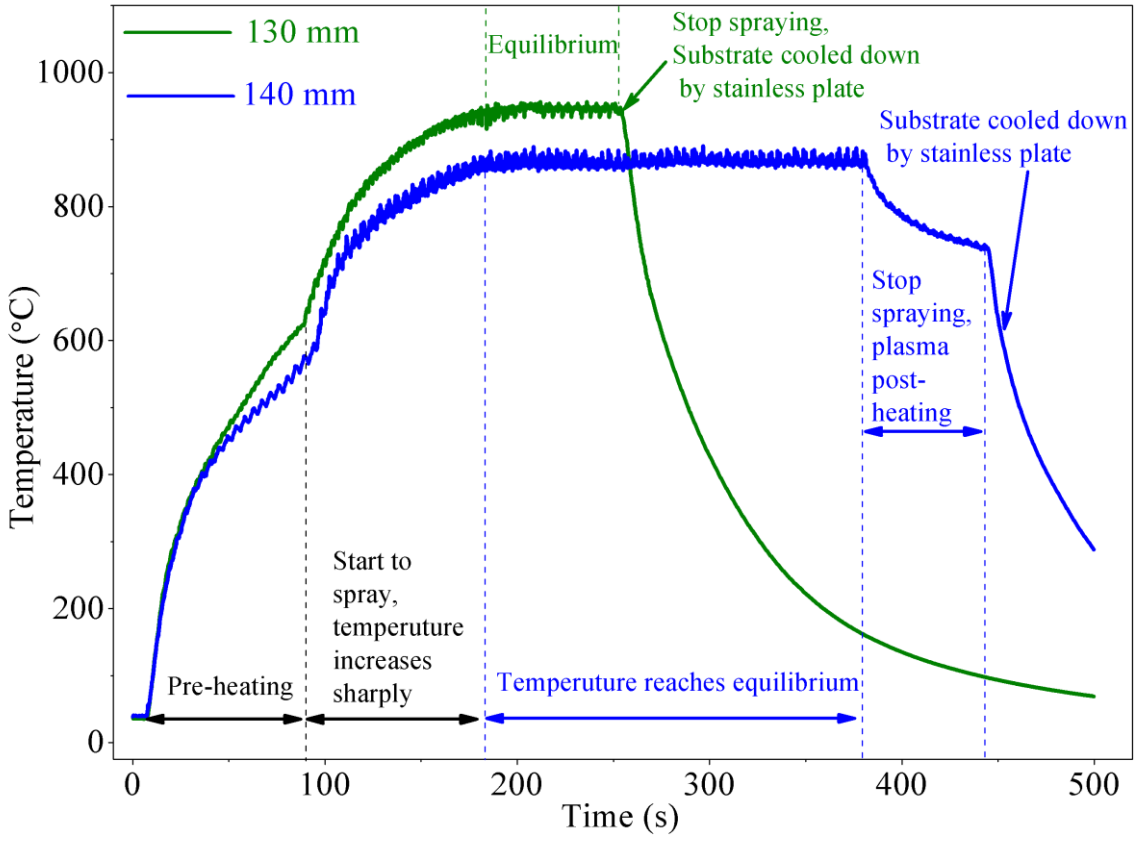

Figure 4.26 Curves of substrate temperature trends during coating deposition at different spraying distances with/without post-heating

CHPTER 5

Coatings microstructure control

5.1 Avant-propos

Auteurs et affiliation :

- Huidong Hou : étudiant au doctorat, Université de Sherbrooke, Faculté de génie, Département de génie chimique et de génie biotechnologique.

- Jocelyn Veilleux : professeur agrégé, Université de Sherbrooke, Faculté de génie, Département de génie chimique et de génie biotechnologique.

- François Gitzhofer : professeur titulaire, Université de Sherbrooke, Faculté de génie, Département de génie chimique et de génie biotechnologique.

- Quansheng Wang : professeur, Institut de technologie de Pékin, Faculté de science des matériaux et d'ingénierie.

Date d' acceptation :11 mars 2020

État de l'acception : version finale publiée

Revue: Surface and Coatings Technology

Référence : [H.Hou et al., Surface & Coatings Technology 389 (2020) 125633]

Titre français: Étude du contrôle microstructural du revêtement de barrière thermique en pérovskite $Ba(Mg_{1/3}Ta_{2/3})O_3$ déposé par projection plasma de précurseur liquide

Contribution au document: This paper presents the procedure of microstructure evolution from lamellar to columnar structures and discusses their formation mechanism. The influences of substrate surface roughness, precursor concentration and feed rate on the columnar morphologies were explored separately. In addition to columnar structure, a dense vertically cracked (DVC) structure is also presented in this paper. So far, the three most common TBCs structures, lamellar, columnar and DVC structures have been deposited successfully by RF plasma spray in this work.

In fact, a tremendous amount of work has been done into the exploration of columnar structure, especially depositing coatings by different precursors. In order to keep the journal paper concise, the submitted paper doesn't includes these preliminary results, which are only shown in the section 5.6 of the thesis.

Résumé français : La projection plasma à couplage inductif a été utilisée pour déposer des revêtements de barrière thermique en $Ba(Mg_{1/3}Ta_{2/3})O_3$ (BMT) sur un substrat en alliage de titane. En sélectionnant les paramètres de projection appropriés, il a été possible d'ajuster la microstructure du revêtement de BMT, des couches denses en forme de lamelles aux colonnes et aux fissures verticales segmentées. Parmi ces paramètres, une courte distance de projection de 34 mm était le paramètre le plus crucial pour former une microstructure en colonne. Une sonde d'atomisation qui alimente une distribution bimodale de la taille des gouttelettes a été considérée comme une condition préalable importante pour obtenir une structure colonnaire de haute qualité. Les petites gouttelettes atomisées contribuent à la formation de colonnes, tandis que les grosses assurent un taux de dépôt élevé. Cette question est examinée plus en détail dans le cadre du mécanisme de formation de la colonne. Les effets de la rugosité de la surface du

substrat, de la concentration des précurseurs et du taux d'alimentation ont été étudiés séparément. La rugosité de la surface doit être contrôlée entre Ra = 1,3 μm et Ra = 2,7 μm pour réduire les espaces intercolonnaires. La structure colonnaire évolue en une fissure verticale segmentée lors de la projection de précurseurs concentrés (30% en poids). Un débit d'alimentation élevé (> 6 ml / min) peut satisfaire une série d'exigences telles qu'un taux de dépôt élevé, de faibles espaces intercolonnaires et une porosité intracolonne élevée. Enfin, une structure colonnaire souhaitée avec une porosité intracolonnaire de 4,3% et une porosité intercolonnaire de 9,9% a été obtenue en projetant un précurseur concentré à 10% en poids sur un substrat finement sablé (Ra = 1,3 μm) à un débit d'alimentation de 8 ml / min.

Mots-clés : BMT, projection plasma de précurseur liquide, RF plasma à couplage inductif, RF SPPS, contrôle de la microstructure, structure colonnaire.

Note : À la suite des corrections demandées par les membres du jury, le contenu de cet article diffère de celui qui a été accepté.

Title: Study of the Microstructural Control of $Ba(Mg_{1/3}Ta_{2/3})O_3$ Perovskite Thermal Barrier Coating Deposited by Solution Precursor Plasma Spray

Abstract:

Inductively-coupled plasma spraying was used to deposit $Ba(Mg_{1/3}Ta_{2/3})O_3$ (BMT) on a titanium alloy substrate. By selecting the appropriate spraying parameter, it was possible to tune the BMT coating microstructure from dense splat-like layers to columns and segmented vertical cracks. Of those parameters, a short spraying distance of 34 mm was the most crucial parameter to form a columnar microstructure. An atomization probe that fed a bimodal droplet size distribution was considered as an important prerequisite to obtain a high-quality columnar structure. Small atomized droplet sizes contribute to the formation of columns, while the large ones ensure a high deposition rate. This is further discussed as part of the column formation mechanism. The effects of substrate surface roughness, precursor concentration and feed rate were studied separately. The surface roughness should be controlled between Ra = 1.3 μm and Ra = 2.7 μm to reduce the intercolumnar gaps. The columnar structure evolves into a segmented vertical cracked one when spraying concentrated precursors (30 wt. %). High feed rate (> 6 ml/min) can satisfy a series of requirements such as high deposition rate, low intercolumnar gaps and high intracolumnar porosity. Finally, a desired columnar structure with an intracolumnar porosity of 4.3 % and an intercolumnar porosity of 9.9 % was obtained by spraying a 10 wt. % concentration precursor on a finely sand-blasted substrate (Ra = 1.3 μm) at a feed rate of 8 ml/min.

Key words: BMT; Solution precursor plasma spray; Inductively-coupled RF plasma; RF SPPS; Microstructure control; Columnar structure

5.2 Introduction

Thermal barrier coatings (TBC) are widely used in turbine engine to insulate metallic components from hot service environments, such as the combustor chamber and the turbine blades. A widely used method to deposit TBC is atmospheric plasma spraying (APS), which feeds the feedstock powder (normally within 45-125 μm size range) through a plasma jet in order to heat and accelerate the particles [144]. The molten or semi-molten powder then hits onto a substrate and stacks to form a lamellar structure. APS-deposited TBC made of yttria-stabilized zirconia (YSZ) usually have a low thermal conductivity, but also a relatively short lifetime, especially during intense thermal cycling tests [145]. However, TBC should withstand frequent thermal shocks in real service environment, as in the high-pressure part of a turbine engine where they protect the mobile blades [1]. Introducing a large number of segmentation cracks to the lamellar structure was a good method to increase the strain tolerance of TBC [18]. Still, the best microstructure to improve strain tolerance is the quasi-single crystal columnar structure with large intercolumnar gaps [146]. Since 1980s, the most popular method to deposit coatings with this kind of columnar structure on a blade is electron beam physical vapor deposition (EB-PVD) [97]. Due to the high capital cost and low deposition rate of EB-PVD, new methods such as suspension plasma spray (SPS) [83, 85] and plasma spray-physical vapor deposition (PS-PVD) [111, 116] were applied to prepare columnar structure coatings with a high deposition rate.

In addition to processing methods, research and development of new TBC materials was also widely carried out and rare-earth zirconates ($Ln_2Zr_2O_7$) with a pyrochlore structure or $(La,Nd)MAl_{11}O_{19}$ (M could be Mg, Mn, Zn, Cr and Sm) with a hexaaluminate structure were proposed, as well as complex perovskites [35].

In this work, the complex perovskite $Ba(Mg_{1/3}Ta_{2/3})O_3$ (BMT) is chosen as a TBC material owing to its high melting temperature [64] and low thermal conductivity ~2W/m-K (bulk properties) [70]. Until now, the attempts to apply BMT to the TBC field have been limited. Indeed, the BMT coatings prepared by APS from a powder feedstock showed a characteristic dense lamellar structure with low thermal cycling capabilities [5]. Similarly, with a hybrid suspension/solution precursor plasma spray process adopted in our previous work, the as-sprayed BMT coatings showed a fully dense structure [147]. Thus, a new technology should be applied to deposit BMT coating with various microstructures, especially the desired columnar and porous microstructures.

Solution precursor plasma spray (SPPS) was designed to deposit coatings with novel structures and improved performance, such as porous microstructures, nanometer-sized grains and vertical cracks [148]. A major incentive of developing SPPS was to cut the chores of feedstock preparation and suspension formulation [149]. Thus, it is more suitable to test new compositions and materials, for example BMT, with SPPS technology. Different from SPS, precursors are mixed and dissolved molecularly in SPPS [8], which contributes to a far more homogeneous coating and avoids the phase separation observed before. Consequently, SPPS is selected and optimized to deposit BMT coatings in this work. The spraying parameters that are suitable for the growth of columnar structures are explored. The evolution from a dense to a columnar microstructure is discussed through tailoring the spraying distance, atomization probe type, the substrate roughness, the precursor concentration and the precursor feed rate. A secondary objective of maintaining an acceptable deposition rate is also considered throughout the discussion.

5.3 Experimental Procedures

5.3.1 Precursor formulation

Tantalum ethoxide $Ta(OC_2H_5)_5$ (Henan Tianfu Chemical Co., Ltd, China), barium acetate $Ba(CH_3COO)_2$ (Sigma-Aldrich, Germany) and hydrated magnesium acetate $Mg(CH_3COO)_2 \bullet 4H_2O$ (Fisher BioReagents, India) were chosen to prepare the precursor of BMT. Acetic acid (Fisher Chemical, USA) is chosen to dissolve Ba acetate and to stabilize $Ta(OC_2H_5)_5$ against undesirable hydrolysis and gelation, as seen in formula (5.1). The volume ratio of ethanol (Commercial Alcohols, Canada) to acetic acid is 2:1. Mixing the precursor results in a transparent liquid.

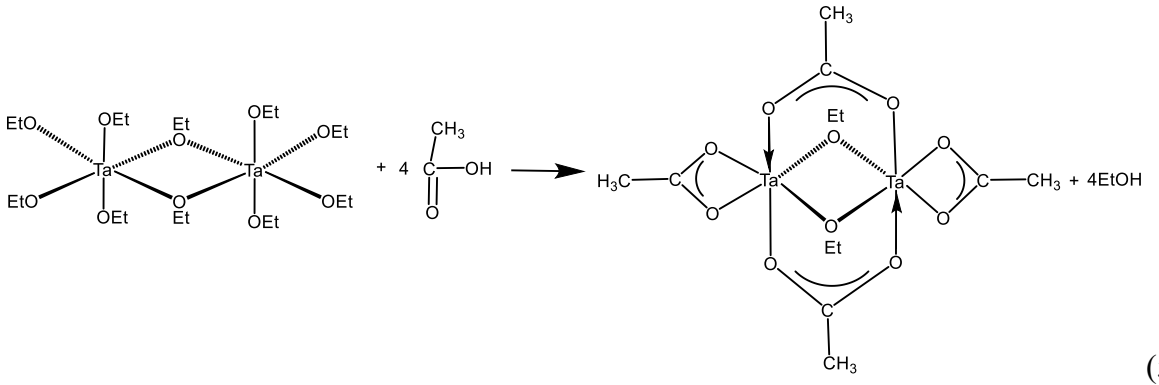

(5.1)

Throughout the experiments, twice the stoichiometric amount of Mg was used to compensate for the preferential Mg loss during plasma spraying [147]. Precursors with three different concentrations of 10 wt.%, 20 wt.% and 30 wt.% were prepared. Unless otherwise stated, the precursor with 10 wt. % concentration was adopted to spray the BMT coatings.

5.3.2 Substrate preparation

Titanium alloy (Ti-6Al-4V) with a diameter of 12.6 mm and a thickness of 2 mm was chosen as substrate. The substrate surfaces were prepared by coarse grain sand-blast (46 grit), fine grain sand-blast (120 grit), and abrasive paper sanding (180 grit). All the substrates were cleaned by acetone and ethanol, successively.

The substrate topographies were observed using a confocal laser-scanning microscope (LUOVIEW FV3000, Olympus, Japan). The results were treated using Fiji (an image processing package based on ImageJ, National Institutes of Health, USA) for background subtraction and color coding, and then using the open source software Icy (http://icy.bioimageanalysis.org.) for 3D rendering. The obtained 3D views of the prepared substrates are shown in Figure 5.1. The surface roughness was measured with a Surftest SJ-210 (Mitutoyo, Japan), and the results are also marked in Figure 5.1.

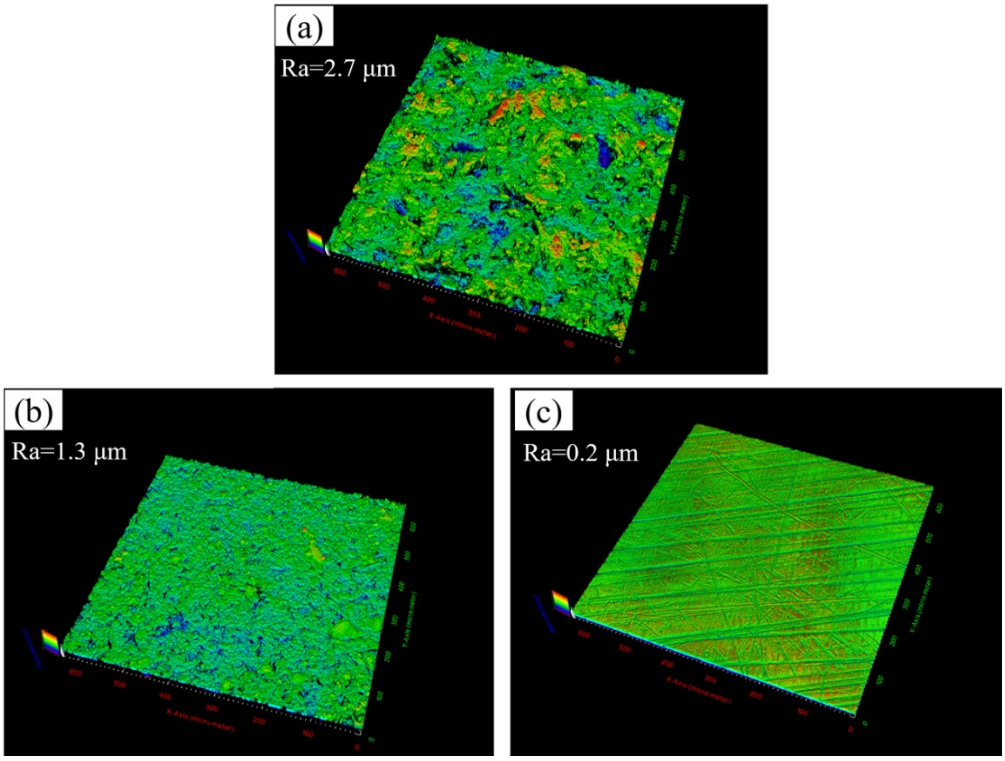

Figure 5.1 Topography of prepared substrates. (a) coarse grain sand-blasted; (b) fine grain sand-blasted and (c) paper sanded

5.3.3 Preparation of BMT coatings

The precursor solution was axially fed into a radio frequency inductively-coupled plasma (RF ICP) torch (PL-50, Tekna Plasma Systems Inc., Sherbrooke, Canada) equipped with a 25-mm converging nozzle, as depicted in Figure 5.2. A commercial atomization injection probe

(SDR79202B1, Tekna Plasma Systems Inc., Sherbrooke, Canada) was chosen in most cases to deposit BMT coatings. Besides, an in-house designed probe with a narrower atomized droplet size distribution was used to analyze the growth mechanism of columnar structures. The size distribution of atomized droplets was measured with a Malvern instrument equipped with a data collector RT sizer (Real Time Particle Sizer) (EPCS, Malvern, San Ramon, CA, USA). The atomization gas and flowrates used in the atomization tests were identical to the real coating preparation process. The spraying parameters are summarized in Table 5.1.

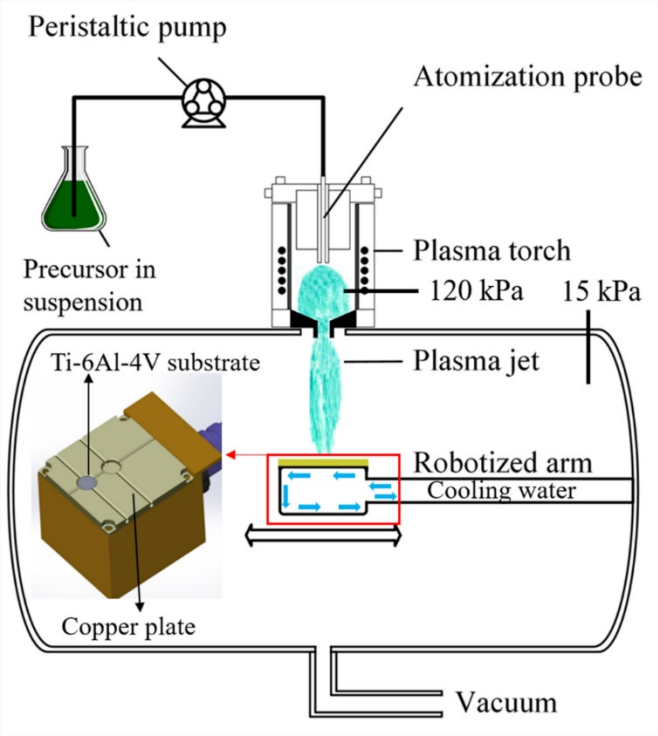

Figure 5.2 Schematic illustration of reactor for BMT coating preparation

Although placing a water-filled container in the path of the plasma gun is a widely used method to collect molten powder during spraying, the low reactor pressure makes this strategy impossible with the current controlled atmosphere (15 kPa) setup. The powder collected randomly from the deposition reactor is not statistically significant because the powder collected from different locations may vary widely. The powder synthesis reactor includes a main reaction chamber and an auxiliary one, which can segregate the coarse and fine powders. Since the

commercial atomization probe also produces a bimodal droplet size distribution, the powder synthesis reactor is suitable for collecting the particles produced by commercial atomization. In this work, a powder synthesis reactor (as seen in Figure 5.3) was used to collect the BMT powder. In order to reproduce as closely as possible the coating deposition environment, all the spraying/synthesis parameters were kept the same, such as plasma parameters, atomization probe and converging nozzle.

Table 5.1 Plasma parameters for coating deposition and powder collection (4 ml/min feed rate was used in most cases, unless otherwise specified)

	Coating preparation	Powder collection
Sheath gas(Ar)	6 slpm	6 slpm
Sheath gas (O_2)	63 slpm	63 slpm
Central gas (Ar)	23 slpm	23 slpm
Carrier gas (Ar)	11 slpm	11 slpm
Reactor pressure	15 kPa	15 kPa
Plasma power	50 kW	50 kW
Feed rate	4/6/8 ml/min	4 ml/min
Standoff distance	80/60/34 mm	NA
Translational speed	50 mm/s	NA
Pre-heating cycles	20 loops (60 s)	NA
Deposition cycles	80 loops (240 s)	NA

5.3.4 Material characterizations

The particle size distributions of collected powders were measured by a Malvern instrument (Mastersizer 2000, Malvern Instruments Limited, UK). The microstructure and the morphology of the deposited BMT coatings were analyzed by Scanning Electron Microscopy (SEM) (S-3000N, Hitachi, Japan). The open source software ImageJ (National Institutes of Health, USA)

was used to calculate the coatings porosity as well as the size distribution of the observed cauliflower shapes and of the deposited splats. The phase structure was analyzed by X-ray diffraction (XRD) (X'pert PRO PHILIPS, Netherlands).

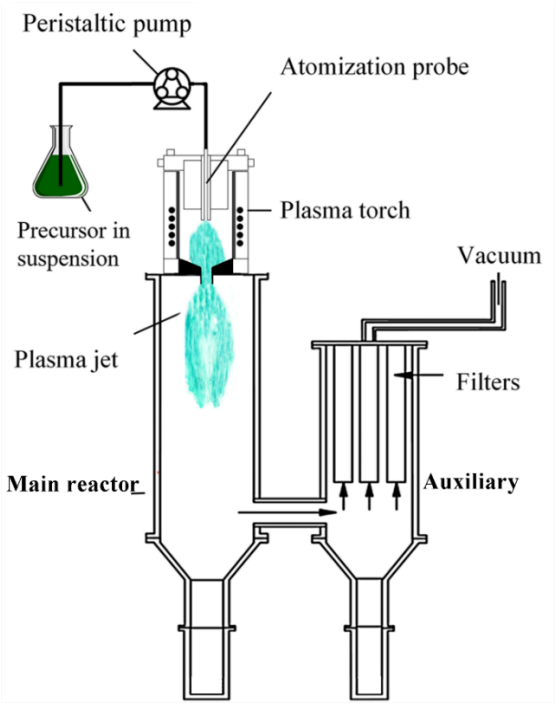

Figure 5.3 Schematic illustration of reactor for BMT powder collection

5.4 Results and Discussion

5.4.1 Microstructure Evolution

It is known that the columnar structure formation mechanisms are different when adopting EB-PVD [146]，PS-PVD [116] and SPS/SPPS [81]. For SPS, the shadow effect is an important factor that facilitates the formation of columns, as demonstrated when spraying at small angles [150]. Considering the dense lamellar structure obtained for BMT coatings sprayed either by Hybrid SPS/SPPS or APS processes, it is hypothesized that the SPPS process would benefit from the shadow effect produced by the asperities of a coarsely sand blasted substrate to grow

columnar structures. As such, the coarse grain sand blasted substrate was studied first, and coatings were prepared using the commercial atomization probe. The cross-sectional microstructures and the surface morphologies of coatings sprayed with 10 wt. % precursor are shown in Figure 5.4.

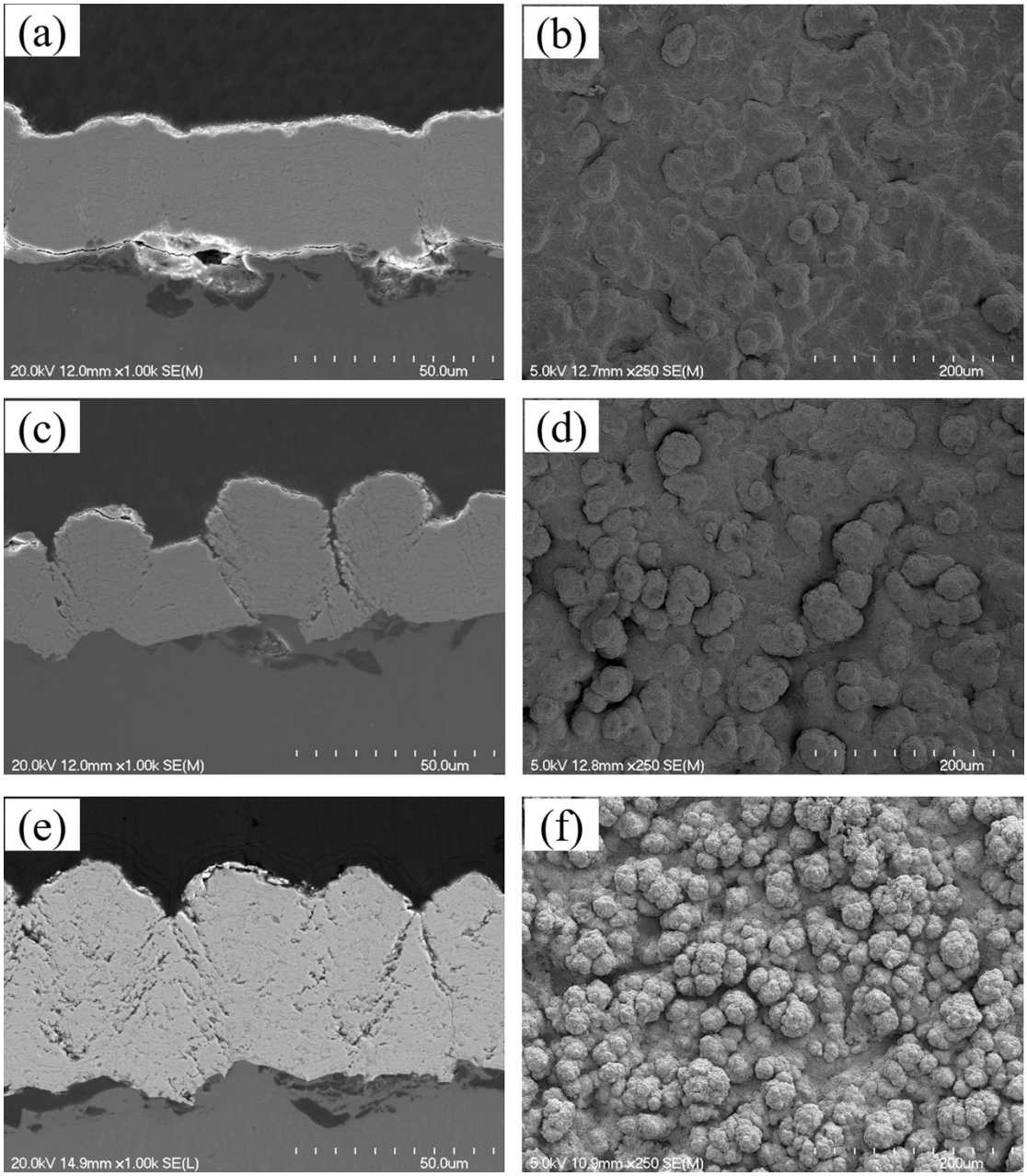

Figure 5.4 SEM micrographs of cross-sections (left side) and surfaces (right side) of coatings sprayed at different spraying distances (a) (b) 80 mm; (c) (d) 60 mm; (e) (f) 34 mm

When decreasing the spraying distance, the coating deposition rate increases because of the higher density of liquid or molten droplets near the torch outlet. The coating sprayed at 80 mm shows a dense lamellar structure (Figure 5.4a). Two columns occur at the humps when sprayed at 60 mm (Figure 5.4c), while a fully columnar structure was obtained with a spraying distance of 34 mm (Figure 5.4e). Accordingly, the top morphology shows a clear cauliflower-shape (Figure 5.4f). It can be inferred that a short spraying distance is essential for the formation of columnar structures, particularly for BMT.

5.4.2 Formation mechanism of the columnar structure

As of today, the largely accepted theory of the column formation mechanism during SPS indicates that small particles (< 5 μm) follow the gas flow in the substrate vicinity and impact on the asperities at angles to form columns [138]. With an axially-fed RF plasma torch, the precursor droplet size distribution can be varied by changing the atomization probe, as indicated in Figure 5.5.

The atomized droplet size of the commercial probe (Figure 5.5a, 5.5c) presents a bimodal distribution while the in-house probe (Figure 5.5b, 5.5d) shows a single peak whose range is similar to the first peak of the commercial probe. The commercial probe also atomizes much larger droplets, as shown by its second peak around 20-70 μm. The two probes were compared to address the effect of droplet size distribution on the coating microstructure. Adopting identical spraying parameters to those used before (with the commercial probe), coating was sprayed with the in-house probe and resulted in the microstructure shown in Figure 5.6. The as-sprayed coating has typical columnar characteristics, while its structure is loose, likely caused by the lateral movement of small particles. Moreover, its thickness is much thinner than that of the coating sprayed with commercial probe (Figure 5.4e). This result suggests that a too small atomization size is detrimental for the deposition rate; droplets either vaporized or had insufficient momentum to hit the substrate.

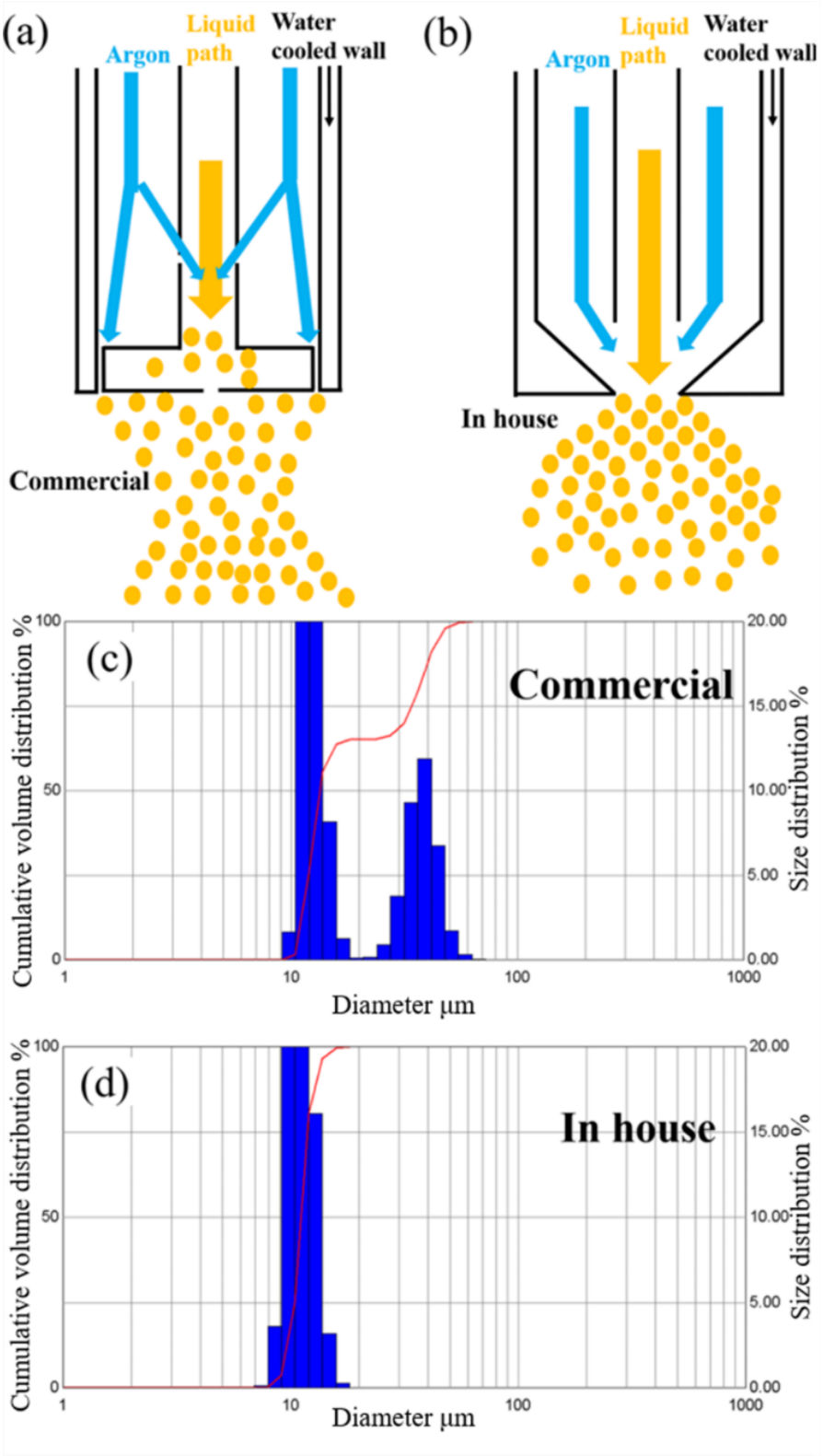

Figure 5.5 Atomization schematic of the commercial (a) and in-house (b) probes, accompanied by their respective droplet size distributions (c) and (d)

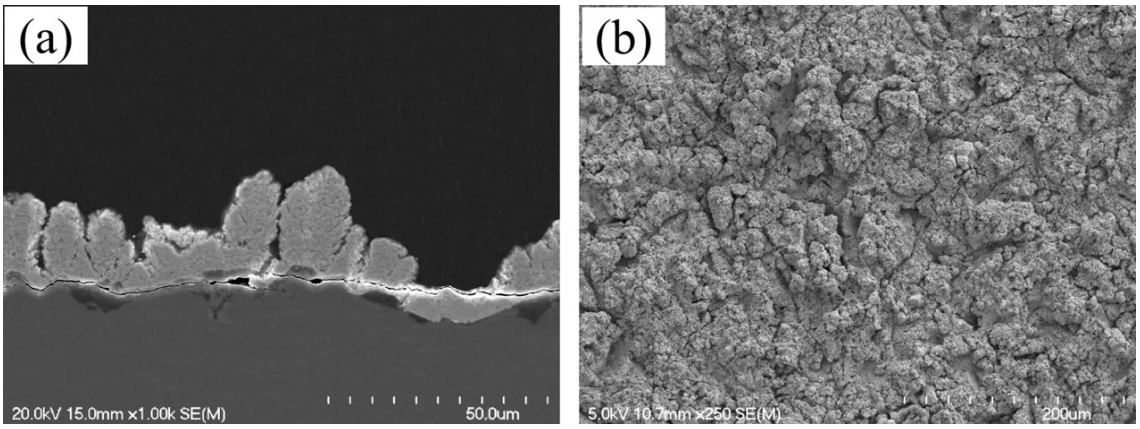

Figure 5.6 SEM micrographs of cross-section (left side) and surface (right side) of a coating sprayed with the in-house atomization probe at a spraying distance of 34 mm

Analyzing the actual powder formed during spraying is propitious to understand the build-up mode of columns. The particle size distributions of the collected powders sprayed with the commercial probe are shown in Figure 5.7. The powder was mainly collected from two chambers: the auxiliary chamber and the main reactor. Because of the little amount of powder sticking to the surface of the filters, this fraction is ignored here. Generally speaking, the vacuum pulls the smaller particles towards the auxiliary chamber and filters, while larger particles remain in the main reactor. It can be reasonably hypothesized that the large particles collected (around 10 μm) in the main reactor (Figure 5.7a) came from the large droplets (Peak 2 in Figure 5.5c), while the small particles (around 3 μm) collected in the auxiliary chamber (Figure 5.7b) originated from the small droplets (Peak 1 in Figure 5.5c). Severe agglomeration of fine particles explains the presence of large size agglomerates around 50-100 μm in Figure 5.7b. In fact, it would be impossible to form single particle that large from droplets below 70 μm in size, each containing a maximum of 10 wt. % solid. Following the solvent evaporation and the solute pyrolysis within the plasma [85], nanoparticles nucleate, grow, collide and agglomerate along their path within the torch (a confined region with high pressure plasma), main reactor and auxiliary chamber. Due to the lower pressure (15 kPa) of the reactor chamber with respect to the inner plasma torch pressure (120 kPa), the plasma quickly expands and steep temperature gradients occur both in the normal and lateral directions.

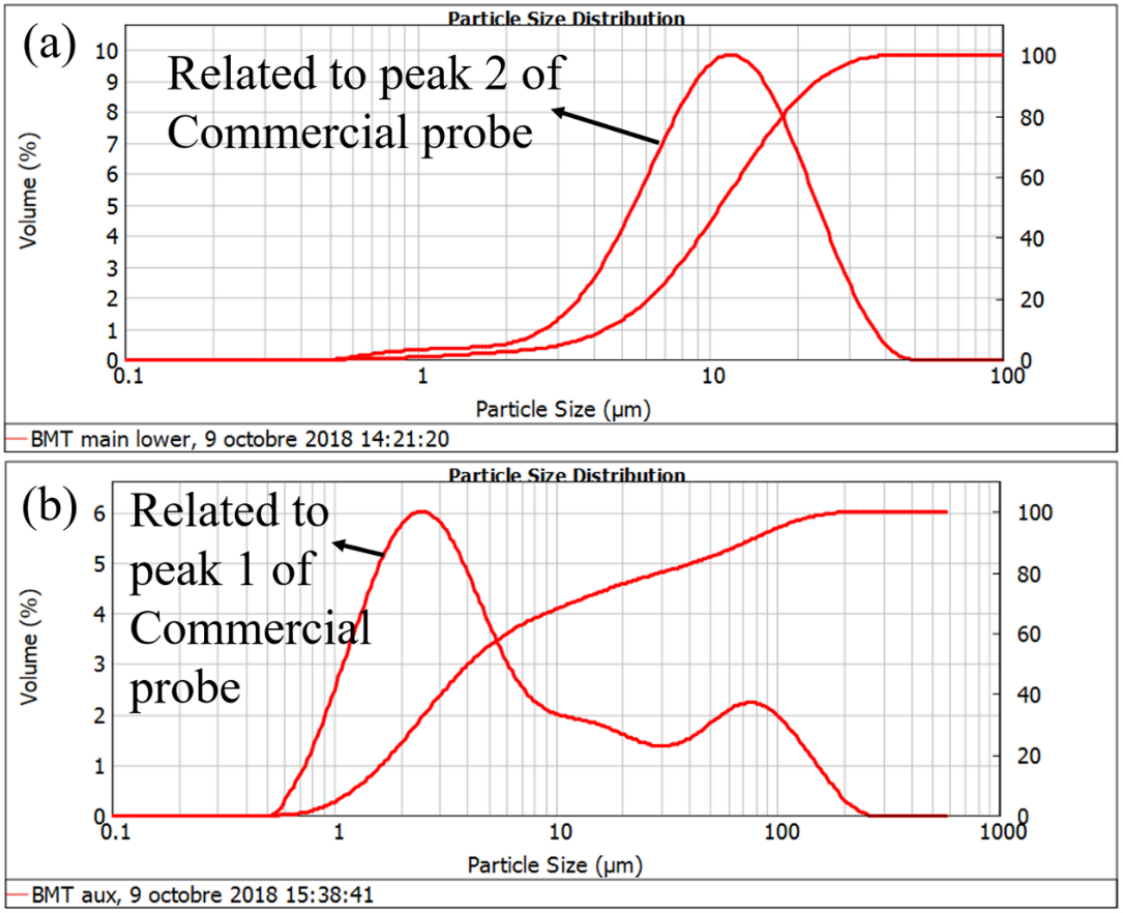

Figure 5.7 Particle size distributions of collected powder from the inner wall of the main reactor (a) and auxiliary chamber (b)

When using the commercial probe, as seen in Figure 5.8a, large particles around 10 µm (Stokes number St > 1) are well accelerated and then impinged on the substrate surface. The big asperities formed in this process contribute to the coating growth. Meanwhile, smaller particles around 3 µm (St < 1) are likely to flow along the plasma gas streamlines in the substrate vicinity and to impinge on large asperities at angle. As such, they contribute to the formation of columns and to the generation of intercolumnar gap within the microstructure. In addition, thermophoresis forces push the smallest particles smaller than1 µm (St << 1) towards the plasma fringes [151], where momentum transfer is not as efficient making their deposition probability much lower.

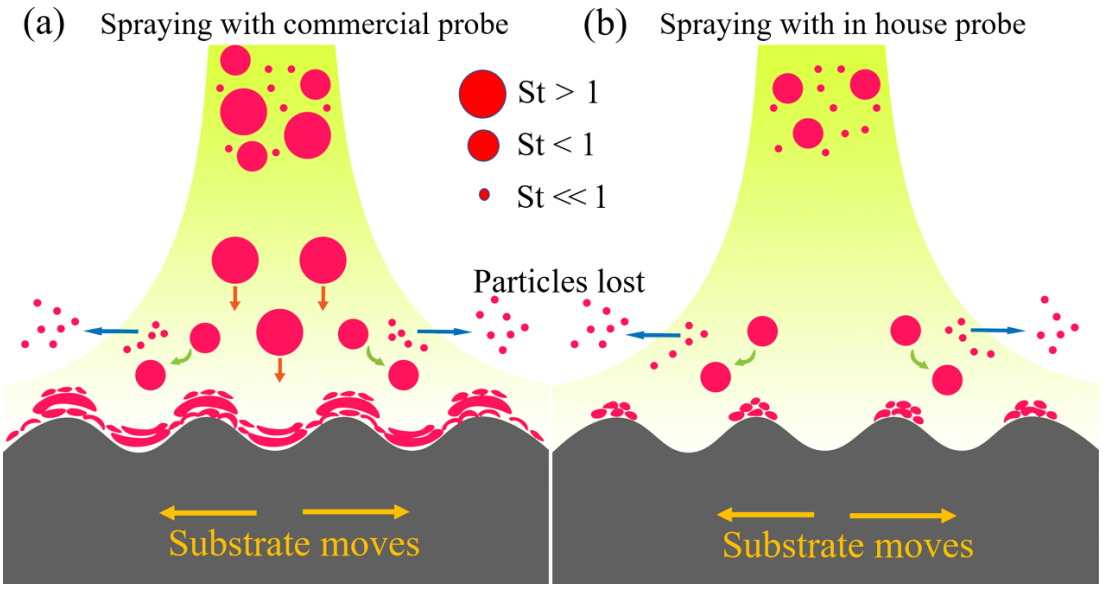

Figure 5.8 Schematic illustration of the columnar structure formation mechanism during spraying with (a) commercial probe; (b) in-house probe

On the contrary, the in-house probe only produces small particle sizes (Figure 5.8b) which form the loose columnar structure. Without the vertical impingement and the pile up of splats, as-sprayed coating shows low deposition rate. To summarize, the columnar structure is built by combining the vertical impingement of large particles and the lateral impingement of small particles [88]. The commercial atomization probe produces a bimodal size distribution which is more suitable to obtain a thick coating with well-defined columns. The in-house probe was only used for this comparative test at a 34 mm spraying distance; the following works were carried out with the commercial probe.

For long spraying distances, the larger particles dominate the formation of the coatings, as only a lamellar structure is formed. However, this is not observed for all precursors. For example, SPPS-sprayed Y_2SiO_7 environmental barrier coating (EBC) at a long distance of 140 mm showed a loose columnar structure on a relatively smooth substrate [118]. The state of feedstock (from gas to liquid to solid) and the incidence angle at the moment of impact on the substrate both play important roles, as columnar structures also form from the vapor phase in PS-PVD [111].

5.4.3 Columnar microstructure control

Substrate roughness

Substrate roughness is known to affect the size, shape and top morphology of columns sprayed by DC SPS at atmospheric pressure [137, 152]. In previous work, EBC coatings were deposited with RF SPPS on a relatively smooth surface and showed a loose columnar structure, as opposed to the results reported here, which indicates that the columns form preferentially on larger bulges. Thus, a causal relation between substrate roughness and columnar structure remains to be fully established for RF SPPS at lower pressure and is discussed below. Substrates with distinct surface roughness (Figure 5.1) were used to deposit BMT coatings, as shown in Figure 5.9.

Some large size columns grew from big asperities on the coarsely sand-blasted substrate (Figure 5.9a), accompanied by vertical cracks from bottom to top surface, as indicated by the white ovals. On the surface of finely sand-blasted substrate (Figure 5.9c), columns also grew from the big asperities, while the average size of cauliflower-shapes decreased. On the contrary, the coating near the polished substrate surface (Figure 5.9e) shows a relatively dense structure (below the white line) and columns started to sprout afterwards. As indicated before, the parallel motion of small particle contributes to the columnar formation and intercolumnar gaps generation, but they need anchoring sites to impact on. Since the polished substrate has a smooth surface, most of these small particles were loss at early deposition times and only large particles impacted on the substrate to form a relatively dense lamellar structure. At later deposition times, the surface roughness increased due to the random stacking of lamellae, creating anchoring sites for small particles and the occurrence of a columnar microstructure.

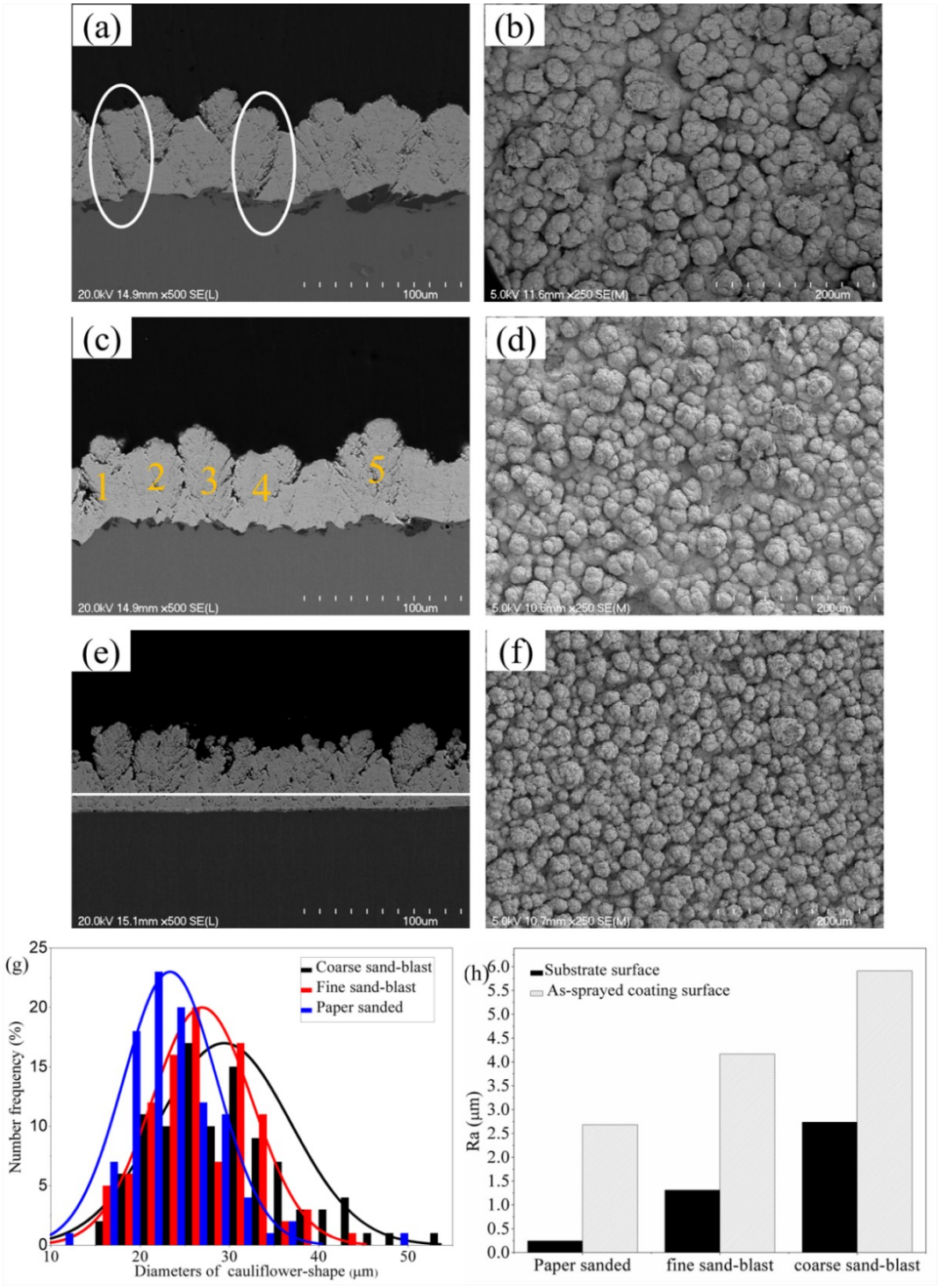

Figure 5.9 SEM micrographs of cross-sections (left side) and top surfaces (right side) of coatings sprayed on the coarse (a) (b)and the finely (c) (d) sand-blasted substrates, and paper-sanded substrate (e) (f). (g) shows the diameter distribution of cauliflower-shapes sprayed on different substrates. (h) shows the comparison of surface roughness of each substrate before and after spraying

Figure 5.9g shows the size distribution of cauliflower-shapes on the top surface. The cauliflower-shape grown on the paper sanded substrate presents the smallest diameter with a d50 = 22 μm, while this diameter increases from d50 = 26 μm to d50 = 30 μm for fine sand-blasted and coarse sand-blasted substrates, respectively. This trend indicates a clear relation between the cauliflower shapes and the substrate roughness, as seen in Figure 5.9h. The coarser the substrate surface is, the rougher the coating is. In real applications, TBCs are usually sprayed on a metallic bonding layer. Accordingly, the roughness of the metallic bonding layer should determine the columnar morphology of TBCs. However, the bonding layer surface roughness impacts the thermal cycling fatigue resistance and the coating lifespan; larger columns deposited on rougher bond coat surfaces showed less intercolumnar organization that led to an inhomogeneous thermal compliance and increased internal stress [88]. Therefore, the smaller the column size, the longer the coating lifespan expected. The paper sanded substrate resulted in coatings having a poor mechanical adhesion. Accordingly, the finely sand-blasted substrate, which produced smaller columns, is selected for the following tests.

Precursor concentration

The precursor concentration determines the solute content in each single atomized droplet. Solid particles with various sizes can precipitate from droplets with same size, but different concentrations [93]. As indicated before, the size of solid particles determines the microstructure and deposition rate. Accordingly, the precursor concentration has an important influence on the columnar structure. In this part, precursors with concentration of 20 wt. % and 30 wt. % were used to spray BMT coatings, as shown in Figure 5.10. The coating sprayed with 10 wt. % precursor (Figure 5.9c, 5.9d) is also considered below for comparison.

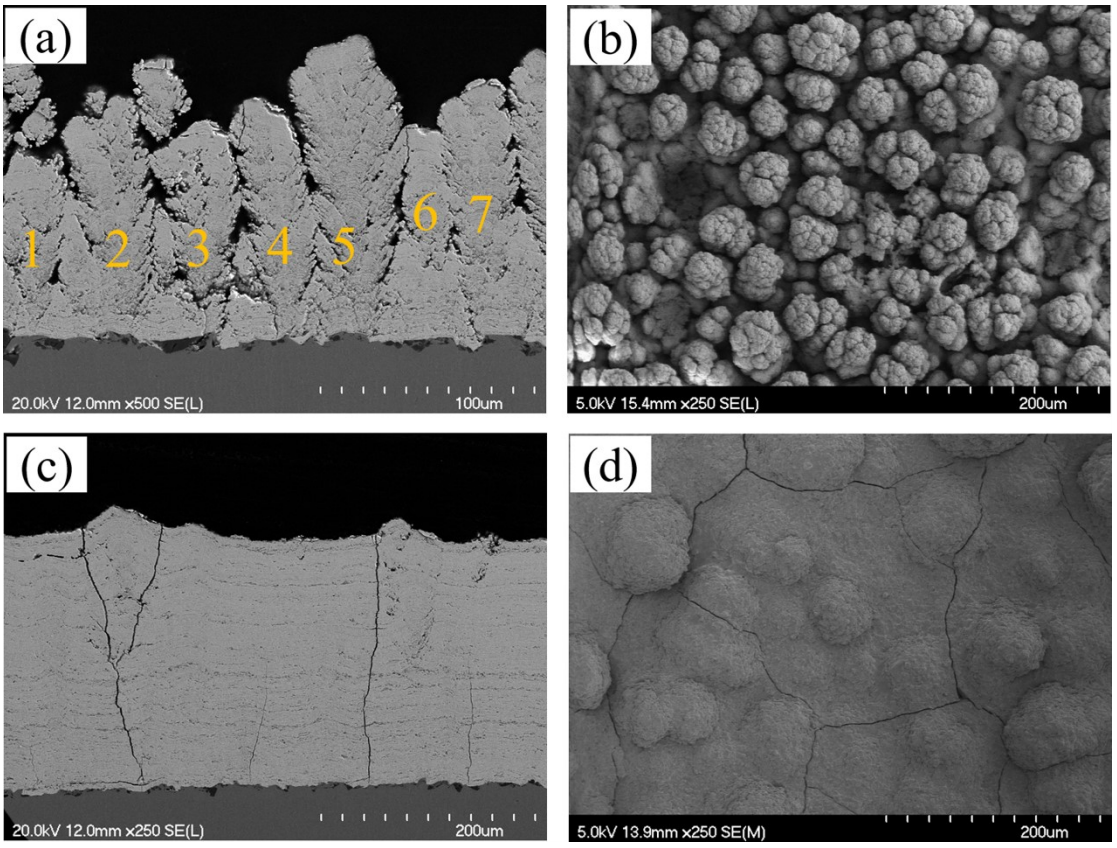

Figure 5.10 SEM micrographs of cross-sections (left side) and surfaces (right side) of coatings sprayed with precursor of different concentration (a) (b) 20 wt. %; (c) (d) 30 wt. %

When spraying the 20 wt. % precursor, the average thickness increased to 130 μm after 80 loops, as seen in Figure 5.10a. This micrograph depicts seven columns with an inverted cone shape, each column having a small average diameter around 30 μm. In contrast, when spraying the 10 wt. % precursor (Figure 5.9c), the thickest point of the coating only reaches 60 μm, and only five columns can be clearly distinguished at the same image magnification. Each column has an average diameter around 40 μm. From this observation, it can be concluded that an increase in precursor concentration can not only increase the deposition rate, but also form much more columns per unit area.

The growth rate of columnar structures can be defined with normal ($v_{\perp}$) and lateral ($v_{//}$) growth velocities. There is a relation between these two growth velocities, as indicated by equation 5.2,

where A_{exp} is the slope of the curve linked to the column expansion during growth [87].

$$\nu_{//} = A_{exp} \times \nu_{\perp} \quad (5.2)$$

This equation means that $\nu_{\perp}$ and $\nu_{//}$ change together with the variation of spraying parameters. When the concentration of precursor increased from 10 wt. % to 20 wt. %, it was equivalent to feeding twice the solute mass per unit time into the plasma. Consequently, more and/or larger solid particles were precipitated from the atomized droplets. Meanwhile, these solid particles vertically impinged on the substrate, which increased $\nu_{\perp}$ and the deposition rate. According to formula 5.2, $\nu_{//}$increased simultaneously; a larger number of solid particles flew horizontally and enhanced the probability of column formation. Therefore, much more columns have sprouted and grown. However, the space for lateral growth of each column being limited, the final columnar structure was mainly composed of small-sized columns, as shown in Figure 5.10a.

When spraying the precursor with a concentration of 30 wt. %, a Dense Vertically Cracked (DVC) structure occurred rather than the columnar one, as seen in Figure 5.10c. Indeed, further increasing the solute concentration stimulated collisions and agglomeration of particles, especially in the high pressure region within the ceramic confinement tube and the supersonic nozzle. Large size particles were formed and mostly impinged vertically on the substrate with St >1. As a result, columns disappeared while the DVC structure formed. The surface morphology was also transformed from cauliflower-like shapes (Figure 5.10b) to turtle-like cracks (Figure 5.10d). Compared to traditional lamellar structure coating which shows decreased cyclic durability when increasing thickness, the through-thickness DVC structure is meaningful in depositing very thick TBC due to its stress-relieving cracks [8].

The DVC structure is similar to segmentation cracks. When there is a large temperature gradient between well-bonded splats and the upper ones, segmentation cracks are caused by the excessive shrink of the upper splats upon cooling in the APS process [18]. In the SPS process, the splats are thinner and have lower energy release rates during cooling; it limits the propagation of

micro-cracks and the tensile stress-relieving. Consequently, the accumulated tensile stress contributes to the segmentation crack formation [84]. Ganvir et al. summarized the relationship between suspension properties and coating microstructure in the SPS process. Droplets with higher momentum result in normal deposition, leading to the lamellar/vertically cracked microstructure [153]. Thus, two key prerequisites, high momentum impinging droplets and thinner splats, result in DVC structure in SPS process. In fact, SPS shares much in common with SPPS where the formed droplets and splats show similar order of magnitude in size and/or momentum. The theory built by SPS may also apply to SPPS, especially upon the process of splats cooling and pile up. In this work, such high momentum droplets were obtained from high solute concentration (30 wt. %), for which agglomeration and precipitation in larger particles are more likely. However, when compared to a 45-120 μm particle size distribution in conventional APS, the relatively smaller particles in SPPS formed thinner splats with low energy release rate. The observed SPPS DVC structure can be seen somewhere between the lamellar and columnar structures. The DVC structure can enhance strain tolerance and prolong thermal cycling life compared to lamellar structure, but its lower porosity may increase thermal conductivity.

Feed rate

Varying the precursor feed rate can also change the mass of solute fed per unit time. Precursor with a 10 wt. % concentration was used in this part, and the feed rate was increased to 6 ml/min and 8 ml/min (standard feed rate was 4 ml/min). In order to better quantify the columnar microstructure differences, the intercolumnar and the intracolumnar porosities were calculated by SEM image analysis performed with ImageJ. As seen in Figure 5.11, a low-magnification area was used to calculate the intercolumnar porosity (Figure 5.11b) and high-magnification area was used for the intracolumnar porosity (Figure 5.11d). Images were binarized using Otsu thresholding technique (Figure 5.11c, 5.11e). Before starting the test, ImageJ can directly set the threshold value, and keep the same value in the subsequent test without artificial adjustment.

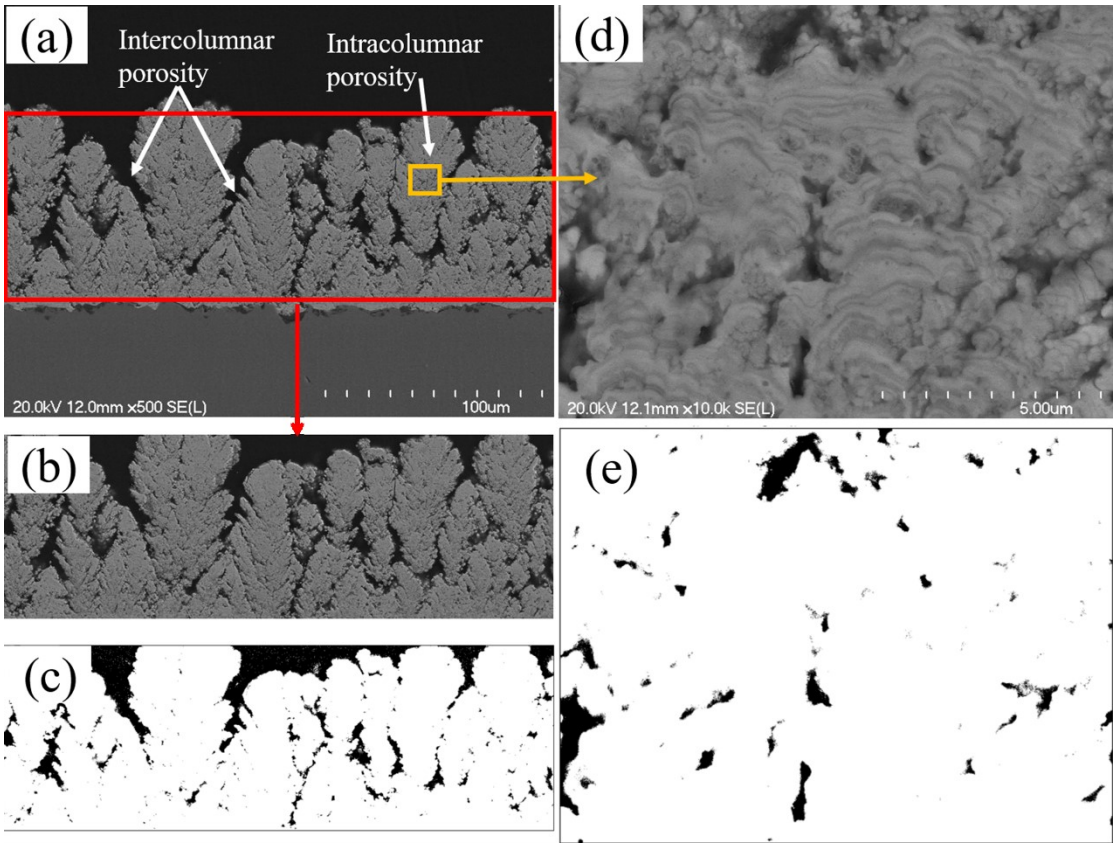

Figure 5.11 (a) Cross-sectional image of BMT coating；(b) Selected area of low magnification (X500); (c) Same area after binarization showing intercolumnar porosity; (d) Selected area of high magnification (X10k); (e) Same area after binarization, showing intracolumnar porosity

Cross-sectional images of coatings sprayed with different feed rates are shown in Figure 5.12, together with porosity levels calculated. When increasing the feed rate from 6 ml/min (Figure 5.12a) to 8 ml/min (Figure 5.12b), the deposition rate increased, as expected. Meanwhile, the intercolumnar porosity decreased, while the intracolumnar one increased (Figure 5.12d). A higher flux of solid content at large feed rate reduces the intercolumnar gaps, but it also comes with a higher energy demand for solvent evaporation, leaving less energy available for the complete melting and densification of solid particles. This leads to the inverse variation trend between intra- and intercolumnar porosity.

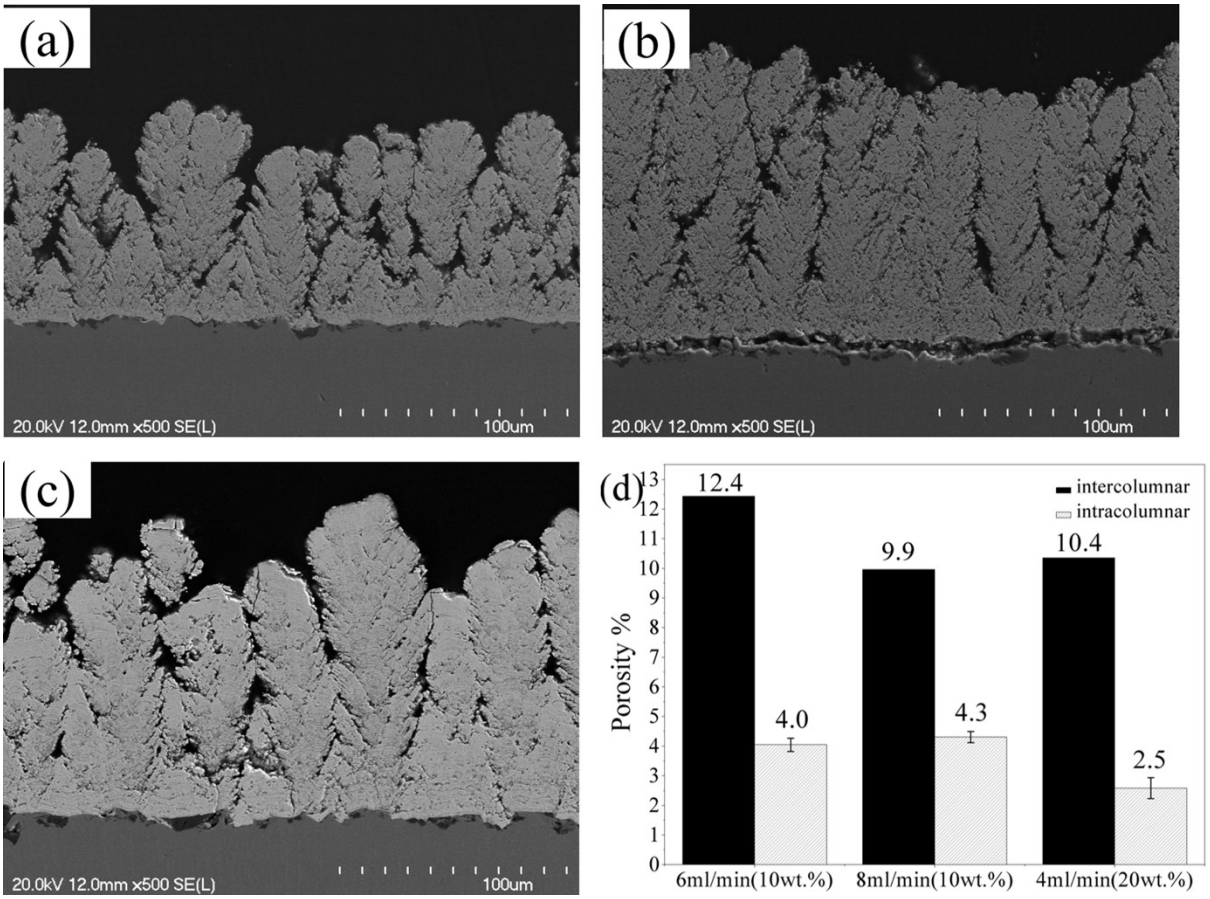

Figure 5.12 Cross-sectional images of coatings sprayed using different feed rates (a) 6 ml/min (10 wt. %); (b) 8 ml/min (10 wt. %); (c) 4ml/min (20 wt. %) was used to compared with (b). (d) shows the variation of intracolumnar and intercolumnar porosities

To further support the previous argument, a comparison between 8ml/min (10 wt. %) and 4 ml/min (20 wt. %) feed rates, for which the same amount of solute was fed into plasma per unit time, is useful. On one hand, these two coatings have similar coating thicknesses and intercolumnar gaps, as seen in Figures 5.12b and 5.12c. Both $\nu_{\perp}$ and $\nu_{/\!/}$ are similar because of the constant solute feed rate. On the other hand, the coating sprayed with 8 ml/min (10 wt. %) possesses an intracolumnar porosity (4.3 %) nearly twice that (2.5 %) of the coating sprayed with 4 ml/min (20 wt. %).

The intracolumnar porosity is formed by incomplete sintering of lamellae and coalescence of pores. Pores are caused by the random stacking of impinging particles [118]. When the

impinging agglomerated particles possess various morphologies, the stacked coatings may show different intracolumnar porosities. The evolution process from solution droplets to solid particles includes solvent evaporation/combustion and solute precipitation/pyrolysis. When the solvent contains organics, its combustion in presence of oxygen releases heat and gases. Thus, the formed solid agglomerated particles are characterized by a loose and porous structure [93]. In this work, the solvent consists in a mixture of ethanol and acetic acid. When adopting a feed rate of 8ml/min (10 wt.%), the same amount of solute but twice the solvent was fed in the plasma compared to a feed rate of 4 ml/min (20 wt. %). In the former case, the combustion of a large amount of solvent resulted in porous agglomerated particles. Accordingly, coating sprayed with a feed rate of 8 ml/min (10 wt. %) presented the highest intracolumnar porosity.

The columnar structure evolution process is summarized in Figure 5.13. Increasing the precursor concentration leads to a compact columnar structure with thin columns, and it simultaneously reduces the inter and intracolumnar porosities. If concentration is further increased, the columnar structure eventually transforms into a DVC one. In contrast, increasing the feed rate offers a compact columnar structure, but with higher intracolumnar porosity. According to the thermal insulation principle [83], the columnar structure (Figure 5.12b) with the lowest intercolumnar porosity (9.9 %) and the largest intracolumnar porosity (4.3 %) has the most potential for TBC application.

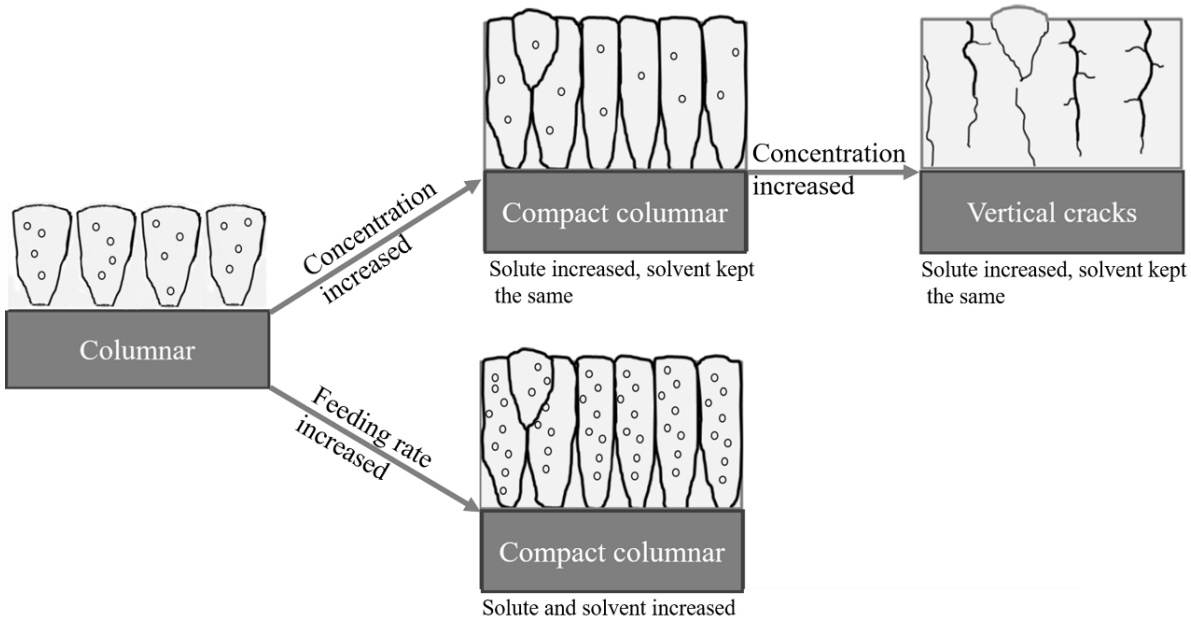

Figure 5.13 Schematic of evolution of columnar structure. The black circles indicate the pores. Building on the idea of N. Curry et al. [110] that was limited to particle size

5.4.4 Phase structure of columnar coating

This section focusses on the phase structure of the coatings deposited at a 34 mm spraying distance (which possess the columnar structure), as seen in Figure 5.14. No matter the precursor concentration, the coatings are composed of the main phase BMT and of the secondary phases $Ba_3Ta_5O_{15}$ and $BaTa_2O_6$ (Figure 5.14a). The formation mechanisms and influences of the secondary phases were discussed clearly in a previous paper [147]. The increased feed rate leads to a high crystallinity of the BMT phase, as seen in Figure 5.14b. This trend could be attributed to the energy released by the combustion of the organic solvent.

The former discussions have come to the conclusion that the coating deposited with a feed rate of 8 ml/min (10 wt. %) has the optimal columnar structure. However, it is necessary to analyze its composition quantitatively using whole pattern fitting (WPF) and Rietveld refinement method, as seen in Figure 5.15. The ICDD cards and lattice parameters used for hexagonal BMT, cubic BMT and $Ba_3Ta_5O_{15}$ are No. 04-010-5437 (a=5.773 Å, c=7.095 Å, c/a=1.229), No. 04-

014-7667 (a=4.0893 Å) and No.04-012-1438 (a=12.590 Å, c=3.967 Å, c/a=0.315), respectively. The estimated amounts of hexagonal and cubic BMT account for 76.4 wt. % and 17.7 wt. %. As-sprayed coating presents a higher ordering degree (amount of hexagonal phase) which is beneficial to TBC application [147]. The secondary phase $Ba_3Ta_5O_{15}$ is limited to 5.9 wt. %.

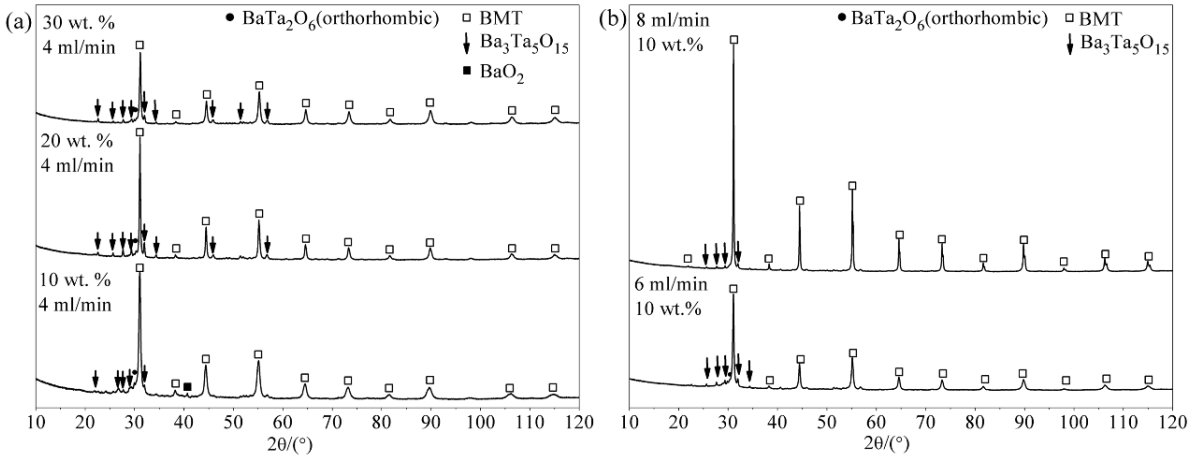

Figure 5.14 XRD patterns of as-sprayed coatings prepared at 34 mm (a) with various precursor concentrations and (b) with different feed rate

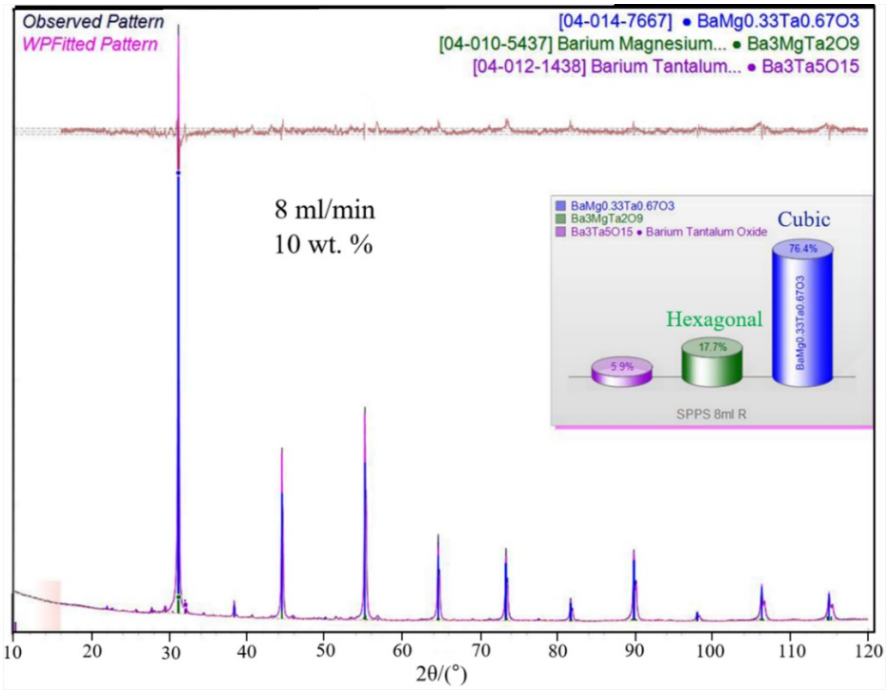

Figure 5.15 Rietveld WPF patterns of as-sprayed BMT coating prepared by precursor with 10 wt. % concentration and 8 ml/min feed rate

5.5 Conclusion

1. BMT coatings with a columnar structure were successfully prepared in this work. It was shown that the most common TBCs structures can be obtained by applying RF SPPS. A short spray distance (34 mm) is a crucial prerequisite for column formation.

2. The columnar structure was built by combining the lateral impingement of small particles and the vertical impingement of large particles. An atomization probe that produces a bimodal droplet size distribution was proven to increase the deposition rate during spraying.

3. It was shown that the substrate roughness affects the coating surface morphology as well as the width of the cauliflower shapes, as expected. A finely sand-blasted substrate (Ra = 1.3 μm) can offer a fine-deposited columnar structure, as well as good bonding.

4. The structural evolution and the optimization of the columnar structure in particular can be achieved by changing the precursor concentration and feed rate. An increased precursor concentration can narrow the column size and produce a compact columnar structure. This process reduces the inter and intracolumnar porosities simultaneously. A vertically cracked structure evolves from the compact columnar one when further increasing the precursor concentration. In contrast, increasing the feed rate offers a compact columnar structure, but with higher intracolumnar porosity.

5. The combination of commercial atomization probe, finely sand-blasted substrate, 10 wt. % concentration and 8 ml/min feed rate led to the desired columnar structure with more intracolumnar porosity (4.3 %), less intercolumnar porosity (9.9 %) and high amount of the BMT phase (94.1 wt. %), which is suitable for industrial applications.

5.6 Supplemental work - Exploration of columnar structure by spraying other liquid precursors

In Chapter 4, the hybrid suspension/solution prepared by nitrate-based salts and nanocrystallized Ta_2O_5 was the most suitable liquid precursor for depositing BMT coating, especially when only considering the phase structure and deposition rate. However, due to the bad solubility of barium nitrate in commonly used solvents (ethanol or weak acid), it was impossible to prepare the transparent solution precursor unless strong acid (nitric acid) was used as the solvent. When choosing acetate-salts and tantalum ethoxide as precursors, a transparent solution could be prepared with environmentally-friendly and safer solvent which is composed of weak acid (acetic acid) and ethanol. Based on the successful preparation of this solution precursor, Chapter 5 presents an interesting columnar evolution process by adopting the RF SPPS method. In order to facilitate the publication of the scientific article and highlight its core, the main part of Chapter 5 did not explain why acetate-based precursor is used to replace nitrate-based one. The supplementary work's purpose is to better understand this transition. For example, we explicit why the hybrid SPS/SPPS cannot be deposit as a columnar structure, why the solution precursor is a prerequisite for obtaining this structure and address a number of other questions.

This section presents some comparative results. Three kinds of solutions and/or suspensions, which are labelled S1, S2 and S3, were prepared to synthesize and deposit BMT coatings, as seen in Table 5.2. S1 is the liquid precursor mentioned in section 5.3.1. To facilitate comparison, S1 is listed here with the other two precursors. Mg nitrate $Mg(NO_3)_2•6H_2O$ (Alfa Aesar, America, 11564) and Ba nitrate $Ba(NO_3)_2$ (Sigma-Aldrich, Germany, 217571) were chosen as Mg and Ba precursors in both conditions S2 and S3. For the precursors S2, water was added to the solvent to fully dissolve $Ba(NO_3)_2$. Moreover, the large amount of water hydrolysed the tantalum ethoxide ($Ta(OC_2H_5)_5$) and produced a gel. The complex chemical reaction is summarized in

formula 5.3. The gelatinous precursors S2 have a homogeneous morphology.

$$Ta_2(OC_2H_5)_{10} + 5\ H_2O \rightarrow Ta_2O_5\ (gel) + 10\ C_2H_5OH \quad (5.3)$$

Finally, nanocrystallized Ta_2O_5 was dispersed in Mg nitrate and Ba nitrate salt solution to prepare the precursors S3. Precursors S2 and S3 are mainly used to compare the effect of the precursor chemistry on the resulting coating microstructure. Schematics of the different precursors are shown in Figure 5.16.

Table 5.2 List of suspension/solution precursors combinations

No	Solute	Solvent	Concentration
S1: Ta ethoxide-acetate-based	$Ta(OC_2H_5)_5$, Ba acetate, Mg acetate	Ethanol : acetic acid (2:1, Vol.)	10 wt. %
S2: Ta ethoxide-nitrate-based	$Ta(OC_2H_5)_5$, Ba nitrate, Mg nitrate	Ethanol : water (1:1, Vol.)	10 wt. %
S3: Ta_2O_5-nitrate-based	Nano-crystalized Ta_2O_5, Ba nitrate, Mg nitrate	Ethanol	10 wt. %

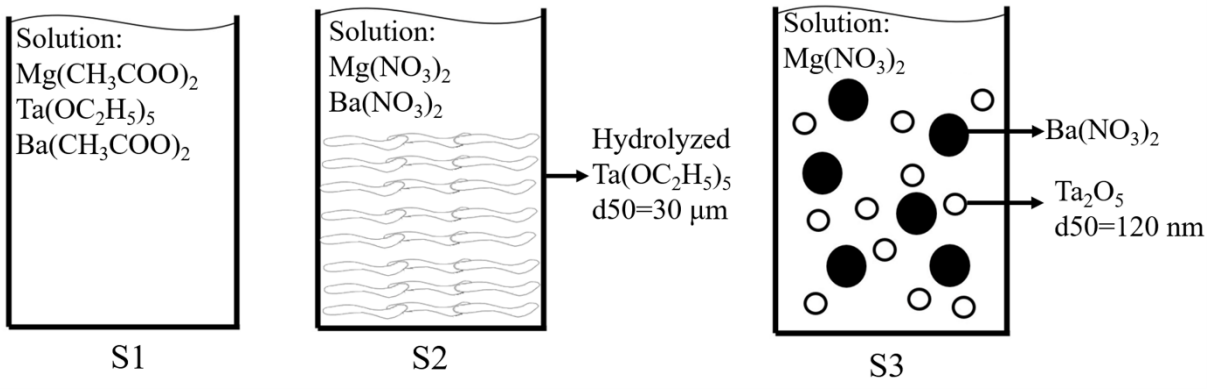

Figure 5.16 Schematics of the liquid precursors

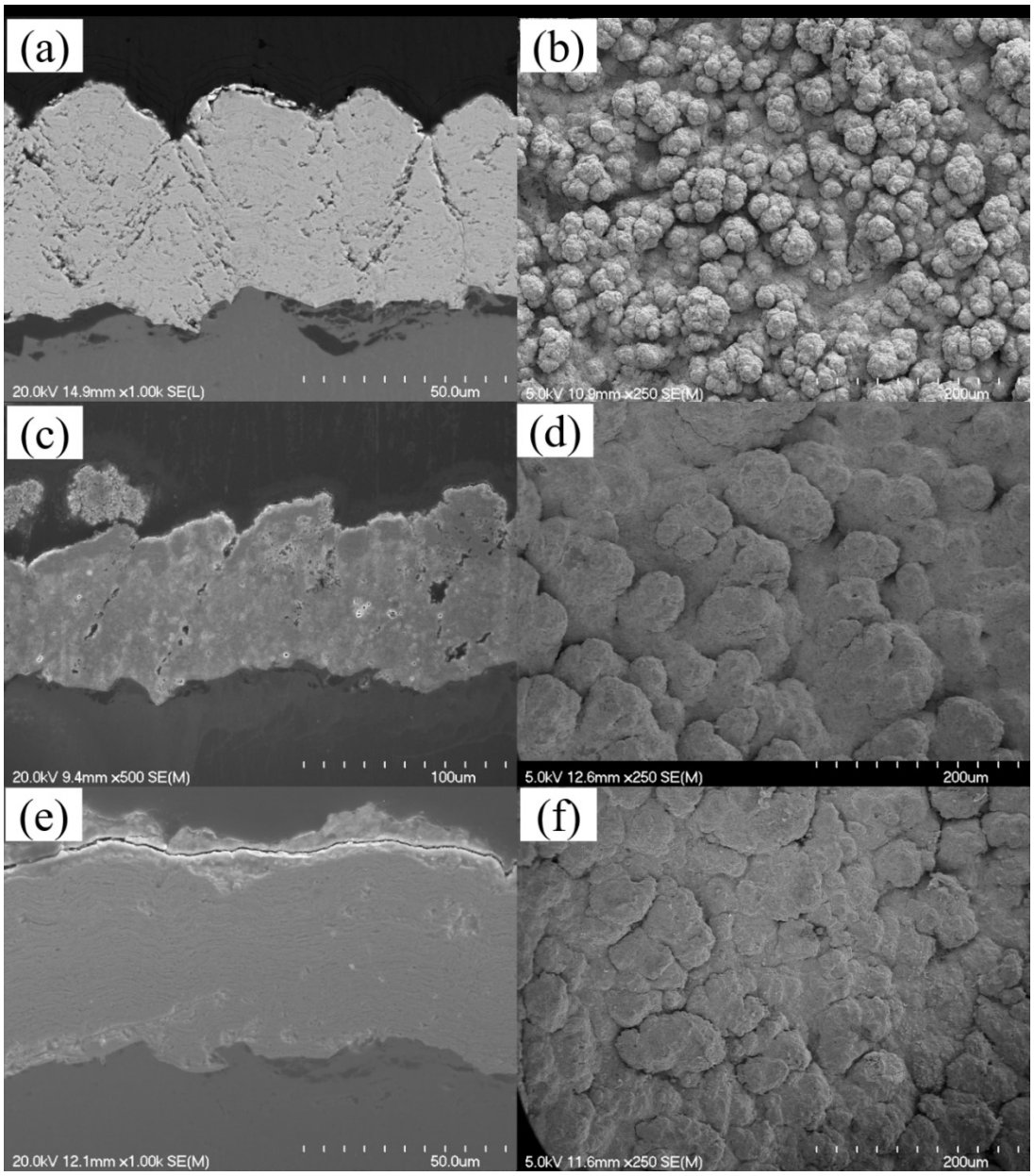

Figure 5.17 SEM micrographs of cross-sections (left side) and surfaces (right side) of coatings sprayed with S1 (a) (b), S2 (c) (d) and S3 (e) (f) at a spray distance of 34 mm

As discussed in sections 5.4.1 and 5.4.2, a short spray distance is a prerequisite for BMT to form a columnar structure with precursor S1. For the purpose of comparison and to test if this observation also applies to precursors with various chemistries, precursors S2 and S3 were sprayed at the same 34 mm spraying distance. Other spraying parameters are identical to the conditions mentioned in section 5.3.3.

Columnar structure sprayed by precursor S1 is listed in Figures 5.17a and 5.17b to make a comparison. The coating sprayed with precursor S2 shows some incomplete vertical cracks instead of columns, as seen in Figures 5.17c, 5.17d. The incomplete vertical cracks can be called pseudo-vertical cracks, which are quite distinct from the segmentation/vertical crack structure observed in the literature [18]. As for the coating sprayed with precursor S3, it shows a dense lamellar structure even at short spray distances, as seen in Figures 5.17e and 5.17f. When comparing the obviously different structures obtained at the same spraying distance (Figures 5.17a, 5.17c, 5.17e), one can conclude that the precursor chemistry has a large influence on the resulting microstructure. To be more specific, the initial Ta state in the precursors, such as Ta ethoxide in S1, hydrolyzed Ta gel in S2 and solid Ta_2O_5 particles in S3, affects the microstructure.

After being fed in the plasma, the liquid precursors evaporated, precipitated and also formed molten droplets. In order to appreciate the differences between the molten droplets of precursors S1, S2 and S3 during spraying, collected lamellae morphologies and diameters are analyzed in Figure 5.18. The lamellae mentioned here means the flat-shaped splats, which may also include some unmolten or re-solidified particles. Because of the high density of molten droplets at the torch outlet, it is hard to collect separate lamellae at 34 mm, even with a single pass coating. The diameter distributions (analyzed by ImageJ) of distinguishable lamellae are shown in Figure 5.18d. Single pass coatings sprayed with S1 (Figure 5.18a) and S3 (Figure 5.18c) have much smaller lamellae diameters, whereas the gelated precursor S2 formed the largest lamellae, as seen in Figures 5.18b and 5.18d.

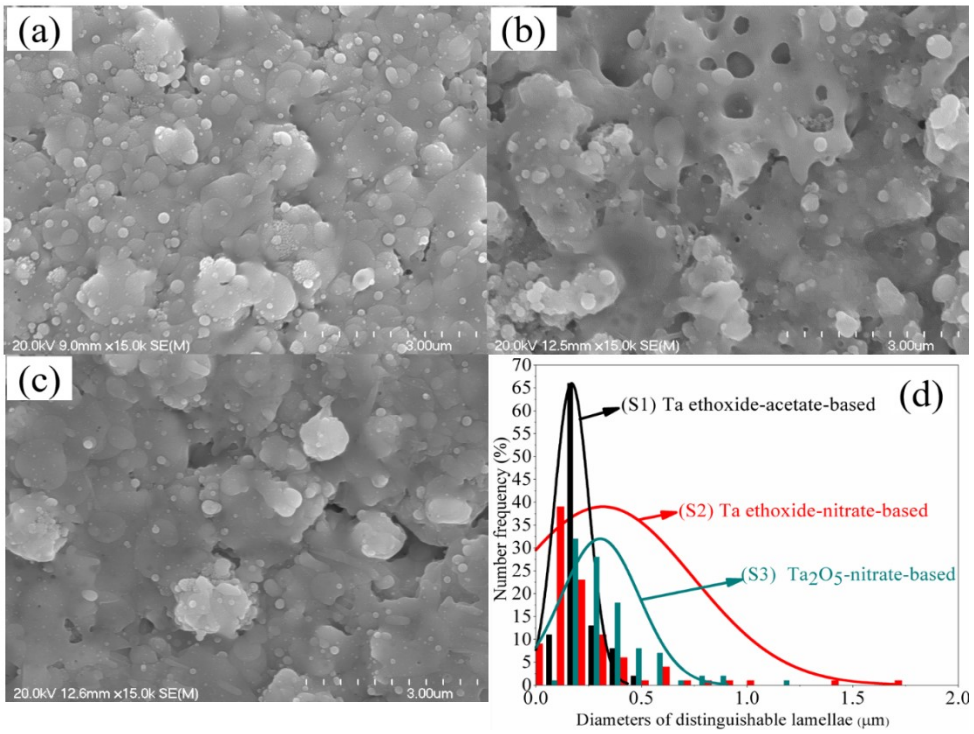

Figure 5.18 SEM micrographs of single pass coatings at 34 mm sprayed with precursors (a) S1, (b) S2 and (c) S3. (d) Distributions of distinguishable lamellae diameters.

Since the lamellae are formed by the impact and the flattening of molten droplets, the final diameter of a lamella is related to the one of a molten droplet. The flattening ratio can be calculated by formula 5.4.

$$\xi = \frac{\text{The average size of lamellae}}{\text{The diameter of an equivalent spherical molten droplet}} \tag{5.4}$$

The flattening ratio for SPPS ($\xi_{SPPS} \approx 3.2$) is usually higher than the one for SPS ($\xi_{SPS} \approx 2.1$) [154]. Due to the different liquid states of the precursors, as indicated in Figure 5.16, the spraying method can be defined as SPPS when adopting precursor S1, and as SPS or hybrid SPS/SPPS when adopting precursors S2 and S3, respectively. Accordingly, the initial state of Ta in the precursors leads to the various molten droplet sizes and, finally, determines the different lamellae and microstructures of as-sprayed coatings. Thus, there would be three kinds of transformation processes from precursors to coatings, as schematically depicted in Figure 5.19.

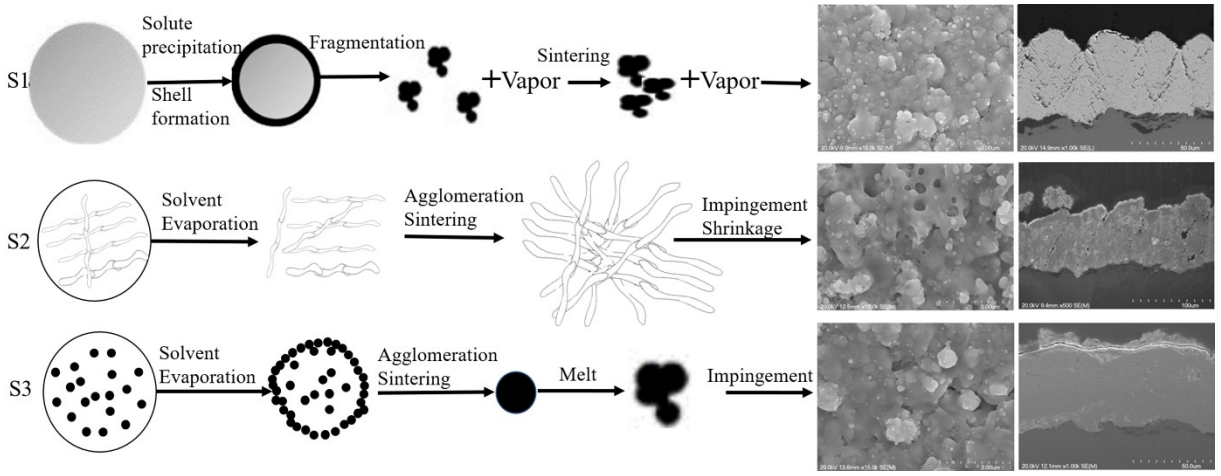

Figure 5.19 Schematic representation of the three transformation processes from droplets to coating

The process for S1 droplets is typical SPPS. The heating effect of the plasma causes solute precipitation on the periphery of the droplet and forms a shell, which is subsequently fragmented into tiny particles owing to a high inner pressure [85]. As opposed to the heating of gelatinous particles (S2) or solid particles (S3), it was easier to form a vapor phase when the plasma heated the liquid droplets in S1. In addition, the smaller fragmented particles in S1 were more likely to follow the gas trajectory [137]. For these reasons, the SPPS process makes the columnar structure possible. Besides, the precursor S2 being a sol-gel, the splats that resulted from the large volume gel may have shrunk and formed the incomplete vertical cracks observed when they cooled down. For precursor S3, the sintering of the solid Ta_2O_5 particles suspended in the solvent results in a dense lamellar structure. In accordance with these observations and arguments, the precursor S1 and SPPS method were considered as the prerequisites in order to obtain a well-distributed columnar structure. The coatings deposited from acetate-based precursor at 140 mm distance (Chapter 4) contained an intermediate product of $BaTaO_6$ due to the insufficient heating. As such, the selective nitrate-based precursor optimised the phase structure. Using precursor S1 (acetate-based) in Chapter 5, we could provide sufficient heating at 34 mm distance and avoid the formation of intermediate phase and facilitate the growth of columns. Therefore, there was no compromise between phase and microstructure.

CHAPTER 6

Distinctive structure and potential application

6.1 Avant-propos

Auteurs et affiliation :

- Huidong Hou : étudiant au doctorat, Université de Sherbrooke, Faculté de génie, Département de génie chimique et de génie biotechnologique.

- Jocelyn Veilleux : professeur agrégé, Université de Sherbrooke, Faculté de génie, Département de génie chimique et de génie biotechnologique.

- François Gitzhofer : professeur titulaire, Université de Sherbrooke, Faculté de génie, Département de génie chimique et de génie biotechnologique.

- Quansheng Wang : professeur, Institut de technologie de Pékin, Faculté de science des matériaux et d'ingénierie.

Date d' acceptation :15 avril 2020

État de l'acception : version finale publiée

Revue : Surface and Coatings Technology

Référence : [H.Hou et al., Surface & Coatings Technology 393 (2020) 125803]

Titre français : Grains verticaux dans une structure colonnaire de barrière thermique de $Ba(Mg_{1/3}Ta_{2/3})O_3$ déposée par projection par plasma de précurseurs en solution.

Contribution au document:

The paper presents a distinctive TBC structure with vertical and dendrite grains growing inside columns, which has never been noticed before in the field of plasma spray. The elements distribution and morphology of this structure are discussed clearly. In addition, its formation mechanism is explained from measured plasma and substrate temperatures. Finally, a potential application of BMT coatings is proposed in this paper.

Résumé français :

Les revêtements de barrière thermique (TBC) à structure lamellaire sont plus sensibles à l'érosion que les céramiques entièrement denses et les revêtements déposés en phase vapeur par faisceau d'électrons (EB-PVD). Cet article présente une structure distinctive de $Ba(Mg_{1}/_{3}Ta_{2/3})O_3$ (BMT) avec un aspect orienté en colonne et une nature de grain verticale, qui a été déposée par projection plasma plutôt que par EB-PVD. En effet, un procédé de projection par plasma radiofréquence d'un précurseur en solution a été adopté pour le dépôt du revêtement. La morphologie et la composition élémentaire des grains verticaux sont d'abord analysées. À l'aide de la spectroscopie d'émission optique (OES), le mécanisme de formation des grains verticaux est examiné en détail. En outre, un nouveau système TBC conçu pour l'alliage de niobium est proposé dans cet article. En raison de son coefficient de dilatation thermique élevé et de la structure unique des grains verticaux, le BMT est considéré comme le matériau d'isolation le plus prometteur dans ce système TBC.

Mots-clés : BMT, RF SPPS, Grains verticaux, Gradient de température, Revêtements de barrière thermique.

Title: Vertical Grain and Columnar Structured $Ba(Mg_{1/3}Ta_{2/3})O_3$ Thermal Barrier Coating Deposited by Solution Precursor Plasma Spray

Abstract: Thermal barrier coatings (TBC) with a lamellar structure are more susceptible to erosion than fully dense ceramics and electron beam physical vapor deposited (EB-PVD) coatings. This paper presents a distinctive structure of $Ba(Mg_{1/3}Ta_{2/3})O_3$ (BMT) with a columnar-oriented appearance and vertical grain nature, which was deposited by plasma spray rather than EB-PVD. Indeed, a radio frequency solution precursor plasma spray (RF SPPS) process was adopted for the coating deposition. The morphology and elemental composition of the vertical grains are analysed first. With the assistance of optical emission spectroscopy (OES), the formation mechanism of the vertical grains is discussed in detail. In addition, a new TBC system designed for niobium alloy is proposed in this paper. Owing to its high thermal expansion coefficient and unique vertical grain structure, BMT has been considered as the most promising insulation material candidate in this TBC system.

Keywords: BMT， RF SPPS, Vertical grains, Large temperature gradient, Thermal barrier coatings.

6.2 Introduction

Thermal barrier coating (TBC) technology is widely used to protect underneath metallic components against the hot gases in turbine engines. The state-of-the-art processes to manufacture TBCs are air plasma spray (APS) and electron beam physical vapor deposition (EB-PVD) [155]. The coatings deposited by APS normally have a lamellar structure and lower thermal conductivity, and are widely used in land based gas turbine and static components such as combustor and afterburners [109]. Some dynamic components, for example the turbine blade of aero engine, rotate at high speed under high temperatures. In such conditions, the centrifugal

force is large enough to induce creep on dynamic components. As such, the separated columns and intercolumnar gaps, typically built by EB-PVD, are required to accommodate the creep. This is the main reason why EB-PVD is employed on the jet engine turbine blades [101]. Besides the negative effect of centrifugal force, the hot gases which normally mingle with foreign objects, for example calcium magnesium aluminosilicate (CMAS), impinge on the turbine blade surface with varied angles and deteriorate the components. The severe erosive damage of TBC coating becomes a non-negligible factor affecting lifetime, in addition to thermal cycling and thermal grown oxide (TGO) [108].

Many investigations have already demonstrated that EB-PVD TBCs possess significantly better erosion resistance compared to their APS counterparts [105-107]. Since the APS lamellar coatings are characterized by stacking of lamellae/splats and a horizontal micro-cracks network, the impact of erodent causes rapid cracks propagation along the splats boundaries and neighbouring lamellae, inducing the spallation of whole splats [106, 156, 157]. Unlike the crack-like feature of APS coatings, EB-PVD coatings present a single crystal column without inner horizontal crack. The impact of erodent only causes cracks near the surface (top 20 μm) of a single column, which propagate until they reach the inter-columnar gaps [105-107]. Consequently, the most advanced TBCs for aircraft engine are, to this day, normally deposited by EB-PVD [109]. However, the high investment and complex operating conditions of EB-PVD motivate the development of alternative methods. Suspension plasma spray (SPS) [158] and solution precursor plasma spray (SPPS) [8] imitate the columnar-oriented structure and combine the coatings benefit of both APS and EB-PVD. However, the erosion resistance of SPS/SPPS coatings is rarely reported in the literature [101, 108, 159] and it is unclear how it compares to that of APS or EB-PVD. Some methods have been proposed to increase the erosion resistance of SPS/SPPS coating, such as incorporating solid solution into yttria-stabilized zirconia (7YSZ) [160], applying a dense top layer [161] and adopting a new coating material [162]. However, the essence of SPS/SPPS coating formation mechanism, the stacking of splat and/or cluster,

remains the same [154]: there is still a large amount of interfaces between lamellae with weak bonding. Thus, the erosion resistance improvement effect is not optimistic.

Apart from the dominant TBC material 6-8 wt.% yttria-stabilized zirconia (YSZ), a large number of TBC candidates have been proposed for decades, such as Yb_2O_3 and Gd_2O_3 doped strontium zirconate ($SrZrO_3$) [70], yttrium aluminium garnet ($Y_3Al_5O_{12}$; YAG) [73], lanthanum cerium oxide ($La_2Ce_2O_7$; LCO) [163] and barium magnesium tantalite ($Ba(Mg_{1/3}Ta_{2/3})O_3$; BMT) [6, 147]. Considering its high melting temperature [64] and low thermal conductivity at high temperature [5], BMT was chosen as the candidate material in this paper. It is deposited by means of a radio-frequency inductively-coupled plasma (RF ICP) torch. As opposed to the conventional radial feedstock injection used with most direct current (DC) plasma torches, feedstock is fed axially in a RF ICP torch owing to its unique design [89]. In addition, a RF ICP torch has a long residence time, which is highly suitable for refractive materials such as BMT. Finally, instead of adopting 45-125 μm powder BMT as feedstock in APS [4], RF SPPS feeds solution precursors directly into the core of the plasma jet to fabricate advanced coatings with unique microstructural feature [164].

Following our previous reports on BMT deposition by means of RF ICP, where precursors and spraying parameters have been optimized for phase and microstructural control [147, 164], this paper presents a new BMT coating microstructure deposited by RF SPPS. The vertical grains of this structure are distinct features that depart from the ones obtained by DC SPS/SPPS and EB-PVD processes. The formation mechanism of the vertical grains is discussed as a function of the processing parameters. Considering its high melting temperature, this paper proposes a new application for BMT, namely applying BMT as a thermal insulation coating material for niobium alloy, which is recognized as the next-generation structural material for aerospace and a substitute for nickel alloy at higher temperatures [165]. Referring to the results obtained in previous work [164], three representative parameters related to precursor feed rate and

atomization, spraying distance and surface roughness are chosen to deposit BMT on niobium alloy and to assess feasibility.

6.3 Experimental Procedures

6.3.1 Precursor formulation

Tantalum ethoxide $Ta(OC_2H_5)_5$ (Henan Tianfu Chemical Co. Ltd, China), barium acetate $Ba(CH_3COO)_2$ (Sigma-Aldrich, Germany, 32305) and hydrated magnesium acetate $Mg(CH_3COO)_2 \bullet 4H_2O$ (Fisher BioReagents, India, BP215-500) were chosen as precursors of Ta, Ba and Mg, respectively. A mixed solvent, ethanol and acetic acid with a volume ratio of 2:1, was chosen to dissolve the precursors and prepare a transparent solution. A total solid content of 10 wt. % was used in most cases, unless otherwise specified. Twice the stoichiometric amount of Mg was used when preparing the solution precursor to compensate for preferential losses upon plasma spraying [147].

6.3.2 Coating preparation

A radio frequency inductively-coupled plasma (RF ICP) torch (PL-50, Tekna Plasma Systems Inc., Sherbrooke, Canada) was used to spray BMT precursors, as depicted in Figure 6.1. A 25-mm converging nozzle was installed at the outlet of the torch in order to increase the plasma jet velocity. Titanium alloy (Ti-6Al-4V) buttons, with a diameter of 12.6 mm and a thickness of 2 mm, were used as substrates for the deposition of single layer BMT coating, are used as a reference in this paper. A k-type thermocouple (TJ36-NNXL-116U-36, OMEGA, USA) was in contact with the substrate (see Figure 6.1) to measure its temperature during the whole spraying process, including the pre-heating, spraying and cooling steps. Optical emission spectroscopy (OES) (IsoPlane SCT 320 spectrograph, Princeton Instruments, USA) was installed to observe the atomic and molecular emission lines, enabling the drawing of complete temperature and

species mapping of the plasma jet. The detailed manipulations and data treatment processes were described in the work of J. Menneveux and J. Veilleux [166]. The spraying parameters are summarized in Table 6.1.

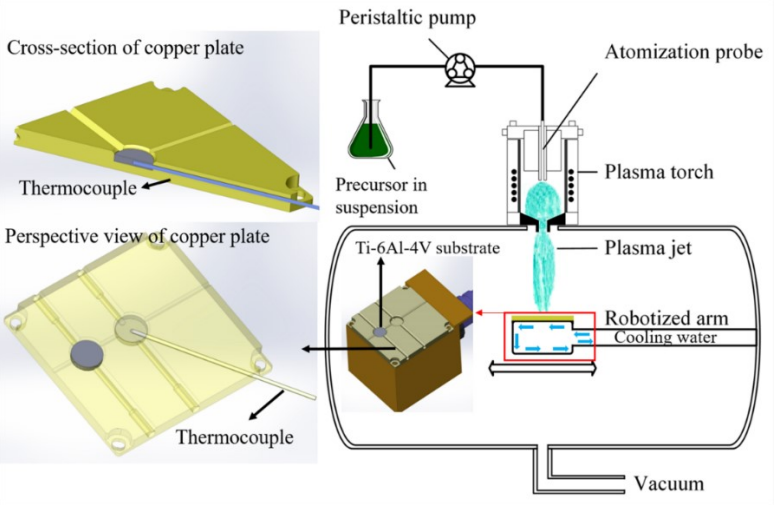

Figure 6.1 Schematic illustration of reactor for BMT coating deposition

Table 6.1 Plasma parameters for BMT coating deposition

Sheath gas(Ar)	6 slpm
Sheath gas (O_2)	63 slpm
Central gas (Ar)	23 slpm
Carrier gas (Ar)	11 slpm
Reactor pressure	15 kPa
Plasma power	50 kW
Feed rate	4/8 ml/min
Standoff distance	34 mm
Translational speed	50 mm/s
Pre-heating cycles	20 loops (60 s)
Deposition cycles	80 loops (240 s)

Niobium alloy (Nb-5W-2Mo-1Zr, wt. %, Nb521) (Ningxia Orient Tantalum Industry Co., Ltd, China) was selected to carry out the real application investigation. Nb521 substrates were grit-blasted by corundum particles (20 mesh) and were blown with compressed air prior to depositing the bond coat by APS. Before depositing BMT, a bonding layer of $Mo(Si, Al)_2$ was deposited using a 5500 Model APS system (Praxair- TAFA, USA) with a SG-100 plasma torch. The main parameters of APS and $Mo(Si, Al)_2$ feedstock preparation were described in previous work [121]. After the bond coat deposition, abrasive paper (180 grit) was used to smooth the coating surface, which was proven to later reduce the topcoat intercolumnar gaps [164]. The samples were then cleaned using acetone and ethanol, in an ultrasonic bath. Finally, three sets of experiments were chosen to deposit the BMT thermal insulation layer above bonding layer, as indicated in Table 6.2.

Table 6.2 Experimental sets for BMT thermal insulation layer

	Preparation method of bonding layer	Surface roughness of bonding layer	Feeding rate during RF SPPS
P1	APS sprayed $Mo(Si, Al)_2$	Ra=6.4 μm	4 ml/min
P2	APS sprayed $Mo(Si, Al)_2$	Ra=6.4 μm	8 ml/min
P3	APS sprayed $Mo(Si, Al)_2$ followed by paper-sanded	Ra=2.1 μm	8 ml/min

6.3.3 Material characterizations

The microstructure and morphology of the deposited coatings were analyzed by scanning electron microscopy (SEM) (S-3000N, Hitachi, Japan). Another SEM (SU8230, Hitachi, Japan), equipped with a low angle backscattered electron (LA-BSE) detector, was used to observe the nature of vertical grain. The phase structure was analyzed by X-ray diffraction (XRD) (X'pert PRO PHILIPS, Netherlands). The thermal expansion coefficient (TEC) of densified samples

was measured from room temperature to 1200 °C in an argon atmosphere by using a dilatometer (DIL-402C, Netzsch, Germany). The TEC samples were prepared in accordance with the method mentioned in Jarligo et al. work [5]. The surface roughness of the coating was measured with a Surftest SJ-210 (Mitutoyo, Japan). The coatings' porosity was calculated with an open source software ImageJ (National Institutes of Health, USA), for which the algorithm was described in previous work [164].

6.4 Results and Discussion

6.4.1 Vertical grain microstructure

The columnar structure prepared with DC SPS/SPPS shows an appearance similar to that of EB-PVD, but still has a distinctive, lamellae nature (DC SPS/SPPS) as opposed to vertical grains (EB-PVD). As for columnar BMT coatings sprayed by RF SPPS, their crystallization and growth phenomena are investigated in details below. When spraying a 10 wt. % concentration precursor with a feed rate of 8 ml/min or spraying a 20 wt.% one with 4 ml/min feed rate, as-sprayed coatings all present the columnar structure with high quality: narrow columns having low inter-columnar and high intra-columnar porosities, as seen in Figure 6.2.

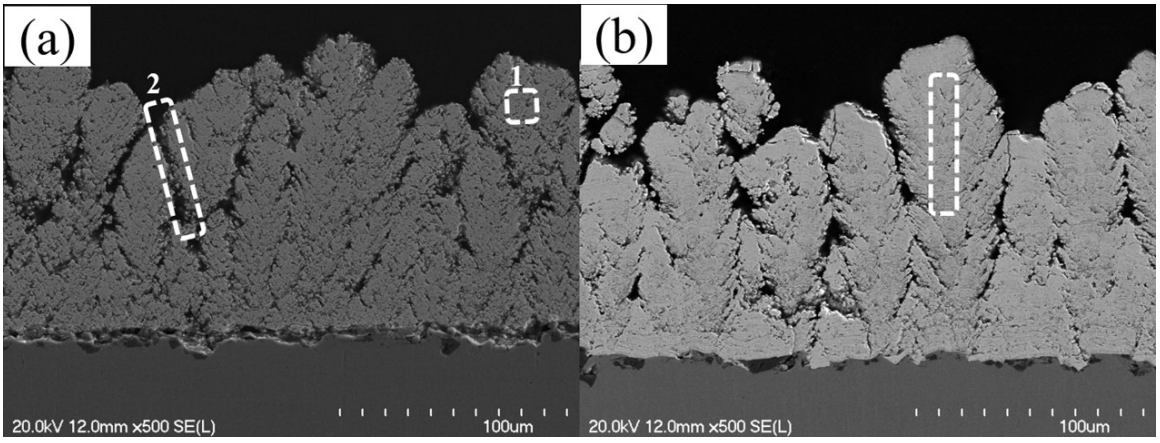

Figure 6.2 The typical columnar structure coatings sprayed by parameters of 10 wt.%, 8 ml/min (a) and 20 wt. %, 4 ml/min (b)

Since BMT is an electrical insulator, a metallization (Au and Pd film) process was applied to cross-section sample to facilitate the observation of microstructures and pores. In order to better observe the nature of the grain growth, the metallization layer was partially removed to expose the vertical grains, while a residual part was needed to maintain electrical conduction. The LA-BSE signal provides topographical and compositional information simultaneously. The details of some typical regions in Figure 6.2a, intracolumnar (region 1) and columnar periphery (region 2), are magnified with LA-BSE pictures, as shown in Figures 6.3a, 6.3b and Figures 6.3c, 6.3d, respectively.

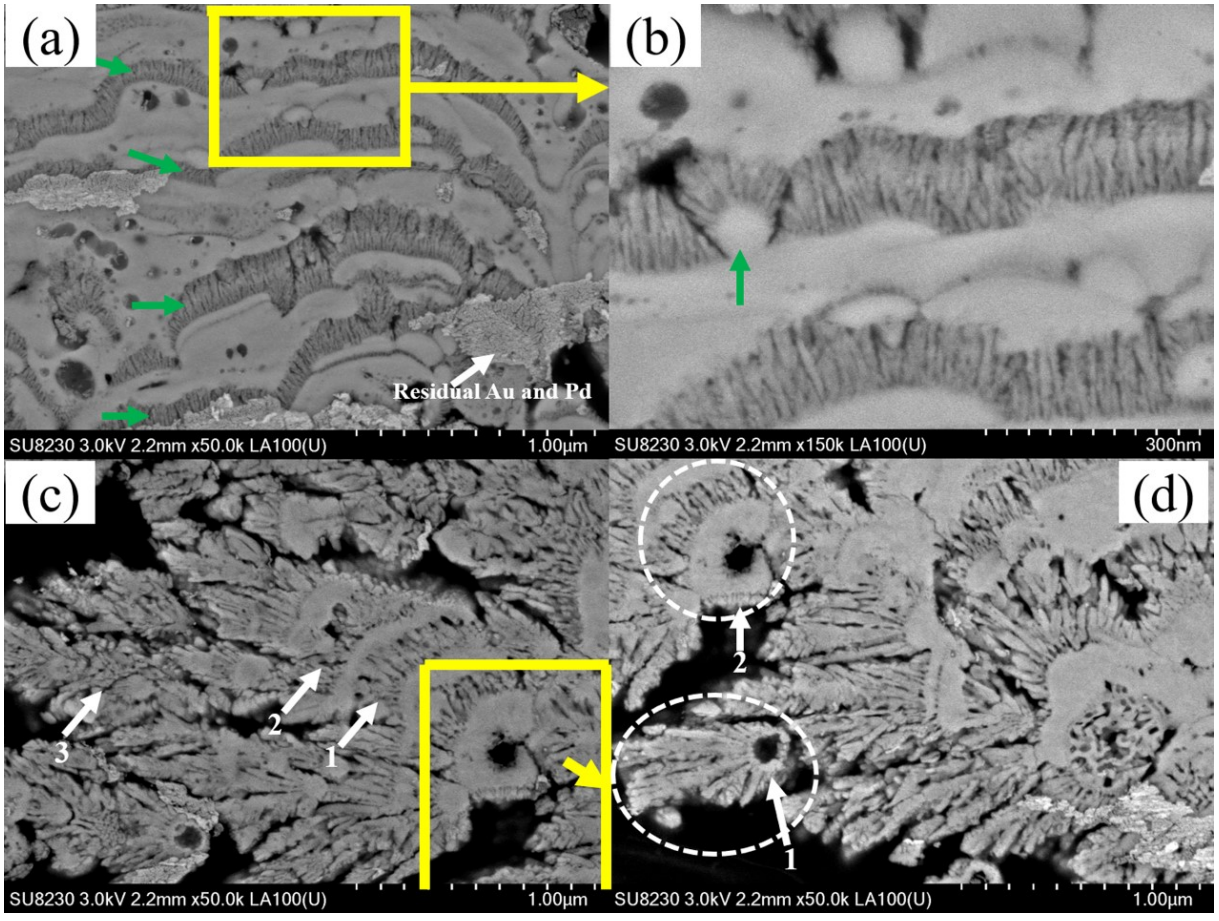

Figure 6.3 LA-BSE pictures of intracolumnar (a) (b) and columnar periphery (c) (d) regions

The intracolumnar structure is built by an alternation of dense lamellae and vertical grains, as indicated by the green arrows in Figure 6.3a. The thickness of dense lamellae varied from 90 to

200 nm. The vertical grains possess a finer structure, with less than 20 nm in diameter and an average height of 150 nm, as seen in the magnified region (Figure 6.3b). It is hypothesized that the growth of vertical grains, mainly from vapor phase deposition, is hindered by the impingement of a newly coming droplet, which rapidly forms a dense lamella.

In fact, at the periphery of a columnar structure (Figure 6.3c), the columns also grew by an alternation of dense lamellae and grains (arrow #1 and #2), the lamellae hindering the growth of the grains. However, owing to the shadowing effect that blocked newly incoming droplets, a third group of free growing grains (arrow # 3) were allowed to grow much longer without the hindering of lamellae. The zoomed region in Figure 6.3d, which shows two hollow circular lamellae, also supports the hypothesis. These structures are resulting from processes occurring in-flight in SPPS, with the precipitation of low and high permeable shells [167]. The circle 1 possesses a small lamella volume while connecting to long grains. In contrast, the circle 2 possesses a large lamella volume with short grains. This comparison implies that a given droplet could form dense lamella from which vertical grains are growing, with different volumes. In other words, the vertical grains nucleate and grow from the lamella. A similar phenomenon is also pointed by the arrow in Figure 6.3b. At the periphery of a columnar structure, one observes the formation of very loosely held columnar grains, which might affect the thermo-mechanical performance of the intended TBC material.

Figure 6.4 shows an energy-dispersive X-ray spectroscopy (EDS) elemental mapping of a typical region. Numbers 1-2 mark the vertical grain zones and numbers 3-7 mark the zones of dense lamellae. The vertical grain zones (1-2) are Mg-rich, Ta-depleted regions, as indicated in Figures 6.4c, 6.4d. The lamellae zones (3-5) have higher Ta content, but are depleted in Mg and Ba. Other lamellae zones (6-8) are not Ta-rich regions. Through all the selected regions, O content (Figure 6.4e) is relatively homogeneous. Table 6.3 qualitatively summarize the elemental distribution within the various regions studied. A detailed Rietveld analysis of the

diffractogram of the deposited BMT coating showed the following content: 76.4 % cubic BMT, 17.7 % hexagonal BMT and 5.9 % $Ba_3Ta_5O_{15}$ [164].

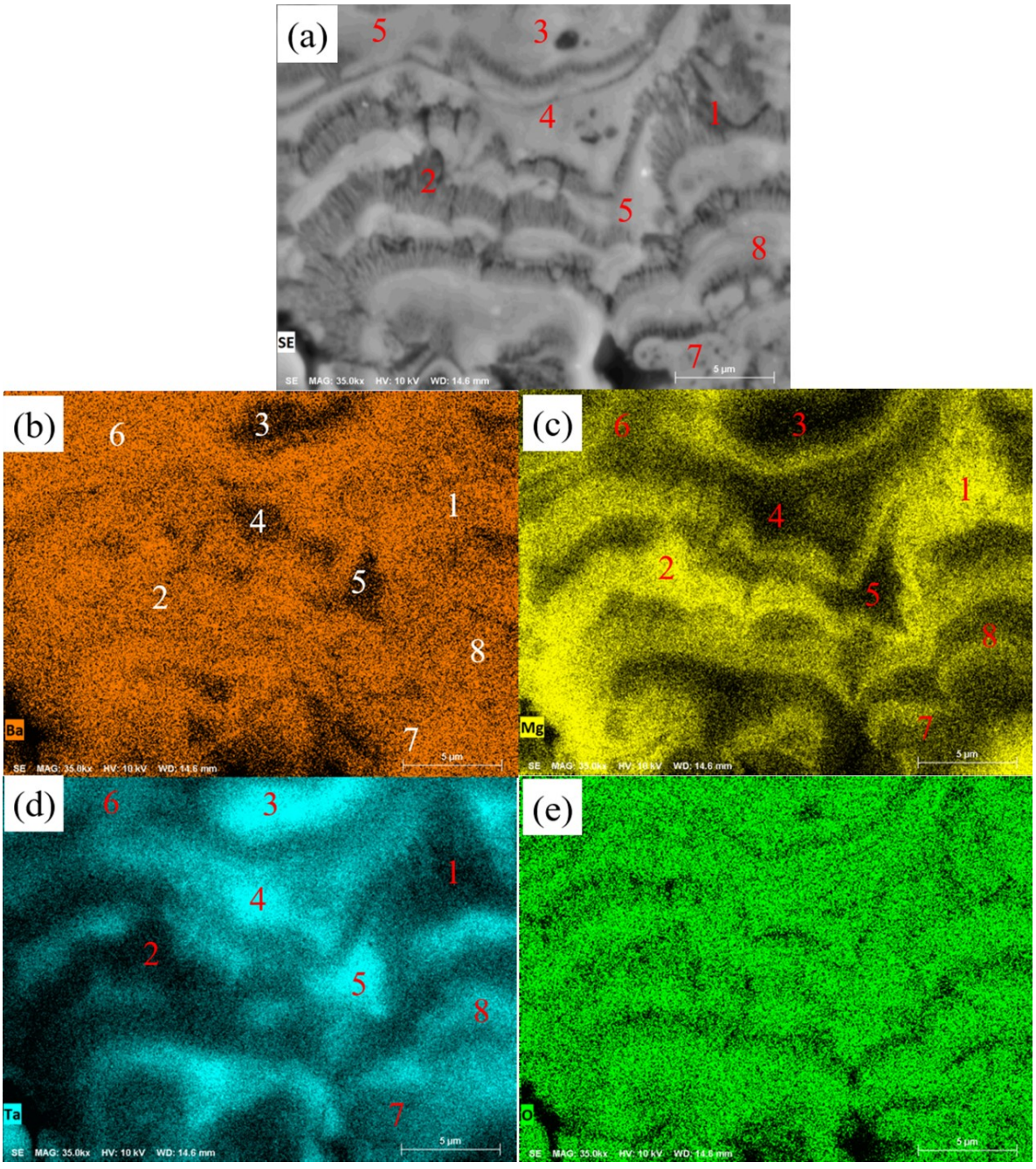

Figure 6.4 EDS element mapping of the as-sprayed coating. (a) is the image of testing region. (b), (c), (d), (e) show the maps of major elements Ba, Mg, Ta and O, respectively

Table 6.3 Elemental distribution within different zone as marked in Figure 6.4, symbol UN means unchanged content

	Vertical grain		Dense lamellae					
zone	1	2	3	4	5	6	7	8
Ba	UN	UN	Poor	Poor	Poor	UN	UN	UN
Mg	Rich	Rich	Poor	Poor	Poor	UN	UN	UN
Ta	Poor	Poor	Rich	Rich	Rich	UN	UN	UN

According to the ternary phase diagram of BaO-MgO-Ta_2O_5 [168] (as seen in Figure 6.5), the BMT phase extends conspicuously along the BMT-$Ba_3Ta_2O_8$, BMT-$Ba_4Ta_2O_9$, BMT-$Ba_5Ta_4O_{15}$, BMT-$Mg_4Ta_2O_9$ and BMT-MgO tie lines. The green line constitutes an estimated boundary of the single-phase BMT region (dumbbell shape), which covers a large MgO-rich and MgO-depleted range. When compared to the BMT chemical formula ($Ba_3MgTa_2O_9$), $Ba_3Ta_5O_{15}$ can be regarded as a Ba-depleted, Mg-depleted and Ta-rich phase. Combining the previous analysis with the results shown in Figure 6.4 and Table 6.3, some lamellae (3-5) can be considered as $Ba_3Ta_5O_{15}$, while other lamellae (6-8) and vertical grains (1-2) are closer to the BMT phase, which includes a large MgO-rich and MgO-depleted range.

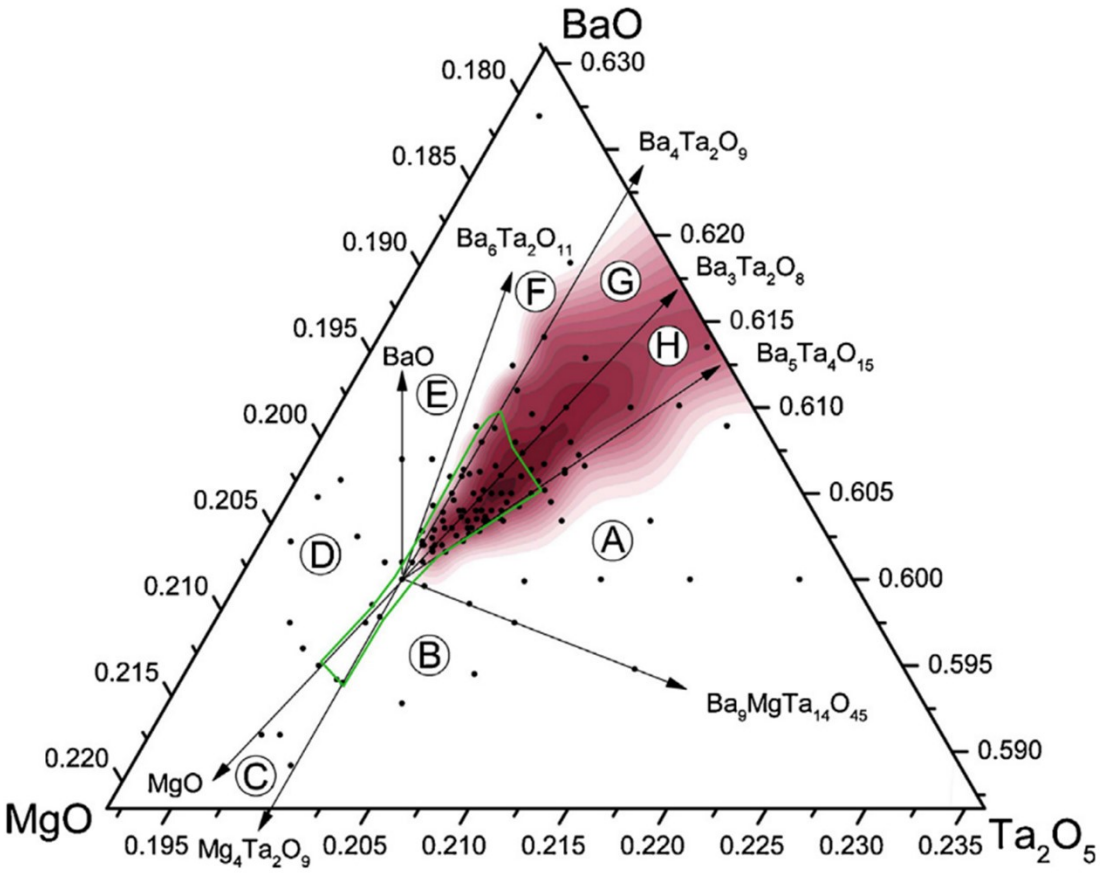

Figure 6.5 Part of the BaO-MgO-Ta_2O_5 phase diagram in the vicinity of BMT phase. The green line indicates an approximate boundary of the single-phase BMT. Reprinted from Journal of the European Ceramic Society, Vol 34, No 7, T. Kolodiazhnyi, Origin of extrinsic dielectric loss in 1:2 ordered, single-phase $BaMg_{1/3}Ta_{2/3}O_3$, p. 1741-1753, Copyright (2014), with permission from Elsevier

The vertical grains structure is also widely observed in other columnar coatings (Figure 6.2b). After partially removing the Au-Pd film, the morphology consisting in an alternation of dense lamellae and vertical grains was revealed, as shown in Figure 6.6a. Because of the lamellae hindering, the growth of vertical grains was restrained to a limited height. The short vertical grains present a straight needle-like shape (Figure 6.6b) or a curve laminaria-like shape (Figure 6.6c). However, when the short vertical grains grew longer, they broke the “limit” imposed by the subsequent lamellae and formed a dendrite shape, as seen in Figure 6.6d.

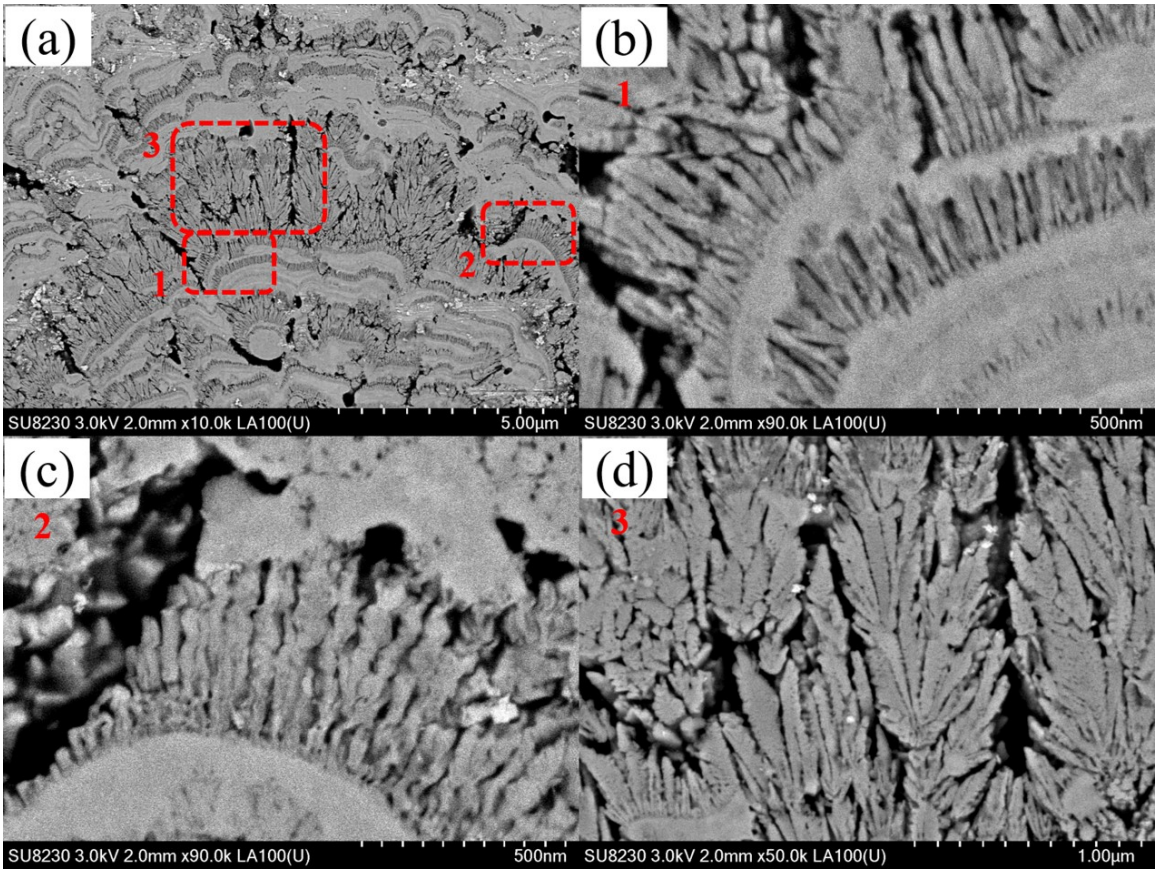

Figure 6.6 LA-BSE pictures of coating sprayed with 20 wt. % precursor and 4 ml/min feed rate. (b), (c), (d) show the morphologies of magnified zones 1, 2 and 3 marked in (a), respectively

6.4.2 Formation mechanism of vertical grain

Opposite to the vertical grain growth in a long-term isothermal oxidation process [169], vertical grains grew instantaneously during spraying in this work. In the field of thermal spray, the cooling behavior of splats could be considered as a directional solidification. The growth of grain follows a preferred direction which is parallel to the direction of heat flux and driven by temperature gradients [170]. For example, Y. Wei et al. sprayed TiO_2 on the surface of rutile TiO_2 and α-Al_2O_3. A group of equiaxial columnar grains formed whose growth direction is perpendicular to the substrate [171]. In M. Fukumoto et al. work, molten metal droplet fell freely on a substrate. Depending on the substrate temperature, isotropic fine or coarse vertical grains were formed [172]. B. Kang et al. proved that during the solidification process of a splat, the

heat transfer within the splat propagated in the axial direction, which is also that of grain growth [173]. Thus, several studies showed that the processes of nucleation and grain growth are attributed to the fast cooling of high temperature molten droplets touching a cold substrate, making it a key mechanism determining the growth of vertical grains.

That being said, there is another key point that could explain the growth of vertical grains for coatings sprayed by SPPS. Indeed, the microstructure shown in Figure 6.3 and Figure 6.6 shows an alternation between lamellae and vertical grains. Lamellae are likely resulting from solute precursors that have precipitated and molten before impingement on the substrate, whereas the vertical grains have a structure similar to what is obtained from plasma-spray physical vapor deposition (PS-PVD) [99]. One can then hypothesize that the vertical grains grew from the vapor phase until another molten droplet hindered their growth. This hypothesis is further supported by the observation of optical emission from the elemental precursors (Ba, Mg and Ta), on maps similar to that shown in Figure 6.7.

Limited by experimental conditions and deposition chamber geometry, the temperature of molten droplets and of the substrate surface cannot be monitored in this work. However, under local thermodynamic equilibrium, the excitation electron temperature can approximately reflect the plasma temperature during the actual spraying process [166]. OES was thus adopted here to draw the excitation temperature mapping of Ba, as seen in Figure 6.7.

In addition, the internal temperature of the substrates was measured during spraying with a thermocouple, as seen in Figure 6.8. This picture shows the temperature trends during the whole spraying process, including pre-heating, temperature rise due to the spraying process, temperature equilibrium upon continuous spraying and cooling. Combining Figure 6.7 and Figure 6.8, a simple temperature comparison between the plasma and the substrate was made, as presented in Table 6.4.

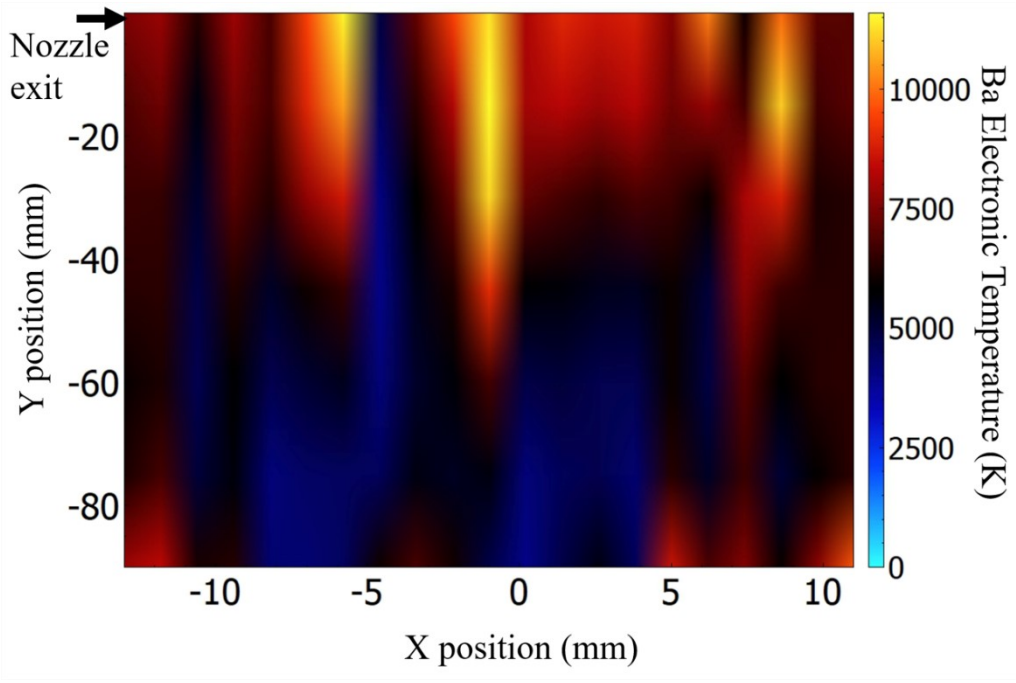

Figure 6.7 Excitation temperature mapping of Ba. The plasma parameters are identical to the actual spraying conditions

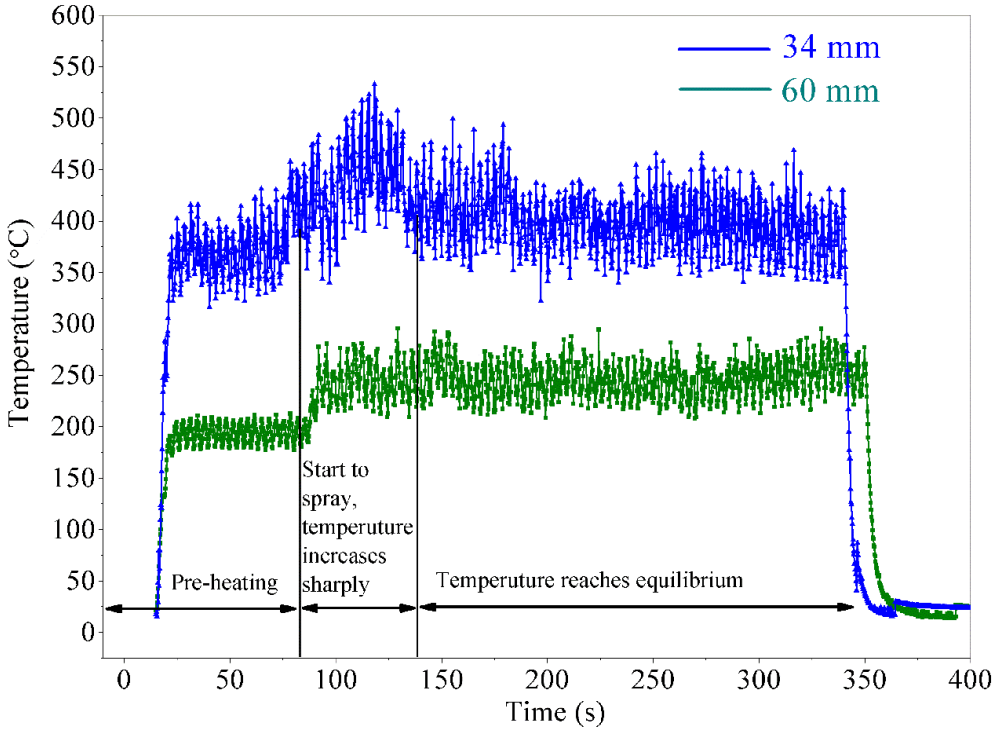

Figure 6.8 Curves of substrate temperature trends during coating deposition at different spraying distances.

Table 6.4 Temperature comparation of substrate center and plasma at different spraying distance

Spray distance (mm)	Substrate temperature (K)	Plasma temperature (K)
34	673	7500-10000
60	523	5000-7500
80	Not measured	2500-5000

The shorter the spray distance, the larger the temperature difference between the plasma and the substrate. At a spray distance of 34 mm (Y axis -34 mm in Figure 6.7), the molten droplets were heated by a 7500-10000 K plasma. Then, the droplet impinged on the 400 °C water-cooled substrate and formed a splat. Rapid solidification and nucleation occurred on the bottom side of the droplet that first contacted the substrate, while the side far from the substrate was still under high-temperature plasma heating and immersed in a vapor cloud. When there is an extremely high temperature gradient along the normal direction between the plasma and the coating, as well as between the coating and the substrate, the molten droplets will solidify from the bottom along the direction of this temperature gradient and form vertical grains that can then act as nucleation sites for growth from vapor phase. The morphology of unflatten droplets, as pointed by green arrow in Figure 6.3b, strongly supports this process.

The formation mechanism of vertical grains is illustrated in Figure 6.9. Both DC SPPS and RF SPPS could obtain a coating with columnar structure. When applying DC SPPS, the spray distance is usually longer than the length of the plasma jet [150]. The molten or semi-molten droplets impinge on the substrate without post direct heating by the plasma. During the formation process, the lower temperature gradient between the upper and bottom side of splat results in an ordinary lamellar stacking structure (grey color). In addition, little or no vapor is formed. However, when applying RF SPPS to work at reduced pressure (e.g. 15 kPa), the length of the plasma jet reaches 70 mm, which is longer than the spray distance. The substrate upper surface (34 mm away from torch) is thus heated by the plasma and exposed to vapor, while its periphery and underside are cooled by circulating water. Consequently, a large temperature

gradient exists within the splat. Precursor that have precipitated and melted forms the lamellae (grey color) while the vapor deposition result in the growth of vertical grains (green color). In this way, droplets are constantly impinging on previously solidified layers, and repeating the process leads to the alternative stacking of vertical grains and dense lamellae. If the temperature gradient raises again, the vapor growth is prolonged which forms dendrite-shapes and finally break through the usual limit of lamellae, as illustrated by the ideal BMT coating in Figure 6.9. If the columnar structure deposited by RF SPPS could possess fully vertical grains throughout the whole coating thickness, then RF SPPS would likely be an interesting alternative to replace the high-cost EB-PVD and be used in the dynamic component field. That being said, thermo-mechanical tests are still needed to ensure a satisfying cycling life of RF SPPS deposited BMT coatings.

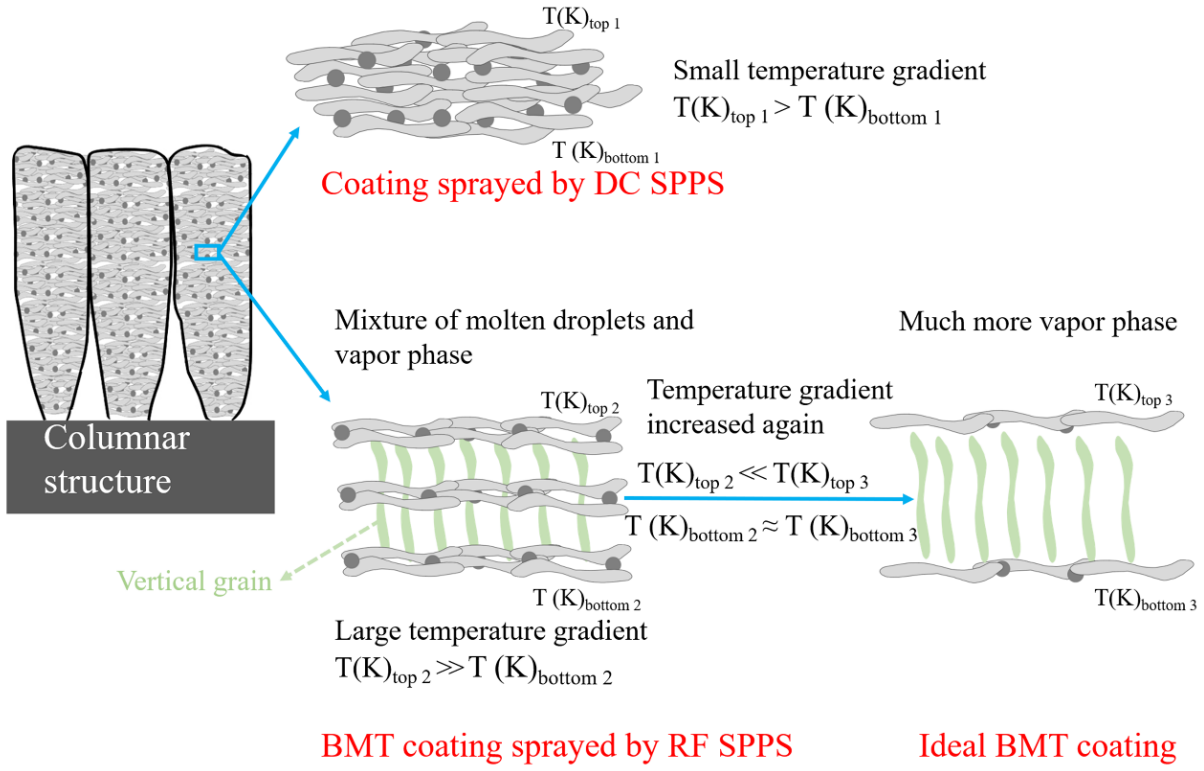

Figure 6.9 Schematic illustration of columnar structure, vertical columnar grain and its growth evolution process

6.4.3 BMT Deposition on Niobium Substrate

In this work, BMT is chosen as a thermal insulation material for niobium alloy. Due to the poor oxidation resistance of niobium alloy, an oxidation-resistant layer of $Mo(Si, Al)_2$ is necessary to serve as a bond coat material [121, 174]. As for the deposition sequence, a comparison of TEC should be considered first, as seen in Figure 6.10.

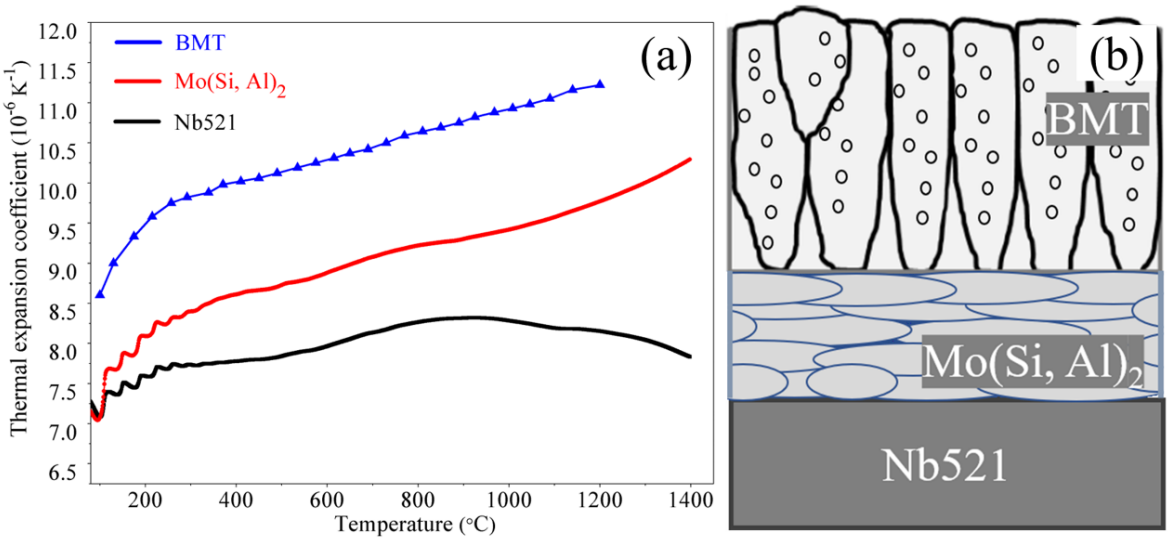

Figure 6.10 Curves of thermal expansion coefficient of Nb521, $Mo(Si, Al)_2$, BMT[6] (a) and schematic design of thermal protection coatings used for niobium alloy (b)

Figure 6.10a indicates that the TEC of BMT and of Mo $(Si, Al)_2$ increases continuously from room temperature to 1400 °C and is always higher than that of the Nb521 substrate. The TEC of Nb521 will slowly decrease when temperature exceeds 900 °C. In order to alleviate the TEC mismatch between the substrate and coating, as well as to avoid stress accumulation during service, the $Mo(Si, Al)_2$ layer should be deposited directly on the Nb521 substrate to act as bonding layer. The designed TBC system for niobium alloy is shown in Figure 6.10b. A dense lamellar bonding layer is required to avoid oxygen penetration. The ideal BMT thermal insulation coating should contain three characteristics: close-packed columnar structure, low inter-columnar porosity and high intra-columnar porosity. Applying the parameters mentioned

in Tables 6.1 and 6.2 to deposit BMT coatings, the prepared TBC systems for niobium alloy are shown in Figure 6.11.

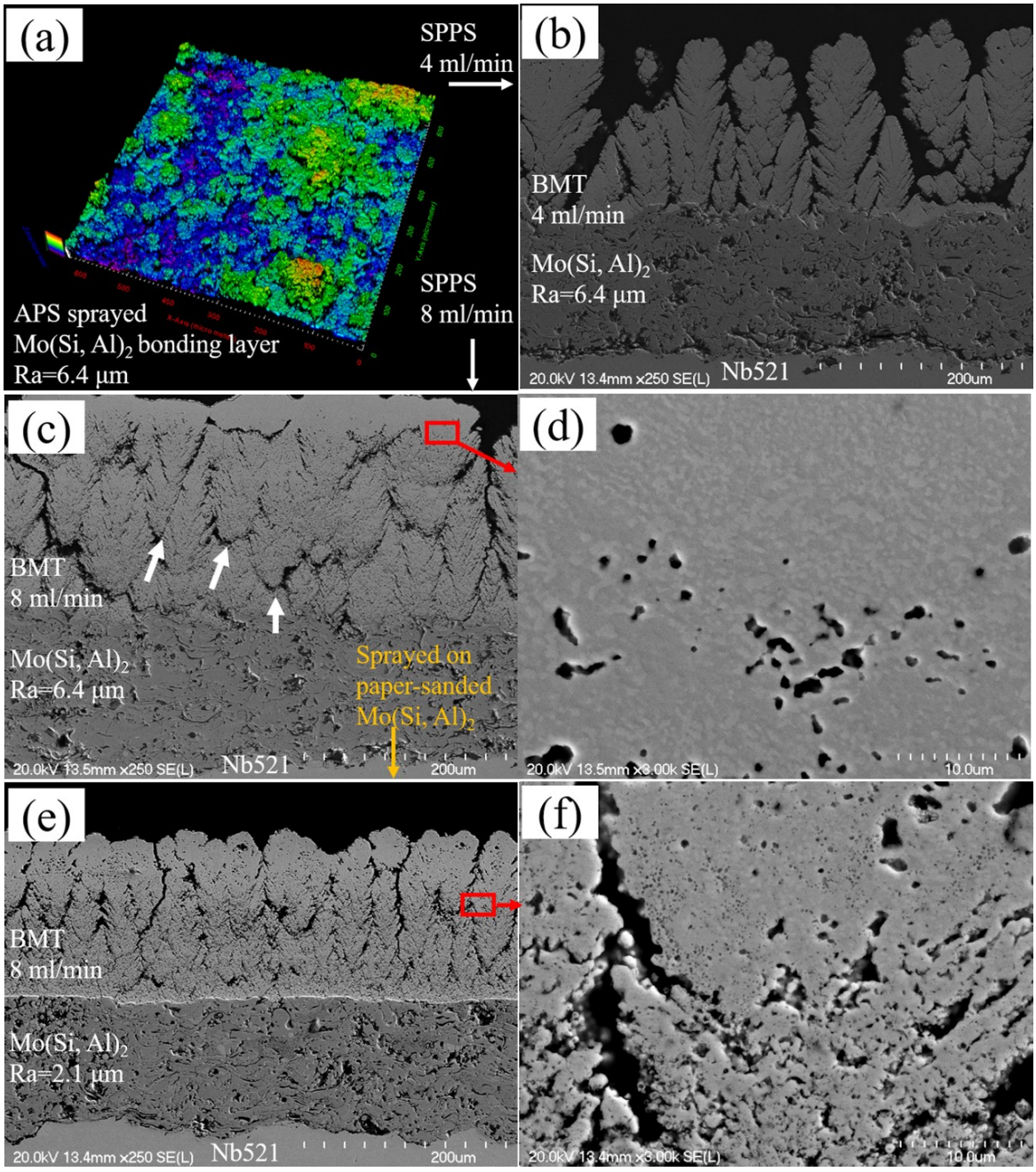

Figure 6.11 Topography of as-sprayed $Mo(Si, Al)_2$ coating (a) and the BMT cross-sectional microstructure applying P1 (b); The cross-sectional and surface morphologies of P2 (c) (d) and P3 (e) (f)

The as-sprayed Mo(Si, Al)$_2$ bonding layer possesses a high surface roughness of Ra=6.4 μm (Figure 6.11a), presenting large area of lowland (blue and purple) and highland (green and red). The BMT coating deposited on the bonding layer shows "disconnected" columns with a calculated inter-columnar porosity of 20.1 %. This characteristic is attributed to the low feed rate of 4 ml/min and layer surface roughness of the bonding layer. When increasing the feed rate to 8 ml/min, the columns compact each other (Figure 6.11c). Due to the same surface roughness of bonding layer, every single column still has a large average diameter. A lot of re-nucleation sites for new columns also occurred when the coating thickness reached 30 μm, as pointed by the white arrows. In the process of plasma spray-physical vapor deposition (PS-PVD), a high deposition rate accompanied by a large proportion of clusters leads to an increased driving force for re-nucleation [111]. In the RF SPPS process, the small particles with a motion parallel to the substrate surface impact on asperities to form new columns in the first stage [164]. Subsequently, parallel motion controls the horizontal growth of columns and reduces the intercolumnar gaps. Due to the high roughness of bonding layer, a lot of columns with large initial diameter formed. When the lateral expansion of columns ends in a limited space, the droplets with parallel velocity will impact on the asperities of the newly deposited coating and form re-nucleation sites. When spraying on the paper-sanded Mo(Si, Al)$_2$ bonding layer using the same 8 ml/min feed rate, its columnar structure is tightly arranged (Figure 6.11e). The entire coating is composed of some fine-diameter columns with fewer re-nucleation sites.

The intercolumnar gaps of coating P1 (Figure 6.11b) offer large air penetration paths. In the cases of compact columnar structure, coatings P2 and P3 (Figures 6.11c, 6.11e) reduce the air penetration because of the thin and tortuous paths. In addition, the heat conduction inside the columns is also hindered because of the well dispersed multiscale porosity. According to solid state physics, when the temperature inside the ceramic is lower than 1200 °C, the heat conduction mainly depends on the lattice vibration (phonons transport). The thermal conductivity is given by formula 6.1 [175].

$$k_p = \frac{1}{3}\int C_v \, \rho l_p \bar{v} \tag{6.1}$$

Where C_v is the specific heat, ρ is the density, $\bar{v}$ is the phonon velocity and l_P is the phonon mean free path. The phonon can be scattered by the intracolumnar porosity [83] as well as the grain boundaries of coating P2 and P3, which reduces their mean free path. Consequently, the decreased thermal conductivity and hindered air penetration result in the accumulation of heat inside the coatings and lead to the top surface sintering, as seen in Figures 6.11d, 6.11f. The microstructure at the interface of sintered and underlying zone indicates the annihilation of pores caused by the sintering behavior. As a result, a fully dense ceramic top layer was formed. The boundaries of lamellae or vertical grains no longer exist in the sintered region.

Referring to the topographies of as-sprayed BMT coatings (Figure 6.12), without the sintering behavior, a disconnected cauliflower-shape appears clearly (Figure 6.12a). A lot of particles and splats with various shapes remain on the surface (Figures 6.12b, 6.12c). Meanwhile, the sintering behavior observed in coatings P2 and P3 sealed the top of the cauliflower shapes (Figures 6.12e, 6.12h). This sealed top layer could act as a blanket that may block out the O_2 and hot gases. The magnified pictures indicate the typical characteristics of BMT ceramic sintering [147], presenting the compact equiaxed crystals with different sizes (Figures 6.12f, 6.12i).

In some cases, the sintered top layer offers positive effects, such as the hot corrosion and erosion resistance. When applying TBC in a gas turbine or diesel engine, molten salts such as Na_2SO_4 and Va_2O_5 that come from the burning of low-quality fuel could react with yttria in YSZ coatings and cause a thermal corrosion failure [176, 177]. In addition, the molten salts could penetrate deeply into the bond coat through the cracks [178]. In order to solve this problem, many methods were proposed [179]. Some sealing treatments, namely laser-glazing (LG) can re-melt the coating surface using a high-energy plasma. In the subsequent curing process, a dense top layer is formed which can effectively prevent molten salts from penetrating into the coating [180].

Meanwhile, the surface roughness and specific surface area are reduced after densification which finally lower the corrosion reaction of molten salts with the coating [181]. The sintering behavior observed in this work could be considered as a “self-healing” process, which has a function similar to that of LG post-processing.

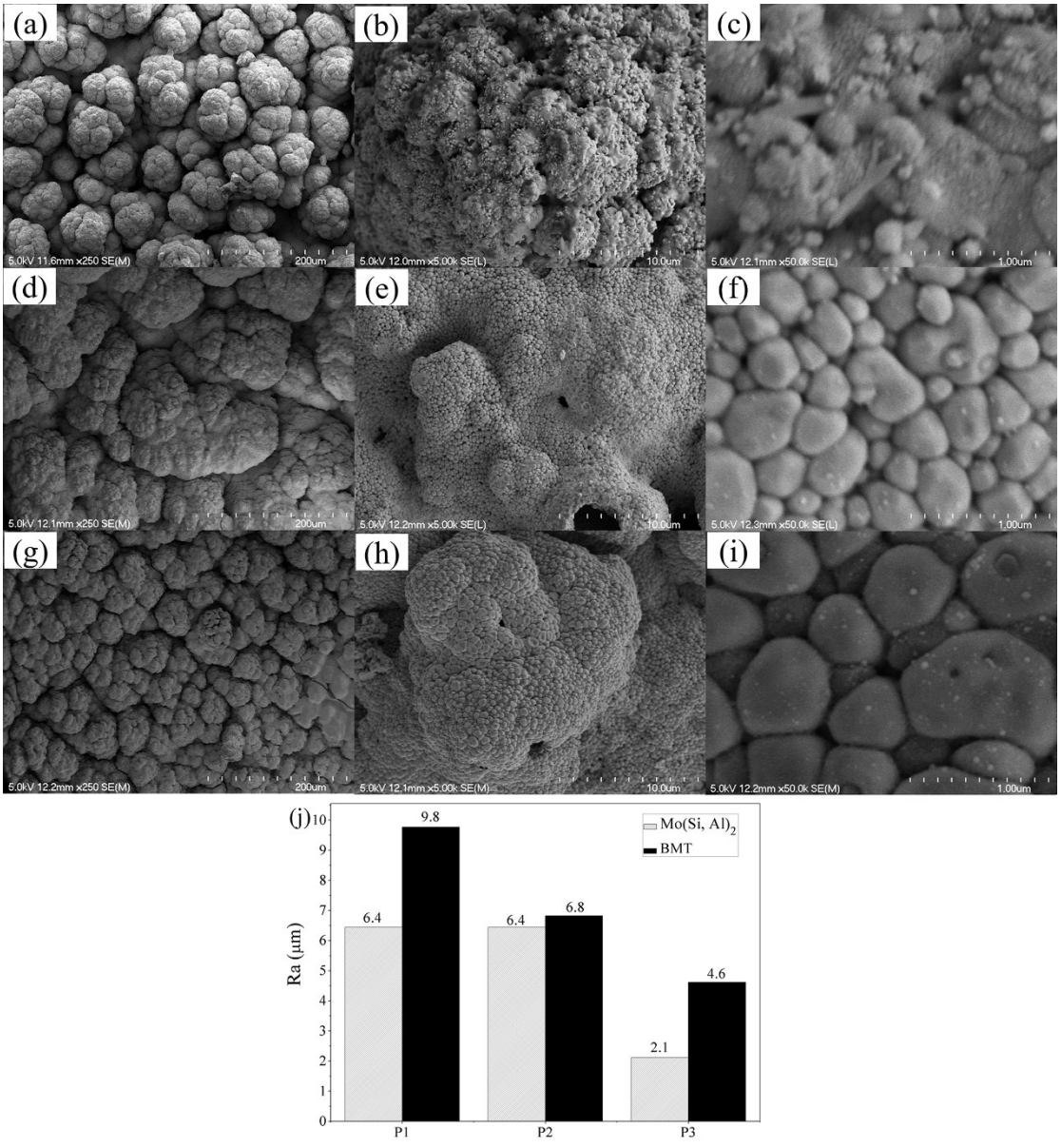

Figure 6.12 Topographies of as-sprayed BMT coating of P1 (a) (b) (c), P2 (d) (e) (f) and P3 (g) (h) (i) and (j) comparison of surface roughness before and after RF SPPS

In addition to hot corrosion resistance, the sintering behavior may exert a positive effect on erosion resistance. Because the spallation caused by an erodent frequently occurs at the boundary of lamellae, the surface sintering process, which strengthens the bonding between lamellae, would be beneficial to improve the erosion resistance of this coating. A similar phenomenon has been proved in APS coatings [105, 157].

Apart from the surface densification, the sintering behavior also comes with component segregation, unfortunately. EDS mapping of a typical sintered region is shown in Figure 6.13. The BSE picture (Figure 6.13a) indicates that at least three different phases formed in the sintered zone: the brighter grain of quasi-hexagonal shape, the grey one and darker one. Brighter grains in BSE mode correspond to regions richer in Ta. Mg depletion is observed where Ta is enriched. However, Mg rich regions are also observed, mainly close to the sample pores. In addition, Ba is also depleted where Ta is enriched. The component segregation results in the formation of low melting point oxide and other secondary phases. Accordingly, the level of sintering behavior should be controlled, especially for the complex oxide of BMT.

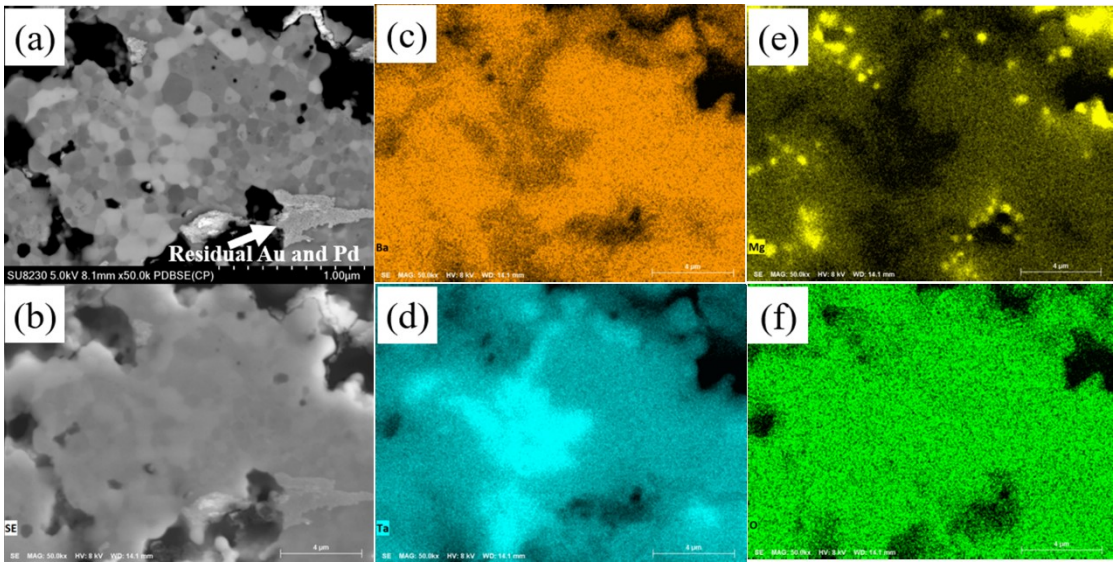

Figure 6.13 EDS element mapping of the sintered zone of P3 coating. (a) (b) are the BSE and SE pictures which present the element contrast detail and morphology, separately. (c), (d), (e) and (f) show the maps of major elements Ba, Ta, Mg and O, separately

6.4.4 Future work

In this work, a short spray distance ensures a sufficient heating for droplets and coating. Besides, the circulating water cools the substrates constantly and creates a huge temperature gradient along the direction of heat flux. Unfortunately, the one-axis robot translation and limited radial expansion of the plasma plume at short distances were insufficient to fully cover the substrate surface (Φ12.6 mm) with BMT. As such, it makes the subsequent erosion and thermal cycling tests hardly possible, since the substrate and/or the bonding layer would constantly be exposed. In the future, the robot arm will be updated with a second axis of translation (which is a non-trivial modification inside a controlled atmosphere deposition reactor). Then, BMT coatings fully covering the substrate and bonding layer will be prepared and erosion and thermal cycling tests will be carried out. A qualitative comparison with EB-PVD coatings will be given.

6.5 Conclusion

Columnar BMT coatings with an alternation of dense lamellae and vertical grains were deposited by RF SPPS in this work. Due to the lower reactor pressure (15 kPa), the enlarged RF ICP plume formed a large heat affected/high temperature zone, which spanned close to 80 mm in the axial direction. As such, it brought a large amount of heat to the substrate located at 34 mm. The latter being deposited on a water-cooled holder, large temperature gradients were created from the plasma to the substrate and promoted the nucleation of grains inside the splats as well as their subsequent growth from the vapor phase. The closely packed vertical grains in the intracolumnar region had an average size of 20 nm in diameter and 150 nm in height. However, loosely packed columnar grains were found in the periphery of columns, and may ultimately determine the thermo-mechanical properties of the coatings. Coatings with such a microstructure, columnar-oriented appearance and vertical grain nature, are promising and are likely to have the potential to replace EB-PVD coatings in the future.

In addition, a promising application of BMT was proposed in this work. $Mo(Si, Al)_2$ and BMT were used as bonding and thermal insulation layers, respectively, on a niobium alloy substrate. When narrowing the inter-columnar gaps, it was shown that the top layer could be sintered in-situ during spraying, due to the accumulation of heat. The excessive sintering behavior led to component segregation and formation of low melting temperature oxide. Further improvements to the RF SPPS deposition facilities are needed to avoid the excessing sintering of BMT coatings and to broaden the deposition region over the substrate, allowing for representative thermal cycling tests to be performed on BMT coatings.

CHAPTER 7

Conclusion

7.1 Summary and discussion

Induction plasma spray has been successfully applied to deposit high melting temperature oxide BMT coatings, which have a promising application in the field of TBCs, especially suitable for the thermal protection of turbine blade. The key experimental observations and conclusions of this work are listed below.

In the process of plasma spraying, BMT forms and it is accompanied by Mg evaporation. According to the XPS results, twice the Mg stoichiometric amount should be added to compensate for the preferential Mg loss. In addition to BMT main phase, the as-sprayed coatings contain part or all the secondary phases: three Mg-depleted phases ($BaTa_2O_6$, $Ba_3Ta_5O_{15}$ and $Ba_4Ta_2O_9$) and one Mg-rich phase ($Mg_4Ta_2O_9$). Some key parameters such as spraying distance, substrate pre-heating, plasma power and precursor chemistry determined the phase structure in the as-sprayed coatings. Precursor chemistry played a key role in BMT synthesis and coating preparation. In order to deposit a BMT coating with high purity phase structure and high coating deposition rate, 50 kW plasma power as well as a precursor combination of nanocrystallized Ta_2O_5 and nitrate-based barium and magnesium salts were the necessary processing parameters to be applied.

Hybrid SPS/SPPS process could only deposit the dense lamellar BMT coating in this work. Applying SPPS process and short spray distance (34 mm) are the crucial prerequisites for column formation. The combined action of the vertical impingement of large particles and the lateral impingement of small particles built the columnar-orientated structure with a high

deposition rate. The substrate surface roughness, the precursor concentration and the feed rate influence the column morphology. When spraying the precursor with a concentration of 30 wt. %, a DVC structure occurred rather than the columnar one. Suitable combination of bimodal atomization probe, 8 ml/min feed rate and 10 wt. % concentration precursor led to the desired columnar structure with more intracolumnar porosity of 4.3 %, less intercolumnar porosity of 9.9 % and high amount of the BMT phase of 94.1 wt. %.

When applying SPPS to work at a short spray distance (34 mm), the large temperature gradient from the plasma to the substrate promoted a distinctive coating structure, which was built by an alternation of dense lamellae and vertical grains but showed the columnar-oriented appearance. This special structure equips the as-sprayed coatings with both merits of DC plasma spray and EV-PVD deposited counterparts. Therefore, it has the potential to replace EB-PVD coatings in the future. In addition, this work presents a promising application of BMT. According to their thermal expansion coefficients change trend and material properties, $Mo(Si, Al)_2$ and BMT were chosen to protect niobium alloy by acting as the bonding and thermal insulation layers, respectively. The narrowed inter-columnar gaps and increased thermal conductivity resulted in the accumulation of heat inside the BMT coatings and led to the top surface sintering. This sealed top layer has the potential to act as a blanket that may block out the O_2, hot gases and even the CMAS attack.

7.2 Statement of contributions

- This work succeeded in synthesizing complex oxide BMT material and in depositing their coatings simultaneously by feeding liquid precursors into an induction plasma. Applying liquid precursors avoided the complex procedures of solid feedstock preparation. As-sprayed coatings by RF SPPS presented a nanosized characteristic and controllable phase structure which differ from their APS counterpart.

- The three most common TBCs structures, lamellar, columnar and DVC structures have been deposited successfully by RF induction plasma spray in this work. According to the various requirements of service environment, one structure could be tuned into another one through adjusting the spray parameters. It means the technique of induction plasma spray could be applied into the field of TBCs in addition to DC plasma spray and EB-PVD.

- As-sprayed BMT coatings present a distinctive columnar structure of alternative stacking between horizontal lamellae and vertical grains. This structure could be considered as the combination of two kind of coatings deposited by DC SPS and EB-PVD, which has never been reported before. The columnar appearance, horizontal lamellae and vertical grains contribute to improving the performances of thermal cycling, thermal conductivity and erosion resistance, respectively. Therefore, RF SPPS process could fill the gap between the conventional DC plasma spray process and EB-PVD technology.

7.3 Recommendation of future work

After investigating 10 different precursor combinations in this project, a solution precursor combination of tantalum ethoxide, barium and magnesium acetates (the precursors used in chapter 6) has been finally identified as the most suitable one to deposit BMT coating. However, an undesired sedimentation formed slowly after remaining 1h at room condition or refrigerator. This phenomenon caused an uncertainty in the process of coating deposition. It could be solved by increasing the relative proportion of acetic acid in the mixed solvent including ethanol. Considering the different exothermic combustions of acetic acid and ethanol, the microstructure, especially the inner-columnar porosity, may be changed. Designing a stable solution and solving this problem could facilitate the transfer to industrial applications.

In this work, a short spray distance ensures the formation of columnar structure as well as the large temperature gradient between top coating surface and substrate with the assistance of a cooling water underneath the substrate. However, the limited radial expansion of the plasma at short distances could not cover the full substrate (Φ12.6 mm) with molten droplets. In fact, the substrate was driven by a water-cooled 3-axis robotic arm, which was designed for linear motion in one horizontal direction only. As such, the exposed substrate makes the subsequent erosion and thermal cycling tests hardly possible. In the future, the robot arm should be updated with a five-axis robot. Hopefully, intact coatings would be deposited so that subsequent tests such as erosion-resistance and thermal cycling could be carried out.

The formation mechanism of columnar structure for BMT was discussed clearly. However, this mechanism is not suitable for other materials such as $BaTiO_3$, $Lu_2Si_2O_7$ and $Y_2Si_2O_7$. Even under the same condition of induction plasma spray, the applicable parameters for BMT and other materials are completely opposite. Therefore, the relations and links between these various precursors, materials, spray parameters, phases and microstructure should be explored in a systematic way in the future.

Air plasma sprayed LAMT coatings present promising TBC performance on thermal cycling compared to BMT. It is worth looking forward to carrying out the comparative experiments on the performance of BMT and LAMT coatings, especially deposited by RF liquid precursor plasma spray. Since this thesis has systematically summarized the methods of compensating the preferential element losses upon plasma spraying, it will not be too difficult to deposit a LAMT coating with limited secondary phases.

7.4 Interprétation des résultats

La projection plasma à couplage inductif a été appliquée avec succès pour déposer des

revêtements d'oxyde BMT à température de fusion élevée, qui ont une application prometteuse dans le domaine des TBC, particulièrement adaptés à la protection thermique des aubes de turbine. Les principales observations expérimentales et conclusions de ce travail sont énumérées ci-dessous.

Dans le processus de projection plasma, le BMT se forme et s'accompagne d'une évaporation du Mg. Selon les résultats XPS, il faut ajouter deux fois la quantité stœchiométrique de Mg pour compenser sa perte préférentielle. En plus de la phase principale du BMT, les revêtements tels que projetés contiennent une partie ou la totalité des phases secondaires: trois phases appauvries en Mg ($BaTa_2O_6$, $Ba_3Ta_5O_{15}$ et $Ba_4Ta_2O_9$) et une phase riche en Mg ($Mg_4Ta_2O_9$). Certains paramètres clés tels que la distance de projection, le préchauffage du substrat, la puissance du plasma et la chimie des précurseurs ont déterminé la structure de la phase dans les revêtements projetés. La chimie des précurseurs a joué un rôle clé dans la synthèse du BMT et la préparation du revêtement. Afin de déposer un revêtement BMT avec une structure de phase de haute pureté et un taux de dépôt élevé, une puissance de plasma de 50 kW ainsi qu'une combinaison de précurseurs constitués de Ta_2O_5 nanocristallisé et de nitrates de baryum et de magnésium étaient les paramètres de traitement nécessaires à appliquer.

Le procédé hybride SPS/SPPS n'a pu déposer que le revêtement BMT lamellaire dense dans ce travail. L'application du procédé SPPS et la courte distance de projection (34 mm) sont les conditions préalables cruciales pour la formation de colonnes. L'action combinée de l'impact vertical des grosses particules et de l'impact latéral des petites particules a permis de construire la structure à orientation colonnaire avec un taux de dépôt élevé. La rugosité de la surface du substrat, la concentration des précurseurs et le taux d'alimentation influencent la morphologie de la colonne. Lors de la projection du précurseur avec une concentration de 30 % en poids, une structure DVC s'est produite plutôt que la structure en colonne. La combinaison appropriée d'une sonde d'atomisation bimodale, d'un taux d'alimentation de 8 ml/min et d'une concentration de

précurseur de 10 % en poids a conduit à la structure colonnaire souhaitée avec une porosité intracolonnaire plus importante de 4.3 %, une porosité intercolonnaire moins importante de 9.9 % et une quantité élevée de phases BMT de 94.1 % en poids.

Lors de l'application du SPPS pour travailler à une courte distance de projection (34 mm), le grand gradient de température entre le plasma et le substrat a favorisé une structure de revêtement distinctive, qui a été construite par une alternance de lamelles denses et de grains verticaux, mais a montré l'aspect orienté en colonne. Cette structure spéciale confère aux revêtements projetés les deux avantages de la projection plasma DC et des équivalents déposés par EV-PVD. Elle a donc le potentiel de remplacer les revêtements EB-PVD à l'avenir. En outre, ce travail présente une application prometteuse du BMT. En fonction de leur coefficient de dilatation thermique, de leur tendance à changer et des propriétés du matériau, le $Mo(Si, Al)_2$ et le BMT ont été choisis pour protéger l'alliage de niobium en agissant respectivement comme couche de liaison et d'isolation thermique. Le rétrécissement des espaces inter-colonnes et l'augmentation de la conductivité thermique ont entraîné l'accumulation de chaleur à l'intérieur des revêtements de BMT et ont conduit au frittage de la surface supérieure. Cette couche supérieure scellée a le potentiel d'agir comme une couverture qui peut bloquer l'O_2, les gaz chauds et même l'attaque du CMAS.

7.5 État des contributions

- Ce travail a réussi à synthétiser des matériaux BMT d'oxyde complexe et à déposer leurs revêtements simultanément en introduisant des précurseurs liquides dans un plasma à couplage inductif. L'application de précurseurs liquides a permis d'éviter les procédures complexes de préparation des matières premières solides. Les revêtements projetés par SPPS RF présentaient une structure de phase caractéristique et contrôlable à l'échelle nanométrique, qui diffère de leur homologue APS.

- Les trois structures TBC les plus courantes, à savoir les structures lamellaires, colonnaires et DVC, ont été déposées avec succès par projection plasma RF dans le cadre de ces travaux. En fonction des différentes exigences de l'environnement de service, une structure peut être adaptée à une autre en ajustant les paramètres de projection. Cela signifie que la technique de projection par plasma RF pourrait être appliquée dans le domaine des TBC en plus de la projection par plasma DC et de l'EB-PVD.

- Les revêtements BMT projetés présentent une structure colonnaire distinctive d'empilage alternatif entre les lamelles horizontales et les grains verticaux. Cette structure pourrait être considérée comme la combinaison de deux types de revêtements déposés par SPS DC et EB-PVD, ce qui n'a jamais été signalé auparavant. L'aspect colonnaire, les lamelles horizontales et les grains verticaux pourraient contribuer respectivement à améliorer les performances du cycle thermique, la conductivité thermique et la résistance à l'érosion. Par conséquent, le procédé SPPS RF pourrait combler l'écart entre le procédé conventionnel de projection par plasma DC et la technologie EB-PVD.

7.6 Recommandation de travaux futurs

Après avoir étudié 10 combinaisons différentes de précurseurs dans le cadre de ce projet, une combinaison de précurseurs en solution d'éthoxyde de tantale, d'acétates de baryum et de magnésium (les précurseurs utilisés au chapitre 6) a finalement été identifiée comme la plus appropriée pour déposer un revêtement de BMT. Cependant, une sédimentation indésirable s'est formée lentement après une heure de séjour dans la pièce ou au réfrigérateur. Ce phénomène a entraîné une incertitude dans le processus de dépôt du revêtement. Il pourrait être résolu en augmentant la proportion relative d'acide acétique dans le solvant mixte comprenant de l'éthanol. Compte tenu des différentes combustions exothermiques de l'acide acétique et de l'éthanol, la

microstructure, en particulier la porosité intérieure de la colonne, peut être modifiée. La conception d'une solution stable et la résolution de ce problème pourraient faciliter le transfert vers des applications industrielles.

Dans ce travail, une courte distance de projection assure la formation d'une structure colonnaire ainsi que le grand gradient de température entre la surface du revêtement supérieur et le substrat avec l'aide d'une eau de refroidissement sous le substrat. Cependant, l'expansion radiale limitée du plasma sur courtes distances n'a pas permis de couvrir la totalité du substrat (Φ12.6 mm) de gouttelettes fondues. En fait, le substrat était entraîné par un bras robotique à trois axes refroidi par eau, qui était conçue pour un mouvement linéaire dans une seule direction horizontale. Ainsi, le substrat exposé rend à peine possible les tests d'érosion et de cycles thermiques ultérieurs. À l'avenir, le bras robotique devrait être mis à jour avec un robot à cinq axes. Il est à espérer que des revêtements intacts seront déposés afin que des tests ultérieurs tels que la résistance à l'érosion et les cycles thermiques puissent être effectués.

Le mécanisme de formation de la structure colonnaire pour le BMT a été clairement discuté. Toutefois, ce mécanisme ne convient pas à d'autres matériaux tels que le $BaTiO_3$, $Lu_2Si_2O_7$ et $Y_2Si_2O_7$. Dans les mêmes conditions de projection par plasma à couplage inductif, les paramètres applicables au BMT et aux autres matériaux sont complètement opposés. Par conséquent, les relations et les liens entre ces différents précurseurs, matériaux, paramètres de projection, phases et microstructures devraient être explorés de manière systématique à l'avenir.

Les revêtements LAMT déposés par projection plasma à air présentent des performances TBC prometteuses sur le cycle thermique par rapport au BMT. Il serait intéressant de mener des expériences comparatives sur les performances des revêtements BMT et LAMT, en particulier sur des revêtements déposés par RF projection plasma de précurseurs liquides. Comme cette thèse a systématiquement résumé les méthodes de compensation des pertes d'éléments

préférentiels lors de la projection par plasma, il ne sera pas trop difficile de déposer un revêtement LAMT avec des phases secondaires limitées.

LIST OF REFERENCES

[1] Padture, N.P., Gell, M. and Jordan, E.H. (2002). Thermal barrier coatings for gas-turbine engine applications. *Science*, volumne 296, p. 280-284.

[2] Gupta, M., Curry, N., Nylen, P., Markocsan, N. and Vassen, R. (2013). Design of next generation thermal barrier coatings - Experiments and modelling. *Surface & Coatings Technology*, volumne 220, p. 20-26.

[3] Cao, X.Q., Vassen, R. and Stöver, D. (2004). Ceramic materials for thermal barrier coatings. *Journal of the European Ceramic Society*, volumne 24, p. 1-10.

[4] Jarligo, M.O., Mauer, G., Sebold, D., Mack, D.E., Vassen R. and Stöver, D. (2012). Decomposition of $Ba(Mg_{1/3}Ta_{2/3})O_3$ perovskite during atmospheric plasma spraying. *Surface & Coatings Technology*, volumne 206, p. 2515-2520.

[5] Jarligo, M.O., Mack, D.E., Vassen R. and Stöver, D. (2009). Application of Plasma-Sprayed Complex Perovskites as Thermal Barrier Coatings. *Journal of Thermal Spray Technology*, volume 18, p. 187-193.

[6] Jarligo, M.O., Mack, D.E., Mauer, G., Vassen, R. and Stöver, D. (2010). Atmospheric Plasma Spraying of High Melting Temperature Complex Perovskites for TBC Application. *Journal of Thermal Spray Technology*, volumne 19, p. 303-310.

[7] Gitzhofer, F., Bouyer, E., and Boulos, M.I. (1997). Suspension plasma spray. *Patent US5609921A*.

[8] Jordan, E.H., Jiang, C. and Gell, M. (2015). The solution precursor plasma spray (SPPS) process: a review with energy considerations. *Journal of Thermal Spray Technology*, volume 24, p. 1153-1165.

[9] Brinley, E., Babu, K.S. and Seal, S. (2007). The Solution Precursor Plasma Spray processing of nano materials. *Functional coatings*, volume 59, p.54-59.

[10] Ohnabe, H., Masaki, S., Onozuka, M., Miyahara, K. and Sasa, (1999). Potential application of ceramic matrix composites to aero-engine components. *Composites Part A: Applied Science and Manufacturing*, volumne 30, p. 489-496.

[11] Goward, G. (1986). Protective coatings–purpose, role, and design. *Materials Science and Technology*, volume 2, 194-200.

[12] Meier, S.M. and Gupta, D.K. (1994). The evolution of thermal barrier coatings in gas turbine engine applications. *Journal of Engineering for Gas Turbines and Power*, volume 116, 250-257.

[13] Clarke, D.R. and Levi, C.G. (2003). Materials design for the next generation thermal barrier coatings. *Annual Review of Materials Research*, volumne 33, p. 383-417.

[14] Sims, C.T., Stoloff, N.S. and Hagel, W.C., (1987). Superalloys II. United States: Wiley-Interscience, New York, NY, p. 293-326.

[15] Goldstein, R.J., Eckert, E.R.G. and Burggraf, F. (1974). Effects of hole geometry and density on three-dimensional film cooling. *International Journal of Heat and Mass Transfer*, volume 17, p. 595-607.

[16] Clarke, D.R., Oechsner, M. and Padture, N.P. (2012). Thermal-barrier coatings for more efficient gas-turbine engines. *MRS bulletin*, volume 37, p. 891-898.

[17] Bakan, E., Mack, D.E., Mauer, G., Vassen, R., Lamon, J. and Padture, N.P. (2020). High-temperature materials for power generation in gas turbines. *Advanced Ceramics for Energy Conversion and Storage*, Elsevier, p. 3-62.

[18] Karger, M., Vassen, R. and Stöver, D. (2011). Atmospheric plasma sprayed thermal barrier coatings with high segmentation crack densities: Spraying process, microstructure and thermal cycling behavior. *Surface & Coatings Technology*, volume 206, p. 16-23.

[19] Schlichting, K.W., Padture, N.P., Jordan, E.H. and Gell, M. (2003). Failure modes in plasma-sprayed thermal barrier coatings. *Materials Science and Engineering a-Structural Materials Properties Microstructure and Processing*, volume 342, p.120-130.

[20] Xu, H., Gong, S. and Liu, F. (2000). Recent development in materials design of thermal barrier coatings for gas turbine (In Chinese). *Acta Aeronautica et Astronautica Sinica*, volume 1, p. 8-13.

[21] Gell, M., Duhl, D., Gupta, D. and Sheffler, K. (1987). Advanced superalloy airfoils. *JOM*, volume 39, p.11-15.

[22] Bakan, E. and Vassen, R. (2017), Ceramic Top Coats of Plasma-Sprayed Thermal Barrier Coatings: Materials, Processes, and Properties. *Journal of Thermal Spray Technology*, volume 26, p. 992-1010.

[23] Zheng, L., Guo, H., Guo, L., Peng, H., Gong, S. and Xu, H. (2012). New generation thermal barrier coatings for ultrahigh temperature application (In Chinese). *Journal of Aeronautical Materials*, 32, 6, p.14-24.

[24] Achar, D.R.G., Munoz-Arroyo, R., Singheiser, L. and Quadakkers, W.J. (2004). Modelling of phase equilibria in MCrAlY coating systems. *Surface & Coatings Technology*, 2004;187:272-83.

[25] Nickel, H., Clemens, D., Quadakkers, W. and Singheiser, L. (1999). Development of NiCrAlY alloys for corrosion-resistant coatings and thermal barrier coatings of gas turbine components. *Journal of pressure vessel technology*, volume 121, p. 384-387.

[26] Yu, Z., Hass, D.D. and Wadley, H.N.G. (2005). NiAl bond coats made by a directed vapor deposition approach. *Materials Science and Engineering:A*, volume 394, p. 43-52.

[27] Tryon, B., Murphy, K., Yang, J., Levi, C. and Pollock, T. (2007). Hybrid intermetallic Ru/Pt-modified bond coatings for thermal barrier systems. *Surface & Coatings Technology*, volume 202, p. 349-361.

[28] Li, D., Wang, L., Peng, H., Zhao, X., Guo, H. and Gong, S. (2012). Cyclic oxidation behavior of β-NiAlDy alloys containing varying aluminum content at 1200 °C. *Progress in Natural Science: Materials International*, volume 22, p. 311-317.

[29] Pint, B. and Hobbs, L. (2004). The oxidation behavior of Y_2O_3-dispersed β-NiAl. *Oxidation of metals*, volume 61, p.273-292.

[30] Bruce, R.W., Skelly, D.W., Viguie, R. and Wortman, D.J. (2000). Thermal barrier coating system. *Europent Patents*, EP0987345A1.

[31] Vassen, R., Stuke, A. and Stöver, D.(2009). Recent Developments in the Field of Thermal Barrier Coatings. *Journal of Thermal Spray Technology*, volume 18, p. 181-186.

[32] Miller, R.A. (1997). Thermal barrier coatings for aircraft engines: history and directions. *Journal of thermal spray technology*, volume 6, p. 35-42.

[33] Meier, S.M., Gupta, D.K.and Sheffler, K.D. (1991). Ceramic thermal barrier coatings for commercial gas turbine engines. *JOM*, volume 43, p. 50-53.

[34] Jones, R.L. and Williams, C.E. (1987). Hot corrosion studies of zirconia ceramics. *Surface & Coatings Technology*, volume 32, P. 349-358.

[35] Vassen, R., Jarligo, M.O., Steinke, T., Mack, D.E. and Stöver, D. (2010). Overview on advanced thermal barrier coatings. *Surface & Coatings Technology*, volume 205, p. 938-942.

[36] Stecura, S. (1985). Optimization of the NiCrAl-Y/ZrO-Y_2O_3 thermal barrier system. *NASA Technical Memorandum 86905*, Eighty-seventh Annual Meeting of the American Ceramic Society, Cincinnati, Ohio, May 5-9, 1985.

[37] Mercer, C., Williams, J.R., Clarke, D. R. and Evans, A.G. (2007). On a ferroelastic mechanism governing the toughness of metastable tetragonal-prime (t′) yttria-stabilized zirconia. *Proceedings of the Royal Society A*, volume 463, p. 1393-1408.

[38] Ilavsky, J., Berndt, C.C., Herman, H., Chraska, P. and Dubsky, J. (1997). Alumina-base plasma-sprayed materials—Part II: Phase transformations in aluminas. *Journal of thermal spray technology*, volume 6, p. 439-444.

[39] Kokini K., Takeuchi Y.R. and Choules, B.D. (1996). Surface thermal cracking of thermal barrier coatings owing to stress relaxation: zirconia vs. mullite. *Surface & Coatings Technology*, volume 82, p. 77-82.

[40] Bansal, N.P. and Zhu, D. (2007). Effects of doping on thermal conductivity of pyrochlore oxides for advanced thermal barrier coatings. *Materials Science and Engineering: A*, volume 459, p. 192-195.

[41] Saruhan, B., Francois, P., Fritscher, K. and Schulz, U. (2004). EB-PVD processing of pyrochlore-structured $La_2Zr_2O_7$-based TBCs. *Surface & Coatings Technology*, volume 182, p. 175-183.

[42] Mahade, S., Li, R., Björklund, S., Markocsan, N., Nylén, P. and Curry, N. (2016). Isothermal Oxidation Behavior of $Gd_2Zr_2O_7$/YSZ Multilayered Thermal Barrier Coatings. *International Journal of Applied Ceramic Technology*, volume 13, p. 443-450.

[43] Liu, Z.G., Ouyang, J.H., Wang, B.H., Zhou, Y. and Li, J. (2009). Thermal expansion and thermal conductivity of $Sm_xZr_{1-x}O_{2-x/2}$ ($0.1 \leq x \leq 0.5$) ceramics. *Ceramics International*, volume

35, p. 791-796.

[44] Rao, K.K., Banu, T., Vithal, M., Swamy, G.Y.S.K. and Kumar, K.R. (2002). Preparation and characterization of bulk and nano particles of $La_2Zr_2O_7$ and $Nd_2Zr_2O_7$ by sol–gel method. *Materials Letters*, volume 54, p. 205-210.

[45] Evans, A.G., Mumm, D.R., Hutchinson, J.W., Meier, G.H. and Pettit, F.S. (2001). Mechanisms controlling the durability of thermal barrier coatings. *Progress in Materials Science*, volume 46, p.505-553.

[46] Govindan Kutty, K.V., Rajagopalan, S., Mathews, C.K. and Varadaraju, U.V. (1994). Thermal expansion behaviour of some rare earth oxide pyrochlores. *Materials research bulletin*, volume 29, p.759-766.

[47] Vassen, R., Traeger, F. and Stöver D. (2004). New Thermal Barrier Coatings Based on Pyrochlore/YSZ Double ‐ Layer Systems. *International Journal of Applied Ceramic Technology*, volume 1, p. 351-361.

[48] Friedrich, C., Gadow, R. and Schirmer, T. (2001). Lanthanum hexaaluminate—a new material for atmospheric plasma spraying of advanced thermal barrier coatings. *Journal of thermal spray technology*, volume 10, p. 592-598.

[49] Xie, X., Guo, H., Gong, S. and Xu, H. (2011). Lanthanum–titanium–aluminum oxide: a novel thermal barrier coating material for applications at 1300 °C. *Journal of the European Ceramic Society*, volume 31, p. 1677-1683.

[50] Ma. W., Mack, D.E., Malzbender, J., Vassen, R. and Stöver, D. (2008). Yb_2O_3 and Gd_2O_3 doped strontium zirconate for thermal barrier coatings. *Journal of the European Ceramic Society*, volume 28, p. 3071-3081.

[51] Vassen, R., Cao, X., Tietz, F., Basu, D. and Stöver, D. (2000). Zirconates as New Materials for Thermal Barrie. *Journal of the American Ceramic Society*, volume 83, p. 2023-2028.

[52] Ma, W., Mack, D.E., Vassen, R. and Stöver, D. (2008). Perovskite-type strontium zirconate as a new material for thermal barrier coatings. *Journal of the American Ceramic Society*, volume 91, p. 2630-2635.

[53] Guo, H., Zhang, H., Ma, G. and Gong, S. (2009). Thermo-physical and thermal cycling properties of plasma-sprayed $BaLa_2Ti_3O_{10}$ coating as potential thermal barrier materials.

Surface & Coatings Technology, volume 204, p. 691-696.

[54] Mauer, G., Jarligo, M.O., Mack, D.E. and Vassen, R. (2013). Plasma-Sprayed Thermal Barrier Coatings: New Materials, Processing Issues, and Solutions. *Journal of Thermal Spray Technology*, volume 22, p. 646-658.

[55] Johnsson, M. and Lemmens, P. Crystallography and Chemistry of Perovskites. (2007). *Handbook of Magnetism and Advanced Magnetic Materials:* John Wiley & Sons, Ltd;. p.1-11. DOI: 10.1002/9780470022184.

[56] Bhalla, A.S., Guo, R.Y. and Roy, R. (2000). The perovskite structure - a review of its role in ceramic science and technology. *Materials Research Innovations*, volume 4, p. 3-26.

[57] Roy, R. (1954). Multiple ion substitution in the perovskite lattice. *Journal of the American Ceramic Society*, volume 37, p. 581-588.

[58] Fang, Y., Hu, A., Gu, Y. and Oh, Y.J. (2003). Synthesis of $Ba(Mg_{1/3}Ta_{2/3})O_3$ microwave dielectrics by solid state processing. *Journal of the European Ceramic Society*, volume 23, p. 2497-2502.

[59] Park, T.K. and Kim, N.K. (2008). Phase development in Ba $(Mg_{1/3}Ta_{2/3})O_3$ via conventional and B-site precursor routes. *Ceramics International*, volume 34, p. 1955-1958.

[60] Katayama, S. and Sekine, M. (1992). Low-temperature synthesis of $Ba(_{1/3}Ta_{2/3})O_3$ perovskite by the metal alkoxide method. *Journal of Materials Chemistry*, volume 2, p. 889-890.

[61] Srinivas, J., Dias E.D. and Murthy, G.S. (1997). Crystal structure of Ba $(Mg_{1/3}Ta_{2/3})O_3$ calcinated at 1400 °C. *Bulletin of materials science*, volume 20, p.23-25.

[62] Janaswamy, S., Sreenivasa Murthy, G, Dias, E.D. and Murthy, V.R.K. (2002). Structural analysis of $BaMg_{1/3}(Ta,Nb)_{2/3}O_3$ ceramics. *Materials Letters*, volume 55, p. 414-419.

[63] Wang, C.H., Jing, X.P., Wang, L. and Lu, J. (2009). XRD and Raman studies on the ordering/disordering of $Ba(Mg_{1/3}Ta_{2/3})O_3$. *Journal of the American Ceramic Society*, volume 92, p.1547-1551.

[64] Guo, R., Bhalla, A.S. and Cross, L.E. (1994). $Ba(Mg_{1/3}Ta_{2/3})O_3$ single crystal fiber grown by the laser heated pedestal growth technique. *Journal of Applied Physics*, volume 75, p. 4704-

4708.

[65] Galasso, F. and Pyle, J. (1963). Ordering in compounds of $A(B'_{0.33}Ta_{0.67})O_3$ type. *Inorganic Chemistry*, volume 2, p. 482-484.

[66] Galasso, F and Pyle, J. (1963). Preparation and study of ordering in $A(B'_{0.33}Nb_{0.67})O_3$ perovskite-type compounds. *Journal of Physical Chemistry*, volume 67, p. 1561-1562.

[67] Surendran, K.P., Rajath Varma, P.C. and Varma, M.R. (2007). Solid state and solution synthesis of $Ba(Mg_{1/3}Ta_{2/3})O_3$: A comparative study. *Materials Research Bulletin*, volume 42, p. 1831-1844.

[68] Chen, X.M. and Wu, Y.J. (1996). Effects of NaF upon sintering temperature of $Ba(Mg_{1/3}Ta_{2/3})O_3$ dielectric ceramics. *Journal of Materials Science: Materials in Electronics* volume 7, p. 427-431.

[69] Jinga, C., Andronescu, E., Jinga, S., Ioachim, A., Nedelcu, L. and Toacsan, M.I. (2010). Synthesis and characterization of doped $Ba(Mg_{1/3}Ta_{2/3})O_3$ ceramics. *Journal of Optoelectronics and Advanced Materials*, volume 12, p. 282-287.

[70] Ma, W., Jarligo, M.O., Mack, D.E., Pitzer, D., Malzbender, J., Vassen, R. and Stöver, D. (2008). New Generation Perovskite Thermal Barrier Coating Materials. *Journal of Thermal Spray Technology*, volume 17, p. 831-837.

[71] Cipitria, A., Golosnoy, I.O. and Clyne, T.W. (2009). A sintering model for plasma-sprayed zirconia thermal barrier coatings. Part II: Coatings bonded to a rigid substrate. *Acta Materialia*, volume 57, p. 993-1003.

[72] Bakan, E., Mack, D.E., Mauer, G. and Vassen, R. (2014). Gadolinium zirconate/YSZ thermal barrier coatings: plasma spraying, microstructure, and thermal cycling behavior. *Journal of the American Ceramic Society*, volume 97, p. 4045-4051.

[73] Gell, M., Wang, J., Kumar, R., Roth, J., Jiang, C. and Jordan, E.H. (2018). Higher temperature thermal barrier coatings with the combined use of yttrium aluminum garnet and the solution precursor plasma spray process. *Journal of Thermal Spray Technology*, volume 27, p. 543-555.

[74] Cao, X.Q., Zhang, Y.F., Zhang, J.F., Zhong, X.H., Wang, Y., Ma, H.M., Xu, Z.H., He, L.M. and Lu, F. (2008). Failure of the plasma-sprayed coating of lanthanum hexaluminate. *Journal*

of the European Ceramic Society, volume 28, p. 1979-1986.

[75] Monterrubio-Badillo, C., Ageorges, H., Chartier, T., Coudert, J.F. and Fauchais, P. (2006). Preparation of $LaMnO_3$ perovskite thin films by suspension plasma spraying for SOFC cathodes. *Surface & Coatings Technology*, volume 200, p. 3743-3756.

[76] Ma, W., Gong, S., Li, H. and Xu, H. (2008). Novel thermal barrier coatings based on $La_2Ce_2O_7/_8$YSZ double-ceramic-layer systems deposited by electron beam physical vapor deposition. *Surface & Coatings Technology*, volume 202, p. 2704-2708.

[77] McPherson, R. (1989). A review of microstructure and properties of plasma sprayed ceramic coatings. *Surface & Coatings Technology*, volumne 39, p. 173-181.

[78] Zhang, D., Zheng, L., Hu, X. and Zhang, H. (2016). Numerical studies of arc plasma generation in single cathode and three-cathode plasma torch and its impact on plasma spraying. *International Journal of Heat and Mass Transfer*, volume 98, p. 508-522.

[79] Fauchais, P.L., Heberlein, J.V.R. and Boulos, M.I. (2014). Overview of Thermal Spray. T*hermal Spray Fundamentals:From Powder to Part*, Springer Science+Business Media, New York, p. 17-72.

[80] Fauchais, P.L., Heberlein, J.V.R. and Boulos, M.I. (2014). DC Plasma Spraying. T*hermal Spray Fundamentals:From Powder to Part*, Springer Science+Business Media, New York, p. 383-477.

[81] VanEvery, K., Krane, M.J.M., Trice, R.W., Wang, H., Porter, W., Besser, M., Sordelet, D., Ilavsky, J. and Almer, J. (2011). Column Formation in Suspension Plasma-Sprayed Coatings and Resultant Thermal Properties. *Journal of Thermal Spray Technology*, volume 20, p. 817-828.

[82] Fauchais, P., Etchart-Salas, R., Rat, V., Coudert J.F., Caron, N. and Wittmann-Ténèze, K. (2008). Parameters Controlling Liquid Plasma Spraying: Solutions, Sols, or Suspensions. *Journal of Thermal Spray Technology*, volume 17, p. 31-59.

[83] Bernard, B., Quet, A., Bianchi, L., Joulia, A., Malié, A., Schick, V and Rémy B. (2017). Thermal insulation properties of YSZ coatings: suspension plasma spraying (SPS) versus electron beam physical vapor deposition (EB-PVD) and atmospheric plasma spraying (APS). *Surface & Coatings Technology*, volume 318, p.122-128.

[84] Vassen, R., Kassner, H., Mauer, G. and Stöver, D. (2010). Suspension Plasma Spraying: Process Characteristics and Applications. Journal of Thermal Spray Technology, volume 19, p. 219-225.

[85] Pawlowski, L. (2009). Suspension and solution thermal spray coatings. *Surface & Coatings Technology*, volume 203, p. 2807-2829.

[86] Guignard, A., Mauer, G., Vassen, R. and Stöver, D. (2012). Deposition and Characteristics of Submicrometer-Structured Thermal Barrier Coatings by Suspension Plasma Spraying. *Journal of Thermal Spray Technology*, volume 21, p. 416-424.

[87] Bernard, B., Bianchi, L., Malié A., Joulia, A. and Rémy, B. (2016). Columnar suspension plasma sprayed coating microstructural control for thermal barrier coating application. *Journal of the European Ceramic Society*, volume 36, p. 1081-1089.

[88] Bernard, B., Quet, A., Bianchi, L., Schick, V., Joulia, A., Malié, A. Rémy B. (2017). Effect of Suspension Plasma-Sprayed YSZ Columnar Microstructure and Bond Coat Surface Preparation on Thermal Barrier Coating Properties. *Journal of Thermal Spray Technology*, volume 26, p. 1025-1037.

[89] Fauchais, P.L., Heberlein, J.V.R. and Boulos, M.I. (2014). RF Induction Plasma Spraying. T*hermal Spray Fundamentals:From Powder to Part*, Springer Science+Business Media, New York, p. 479-576.

[90] Gitzhofer, F. and Jia, L. (2008). Induction Plasma Technology Applied to Materials Synthesis for Solid Oxide Fuel Cells. *International Journal of Applied Ceramic Technology*, volume 5, p. 537-547.

[91] Jia, L. and Gitzhofer, F. (2010). Induction plasma synthesis of nano-structured SOFCs electrolyte using solution and suspension plasma spraying: a comparative study. *Journal of thermal spray technology*, volume 19, p. 566-574.

[92] Fauchais, P., Vardelle, M., Vardelle, A. and Goutier, S. (2015). What Do We Know, What are the Current Limitations of Suspension Plasma Spraying? *Journal of Thermal Spray Technology*, volume 24, p. 1120-1129.

[93] Darthout, É., Quet, A., Braidy, N. and Gitzhofer, F. (2013). Lu_2O_3-SiO_2-ZrO_2 Coatings for Environmental Barrier Application by Solution Precursor Plasma Spraying and Influence of Precursor Chemistry. *Journal of Thermal Spray Technology*, volume 23, p. 325-332.

[94] Kobayashi, N., Ishigaki, T., Watanabe, T. and Li, J.G. (2011). Synthesis of Pure, Crystalline (Ba,Sr)TiO_3 Nanosized Powders in Radio Frequency Induction Thermal Plasma. *International Journal of Applied Ceramic Technology*, volume 8, p.1125-1135.

[95] Jia, L. and Gitzhofer, F. (2009). Nano-Particle Sizing in a Thermal Plasma Synthesis Reactor. *Plasma Chemistry and Plasma Processing*, volume 29, p. 497-513.

[96] Boulos, M.I. (2004). Plasma power can make better powders. *Metal Powder Report*, volume 59, p.16-21.

[97] Schulz, U., Saruhan, B., Fritscher, K. and Leyens, C. (2004). Review on Advanced EB‐PVD Ceramic Topcoats for TBC Applications. *International Journal of Applied Ceramic Technology*, volume 1, p.302-315.

[98] Sridhar, K., Reji Kumar, R. and Narasimha, M. (2013). Thermal barrier Analysis in Diesel. *International Journal of Modern Engineering Research (IJMER)*, volume 3, p.1435-1441.

[99] Von Niessen, K. and Gindrat, M. (2011). Plasma spray-PVD: a new thermal spray process to deposit out of the vapor phase. *Journal of thermal spray technology*, volume 20, p. 736-743.

[100] Flores Renteria, A., Saruhan, B., Schulz, U., Raetzer-Scheibe, H.J., Haug, J. and Wiedenmann, A. (2006). Effect of morphology on thermal conductivity of EB-PVD PYSZ TBCs. *Surface & Coatings Technology*, volume 201, p. 2611-2620.

[101] Lima, R.S., Guerreiro, B.MH. and Aghasibeig, M. (2019). Microstructural Characterization and Room-Temperature Erosion Behavior of As-Deposited SPS, EB-PVD and APS YSZ-Based TBCs. *Journal of Thermal Spray Technology*, volume 28, p. 223-232.

[102] Wellman, R., Whitman, G. and Nicholls, J.R. (2010). CMAS corrosion of EB PVD TBCs: Identifying the minimum level to initiate damage. *International Journal of Refractory Metals and Hard Materials*, volume 28, p. 124-132.

[103] Costa, G., Harder, B.J., Wiesner, V.L., Zhu, D., Bansal, N., Lee, K.N., Jacobson, N.S. Kapush, D., Ushakov, S.V. and Navrotsky, A. (2019). Thermodynamics of reaction between gas‐turbine ceramic coatings and ingested CMAS corrodents. *Journal of the American Ceramic Society*, volume 102, p. 2948-2964.

[104] Craig, M., Ndamka, N.L., Wellman, R.G. and Nicholls, J.R. (2015), CMAS degradation of EB-PVD TBCs: the effect of basicity. *Surface & Coatings Technology*, volume 270, p. 145-

153.

[105] Wellman, R.G. and Nicholls, J.R. (2007). A review of the erosion of thermal barrier coatings. *Journal of Physics D: Applied Physics*, volume 40, p. R293-R305.

[106] Nicholls, J.R., Deakin, M.J. and Rickerby, D.S. (1999). A comparison between the erosion behaviour of thermal spray and electron beam physical vapour deposition thermal barrier coatings. *Wear*, volume 233, p. 352-361.

[107] Cernuschi, F., Lorenzoni, L., Capelli, S., Guardamagna, C., Karger, M., Vassen, R. Von Niessen, K., Markocsan, N., Menuey, J. and Giolli C. (2011). Solid particle erosion of thermal spray and physical vapour deposition thermal barrier coatings. *Wear*. volume 271, p. 2909-2918.

[108] Algenaid, W., Ganvir, A., Calinas, R.F., Varghese, J., Rajulapati, K.V. and Joshi, S. (2019). Influence of microstructure on the erosion behaviour of suspension plasma sprayed thermal barrier coatings. *Surface & Coatings Technology*, volume 375, p. 86-99.

[109] Feuerstein, A., Knapp, J., Taylor, T., Ashary, A., Bolcavage, A. and Hitchman, N. (2008). Technical and economical aspects of current thermal barrier coating systems for gas turbine engines by thermal spray and EBPVD: a review. *Journal of Thermal Spray Technology*, volume 17, p. 199-213.

[110] Curry, N., VanEvery, K., Snyder, T., Susnjar, J. and Bjorklund, S. (2015). Performance testing of suspension plasma sprayed thermal barrier coatings produced with varied suspension parameters. *Coatings*, volume 5, p. 338-356.

[111] Harder, B.J., Zhu, D., Schmitt, M.P. and Wolfe, D.E. (2017). Microstructural Effects and Properties of Non-line-of-Sight Coating Processing via Plasma Spray-Physical Vapor Deposition. *Journal of Thermal Spray Technology*, volume 26, p.1052-1061.

[112] Hospach, A., Mauer, G., Vassen, R and Stöver, D. (2011). Columnar-Structured Thermal Barrier Coatings (TBCs) by Thin Film Low-Pressure Plasma Spraying (LPPS-TF). *Journal of Thermal Spray Technology*, volume 20, p. 116-120.

[113] Rezanka, S., Mauer, G. and Vassen, R. (2014) Improved thermal cycling durability of thermal barrier coatings manufactured by PS-PVD. *Journal of Thermal Spray Technology*, volum 23(1-2), p. 182-189.

[114] Mauer, G. and Vassen, R. (2012). Plasma Spray-PVD: Plasma Characteristics and Impact

on Coating Properties. *Journal of Physics: Conference Series*, volume 406, 012005, p. 1-12.

[115] Schulz, U., Terry, S.G. and Levi, C.G. (2003). Microstructure and texture of EB-PVD TBCs grown under different rotation modes. *Materials Science and Engineering: A*, volume 360, p. 319-329.

[116] Mauer, G., Jarligo, M.O., Rezanka, S., Hospach, A. and Vassen, R. (2015). Novel opportunities for thermal spray by PS-PVD. *Surface & Coatings Technology*, volume 268, p. 52-57.

[117] Ganvir, A., Kumara, C., Gupta, M. and Nylen, P. (2017). Thermal Conductivity in Suspension Sprayed Thermal Barrier Coatings: Modeling and Experiments. *Journal of Thermal Spray Technology*, volume 26, p. 71-82.

[118] Darthout, É., Laduye, G. and Gitzhofer, F. (2016). Processing Parameter Effects and Thermal Properties of $Y_2Si_2O_7$ Nanostructured Environmental Barrier Coatings Synthesized by Solution Precursor Induction Plasma Spraying. *Journal of Thermal Spray Technology*, volume 25, p. 1264-1279.

[119] Marr, M., Kuhn, J., Metcalfe, C., Harris, J. and Kesler, O. (2014). Electrochemical performance of solid oxide fuel cells having electrolytes made by suspension and solution precursor plasma spraying. *Journal of Power Sources*, volume 245, p. 398-405.

[120] Major, K., Veilleux, J. and Brisard, G. (2016). Lithium iron phosphate powders and coatings obtained by means of inductively coupled thermal plasma. *Journal of Thermal Spray Technology*, volume 25, p. 357-364.

[121] Hou, H., Ning, X., Wang, Q., Liu, Y. and Liu, Y. (2015). Anti-ablation behavior of air plasma-sprayed $Mo(Si, Al)_2$ coating. *Surface & Coatings Technology*, volume 274, p. 60-67.

[122] Guo, J., Fan, X., Richard, D., Xue, S., Jerzy, J. and Boulos, M.I. (2010). Development of Nanopowder Synthesis Using Induction Plasma. *Plasma Science and Technology*, volume 12, p.188-199.

[123] Matsumoto, K., Hiuga, T., Takada, K. and Ichimura, H. (1986). Ba(Mg1/3Ta2/3)O3 ceramics with ultra-low loss at microwave frequencies. *Sixth IEEE International Symposium on Applications of Ferroelectrics.* IEEE, New York, p. 118-121.

[124] Lide, D.R., Ed., (2003). Section 6, Fluid Propertues: vapor pressure. *CRC Handbook of*

Chemistry and Physics, 84th ed., CRC press, Boca Raton.

[125] Layden, G.K. (1967). Polymorphism of $BaTa_2O_6$. *Materials Research Bulletin*, volume 2, p. 533-539.

[126] Kolodiazhnyi, T., Belik, A.A., Ozawa, T.C. and Takayama-Muromachi, E. (2009). Phase equilibria in the BaO-MgO-Ta_2O_5 system. *Journal of Materials Chemistry*, volume 19, p. 8212-8215.

[127] Baskin, Y. and Schell, D.C. (1963). Phase Studies in the Binary System MgO-Ta_2O_5. *Journal of the American Ceramic Society*, volume 46, p. 174-177.

[128] Sun, D., Senz, S. and Hesse, D. (2004). Topotaxial formation of $Mg_4Ta_2O_9$ and $MgTa_2O_6$ thin films by vapour-solid reactions on MgO (001) crystals. *Journal of the European Ceramic Society*, volume 24, p. 2453-2463.

[129] Schiller, G., Muller, M.and Gitzhofer, F. (1999). Preparation of Perovskite powders and coatings by radio frequency suspension plasma spraying. *Journal of Thermal Spray Technology*, volume 8, p. 389-392.

[130] Kolodiazhnyi, T.V., Petric, A., Johari, G.P. and Belous, A.G. (2002). Effect of preparation conditions on cation ordering and dielectric properties of $Ba(Mg_{1/3}Ta_{2/3})O_3$ ceramics. *Journal of the European Ceramic Society*, volume 22, p. 2013-2021.

[131] Fang, Y., Hu, A., Ouyang, S. and Oh, J.J. (2001). The effect of calcination on the microwave dielectric properties of Ba $(Mg_{1/3}Ta_{2/3})O_3$. *Journal of the European Ceramic Society*, volume 21, p. 2745-2750.

[132] Lu, C.H. and Tsai, C.C. (1996). Reaction kinetics, sintering characteristics, and ordering behavior of microwave dielectrics: Barium magnesium tantalate. *Journal of materials research*, volume 11, p. 1219-1227.

[133] Afzal, M., Butt, P., and Ahmad, H. (1991). Kinetics of thermal decomposition of metal acetates. *Journal of Thermal Analysis and Calorimetry*, volume 37, p. 1015-1023.

[134] Sivakumar, G., Ramakrishna, M., Dusane, R.O. and Joshi, S.V. (2015). Effect of SPPS process parameters on in-flight particle generation and splat formation to achieve pure α-Al_2O_3 coatings. *Journal of Thermal Spray Technology*, volume 24, p. 1221-1234.

[135] Govindarajan, S., Dusane, R.O. and Joshi, S.V. (2011). In situ Particle Generation and Splat Formation During Solution Precursor Plasma Spraying of Yttria-Stabilized Zirconia Coatings. *Journal of the American Ceramic Society*, volume 94, p. 4191-4199.

[136] Ismail, H.M. and Hussein, G.A.M. (1996). Texture properties of yttrium oxides generated from different inorganic precursors. *Powder technology*, volume 87, p. 87-92.

[137] Sokołowski, P., Kozerski, S., Pawłowski, L. and Ambroziak, A. (2014). The key process parameters influencing formation of columnar microstructure in suspension plasma sprayed zirconia coatings. *Surface & Coatings Technology*, volume 260, p. 97-106.

[138] Oberste Berghaus, J., Bouaricha, S., Legoux, J.G., and Moreau, C. (2005). Injection conditions and in-flight particle states in suspension plasma spraying of alumina and zirconia nano-ceramics. Proceedings of the International Thermal Spray Conference, Berndt, C. and Lugsheider, E., Ed., May 2-4, (Basel Switzer land), ASM international.

[139] Chen, X., Kuroda, S., Ohnuki, T., Araki, H., Watanabe, M. and Sakka, Y. (2016). Effects of Processing Parameters on the Deposition of Yttria Partially Stabilized Zirconia Coating During Suspension Plasma Spray. *Journal of the American Ceramic Society*, volume 99, p. 3546-3555.

[140] Jiang. X.L. and Boulos, M.I. (2006). Induction plasma spheroidization of tungsten and molybdenum powders. *Transactions of Nonferrous Metals Society of China*, volume 16, p. 13-17.

[141] McCusker, L.B., Von Dreele, R.B., Cox, D.E., Louër, D. and Scardi. P. (1999). Rietveld refinement guidelines. *Journal of Applied Crystallography*, volume 32, p. 36-50.

[142] Young, R.A. Ed., (1993). Introduction to the Rietveld method. *The Rietveld Method*, Oxford University Press, Oxford. p.1-38.

[143] Hill, R.J. and Howard, C.J. (1987). Quantitative phase analysis from neutron powder diffraction data using the Rietveld method. *Journal of Applied Crystallography*, volume 20, p. 467-474.

[144] Fauchais, P., Vardelle, A. and Dussoubs, B. (2001). Quo vadis thermal spraying? *Journal of Thermal Spray Technology*, volume 10, p. 44-66.

[145] Nusair Khan, A. and Lu, J. (2003). Behavior of air plasma sprayed thermal barrier coatings,

subject to intense thermal cycling. *Surface & Coatings Technology*, volume 166, p. 37-43.

[146] Kulkarni, A., Goland, A., Herman, H., Allen, A.J., Dobbins, T., DeCarlo, F., Ilavsky, J., Long, G.G., Fang, S. and Lawton, P. (2006). Advanced neutron and X-ray techniques for insights into the microstructure of EB-PVD thermal barrier coatings. *Materials Science and Engineering: A*, volume 426, p. 43-52.

[147] Hou, H., Veilleux, J., Gitzhofer, F., Wang, Q. and Liu, Y. (2019). Hybrid Suspension/Solution Precursor Plasma Spraying of a Complex Ba $(Mg_{1/3}Ta_{2/3})O_3$ Perovskite: Effects of Processing Parameters and Precursor Chemistry on Phase Formation and Decomposition. *Journal of Thermal Spray Technology*, volume 28, p. 12-26.

[148] Padture, N.P., Schlichting, K.W., Bhatia, T., Ozturk, A., Cetegen, B., Jordan, E.H., Gell, M., Jiang, S., Xiao, T.D., Strutt, P.R., Garcia, E., Miranzo, P. and Osendi, M.I. (2001). Towards durable thermal barrier coatings with novel microstructures deposited by solution-precursor plasma spray. *Acta materialia*, volume 49, p. 2251-2257.

[149] Candidato Jr, R.T., Sokołowski, P., Pawłowski, L. and Denoirjean, A. (2015). Preliminary study of hydroxyapatite coatings synthesis using solution precursor plasma spraying. *Surface & Coatings Technology*, 2015; volume 277, p. 242-250.

[150] Xu, P., Coyle, T.W., Pershin, L. and Mostaghimi, J. (2019). Fabrication of Superhydrophobic Ceramic Coatings via Solution Precursor Plasma Spray Under Atmospheric and Low-Pressure Conditions. *Journal of Thermal Spray Technology*, volume 28, p. 242-254.

[151] Fauchais, P.L., Heberlein, J.V.R. and Boulos, M.I. (2014). Gas Flow-Particle Interaction. *Thermal Spray Fundamentals: From Powder to Part*, Springer Science+Business Media, New York, p. 113-226.

[152] Curry, N., Tang, Z., Markocsan, N. and Nylén P. (2015). Influence of bond coat surface roughness on the structure of axial suspension plasma spray thermal barrier coatings - Thermal and lifetime performance. *Surface & Coatings Technology*, volume 268, p. 15-23.

[153] Ganvir, A., Calinas, R.F., Markocsan, N., Curry, N. and Joshi, S. (2019). Experimental visualization of microstructure evolution during suspension plasma spraying of thermal barrier coatings. *Journal of the European Ceramic Society*, volume 39, p. 470-481.

[154] Joulia, A., Bolelli, G., Gualtieri, E., Lusvarghi, L., Valeri, S., Vardelle, M., Rossignol, S. and Vardelle, A. (2014). Comparing the deposition mechanisms in suspension plasma spray

(SPS) and solution precursor plasma spray (SPPS) deposition of yttria-stabilised zirconia (YSZ). *Journal of the European Ceramic Society*, volume 34, p. 3925-3940.

[155] Sampath, S., Schulz, U., Jarligo, M.O. and Kuroda, S. (2012). Processing science of advanced thermal-barrier systems. *MRS bulletin*, volume 37, p. 903-910.

[156] Wellman, R.G., Deakin, M.J. and Nicholls, J.R. (2005), The effect of TBC morphology on the erosion rate of EB PVD TBCs. *Wear*, volume 258, p. 349-356.

[157] Li, C.J., Yang, G.J. and Ohmori, A. (2006). Relationship between particle erosion and lamellar microstructure for plasma-sprayed alumina coatings. *Wear*, volume 260, p. 1166-1172.

[158] Łatka, L. (2018). Thermal barrier coatings manufactured by suspension plasma spraying-a review. *Advances in Materials Science*, volume 18, p. 95-117.

[159] Curry, N., VanEvery, K., Snyder, T. and Markocsan, N. (2014). Thermal conductivity analysis and lifetime testing of suspension plasma-sprayed thermal barrier coatings. *Coatings*, volume 4, p. 630-650.

[160] Aygun, A., Vasiliev, A.L., Padture, N.P. and Ma, X. (2007). Novel thermal barrier coatings that are resistant to high-temperature attack by glassy deposits. *Acta Materialia*, volume 55, p. 6734-6745.

[161] Viswanathan, V., Dwivedi, G. and Sampath, S. (2015). Multilayer, multimaterial thermal barrier coating systems: design, synthesis, and performance assessment. *Journal of the American Ceramic Society*, volume 98, p. 1769-1777.

[162] Mahade, S., Curry, N., Björklund, S., Markocsan, N., Nylén, P. and Vassen, R. (2017). Erosion performance of gadolinium zirconate-based thermal barrier coatings processed by suspension plasma spray. *Journal of Thermal Spray Technology*, volume 26, p. 108-115.

[163] Feng, B.B., Wang, Y., Jia, Q., Huang, W., Suo, H.L. and Ma, W. (2019). Thermophysical properties of solution precursor plasma-sprayed $La_2Ce_2O_7$ thermal barrier coatings. *Rare Metals*, volume 38, p. 689-694.

[164] Hou, H., Veilleux, J., Gitzhofer, F. and Wang, Q. (2020). Study of the microstructural control of $Ba(Mg_{1/3}Ta_{2/3})O_3$ perovskite thermal barrier coating deposited by solution precursor plasma spray. *Surface & Coatings Technology*, 125633.

[165] Fahrenholtz, W.G. and Hilmas, G.E. (2017). Ultra-high temperature ceramics: materials for extreme environments. *Scripta Materialia*, volume 129, p. 94-99.

[166] Menneveux, J. and Veilleux, J. (2019). An Optical Emission Spectroscopy Study of Plasma–Precursor Interactions in Solution Precursor Plasma Spray. *Journal of Thermal Spray Technology*, volume 28, p. 3-11.

[167] Saha, A., Seal, S., Cetegen, B., Jordan, E., Ozturk, A. and Basu, S. (2009). Thermo-physical processes in cerium nitrate precursor droplets injected into high temperature plasma. *Surface & Coatings Technology*, volume 203, p. 2081-2091.

[168] Kolodiazhnyi, T. (2014). Origin of extrinsic dielectric loss in 1:2 ordered, single-phase $BaMg_{1/3}Ta_{2/3}O_3$. *Journal of the European Ceramic Society*, volume 34, p. 1741-1753.

[169] Li, D.Q., Zhou, L.X., Zhu, K.J., Gu, J. and Zheng, S.H. (2018). Isothermal oxidation behavior of scandium and yttrium co-doped B2-type iron–aluminum intermetallics at elevated temperature. *Rare Metals*, volume 37, p. 690-698.

[170] Salimijazi, H.R., Coyle, T.W., Mostaghimi, J. and Leblanc, L. (2005). Microstructure and failure mechanism in as-deposited, vacuum plasma-sprayed Ti-6Al-4V alloy. *Journal of Thermal Spray Technology*, volume 14, p. 215-223.

[171] Yao, S.W., Liu, T., Li, C.J., Yang, G.J. and Li, C.X. (2017). Epitaxial growth during the rapid solidification of plasma-sprayed molten TiO_2 splat. *Acta Materialia*, volume 134, p. 66-80.

[172] Fukumoto, M., Nishioka, E. and Matsubara, T. (1999). Flattening and solidification behavior of a metal droplet on a flat substrate surface held at various temperatures. *Surface & Coatings Technology*, volume 120, p. 131-137.

[173] Kang, B., Waldvogel, J. and Poulikakos, D. (1995). Remelting phenomena in the process of splat solidification. *Journal of materials science*, volume 30, p. 4912-4925.

[174] Sun, J., Fu, Q.G., Guo, L.P. and Wang, L. (2016). Silicide coating fabricated by HAPC/SAPS combination to protect niobium alloy from oxidation. *ACS applied materials & interfaces*, volume 8, p. 15838-15847.

[175] Nicholls, J.R., Lawson, K.J., Johnstone, A. and Rickerby, D.S. (2002). Methods to reduce the thermal conductivity of EB-PVD TBCs. *Surface & Coatings Technology*, volume 151, p.

383-391.

[176] Huang, H., Liu, C., Ni, L. and Zhou, C. (2011). Evaluation of microstructural evolution of thermal barrier coatings exposed to Na_2SO_4 using impedance spectroscopy. *Corrosion Science*, volume 53, p. 1369-1374.

[177] Habibi, M.H., Wang, L., Liang, J. and Guo, S.M. (2013). An investigation on hot corrosion behavior of YSZ-Ta_2O_5 in Na_2SO_4+ V_2O_5 salt at 1100 °C. *Corrosion Science*, volume 75, p. 409-414.

[178] Park, S.Y., Kim, J.H., Kim, M.C., Song, H.S. and Park, C.G. (2005). Microscopic observation of degradation behavior in yttria and ceria stabilized zirconia thermal barrier coatings under hot corrosion. *Surface & Coatings Technology*, volume 190, p. 357-365.

[179] Jones, R.L. (1997). Some aspects of the hot corrosion of thermal barrier coatings. *Journal of Thermal Spray Technology*, volume 6, p. 77-84.

[180] Zhong, X., Wang, Y., Xu, Z., Zhang, Y., Zhang, J. and Cao, X. (2009). Influence of laser-glazing on hot corrosion resistance of yttria-stabilized zirconia TBC in molten salt mixture of V_2O_5 and Na_2SO_4. *Materials and corrosion*, volume 60, p. 882-888.

[181] Batista, C., Portinha, A., Ribeiro, R.M., Teixeira, V, Oliveira C.R. (2006). Evaluation of laser-glazed plasma-sprayed thermal barrier coatings under high temperature exposure to molten salts. *Surface & Coatings Technology*, volume 200, p. 6783-6791.